

Trapping and Evaporative Cooling of Metastable Helium

Paul Tol

Trapping and Evaporative Cooling of Metastable Helium

VRIJE UNIVERSITEIT

Trapping and Evaporative Cooling of Metastable Helium

ACADEMISCH PROEFSCHRIFT

ter verkrijging van de graad van doctor aan
de Vrije Universiteit Amsterdam,
op gezag van de rector magnificus
prof.dr. T. Sminia,
in het openbaar te verdedigen
ten overstaan van de promotiecommissie
van de faculteit der Exacte Wetenschappen
op woensdag 9 februari 2005 om 13.45 uur
in de aula van de universiteit,
De Boelelaan 1105

door

Paul Johannes Jozef Tol

geboren te Edam

promotor: prof.dr. W. Hogervorst
copromotor: dr. W. Vassen

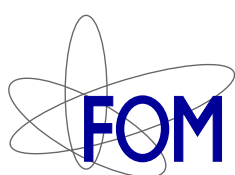
*Voor mijn ouders
Alida en Jan*

*er komen steeds weer mussen uit het ei
er zijn ook telkens kalfjes in de wei
het wordt toch elk jaar een keertje mei*

*weet je wat je denken moet:
elke dag gaat alles beter
ook al gaat het niet zo goed*

Joost Belinfante

ISBN 90-9019004-X



The work described in this thesis was performed as part of the research program of the ‘Stichting voor Fundamenteel Onderzoek der Materie’ (FOM) with financial support of the ‘Nederlandse Organisatie voor Wetenschappelijk Onderzoek’ (NWO), and was carried out at the Laser Centre of the Vrije Universiteit Amsterdam.

Contents

1	Introduction and experimental setup	1
1.1	General introduction	1
1.2	Motivation and outline	4
1.3	The helium source	5
1.4	Collimation and deflection	7
1.5	The Zeeman slower	10
1.6	Magneto-optical trap	15
1.7	Quadrupole and cloverleaf trap	18
1.8	Trap design	24
1.8.1	Implementation	24
1.8.2	Current switching	27
1.8.3	Magnetic field decay	28
1.8.4	Other equipment in trap chamber	30
1.8.5	Pressure	31
1.9	The lasers	31
1.9.1	Laser systems	31
1.9.2	Beam layout	34
1.9.3	Imaging system	36
1.10	Experimental control	37
2	Determination of temperature and number of atoms	39
2.1	Introduction	39
2.2	Time-of-flight measurements	39
2.2.1	MCP detector	39
2.2.2	Magnetic field gradients	40
2.2.3	Offset velocity	42
2.2.4	Examples of fits to TOF signals	45

2.3	Absorption imaging	47
2.3.1	Introduction	47
2.3.2	Two-level system	47
2.3.3	Zeeman sublevels	49
2.3.4	Effective saturation intensity	54
2.3.5	Transmission in practice	60
2.3.6	Fitting absorption images	67
2.3.7	Calibration of MCP detector	68
3	Large numbers of cold He[*] atoms in a MOT	73
3.1	Introduction	73
3.2	Setup	74
3.3	Absorption measurements	75
3.4	Decay experiments	76
3.5	Loss rates	78
3.5.1	Radiative escape	78
3.5.2	Loss rate without light	78
3.5.3	Loss rate with light	78
3.6	Conclusions	80
4	Suppression of Penning ionization by spin polarization of cold He[*] atoms	81
4.1	Introduction	81
4.2	Experiment	82
4.3	Discussion of results	84
4.4	Outlook	85
5	Photoassociation spectroscopy of cold He[*] atoms	87
5.1	Introduction	87
5.2	Photoassociation experiments	88
5.2.1	Setups	88
5.2.2	Ion rate at small detunings	88
5.2.3	Ion rate at large detunings	90
5.2.4	Radiative decay	90
5.3	Analysis of photoassociation spectra	91
5.4	Conclusion	94
6	The three traps	95
6.1	Introduction	95
6.2	Density distribution	95

6.2.1	Density in the traps	95
6.2.2	Density after expansion	98
6.2.3	Density in magnetic traps with finite depth	100
6.3	Magneto-optical trap	102
6.3.1	Characteristics	102
6.3.2	Fluorescence imaging	103
6.3.3	Absorption imaging	105
6.4	Optical molasses and spin polarization	106
6.5	Quadrupole trap	108
6.6	Cloverleaf trap	109
6.6.1	Loading	109
6.6.2	Compression	111
7	Evaporative cooling	115
7.1	Introduction	115
7.2	Scattering length	115
7.3	Theoretical description of cooling experiments	121
7.3.1	Trap depth defined by rf	121
7.3.2	Evaporative cooling model	121
7.3.3	Incorporation of an energy-dependent cross section	125
7.4	Rf experiments	131
7.4.1	Spilling	131
7.4.2	Plain evaporation	132
7.4.3	Potential minimum	134
7.4.4	Tempo of forced evaporation	135
7.4.5	Sweep	137
7.4.6	Optimization	143
Bibliography		147
List of publications		157
Summary		159
Samenvatting		161

1

Introduction and experimental setup

1.1 General introduction

The field of atomic physics has changed drastically since the advent of laser cooling. By manipulating the velocity of atoms with laser light, atomic beams are collimated, deflected, and slowed. Gaseous clouds of atoms can also be confined, especially if the light is combined with a magnetic field in a magneto-optical trap (MOT). In the quest for even colder samples with higher densities, evaporative cooling is the best step forward. To use this technique, the atoms are transferred to a purely magnetic trap. If the more energetic atoms escape from this trap, the mean energy of the remaining atoms decreases, while they occupy a smaller volume. Under the right conditions the density increases even though the number of atoms in the trap decreases. If bosons are used and this process continues until the temperature is so low that the thermal de Broglie wavelength of the atoms is comparable to the distance between them, Bose-Einstein condensation (BEC) sets in. Essentially all atoms will occupy the same lowest quantum state, providing the opportunity to explore quantum phenomena on a macroscopic scale. A Bose-Einstein condensate is very small compared to the gas cloud from which it is formed. However, the interparticle spacing is generally much larger than the scattering length, making it easier to calculate effects of atomic interactions. For some atomic species the interactions can be modified by changing the strength of an applied magnetic field.

To date condensates have been produced of all stable alkali metals, ytterbium, hydrogen, and metastable helium, which is helium in the lowest triplet state (He^*). With a lifetime of more than two hours, He^* can be considered stable in experiments, yet it has a considerable internal energy. In a collision between a He^* atom and another atom this energy can be transferred, leaving the helium atom in the ground state and usually ionizing the other atom. This Penning ionization process is an extra method of detection without actively destroying the sample [69, 76]. Not only the ions and electrons can be detected, but also the He^* atoms themselves, because they almost always release electrons when they hit a metal surface, for instance of an electron multiplier. Another advantage of helium is that properties are easier to calculate. For instance, the scattering length a was expected to be large and positive. This helps evaporative cooling and leads to strong interactions within the condensate, but much weaker than in superfluid liquid

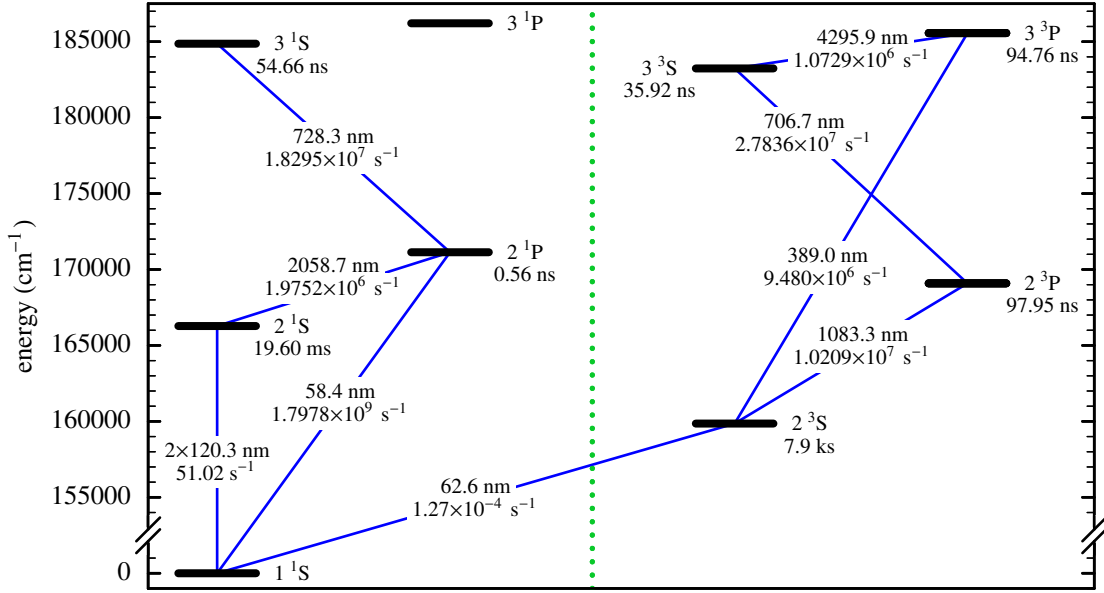


Figure 1.1. Grotrian diagram of the lowest energy levels in helium. The lifetime of each state is given, as well as the vacuum wavelength and theoretical Einstein A coefficient of allowed electric dipole (E1) transitions [17], and of the main decay processes for the metastable states 2^1S_0 (two-photon E1 transition) [15] and 2^3S_1 (single-photon magnetic dipole (M1) transition) [41]. The measured Einstein A coefficient (given with 1σ uncertainty) for the $2^3S_1 - 2^3P_2$ transition is $1.0210(19) \times 10^7 \text{ s}^{-1}$ [43, 44] and for the $2^3S_1 - 1^1S_0$ transition $1.10(17) \times 10^{-4} \text{ s}^{-1}$ [56, 104]. The 2^3P_2 state can also decay directly to the ground state via a magnetic quadrupole transition with $A = 0.327 \text{ s}^{-1}$ according to theory [41] and $A = 0.28(7) \text{ s}^{-1}$ found experimentally [68]. The 2^3P_1 state can decay to the ground state by an E1 transition with $A = 178 \text{ s}^{-1}$ theoretically [41] and $A = 61(14) \text{ s}^{-1}$ experimentally [68]. The 2^3P_0 state can only decay to the ground state using two photons (E1 + M1) or three photons (3 E1), so it should be an extremely weak transition compared to the allowed transition towards 2^3S_1 .

helium, where the interactions cause only a small fraction of atoms to occupy the lowest state.

There are also drawbacks. First, helium has to be excited to the metastable state in a discharge, which is not an efficient process and heats up the gas. Second, Penning ionization limits the density in a MOT. Fortunately, there are fewer restrictions to the density in a magnetic trap, where the atoms are spin-polarized and Penning ionization is forbidden due to the spin conservation rule: collisions take place in the ${}^5\Sigma_g^+$ quasimolecular state with a total spin of 2, while the reaction products have a total spin of at most 1. Some trapped atoms with polarized electron spins are still lost in pair collisions, mainly by relaxation-induced Penning ionization due to the spin-dipole interaction: the interaction between the magnetic (dipole) moments associated with the spin of the two electrons of the colliding atoms leads to a spin-relaxation transition from the ${}^5\Sigma_g^+$ state to the zero spin ${}^1\Sigma_g^+$ state, followed by ionization via the ordinary Penning mechanism. However, the rate at which this process takes place is 4 orders of magnitude smaller than

Table 1.1. Internal energy of the states shown in Fig. 1.1, with 1σ uncertainties evaluated with respect to the ionization limit [18]. The internal energy of the metastable $2\ ^3S_1$ state is enough to ionize any atom, except for helium and neon in the ground state. The intervals between $2\ ^3P_0$, $2\ ^3P_1$, and $2\ ^3P_2$ are 29 616.9509(9) MHz and 2291.1740(14) MHz, respectively [27, 84].

level	energy (cm ⁻¹)	
He ⁺ ($^2S_{1/2}$) limit	198 310.669 1	(24.6 eV)
...		
$3\ ^1P_1$	186 209.365 06(5)	
...		
$3\ ^3P_0$	185 564.854 667(7)	
$3\ ^3P_1$	185 564.584 014(7)	
$3\ ^3P_2$	185 564.562 047(7)	
$3\ ^1S_0$	184 864.830 1(4)	
$3\ ^3S_1$	183 236.792 3(12)	
$2\ ^1P_1$	171 134.896 95(10)	
$2\ ^3P_0$	169 087.830 938(3)	
$2\ ^3P_1$	169 086.843 023(3)	
$2\ ^3P_2$	169 086.766 597(3)	
$2\ ^1S_0$	166 277.440 265(5)	
$2\ ^3S_1$	159 855.974 457(2)	(19.8 eV)
$1\ ^1S_0$	0.000 ± 0.002	

Penning ionization of unpolarized atoms, as was first calculated in 1994 by Shlyapnikov et al. [79].

An overview of the lowest states in helium and the transitions between them is given in Fig. 1.1 and Table 1.1. For all experiments described in this thesis the $2\ ^3S_1 - 2\ ^3P_2$ transition is used, with a vacuum wavelength $\lambda = 1083.330\ 64\ \text{nm}$ [18]. The natural line width Γ of this transition in rad s⁻¹ is equal to the Einstein A coefficient, $\Gamma = A = 1.0209 \times 10^7\ \text{s}^{-1}$, and the saturation intensity is $I_{\text{sat}} = \pi h c \Gamma / 3\lambda^3 = 1.6703\ \text{W/m}^2$. The C_3 coefficient used for the description of the long-range part of the $2\ ^3S - 2\ ^3P$ molecular interaction potential is: $C_3 = 3\hbar\lambda^3\Gamma/32\pi^3 = 6.406a_0\hbar^2/m_e = 6.406E_ha_0^3$. The mass of ${}^4\text{He}$ is 4.002 603 254 153(64) u [93] or $6.646\ 4777(5) \times 10^{-27}\ \text{kg}$.

Although helium is the second most abundant element in the universe, the supply on earth is limited and dwindling: due to its small mass, helium leaves the atmosphere when released into the air. It is extracted from natural gas that contains at least 0.3% helium. Annually 0.1 km³ (1 atm, 15 °C) helium is produced, of which 80% in the United States and 16% in Algeria [61, 62]. The U.S. has about 5 km³ of helium and sells (partly from stocks) 0.13 km³ a year, almost 4 times as much as 20 years ago. A quarter is used for cryogenics, especially as a coolant for superconducting magnets

in magnetic resonance imaging scanners. Other major uses are pressurizing/purging, welding cover gas, and controlled atmospheres. Including resources that are only marginally economic, the world supply of helium is estimated to be 25 km³. There are no natural resources of the ³He isotope; it is available in appreciable quantities only because it is the decay product of tritium, which is used in nuclear weapons to increase their efficiency. The U.S. needs annually about 2.5 kg tritium to compensate the decay in the existing arsenal, corresponding to 20 m³ ³He per year [100].

1.2 Motivation and outline

In short, the experiment aiming at BEC can be described as follows. A dc discharge in a helium source excites a small fraction of atoms to the metastable state. To reduce the velocity of these atoms, the source is cooled with liquid nitrogen. The beam of metastable atoms is collimated, deflected, and separated from the other helium atoms using converging laser beams. Then they are slowed down in a Zeeman slower and captured in a MOT. To be able to reduce the temperature, this trap is replaced by a cloverleaf trap at the same position. To keep as many atoms as possible, the atoms are subjected to optical molasses and spin polarization in the time between the two trapping situations. After the cloud of atoms is compressed, a radio frequency (rf) field is applied for evaporative cooling. Sweeping the field frequency downward, most atoms are removed but the remaining cloud is colder and denser. Penning-ionized atoms (during trapping) and metastable atoms (after the trap is switched off) are detected by microchannel plate (MCP) detectors. Absorption imaging also gives information on the number of atoms, as well as on the cloud size.

The goal was to reach BEC at the end of the rf sweep. However, after 17 s of evaporative cooling there seemed to be $N = 4 \times 10^5$ atoms in the trap at a temperature $T = 6 \mu\text{K}$ (Fig. 1.2, left), while according to a simulation with $a = 10 \text{ nm}$, 10 times more atoms were expected to remain in the trap at this temperature. With a larger scattering length—previously reported values were 16 nm and 20 nm—the discrepancy would be even worse. However, the simulation could not be trusted too much, as it did not include an energy-dependent elastic scattering cross section σ . Concentrating on the experimental data, other difficulties were found. Due to a technical problem the temperature no longer decreased after 17 s, but even if this was solved, a simple extrapolation of the points up to 17 s showed that quantum degeneracy would only be reached far below 1 μK . Gravitational sag does not allow such low temperatures to be reached in our setup. If a condensate could be made, it would contain 10^5 or fewer atoms, which is difficult to detect. Actually, the sweep already had an inauspicious start. The collision rate, which has to be large for efficient evaporation, is proportional to N/T for a thermalized cloud in a harmonic trap assuming σ is a constant, and this ratio showed a rapid decrease as a function of time (Fig. 1.2, right). However, not only the simulation, but also the experimental data needed corrections: the number of atoms in the cloverleaf trap was according to the He* detector more than twice the number determined with absorption imaging. In addition, at low temperatures atoms arrived later at the detector than expected.

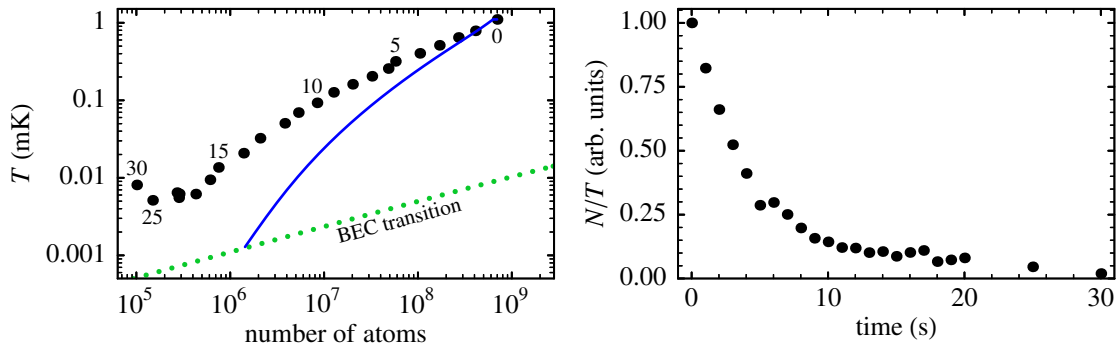


Figure 1.2. Left plot: uncorrected temperature versus uncorrected number of atoms during evaporative cooling, with a simulation for $a = 10 \text{ nm}$; numbers indicate sweep time in seconds. Right plot: quotient of uncorrected number of atoms and temperature as a function of sweep time. Corrected data are given in Figs. 7.17 and 7.20.

Both detection techniques turn out to be influenced by the presence of magnetic fields. Chapter 2 describes how the temperature and number of atoms are determined, corrected, and made consistent. In Chapter 7 the theory of evaporative cooling is given, including an energy-dependent elastic scattering cross section. It is applied to the data, taking into account that the cloud is larger than predicted by theory, but only during the sweep. With these corrections a scattering length of about 10 nm is consistent with the experimental data. According to an exact expression, the collision rate increases during the sweep; the approximation by N/T cannot be used for the cloverleaf trap, at least not for the temperature range in the experiment.

Experiments start with trapping as many atoms as possible in the MOT, minimizing losses due to Penning ionization. The method is described in Chapter 3, together with the determination of loss rate coefficients with and without near-resonant laser light present. Suppression of Penning ionization, when the atoms are spin-polarized, is demonstrated experimentally in Chapter 4. Measurements in Chapter 5 of the loss rate coefficient for ionization in the presence of light as a function of the laser frequency show for the first time photoassociation resonances. Metastable atoms are observed to leave the trap without ionization. In Chapter 6 all trapping stages before evaporative cooling are characterized using the methods described in Chapter 2. Cloud sizes in the magnetic traps are compared with theory, taking into account the effect of expansion and probing on the density distribution. Finally in Chapter 7 evaporative cooling and related experiments are discussed. This chapter continues with a detailed description of the experimental setup, which is shown schematically in Fig. 1.3.

1.3 The helium source

The design of the He^* source has been described by Rooijakers et al. [70]. Helium atoms colliding with electrons in a dc discharge are excited to the metastable $2\ ^3\text{S}_1$ state. If this happens in the 2 cm expansion region between the nozzle (diameter 0.25 mm) and the skimmer, the atoms can stay in this state without further collisions. During

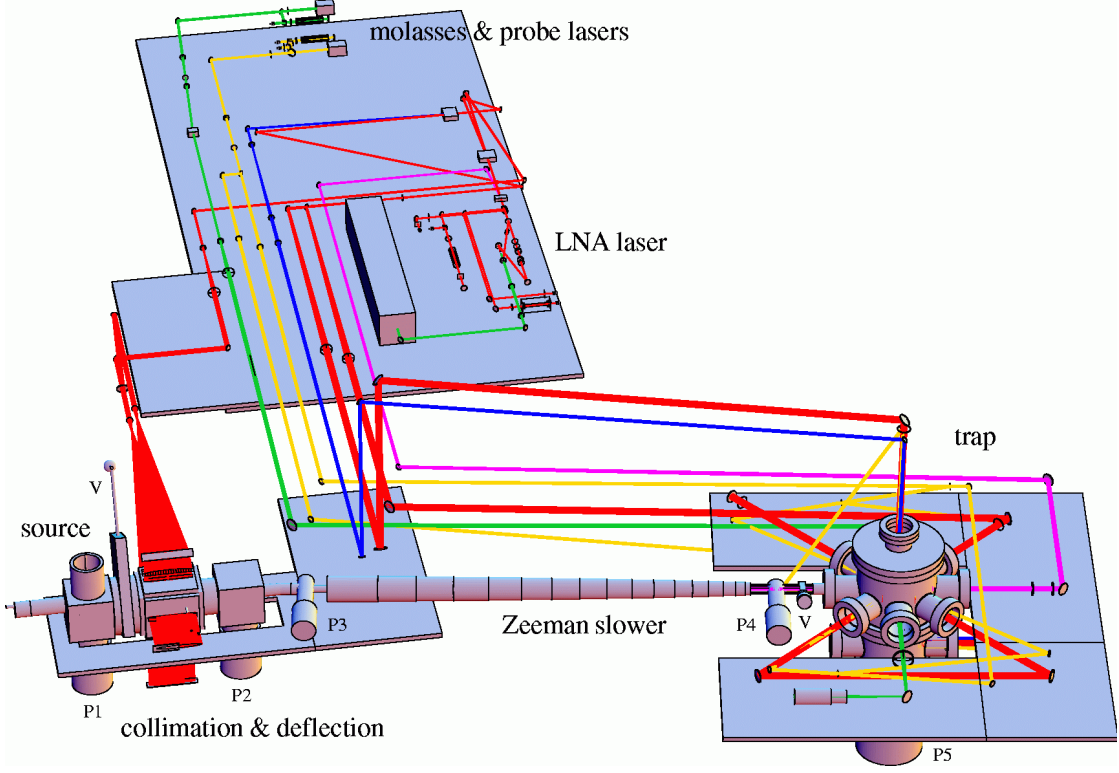


Figure 1.3. The experimental setup, with pumps P1–P5 and valves V. The deflection angle is exaggerated: in reality it is only 0.8° . Figures 1.5, 1.28, 1.31, and 1.32 show more detailed views.

Table 1.2. Characteristics of the turbomolecular drag pumps (Pfeiffer Vacuum) used in the setup, labelled as in Fig. 1.3. Pumps P2–P4 are wide range, i.e. with a longer drag stage that increases the compression ratio. P6 is the backing pump for P5; P1–P4 and P6 are backed by MD 4T diaphragm pumps with a volume flow rate of 0.9 l/s.

pump	type	volume flow rate (l/s)			compression ratio		
		N_2	He	H_2	N_2	He	H_2
P1	TMH 520	520	500	480	$> 10^{12}$	5×10^7	5×10^6
P2	TPH 450 H	450	390	350	$> 10^{12}$	2×10^8	1×10^6
P3, P4	TPU 062 H	56	49	43	$> 10^{13}$	3×10^8	3×10^6
P5	TMU 1600	1500	1450	1150	$> 10^{12}$	1×10^8	3×10^6
P6	TMU 065	56	48	36	$> 10^{10}$	1×10^7	1×10^5

experiments the pressure in the source chamber is 9×10^{-6} mbar, in the collimation chamber behind the skimmer it is two orders of magnitude lower. Information on all pumps is given in Table 1.2.

Figure 1.4 shows the He^* velocity distribution when the discharge current is 5 mA. The most probable velocity is 1110 m/s and the full width at half-maximum (FWHM) is 480 m/s. The He^* source intensity is $3 \times 10^{14} \text{ s}^{-1} \text{ sr}^{-1}$ [70]. The fraction of atoms

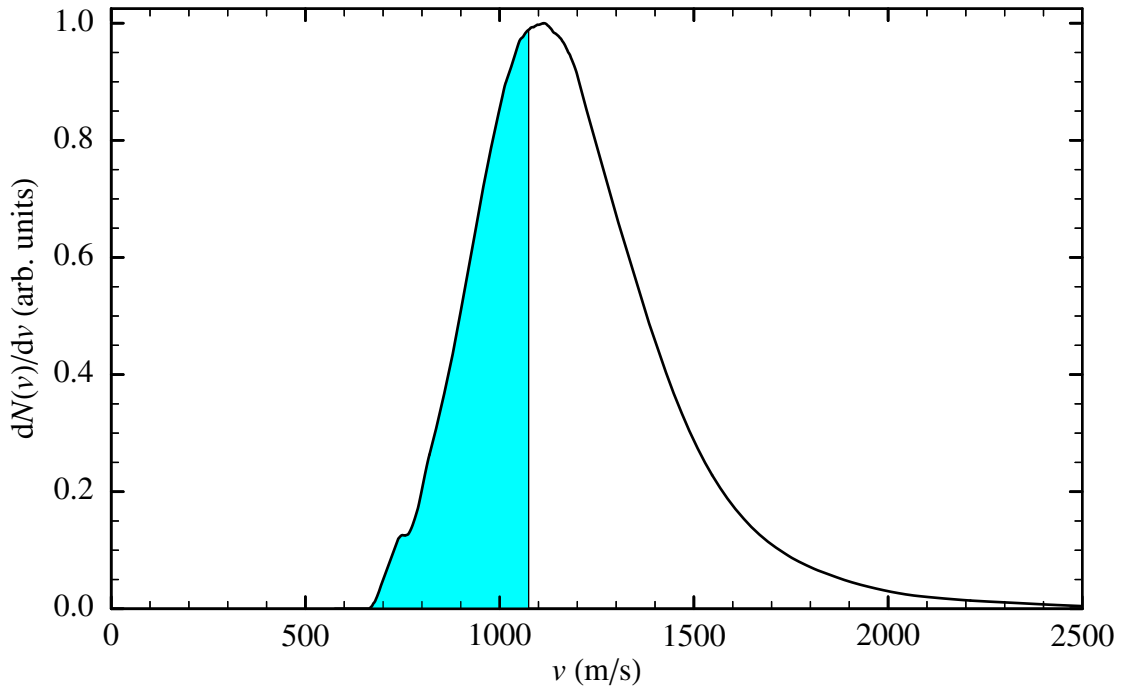


Figure 1.4. Velocity distribution of the He^* source at a discharge current of 5 mA. The fraction that becomes resonant in the Zeeman slower is shaded.

that can be slowed down by the Zeeman slower (§1.5) is 35%, shown as a shaded area in the figure. The source can also be used at a discharge current that is twice as large: although the velocity distribution shifts to higher values, leading to a smaller fraction of slow He^* atoms, the source intensity increases as well, resulting in approximately the same absolute number of He^* atoms that can be slowed.

1.4 Collimation and deflection

If a resonant circularly-polarized plane wave with wave vector \mathbf{k} ($|\mathbf{k}| = 2\pi/\lambda$) travels perpendicularly to an atomic beam with velocity \mathbf{v} , the beam is deflected by the (spontaneous) radiation pressure force[†]

$$F = \hbar k \frac{\Gamma}{2} \frac{I/I_{\text{sat}}}{1 + I/I_{\text{sat}}} \frac{1}{1 + (2\mathbf{k} \cdot \mathbf{v}/\Gamma')^2}, \quad (1.1)$$

with laser intensity I , Doppler shift $\mathbf{k} \cdot \mathbf{v}$, and effective line width $\Gamma' = \Gamma\sqrt{1 + I/I_{\text{sat}}}$. At first the Doppler shift is $\mathbf{k} \cdot \mathbf{v} = 0$ and the maximum force is exerted, but due to the changing direction of \mathbf{v} the atoms will soon get out of resonance and the deflection process

[†]In terms of the treatment of absorption in Chapter 2, this force is the average absorption rate per atom in steady state of $\frac{1}{2}\Gamma(I/I'_{\text{sat}})/(1 + I/I'_{\text{sat}})$ times the momentum $\hbar\mathbf{k}$ of a photon, with effective saturation intensity $I'_{\text{sat}} = fI_{\text{sat}}/\chi$. Because the atoms are excited on a closed transition $f = 1$, and because the laser line width is negligible and Doppler broadening irrelevant, $\chi = 1/[1 + (2\Delta'/\Gamma)^2]$ applies, with effective detuning $\Delta' = \mathbf{k} \cdot \mathbf{v}$. Using Eq. (2.44) the expression for the force given is found.

stops. The curved-wavefront technique [94] uses a converging laser beam, where the wave vector stays almost perpendicular to the atom velocity, keeping the force large.

Consider an atom with velocity $\mathbf{v} = v_x \hat{\mathbf{x}} + v_y \hat{\mathbf{y}} + 0 \hat{\mathbf{z}}$ crossing the y axis at time $t = 0$ at $y(0) = R$. At this moment it enters a laser beam (initially) in the $-\hat{\mathbf{y}}$ direction, which converges at the origin and hence has a wavefront with radius of curvature R . Then we switch to a rotating frame with coordinates $\mathbf{r}' = x' \hat{\mathbf{x}}' + y' \hat{\mathbf{y}}' + z' \hat{\mathbf{z}}'$ and time-dependent angular velocity $\omega = \omega \hat{\mathbf{z}}$ for which the atom remains on the y' axis. The wave vector is $\mathbf{k} = -k \hat{\mathbf{y}}'$. An acceleration \mathbf{a} and velocity \mathbf{v} in the lab frame are given in the rotating frame by [12]

$$\mathbf{a} = \frac{d^2 \mathbf{r}'}{dt^2} + \frac{d\omega}{dt} \times \mathbf{r}' + 2\omega \times \frac{d\mathbf{r}'}{dt} + \omega \times (\omega \times \mathbf{r}'), \quad (1.2)$$

$$\mathbf{v} = \frac{d\mathbf{r}'}{dt} + \omega \times \mathbf{r}'. \quad (1.3)$$

As $\mathbf{F} = m\mathbf{a}$ with helium mass m , this leads to the set of differential equations

$$2\omega v_{y'}' = -y' \frac{d\omega}{dt}, \quad (1.4)$$

$$m \frac{dv_{y'}'}{dt} = m\omega^2 y' - \hbar k \frac{\Gamma}{2} \frac{I/I_{\text{sat}}}{1 + I/I_{\text{sat}}} \frac{1}{1 + (2kv_{y'}'/\Gamma)^2}. \quad (1.5)$$

If the first and last ray of light that the atom encounters make an angle α , the atom leaves the laser beam at an angle $\theta_{\text{out}} = \alpha + \arctan(v_{y'}'/\omega y')$ with the x axis.

Under experimental conditions $\omega(t) \approx \omega(0) = -v_x(0)/R$ and $y'(t) \approx R$, and the laser intensity is assumed to be constant along the atomic trajectory. The steady-state values of $v_{y'}'$ are the solutions of $dv_{y'}'/dt = 0$, which are

$$v_{y'}' = \frac{\Gamma}{2k} \sqrt{\frac{\hbar k \Gamma}{m} \frac{I}{2} \frac{R}{I_{\text{sat}}} \frac{R}{v_x^2(0)} - \frac{I}{I_{\text{sat}}} - 1} \quad (1.6)$$

and $v_B' = -v_A'$, as long as

$$v_x(0) < v_{\text{max}} = \sqrt{\frac{\hbar k \Gamma}{m} \frac{I/I_{\text{sat}}}{2} \frac{R}{1 + I/I_{\text{sat}}}} R. \quad (1.7)$$

For any initial velocities $v_x(0) < v_{\text{max}}$ and $v_y(0) < v_A'$, after sufficient interaction time the result is $v_{y'}' \approx v_B'$ and $\theta_{\text{out}} \approx \alpha + |v_B'|/v_x(0)$: all these atoms leave the laser beam at approximately the same angle, which is larger than α . As a numerical example, in our setup the interaction region for deflection has a length of 9.5 cm, the radius of curvature is $R = 11$ m, and the laser intensity is $I = 1.4$ mW/cm², although it is effectively a factor of 17/10 smaller due to the linear polarization (see Chapter 2). The relevant range of longitudinal velocities is between 700 m/s (lowest available velocity from the source) and 1075 m/s (highest velocity decelerated in Zeeman slower), well within the range that is deflected: $v_{\text{max}} = 2070$ m/s. The laser beam converges over an angle $\alpha = 0.5^\circ$, but the deflection angle ranges from $\theta_{\text{out}} = 0.7^\circ$ for $v_x(0) = 1075$ m/s with $v_B' = -3.5$ m/s,

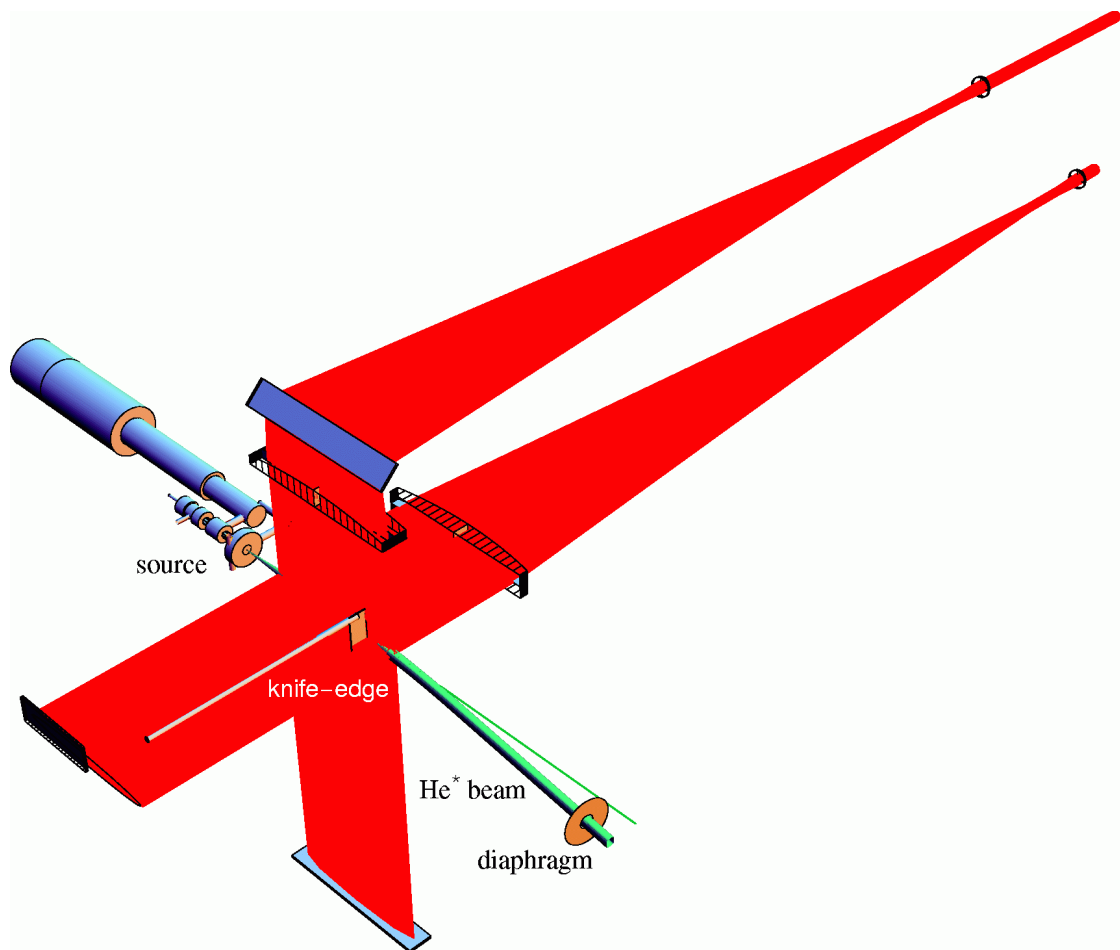


Figure 1.5. Experimental arrangement of collimation and deflection. The atomic beam deviates from a straight trajectory, shown as a line. The angle is exaggerated.

to $\theta_{\text{out}} = 1.0^\circ$ for $v_x(0) = 700 \text{ m/s}$ with $v'_B = -5.9 \text{ m/s}$. Taking into account the velocity distribution and solving Eq. (1.5) exactly, the average angle is $\theta_{\text{out}} = 0.8^\circ$.

If the laser beam is retroreflected with the rays ending the interaction parallel to the y axis, the atoms within a capture angle of $2[\alpha + v'_A/v_x(0)]$ are collimated, without deflection. In the setup both effects are combined: a horizontal ($R = 11 \text{ m}$) and vertical ($R = 15 \text{ m}$) laser beam with widths of 19 cm are retroreflected, but the second half of the horizontal mirror is blocked (Fig. 1.5). Hence, in the vertical direction the full interaction region is used for collimation, whereas in the horizontal direction half is used for collimation and half for deflection. About 4 cm before the end of the interaction region a knife-edge is placed, around which the He^* atoms are deflected, into a tube 40 cm further down the beam line. The knife-edge blocks the straight trajectory between the nozzle and the tube of other helium atoms and photons from the discharge. A diaphragm would also produce a pure He^* beam, but the tube (length 10 cm, inner diameter 0.3 cm) allows better differential pumping. The atomic beam is switched off by removing the light beams. By implementing the deflection, the lifetime of He^* clouds in the cloverleaf trap has become a factor of 5 longer (see also §1.8.5).

The final diameter of the He* beam is proportional to the capture angle; the beam intensity is only increased further by starting the collimation earlier. Here the distance between the source nozzle and the interaction region is about 3 cm. A smaller radius of curvature increases the beam width and therefore the number of atoms with a particular v_x , but v_{\max} decreases. There is a minimum radius of curvature that includes only the longitudinal velocities decelerated by the Zeeman slower. However, best results are achieved with a larger R , because the theory above does not take into account that the atoms interact with four beams simultaneously. In the vertical direction the atomic beam is wider than the tube. Therefore the radius of curvature of the vertical beams is allowed to be even larger.

The capture angle without collimation, i.e. the ratio of the tube diameter and the distance between the nozzle and the further end of the tube, is 4.4 mrad and the corresponding solid angle is 1.5×10^{-5} sr. Collimation increases the solid angle of captured atoms that enter the tube by a factor of 30. Since the source has a He* intensity of $3 \times 10^{14} \text{ s}^{-1} \text{ sr}^{-1}$, of which 35% is slow enough to be decelerated by the slower, the rate at which slow metastable helium atoms enter the Zeeman slower is expected to be about $5 \times 10^{10} \text{ s}^{-1}$. However, in practice the loading rate of the MOT is 70 times larger due to collimation (measured with the deflection light blocked and a straight beam line), resulting in 9 times more atoms in the trap.[†] The different behaviour of the theoretical solid angle and the experimental loading rate can have several causes. First, the theory may be too simple for multiple laser beams, as mentioned above. Indeed, the beam alignment that produces the most atoms in the trap is slightly different from the expected alignment. Second, the enhanced loading rate may be due to the slowing process after the collimation: a parallel atomic beam expands less in the slower than an already diverging beam (see §1.5). When the deflection is added, this extra advantage is cancelled by the spread in angle θ_{out} .

1.5 The Zeeman slower

A counter-propagating laser beam decelerates the atoms, which absorb photons coming from one direction and spontaneously emit them in all directions. The laser excites the closed transition between 2^3S_1 , magnetic sublevel $m_J = +1$ and 2^3P_2 , $m_J = +2$ (a $\Delta m = +1$ transition), so the atoms can cycle many times between the lower and upper state. An atom at position x with velocity $v(x)$ exhibits a Doppler shift $\Delta_D(x) = -kv(x)$, which is compensated by a magnetic field produced by the Zeeman slower. If the quantization axis is chosen in the same direction as the field, a magnetic field B shifts the energy of sublevel m_J in first order by

$$\delta E = g m_J \mu_B B, \quad (1.8)$$

with Bohr magneton μ_B and Landé g factor ($g = 2.002$ for 2^3S_1 and $g = 1.501$ for 2^3P_2). The transition frequency is shifted by the difference of the Zeeman shifts of the upper and lower level, in this case $\Delta_B(x) = 1.000 \mu_B B(x)/\hbar$ (also at high fields). Including

[†]The loading rate is proportional to N^2/V , with number of trapped atoms N in cloud volume V (§§3.3–3.4), and the volume depends only weakly on N (§6.3.2).

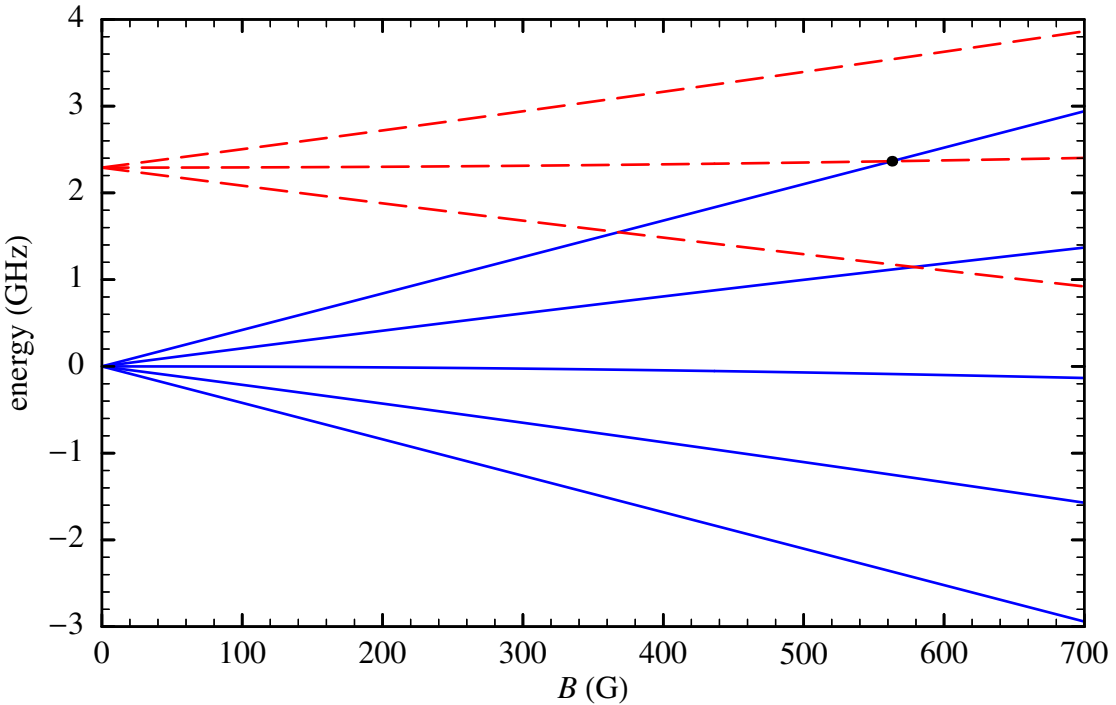


Figure 1.6. Energy of the ${}^3\text{P}_2$ sublevels (solid curves) and ${}^3\text{P}_1$ sublevels (dashed curves) as a function of magnetic field, relative to the ${}^3\text{P}_2$ energy without field. The dot indicates the level crossing at which atoms will be lost from the closed transition used in the Zeeman slower.

a fixed laser detuning Δ , the resonance condition is $\Delta_D(x) + \Delta_B(x) = \Delta$: a decreasing atomic velocity v can be compensated by a decreasing field strength B .

The simplest configuration would be $\Delta = 0$ and a magnetic field decreasing along the atomic trajectory from a high value to almost zero. However, at a field of 563 G the upper level of the transition has the same energy as the $2\ {}^3\text{P}_1, m_J = 0$ level (Fig. 1.6) [13]. If an atom is excited to the wrong level due to an imperfect polarization of the light beam, it can decay to the $2\ {}^3\text{S}_1, m_J = 0$ or -1 level, where it can no longer be excited by the laser (the crossing at 368 G with $2\ {}^3\text{P}_1, m_J = -1$ does not cause this effect, as it would involve a $\Delta m = -2$ transition). Therefore the field is kept smaller than this value, ranging from 517 G to -140 G (Fig. 1.7). With the help of an acousto-optic modulator (AOM), the laser is given a detuning $\Delta/2\pi = -250$ MHz. A large detuning has the additional advantage that atoms trapped in the MOT do not interact with the slower beam. The slower consists of 2.4 km copper wire with a diameter of 0.18 cm, wound in sections of up to 19 layers around a tube with a diameter of 3.8 cm (see Fig. 1.7). The first part of the slower tube has a double wall to allow the use of water cooling.

The laser beam is made circular by a beam expander with cylindrical lenses (not shown in the figures) and is focused weakly with a 2 m spherical lens because the atomic beam becomes wider towards the end of its trajectory. It has a Gaussian intensity profile with an rms radius of 0.6 cm when it enters the slower and 0.2 cm on the other side, with a total power of 11 mW. The light has the same direction as the magnetic field in the main part of the slower (and the quantization axis). To make $\Delta m = +1$ transitions,

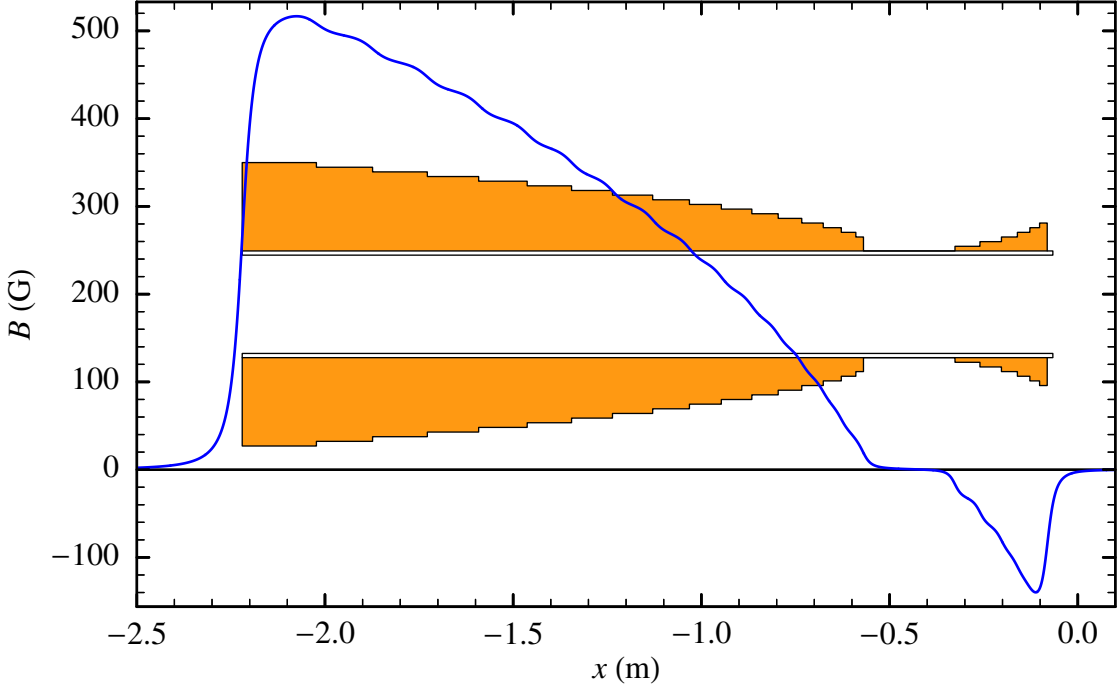


Figure 1.7. Magnetic field produced by the Zeeman slower as a function of position on the slower axis relative to the trap centre. A positive field is in the $-\hat{x}$ direction. In the background is shown a cross section of the slower at the same horizontal scale (and arbitrary vertical scale).

the light is therefore given a right-handed circular polarization, i.e. looking against the oncoming light, the electric field vector rotates clockwise.

The acceleration of the atoms in the $-\hat{x}$ direction due to the radiation pressure force is

$$a = \frac{\hbar k}{m} \frac{\Gamma}{2} \frac{I/I_{\text{sat}}}{1 + I/I_{\text{sat}}} \frac{1}{1 + (2\Delta'/\Gamma')^2}, \quad (1.9)$$

with effective detuning $\Delta' = \Delta - \Delta_B - \Delta_D$. The maximum acceleration is given to the atoms when they are excited resonantly:

$$a_{\text{max}} = \frac{\hbar k}{m} \frac{\Gamma}{2} \frac{I/I_{\text{sat}}}{1 + I/I_{\text{sat}}}. \quad (1.10)$$

If we expect that the atoms are able to follow the field and stay at resonance, $\Delta' = 0$ leads to a velocity $v(x) = [\Delta_B(x) - \Delta]/k$ and an acceleration [59]

$$a_{\text{res}} = -\frac{dv}{dt} = -v \frac{dv}{dx} = -v \frac{\mu_B}{\hbar k} \frac{dB}{dx} = \frac{\mu_B}{\hbar^2 k^2} (\hbar \Delta - \mu_B B) \frac{dB}{dx}. \quad (1.11)$$

As can be seen in Fig. 1.8, a_{res} is not always smaller than a_{max} : at the points where the slower coil changes by 1 turn, the absolute field gradient is too large to keep the atoms exactly at resonance all the time. However, as long as there are stretches between these points where the field gradient is much smaller, the atoms are still slowed down. This can be seen in Fig. 1.9, which shows the solution of Eq. (1.9) for several starting

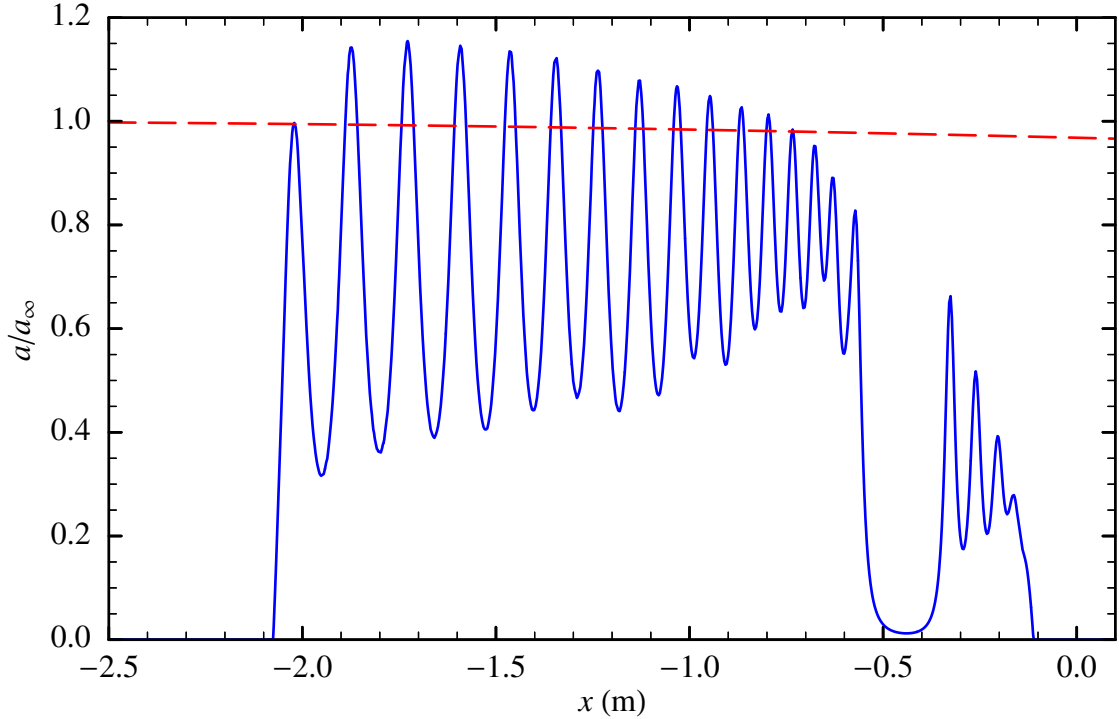


Figure 1.8. The acceleration a_{res} in the $-\hat{x}$ direction as a function of position on the axis of the Zeeman slower if the atom would stay at resonance with the light, given as a fraction of the largest possible acceleration $a_{\infty} = \hbar k \Gamma / 2m = 4.7 \times 10^5 \text{ m/s}^2$ at resonance in the limit of infinite intensity. The dashed curve is the maximum acceleration a_{max} with the intensity used.

velocities in the range produced by the helium source. The grey band constitutes the velocities resonant with the light, with a width corresponding to the effective line width Γ' . The velocity of the atoms has a tendency to stay just below the resonant velocity. All atoms with starting velocities up to 1075 m/s are decelerated to 30 m/s. This includes atoms that are originally in the 2^3S_1 $m = -1$ and $m = 0$ levels. The $\Delta m = 1$ transitions from these two levels exhibit a larger Zeeman shift than from $m = +1$, which means that an atom with a given velocity is resonant with these transitions where the magnetic field is smaller: around 9 cm before entering the slower, atoms are pumped out of $m = -1$ and a centimetre later out of $m = 0$. There is enough time to absorb at least 10 photons on each transition.

As the atoms go through more and more absorption and emission cycles, the atomic beam becomes wider. After N photons have been absorbed, the transversal rms velocity is $v_{\text{rms}} = \sqrt{\alpha N} v_{\text{rec}}$, with recoil velocity $v_{\text{rec}} = \hbar k / m$ and factor α taking into account the anisotropy of spontaneous emission; for circularly polarized light $\alpha = 3/10$ [47]. This can be written as $v_{\text{rms}}^2 = \sum_i^N v_1^2$, with $v_1 = \sqrt{\alpha} v_{\text{rec}}$ the average contribution to v_{rms} of cycle i . A cycle i at time t_i contributes an amount $v_1(t - t_i)$ to the transversal rms position y_{rms} at time t :

$$y_{\text{rms}}^2 = \sum_i^N v_1^2(t - t_i)^2. \quad (1.12)$$

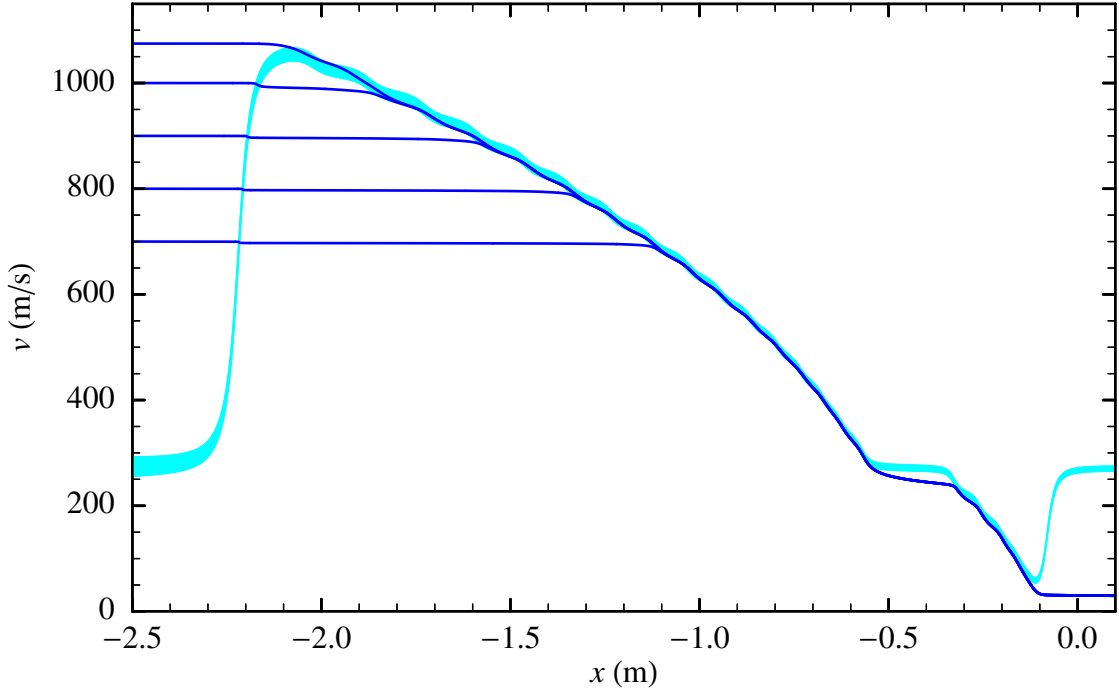


Figure 1.9. Atom velocity as a function of position on the axis of the Zeeman slower, with starting values of (700, 800, 900, 1000, and 1075) m/s before entering the slower. The grey band indicates resonant velocities; for atom velocities at the band edges the deceleration has half the maximum value.

An approximation can be constructed by assuming the average time between two cycles is a constant Δt . Then $t_i = i\Delta t$, $t = N\Delta t$, and

$$y_{\text{rms}}^2 = v_1^2 \sum_i^N (N\Delta t - i\Delta t)^2 \quad (1.13)$$

$$= v_1^2 (\Delta t)^2 \sum_i^N (N - i)^2 \quad (1.14)$$

$$= v_1^2 (\Delta t)^2 \frac{1}{6} N(N - 1)(2N - 1) \quad (1.15)$$

$$= v_1^2 t^2 \left(\frac{N}{3} - \frac{1}{2} + \frac{1}{6N} \right). \quad (1.16)$$

At time t the velocity in the longitudinal direction is $v_x(t) = v_x(0) - Nv_{\text{rec}}$. The relation between $y_{\text{rms}}(t)$ and $v_x(t)$ for large N becomes

$$y_{\text{rms}}(t) \approx \sqrt{\frac{1}{3}} v_{\text{rms}} t \quad (1.17)$$

$$= \sqrt{\frac{1}{3} \alpha N} v_{\text{rec}} t \quad (1.18)$$

$$= \sqrt{\frac{1}{3} \alpha v_{\text{rec}} [v_x(0) - v_x(t)] t}. \quad (1.19)$$

Although Δt is not constant, the error in y_{rms} at the end of the slower is only about 10%. Figure 1.10 shows the path of atoms with transversal position y_{rms} for the highest cap-

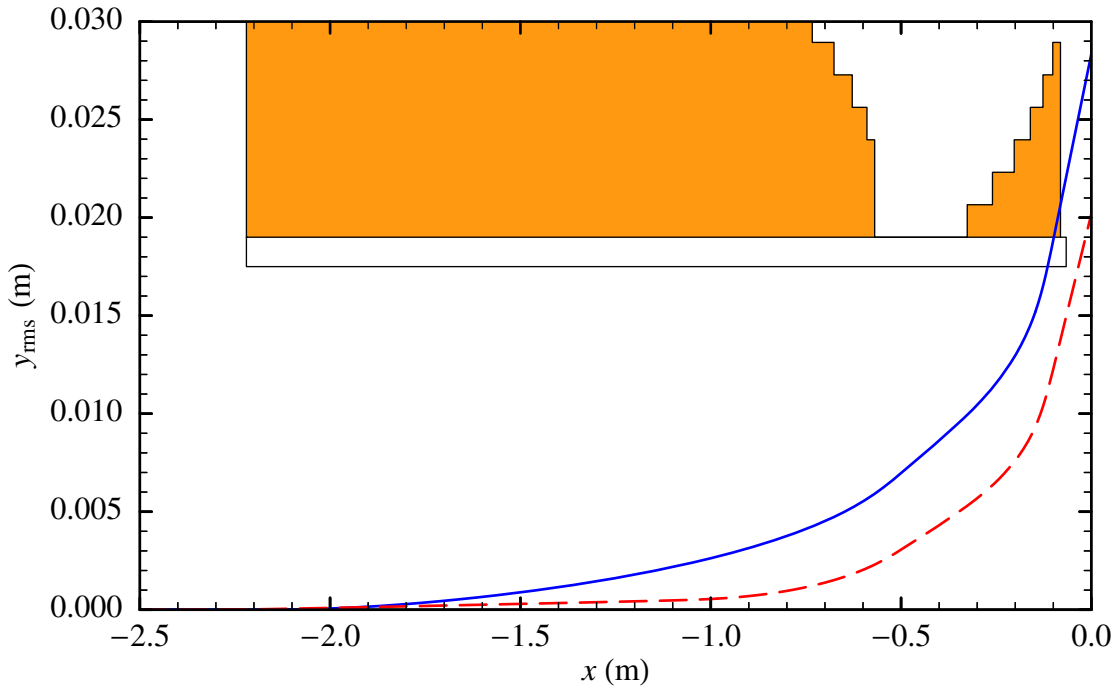


Figure 1.10. The rms radius of the atomic beam due to the radiation pressure force as a function of position in the Zeeman slower relative to the trap centre for the fraction of atoms with the largest starting velocity decelerated by the slower (1075 m/s, solid curve) and with the smallest experimental starting velocity (700 m/s, dashed curve). In the background the cross section of the slower is shown to scale.

tured velocity 1075 m/s and for the lowest available starting velocity 700 m/s, calculated with Eq. (1.12). The atomic beam expands mainly at the end of the slower, until the rms width becomes as large as the inner diameter of the slower tube. To keep the beam width to a minimum, the last slower part should be as short as possible, within the limits set by the maximum absorption rate. However, the slower end should also be placed close to the trap. Due to physical restrictions only this last point was realized. Atoms moving away from the axis have a larger end velocity, due to the smaller off-axis laser intensity. For paths as shown in Fig. 1.10 the end velocity is about 50 m/s. This is still slow enough, because the largest velocity captured by the MOT is estimated to be 60 m/s [32]. The slower and MOT have a combined loading efficiency of about 40%: of the $5 \times 10^{10} \text{ s}^{-1}$ He* atoms with velocities up to 1075 m/s entering the slower, $2 \times 10^{10} \text{ s}^{-1}$ are loaded into the trap.

1.6 Magneto-optical trap

After the atoms are decelerated, they are trapped in a configuration of twelve coils and six laser beams, not all used at the same time (Fig. 1.11). Two pairs of coils are positioned around the same vertical axis, a distance of 10 cm apart, with radii of 3 cm (referred to as the set of ‘small axial coils’) and 7 cm (‘large axial coils’). The other

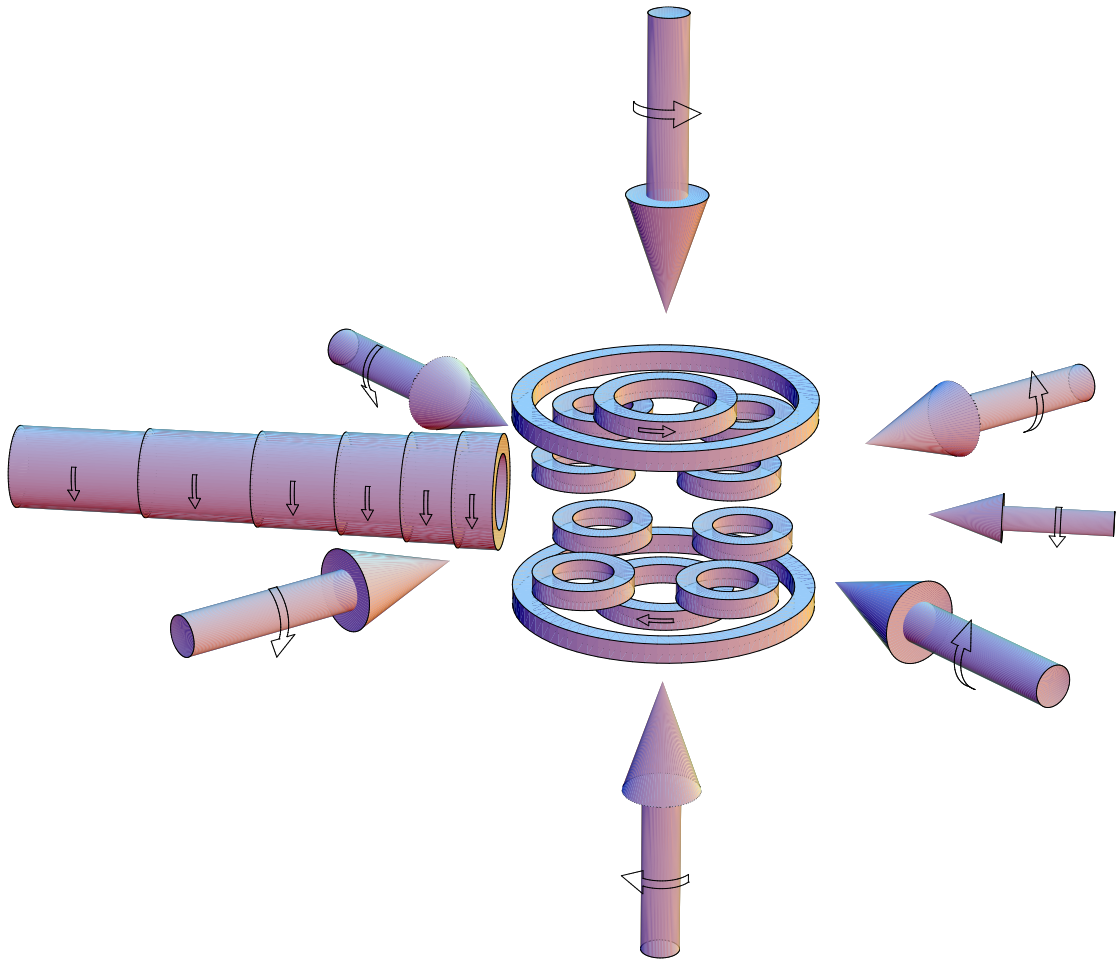


Figure 1.11. The slower and trap configuration for a MOT showing only the coils and light beams (three-dimensional arrows), with black arrows indicating the direction of the current (if running) and the polarization, respectively.

eight ‘radial coils’ have radii of 2 cm and are placed 5 cm away from the vertical axis, forming two cloverleafs of four coils each that are vertically 6 cm apart. All coils consist of 14 turns, made of rectangular coated copper wire with a cross section of 3 mm × 2 mm. Along three orthogonal axes pairs of counterpropagating laser beams can be applied.

While the slower is still on, the atoms are trapped in a MOT, for which only the small axial coils and the laser beams are needed.[†] The horizontal MOT beams are at an angle of 45° with the slower axis (Fig. 1.11) to avoid interference with the slowing process [63]. The coils are used to produce a quadrupole magnetic field: two circular current loops of radius r , in the planes $z = \pm a$ with the centres on the z axis ($a > 0$), carrying a steady current I in opposite directions (at $z = \pm a$ polarization along $\pm \hat{z}$), produce a magnetic field that in cylindrical coordinates near the origin to second order is given by

[†]The MOT field in Chapters 3–5 is produced by a pair of coils with a mutual distance of 6 cm, each consisting of 10 flat copper rings with a diameter of 8 cm separated by 0.5 mm ceramic spacers. This setup is better when only a MOT is made, because switching is faster and no water cooling is required.

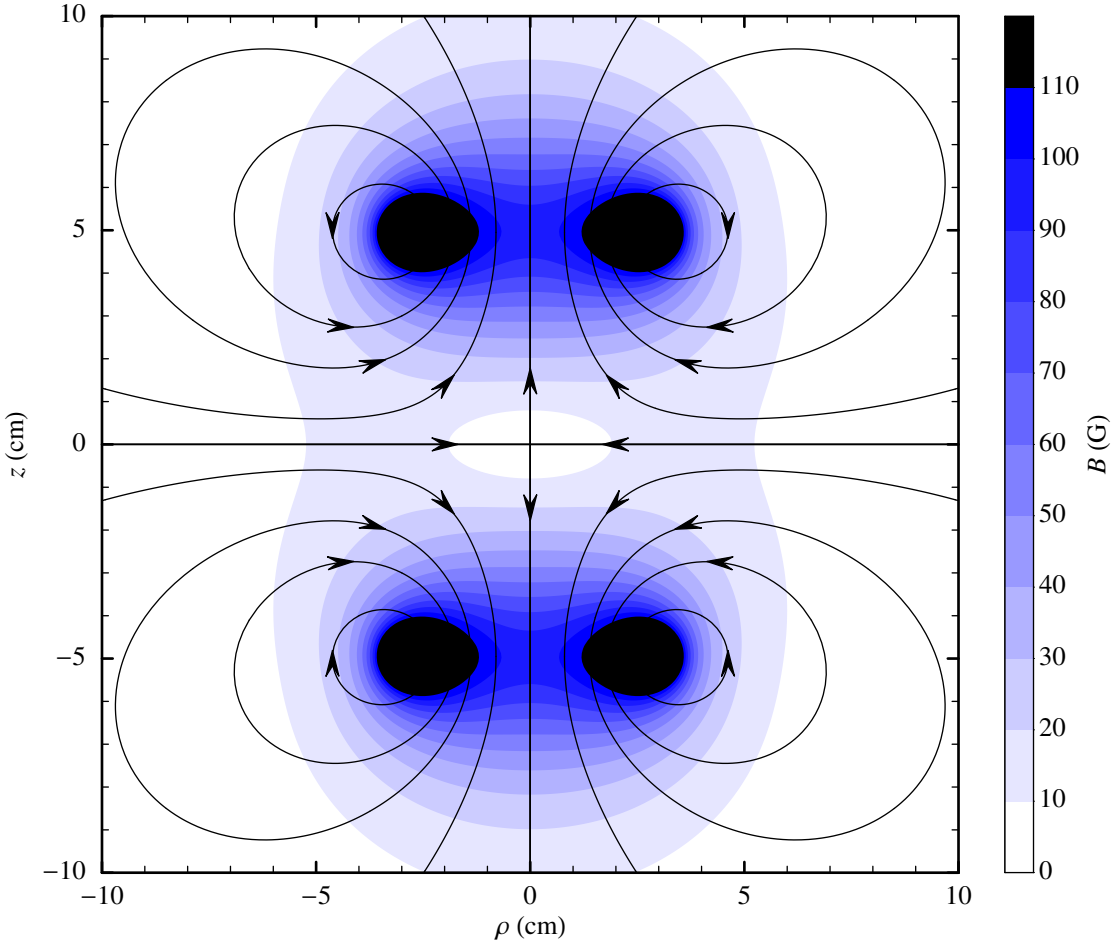


Figure 1.12. Field lines showing the direction of the quadrupole magnetic field used for the MOT in any plane through the z axis. Shading is used to indicate the absolute field.

the vector

$$(B_z, B_\rho, B_\varphi) \approx (2\gamma_0 z, -\gamma_0 \rho, 0), \quad (1.20)$$

with gradient

$$\gamma_0 = \frac{3\mu_0 I a r^2}{2(a^2 + r^2)^{5/2}}. \quad (1.21)$$

The absolute value of the field is $B = |\mathbf{B}| \approx \gamma_0 \sqrt{\rho^2 + 4z^2}$. For the small axial coils $\gamma_0/I = 0.184 \text{ G cm}^{-1} \text{ A}^{-1}$, where the number of turns has already been included: I is the physical current through the wire, 33 A for the MOT. The light is red-detuned by 35 MHz and has a circular polarization, left-handed along axes where the magnetic field vector points towards the trap centre, right-handed when it points away from the centre. Figure 1.12 shows the field vector as a function of position in any plane through the z axis, connected up to form field lines. A negative radial coordinate is defined as $(z, -\rho, \varphi) = (z, \rho, \varphi + \pi)$.

The trapping mechanism can be explained by considering an atom on one of the six half-axes, for instance the positive z axis. The quantization axis is taken along the same

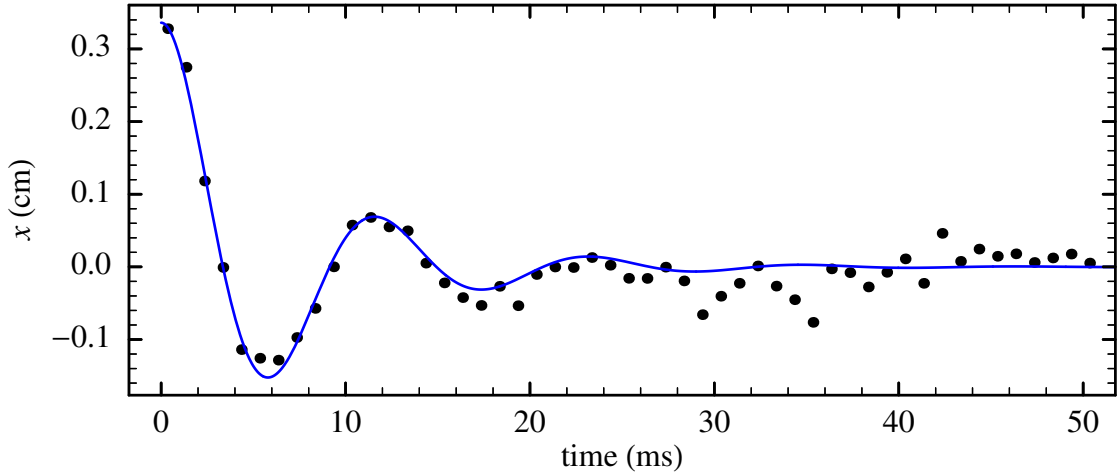


Figure 1.13. Horizontal position of the MOT cloud as a function of time after switching off the uncompensated slower field. The curve is the fitted solution of the equation of motion for a damped harmonic oscillator $x''(t) + \gamma x'(t) + \omega_0^2 x(t) = 0$, with $\omega_0/2\pi = 89$ Hz and $\gamma/2\pi = 44$ Hz.

direction as the local magnetic field. The light pushing the atom towards the centre (in the example directed towards negative z) excites the atom on $\Delta m = -1$ transitions. The beam in the opposite direction has the same polarization and induces $\Delta m = +1$ transitions. Due to the magnetic field the first type of transitions is shifted to the red and the second type to the blue. Because the light has a large red detuning, the atom is closer to resonance with the first beam, absorbs more photons from this beam, and experiences a net force towards the centre. Near the centre the field is almost zero and the atom interacts equally with all six light beams. In this optical molasses the velocity decreases on average to 2 m/s, corresponding to a temperature of 1 mK.

There exist two configurations for the polarizations of the currents and light beams. They are equivalent except for an asymmetry introduced by the slower field. In our setup the field produced by the last part of the slower has the same direction as the MOT quadrupole field in this area, which increases the capture velocity a little. The zero field point, i.e. the trap centre if all light beams have equal intensity, moves 0.38 cm away from the slower. When the slower is switched off while the MOT is still present, the cloud needs about 30 ms to settle closer to the slower (Fig. 1.13). Although in this time only 6% of the atoms are lost, it is more convenient not to have this delay and to compensate the displacement with extra coils outside the trap chamber, which are switched off at the same time as the slower and the MOT. These coils also compensate any shifts due to intensity imbalances in the MOT beams in order to place the MOT at the same position as the cloverleaf trap.

1.7 Quadrupole and cloverleaf trap

The cloud will be made colder and denser in a magnetic trap (without light). The potential energy in a magnetic field, given by Eq. (1.8), is used to keep the atoms in a (local)

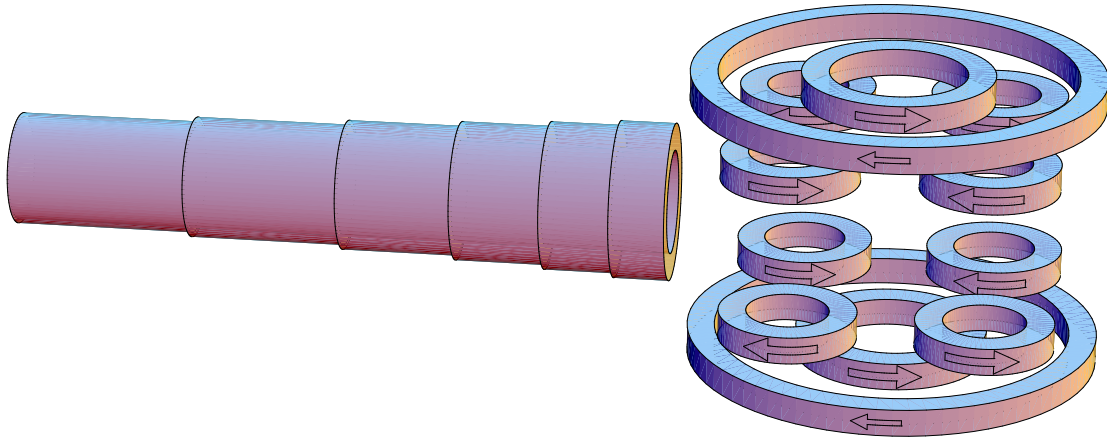


Figure 1.14. The configuration for a cloverleaf trap showing only the coils, with black arrows indicating the direction of the current, if running.

field minimum. This can only be done for atoms whose energy is an increasing function of the field, in the 2^3S_1 case for those in the $m = +1$ level. To trap all atoms, they are first optically pumped to this level. A disadvantage of a magnetic trap is that it is too weak to trap atoms directly from the slower. Therefore the MOT is used as an intermediate stage, and after the MOT is switched off a field-free optical molasses [48] is applied to cool the atoms further before switching on the magnetic trap.

A simple magnetic trap is created by the quadrupole field of the MOT. However, on opposite sides of the centre the field is in opposite directions. For an atom moving through the centre the field vector changes too quickly, causing a Majorana spin flip to a sublevel where the atom is no longer trapped. This happens more at lower temperatures when the atoms move closer to the centre. In a trap with a nonzero field minimum these spin flips are avoided. A Ioffe quadrupole trap is such a trap, consisting usually of two pairs of circular loops and four straight wires. Here a version is used where the wires are replaced by eight more loops, a so-called cloverleaf trap (Fig. 1.14).

Two circular current loops of radius r , in the planes $z = \pm a$ with the centres on the z axis, carrying a steady current I in the same direction (polarization along $+\hat{z}$), produce a magnetic field that in cylindrical coordinates near the origin to second order is given by the vector

$$(B_z, B_\rho, B_\varphi) \approx (B_0 + \gamma_2(z^2 - \frac{1}{2}\rho^2), -\gamma_2 z\rho, 0), \quad (1.22)$$

with central field

$$B_0 = \frac{\mu_0 I r^2}{(a^2 + r^2)^{3/2}} \quad (1.23)$$

and axial curvature

$$\gamma_2 = \frac{3\mu_0 I r^2 (4a^2 - r^2)}{2(a^2 + r^2)^{7/2}}. \quad (1.24)$$

The arrangement with $r = 2a$ and therefore $\gamma_2 = 0$ is known as a Helmholtz coil. The combination of two loop pairs with opposite currents gives the opportunity of setting values for B_0 and γ_2 independently. If one of the pairs is a Helmholtz coil the central field can be made arbitrarily small without reducing the axial curvature.

Four long straight wires, parallel to the z axis, at a distance $\rho = s$ and at angles $\varphi = 0, \pi/2, \pi$, and $3\pi/2$, carrying a steady current I with sign $\cos 2\varphi$ (positive means in the $+\hat{z}$ direction), produce a magnetic field that can be approximated near the origin by

$$(B_z, B_\rho, B_\varphi) \approx (0, \gamma_1 \rho \sin 2\varphi, \gamma_1 \rho \cos 2\varphi), \quad (1.25)$$

with radial gradient $\gamma_1 = 2\mu_0 I / \pi s^2$. Eight circular current loops of radius r , in the planes $z = \pm a$ with the centres at a distance $\rho = s$ and at angles $\varphi = \pi/4, 3\pi/4, 5\pi/4$, and $7\pi/4$, carrying a steady current I with sign $(z \sin 2\varphi)/a$ (positive means polarization along $+\hat{z}$), produce also a magnetic field approximated near the origin by Eq. (1.25), this time with radial gradient

$$\gamma_1 \approx \frac{15\mu_0 I a r^2 s^2}{(a^2 + s^2)^{7/2}}. \quad (1.26)$$

Using loops instead of wires has the advantage of full optical access in the $z = 0$ plane.

The absolute field of a Ioffe quadrupole trap is

$$B \approx \sqrt{(\gamma_1^2 - B_0 \gamma_2) \rho^2 + (B_0 + \gamma_2 z^2)^2 - 2\gamma_1 \gamma_2 z \rho^2 \sin 2\varphi + \frac{1}{4} \gamma_2^2 \rho^4}. \quad (1.27)$$

For the configuration used, this equation is correct within 10% up to a distance of at least 1.8 cm from the centre. However, for modelling purposes it will be simplified to $B \approx \sqrt{(\gamma_1^2 - B_0 \gamma_2) \rho^2 + (B_0 + \gamma_2 z^2)^2}$, which already shows deviations of more than 10% at a distance of 0.6 cm from the centre. The second-order expansion $B \approx B_0 + \gamma_2 z^2 + \frac{1}{2}(\gamma_1^2/B_0 - \gamma_2)\rho^2$ describes the field within a radius of 0.3 cm around the centre before compression, which reduces to 80 μm after compression. Hence for very small He* clouds the potential energy is given by $U = 2\mu_B B \approx U_0 + \frac{1}{2}m(\omega_z^2 z^2 + \omega_\rho^2 \rho^2)$, with mass m , potential minimum $U_0 = 2\mu_B B_0$, and trap frequencies $\omega_z = \sqrt{4\mu_B \gamma_2/m}$ and $\omega_\rho = \sqrt{2\mu_B (\gamma_1^2/B_0 - \gamma_2)/m}$.

The small axial coils in the setup are characterized by $B_0/I = 0.828 \text{ G A}^{-1}$ and $\gamma_2/I = 0.099 \text{ G cm}^{-2} \text{ A}^{-1}$, the large axial coils (with negative current) by $B_0/I = 1.388 \text{ G A}^{-1}$ and $\gamma_2/I = 0.019 \text{ G cm}^{-2} \text{ A}^{-1}$, and the radial coils by $\gamma_1/I = 0.345 \text{ G cm}^{-1} \text{ A}^{-1}$. As before, the numerical values include the number of turns. The axial curvature of the large axial coils is much smaller than that of the small axial coils but not zero, leading to a weaker axial confinement for small B_0 . Because gravity is directed in the $-\hat{z}$ direction, this also increases gravitational sag (see §6.2.3). Ideally the two sets of axial coils are used in series with the same power supply: any deviation in the current would induce opposite changes in the two fields, which cancel at the centre. However, the central field produced by the two sets is not nearly the same for equal currents, which makes the scheme more complicated (§1.8.2). To load the atoms in the trap, the currents through the small axial, large axial, and radial coils are 123 A, -68 A, and 110 A, respectively. Then the axial curvature and radial gradient are increased and the central field decreased to compress the cloud, until the currents are 160 A, -95 A, and 200 A, respectively. Unless stated otherwise, numerical examples below refer to the cloverleaf trap before compression.

The trap depth is determined by the lowest field barrier, the location and height of which have to be found using exact expressions for the magnetic field [7]. Figure 1.15

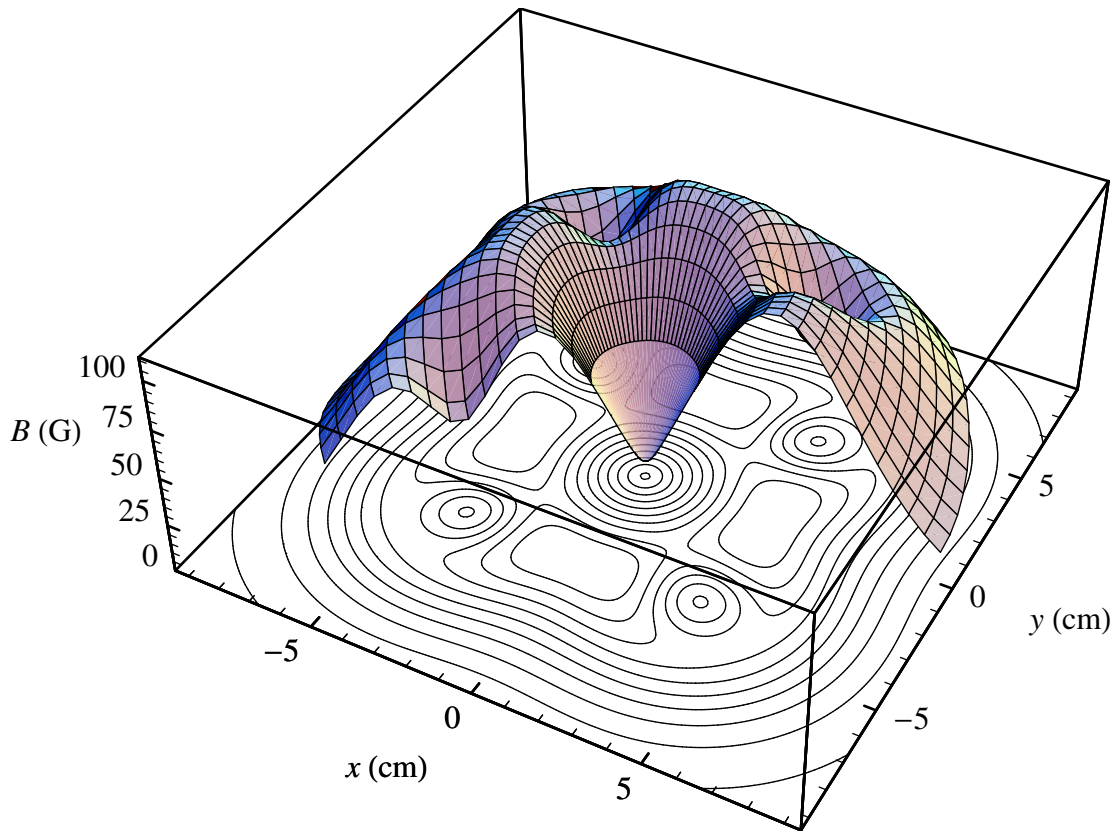


Figure 1.15. Absolute magnetic field of the cloverleaf trap before compression as a function of position in the $z = 0$ plane. In the contour plot lines are drawn at 10, 20, ..., 100 G.

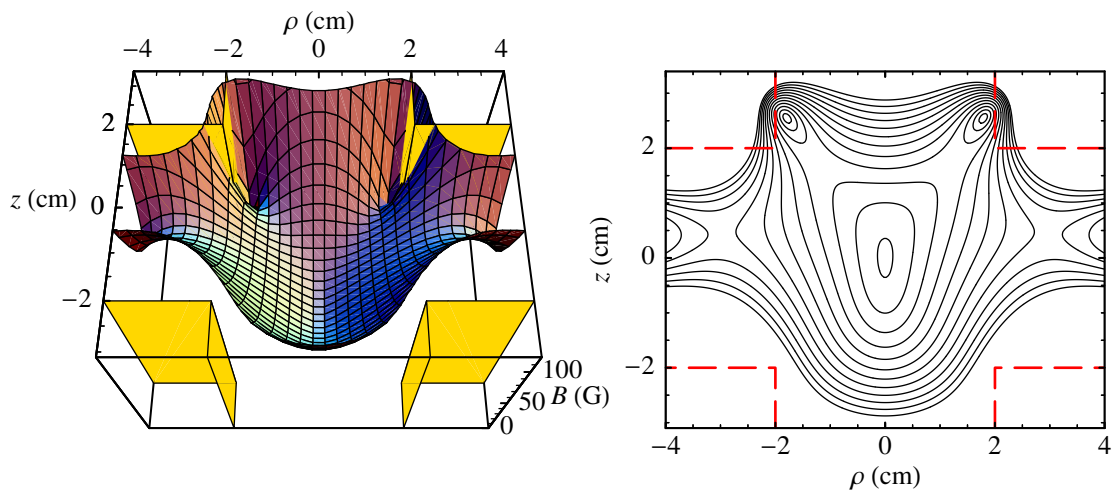


Figure 1.16. Absolute magnetic field of the cloverleaf trap before compression as a function of position in the $x = y$ plane. Contours are given at 10, 20, ..., 120 G. The vertical walls and dashed lines are the outlines of the closest coil containers.

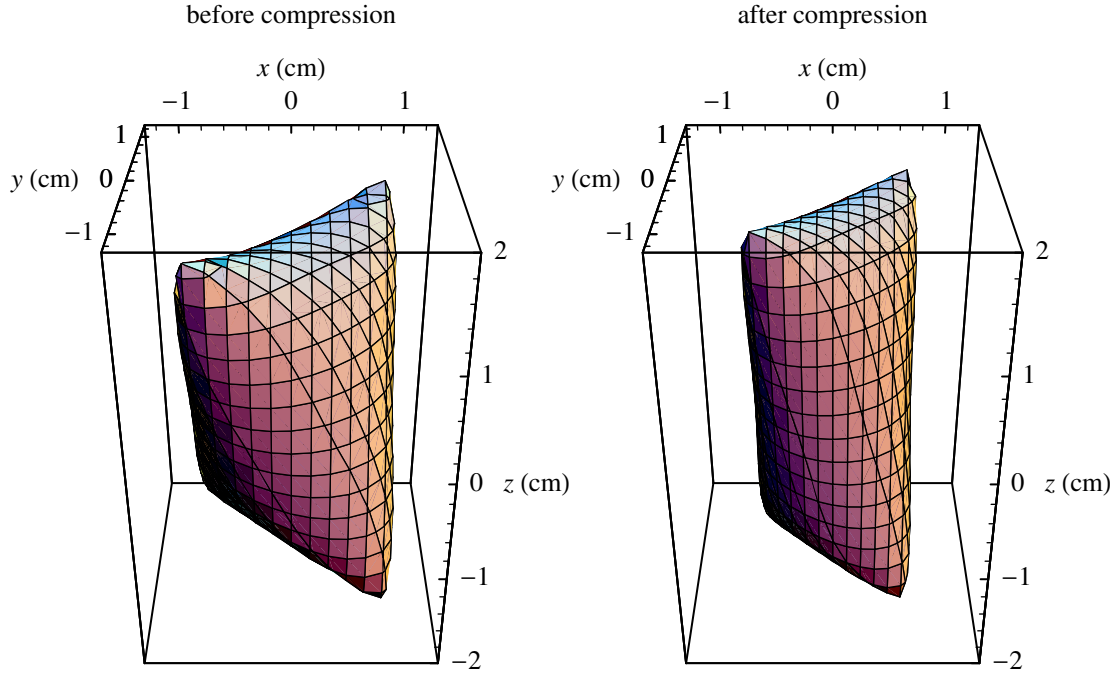


Figure 1.17. The contour where the absolute magnetic field has the value at the lowest saddle points (before compression 34 G and after compression 48 G), defining the trap volume. The saddle points are located at the four ‘corners’ of the contour.

shows the absolute field in the $z = 0$ plane. Near the trap centre the field is cylindrically symmetric around the z axis, but the barrier is lower in the direction of the radial coils than on the axes, with a value of 81 G. Figure 1.16 shows the field in the $x = y$ plane, containing two of those barriers at $(\rho, z) = (\pm 3.0, 0.4)$ cm. At $(\rho, z) = (\pm 1.2, 1.8)$ cm another type of saddle points is seen, which in this realization of a cloverleaf trap is lower: 34 G. The other two saddle points of this type are located in the $x = -y$ plane at $(\rho, z) = (\pm 1.2, -1.8)$ cm. The difference between the height of the lower saddle points and the central field of 8.6 G is the trap depth of 26 G, corresponding to a temperature of 3.4 mK. Trapped atoms acquiring too much energy after an elastic collision will leave the trap via these saddle points. The three-dimensional contour of the saddle point field (Fig. 1.17) encloses the area occupied by trapped atoms. The closest point of the setup lies outside this region. After compression the trap becomes 85% deeper, but the saddle points move only 0.3 cm, leaving the trap volume almost the same. Varying the currents, the saddle points can shift up to 2 cm.

On the z axis, the field is directed parallel to this axis. However, the field cannot be said to point in more or less the same direction in the area where most atoms are located. First, already at small distances the field vector points away from the z direction (Fig. 1.18): for instance, near the centre after compression the radial component is larger than the axial one when $\rho > 67 \mu\text{m}$. Second, although the absolute field near the centre is cylindrically symmetric around the z axis, the field direction is not (Fig. 1.19). Only in the $x = \pm y$ planes does the field not point out of the plane. Even in those planes a plot of the field lines becomes complicated at larger distances (Fig. 1.20).

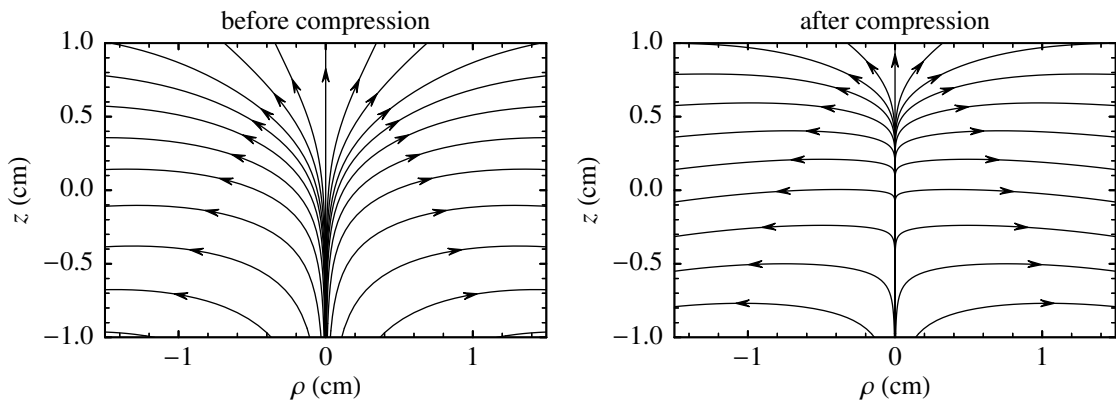


Figure 1.18. Field lines showing the magnetic field direction in the cloverleaf trap in the $x = y$ plane.

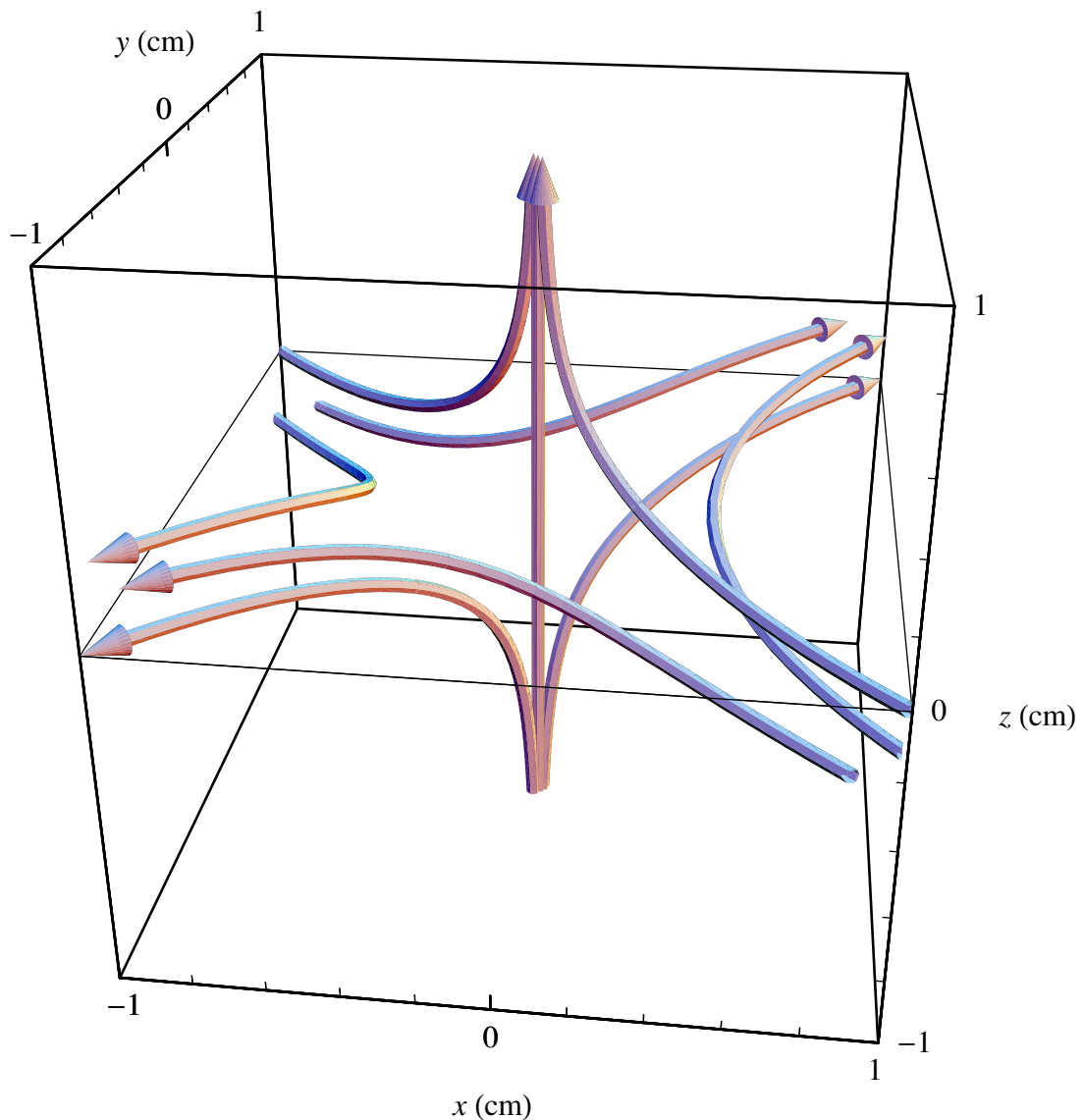


Figure 1.19. Three-dimensional field lines in the cloverleaf trap before compression.

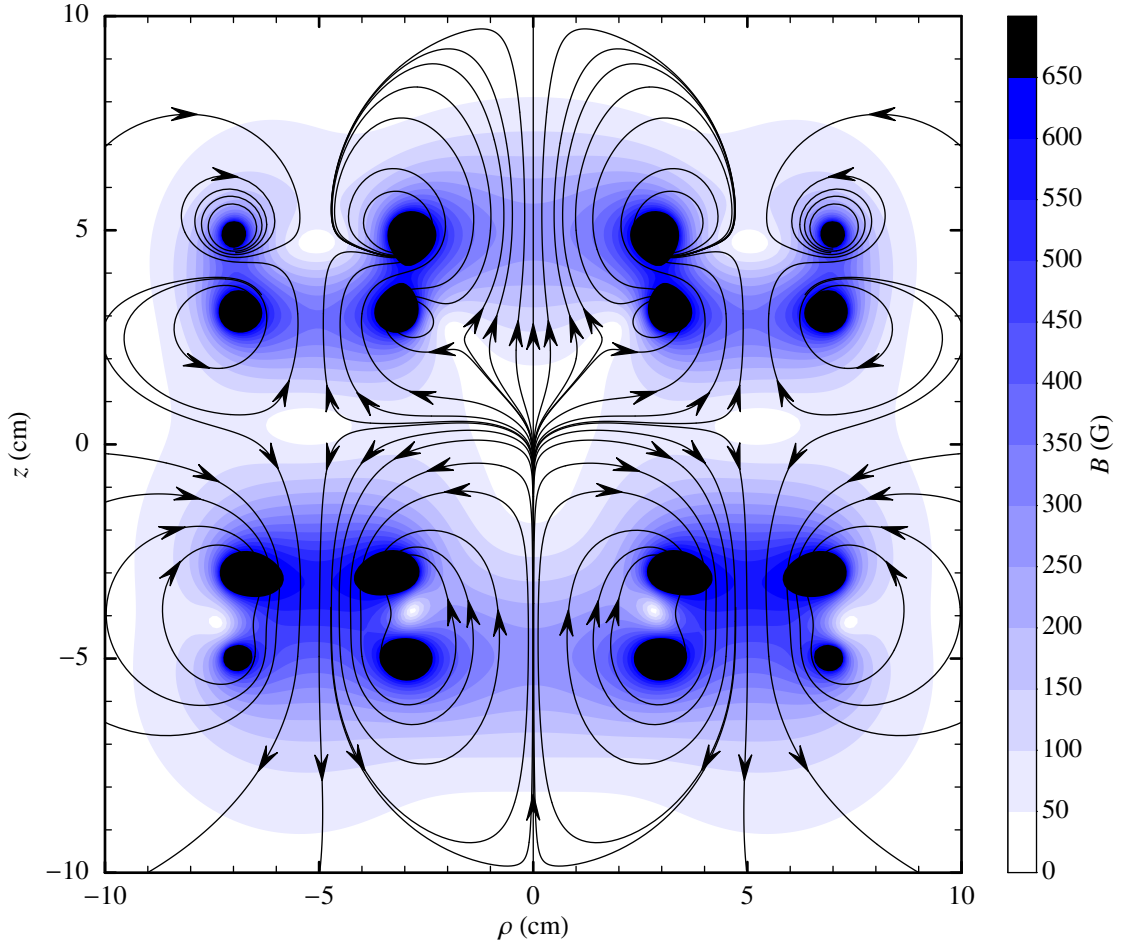


Figure 1.20. Field lines in the cloverleaf trap before compression, in the $x = y$ plane with the same coordinate ranges as in Fig. 1.12. Shading is used to indicate the absolute field.

1.8 Trap design

1.8.1 Implementation

The mechanical structure of the trap consists of two double-sided container sets made of stainless steel with low magnetic permeability (AISI 316), with on one side a container for two axial coils, on the other side four containers for radial coils (Fig. 1.21). The coils are bound with PVC tie wraps, coated with varnish to make them rigid, and glued to the metal with an epoxy resin (Emerson & Cuming Styccast 2850 GT). The ends of the radial coils stick through holes to the other side of the plate, where they are connected in series. The two container sets are attached to steel bars and hung from the lid of the trap chamber (Fig. 1.22). On the covers of the axial coil containers are feedthroughs with ceramic isolation (Fig. 1.23). The six wire ends of each container set (two for each axial coil and two for the radial coil set) are welded on the other side of the ceramic parts to copper tubes. The maximum diameter of the laser beams is 4 cm, which is the vertical distance between the containers and the diameter of the central holes in the container

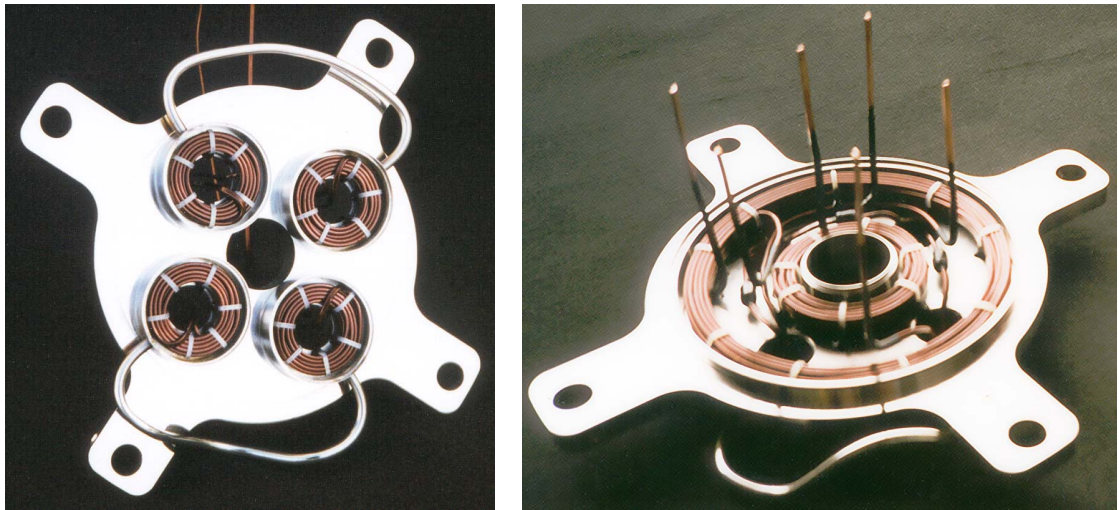


Figure 1.21. Two sides of a container set with coils before the covers are welded, left the radial coils, right the axial coils. The trap consists of two such container sets.

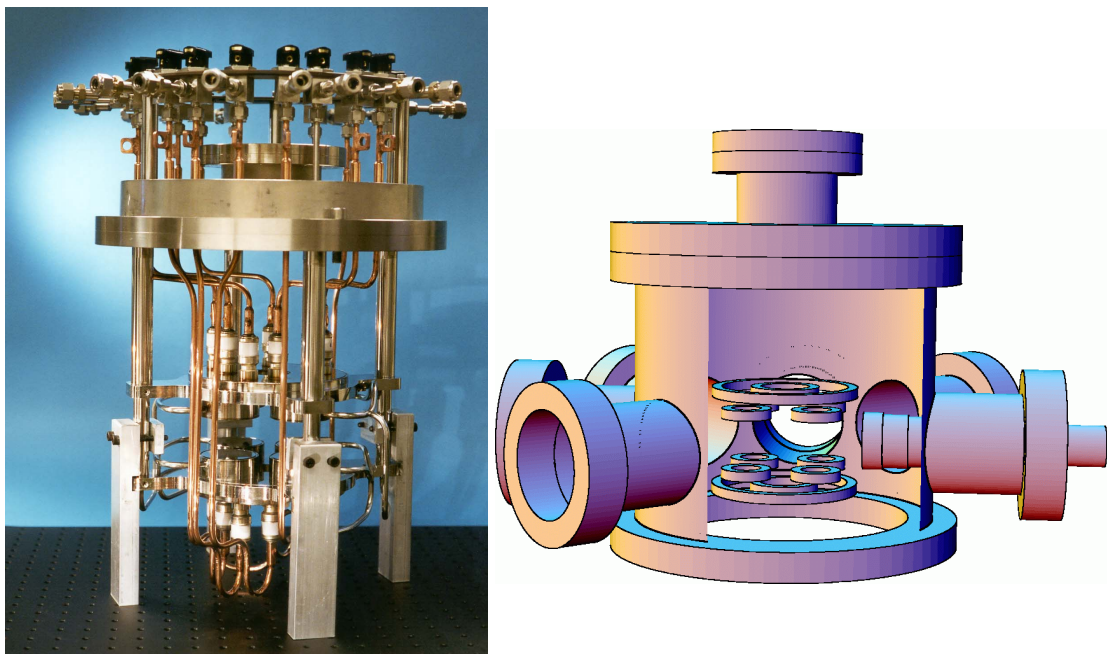


Figure 1.22. A photo of the lid of the trap chamber with the trap setup hanging underneath, with a drawing to the same scale of the chamber, trap coils, and final part of the Zeeman slower. The rectangular blocks in the photo are removed when the setup is placed in the chamber. The lowest tubes extend below this chamber into another with one of the windows for the vertical light beams. At the top of the photo are seen valves and connections of the cooling system. A loose metal ring (not shown in the drawing) is placed on the lid to prevent damage of the feedthroughs behind it when the lid is screwed down. In the drawing the top window is also shown.

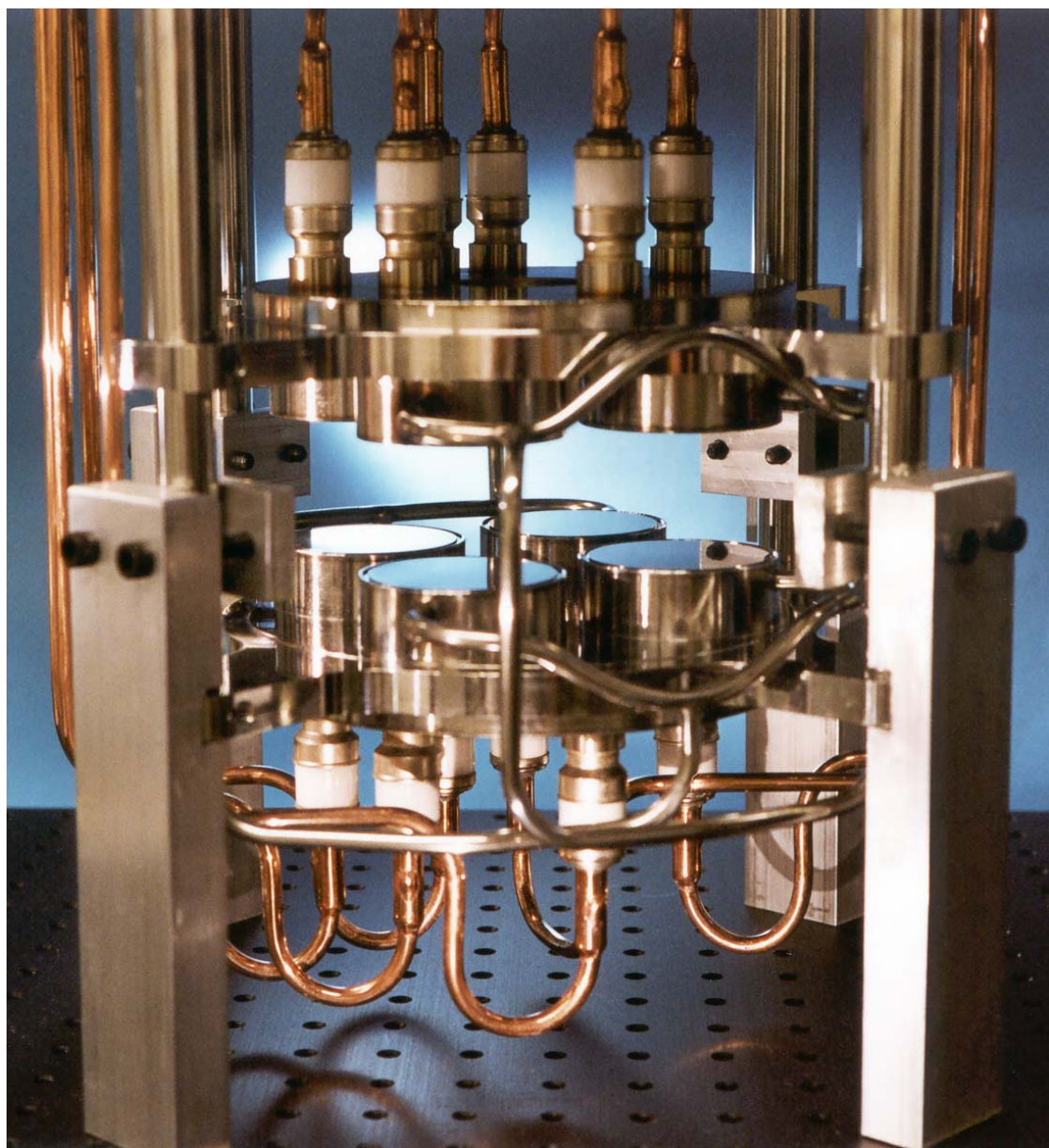


Figure 1.23. Close-up of the trap setup.

sets.

To avoid corrosion of the tubes and feedthroughs, the cooling fluid is a mixture of 70% Dowcal 10 (consisting of 94% ethylene glycol and 6% corrosion inhibitors) and 30% water. Compared with 100% water the conductivity decreases at least with a factor of 20, at the cost of an increase of the viscosity by a factor of 6. The liquid flows with a velocity of about 0.5 l/s through the copper tubes and feedthroughs, around the coils, and through steel tubes back. In the foreground of Fig. 1.23 some of the steel tubing is seen, bent to make room in-between for the slower. At maximum currents the coil temperature increases only a few degrees.

1.8.2 Current switching

The circuit connecting the coils to the current supplies is shown in Fig. 1.24. Current supplies 1 and 3 have a maximum setting of 200 A / 15 V (Delta Elektronika SM15-200 D) and supply 2 a maximum setting of 50 A / 8 V (Lambda LLS 8008). A power diode (SKN130/02) is placed between supply 2 and the coils. Switches consist of parallel pairs of power MOSFETs (S0–S7: SML10J225, on-state resistance 7 mΩ; S8: IRFK4H250, 21 mΩ). The two bypass resistors of the small axial coils are made of 0.5 m copper wire with a diameter of 0.5 mm, held in plastic tubes connected to the same cooling system as the coils and switches. The two dummy coils are long copper ribbons kept under water. The eight radial coils are connected in series.

The current is switched as follows.

- A MOT is realized by setting supply 1 at 41.5 A and having (only) switches S1, S4, and S5 closed.
- The current supplies respond slowly to changes in current settings. Hence a short time before the MOT is switched off, supply 3 is set at 110 A and switch S7 is closed, so current can already flow through a dummy coil, matching the load of the trap coils to avoid oscillations in the current when it will be switched to the trap coils. Supply 2

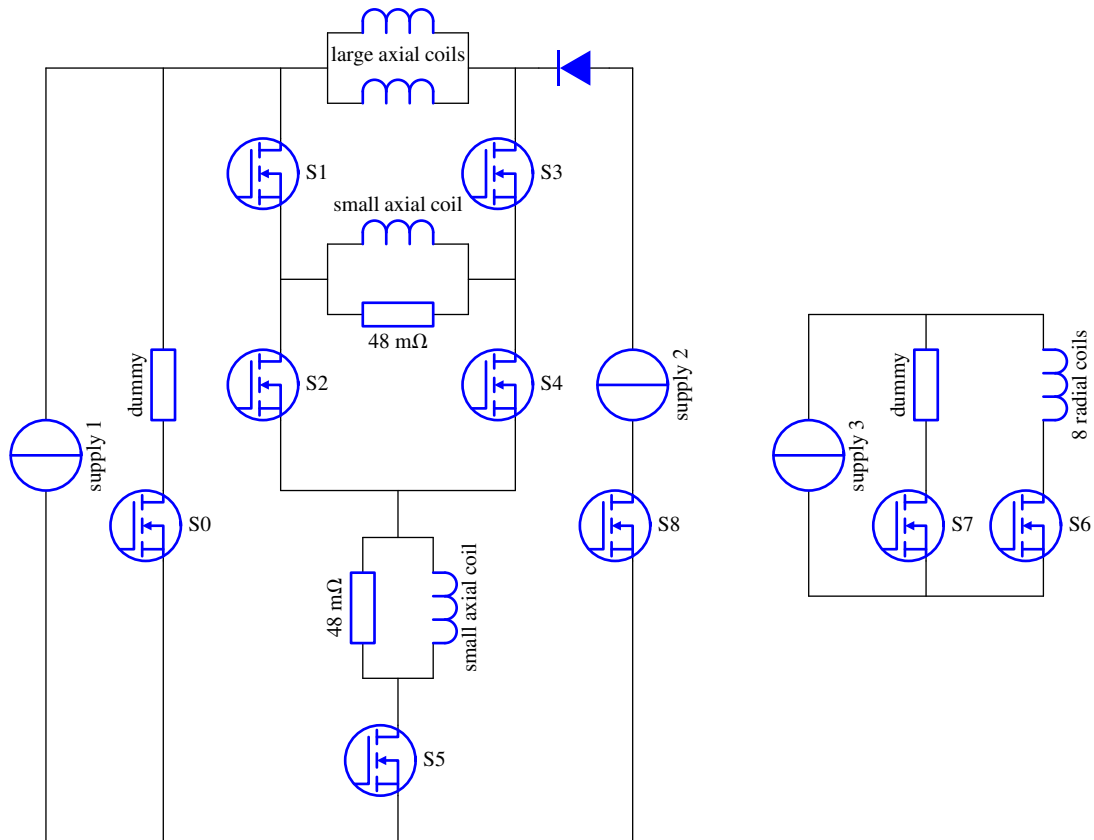


Figure 1.24. Electric circuit for the traps. A MOT is produced with switches S1, S4, S5 closed and a cloverleaf trap with S2, S3, S5, S6, S8 closed, otherwise S0 and S7 are closed.

is set at 20 A, although the current cannot flow yet; this supply produces quickly a stable current when its output capacitor is charged before the current starts to flow.

- The MOT is switched off by opening switches S1, S4, and S5. At the same time supply 1 is set at 135 A and switch S0 is closed, so the higher current needed for the cloverleaf trap can stabilize through the other dummy coil, while optical molasses is applied.
- To create a cloverleaf trap, switches S0 and S7 are opened and switches S2, S3, S5, S6, and S8 closed. Note that the current in one of the small axial coils has reversed direction compared with the MOT situation.
- The He* cloud is compressed by changing the currents from supply 1, 2, and 3 to 190 A, (usually) 10.5 A, and 200 A, respectively, in 20 steps of 25 ms. Afterwards, voltages over the three supplies are 8.5 V, 7 V, and 13 V, respectively. The function of supply 2 is to vary the current through the small axial coils only, producing a B_0 that is proportional to the current. Of the current 17% flows through the bypass resistors, necessary to get a small positive B_0 when supply 2 is set at a low current (more details in §7.4.3). Then there are only field deviations due to noise produced by supply 1, specified as a relative rms ripple of 5×10^{-4} , which will cancel out in the centre of the trap because the two sets of axial coils produce almost the same but opposite fields.
- The cloverleaf trap is switched off by opening all switches and closing S0 and S7, so the current flows through the dummy coils. All supplies are set to zero and the cycle can be repeated.

Originally the large axial coils were connected in series. However, to produce a small potential minimum in the cloverleaf trap with all four axial coils in series, 40% of the current would have to bypass the large axial coils. In the present scheme, the power dissipated in the bypasses is reduced by a factor of 4, but the largest attainable axial curvature has become 20% smaller.

1.8.3 Magnetic field decay

When a trap is switched off, the magnetic field should decay as fast as possible. First, absorption imaging has to be applied preferably without a field present, to increase absorption and to interpret data more easily. Second, the optical molasses between the magneto-optical and cloverleaf trap works best in a constant field, and the time between traps has to be short to avoid a large expansion of the cloud. In principle molasses is applied in a field-free environment, but a constant field can compensate for intensity imbalances [32]. With a Hall probe (Magnet-Physik FH 54) the field decay has been determined *in situ*.

The quadrupole field shows different behaviour depending on the measured field direction: horizontally the exponential decay time is 0.44 ms, vertically the sum of two components is seen with decay times of 0.31 ms and 3.5 ms. The last one, due to induction, is 13 times weaker. At the same time as the MOT, the Zeeman slower and its compensation coils are switched off. The corresponding (horizontal) fields have exponential decay times of 0.28 ms and 0.79 ms, respectively. The background field, including the field due to compensation coils for optical molasses, which stay on during

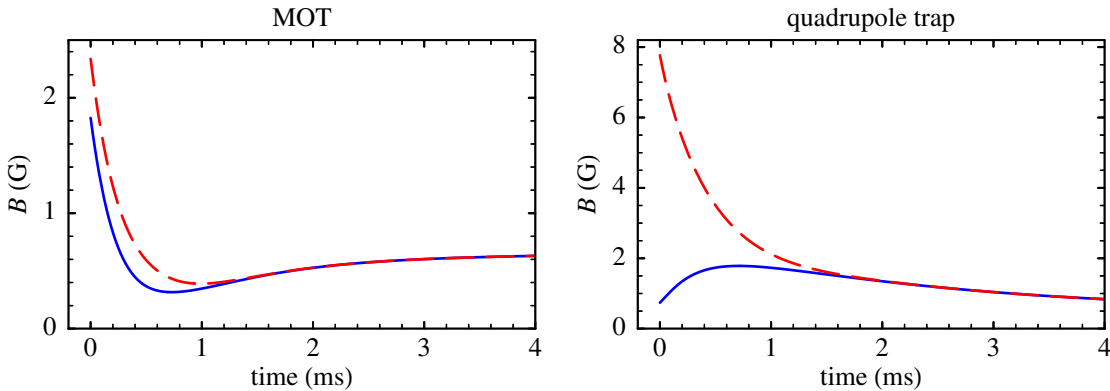


Figure 1.25. The absolute field at the trap centre (solid curves) and averaged over the atom density distribution on the y axis (dashed curves) as a function of time after switching off the MOT and strongest quadrupole trap.

all experiments, is 0.7 G. The total field at the centre of the MOT and the strongest quadrupole trap (trap current 5 times larger) is shown as solid curves in Fig. 1.25. For absorption imaging the average field that the atoms experience is important. If at time t the cloud has a density distribution $n(x, y, z, t)$, the field is given by a function $B(x, y, z, t)$, and the cloud is probed by a light beam along the y axis, the average field along this axis is

$$B_{\text{av}}(t) = \frac{\int B(0, y, 0, t)n(0, y, 0, t) dy}{\int n(0, y, 0, t) dy}. \quad (1.28)$$

The radii of the MOT cloud are given in Fig. 6.8, while theoretical radii are used for the cloud in the quadrupole trap (§6.5). The resulting $B_{\text{av}}(t)$ is given as dashed curves in Fig. 1.25. In the MOT case, after 1 ms the field is small enough to apply absorption imaging or start optical molasses. The field of the strongest quadrupole trap does not decrease sufficiently fast to permit accurate absorption imaging (§6.5). After 1 ms optical molasses the cloverleaf trap is switched on in about 1 ms. Figure 1.26 shows the coil currents, measured with a current probe (LEM PR 1030), and the trap depth during this process. The load of the trap coils is not fully matched by the dummy coils, causing some remaining oscillations.

In the cloverleaf trap, the field of the radial coils has a decay time of 0.065 ms with an induction tail of 0.30 ms. The fields due to the small and large axial coils have decay times of 0.24 ms and 0.16 ms, respectively, and there is an induction tail of 6 ms. After 1 ms the radial field is negligible, leaving only the field due to the axial coils, which is almost independent of position near the centre. The total field and the field direction are shown in Fig. 1.27. Because the time constants of the two sets of axial coils are not the same, the large fields they produce no longer compensate each other, resulting temporarily in a large field at the trap centre. As the field of the large axial coils decays faster, the field direction remains upward. Only after 1 ms, when the fields have become small, does the direction turn downward, but probably slow enough to allow the atoms to follow adiabatically. If the two axial fields would decay in reverse order, the field direction would flip almost instantly, before the large field peak, and the atoms could undergo transitions to unbound states [101].

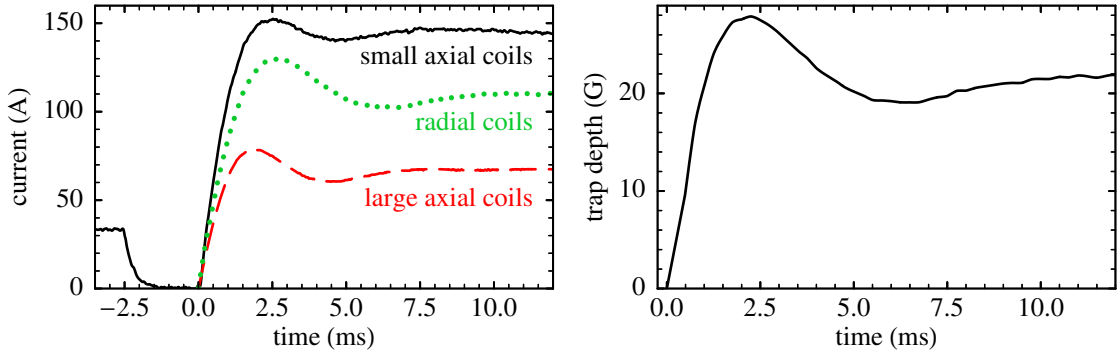


Figure 1.26. The currents through the coils and the trap depth calculated from these currents as a function of time after switching on the cloverleaf trap. The current through the small axial coils stabilizes only after 40 ms at a value of 123 A. The trap depth is then 26 G. In the time before switching on the cloverleaf trap, the current used for the MOT is shown.

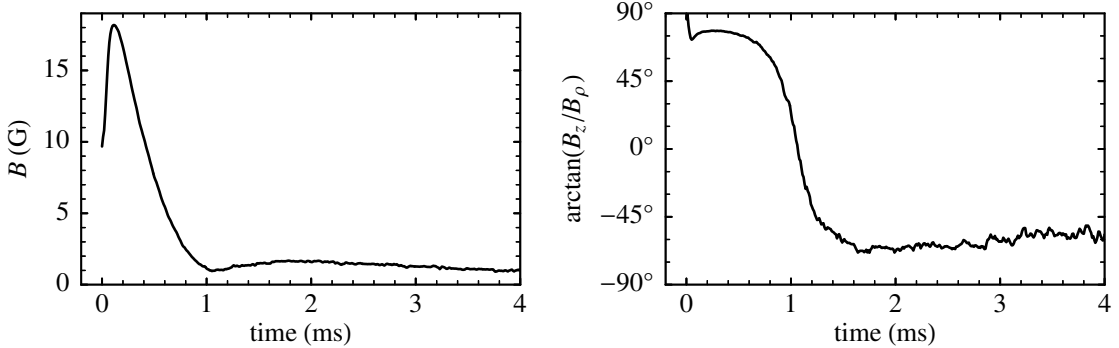


Figure 1.27. The absolute field and the field direction at the trap centre as a function of time after switching off the cloverleaf trap (without compression). The direction is given as an angle between the field vector and a horizontal plane, $+90^\circ$ indicating upward.

1.8.4 Other equipment in trap chamber

The atoms are detected by two double MCP detectors. One is located 18 cm below the trap centre in a grounded Faraday cage, reached by metastable atoms exiting the trap in its direction. The other is positioned 11 cm horizontally from the trap centre, with -1.4 kV on its exposed front plate, attracting all of the ions. More details are given in §2.2.1.

For evaporative cooling the signal from an rf signal generator (IFR 2023A) is amplified up to 16 W by a broadband rf amplifier (ENI 607L) and coupled to a coil of copper wire with 5 turns, a diameter of 0.9 cm, and a length of 0.8 cm. This rf coil is placed between two radial coil containers to obstruct the light beams as little as possible. The distance between the coil centre and the trap centre is 3.0 cm and the coil axis crosses the trap centre at an angle of 30° with the horizontal plane. The rf power is large enough in the relevant frequency range up to 200 MHz to remove atoms, as discussed in §7.4.1.

1.8.5 Pressure

The pressure in the trap chamber is measured with an ion gauge (Granville-Phillips 350) and a quadrupole mass spectrometer (Spectra Vacscan). Four leaks developed in the setup: one where a wire is welded to a tube and three in the feedthroughs, in the metal between ceramic parts and copper tubing. They were closed with epoxy resin (Varian Torr Seal) and covered with steel jackets for mechanical stability. After all leaks were sealed, the chamber was baked gently at 100 °C for three weeks, while the slower was heated using almost boiling water in its cooling system. This was enough to bring the pressure with a closed slower valve down to 8×10^{-11} mbar, corresponding to an extrapolated trap lifetime $\tau = 60$ s. The remaining gas consisted of 75% hydrogen and 15% water, with a partial pressure of chlorine from the epoxy resin of less than 1×10^{-12} mbar. If the valve was opened the pressure increased initially with 5×10^{-11} mbar, but after some weeks of experimenting the slower contribution became 2×10^{-10} mbar. Due to the deflection of the atomic beam, the partial pressure of helium is a negligible 3×10^{-12} mbar.

Four months later a period followed where the pressure repeatedly rose and fell within a few hours, with peaks as high as 6×10^{-9} mbar, consisting mostly of water. The cause seemed to be an opening and closing leak, although the gas composition did not indicate the presence of ethylene glycol from the cooling fluid, which had been the case during previous leaks. Gradually the pressure went up to 3×10^{-10} mbar ($\tau = 20$ s) with the valve closed. The water fraction increased to 35%, while hydrogen accounted for only 40%. This pressure was kept for at least half a year without any peak, during which the final experiments were performed (Chapters 6–7). An open valve led to a pressure of 5×10^{-10} mbar (a number density of 1×10^7 cm⁻³) and a trap lifetime of $\tau = 12.5$ s.

1.9 The lasers

1.9.1 Laser systems

The 1083 nm light used for the transversal cooling, slower (in later experiments), MOT, and spin polarization is generated by a laser based on a lanthanum neodymium magnesium hexaaluminate (LNA) crystal in a ring cavity (Fig. 1.28) [70, 94]. The crystals used are made from a powder mixture of 0.85 part La₂O₃, 0.15 part Nd₂O₃, 2 parts MgO, and 11 parts Al₂O₃. The crystal is pumped longitudinally, originally at 514.5 nm by an argon-ion laser (Spectra-Physics 2040) and later at 532.2 nm by a solid-state laser using a neodymium-doped yttrium vanadate (Nd:YVO₄) gain medium and a lithium triborate (LBO) doubling crystal (Spectra-Physics Millennia V). The second laser is more convenient in everyday use, although the bars of diode lasers pumping the Nd:YVO₄ crystal turned out to have an average lifetime of only 2500 hours, despite frequent servicing. The absorption coefficient α of LNA for the light of the two lasers was found to be $\alpha(514.5 \text{ nm}) = 1.08 \text{ cm}^{-1}$ and $\alpha(532.2 \text{ nm}) = 0.54 \text{ cm}^{-1}$: to absorb the same power from the solid-state laser, the LNA crystal needs to be twice as long. Increasing the pump power does not work, because above 4 W the temperature gradient in the crystal causes thermal lensing and the LNA laser becomes unstable.

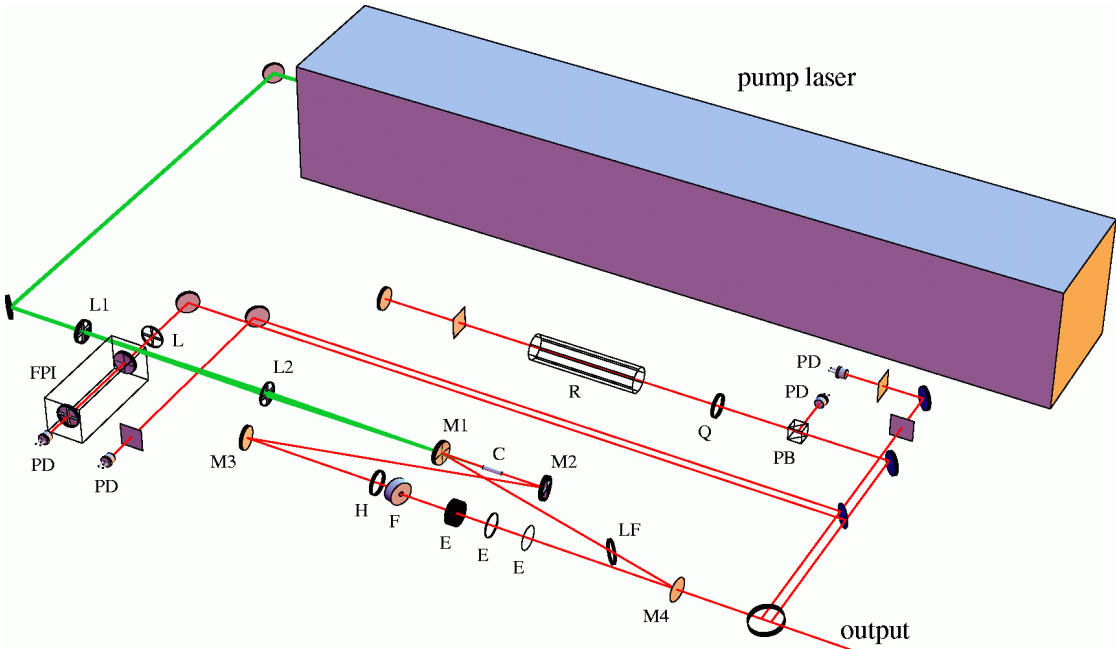


Figure 1.28. The LNA laser system, with LNA crystal C , etalons E , Faraday glass F in magnet, Fabry-Perot interferometer FPI , half-wave plate H , lenses L , Lyot filter LF , cavity mirrors $M1$ – $M4$, polarizing beam-splitter cube PB , photo diodes PD , quarter-wave plate Q , and rf-discharge helium cell R . Other elements are mirrors and beam splitters (round), and filters (square) for intensity reduction.

According to the absorption spectrum of LNA (Fig. 1.29, taken from Schearer et al. [74]), a frequency-doubled neodymium-doped yttrium lithium fluoride (Nd:YLF) laser, working at 523.5 nm using the extraordinary polarization, has a much larger absorption coefficient of 2.1 cm^{-1} . However, no commercial lasers of this type were available. Therefore the crystal has a length of 2.1 cm, close to the maximum length that can be achieved (the LNA crystal is cut parallel to the c axis for better laser action due to a larger induced emission cross section, but LNA grows and cleaves perpendicular to this axis). The diameter is 0.3 cm and the antireflection-coated end surfaces are cut at opposing angles of 3° to avoid interference effects. Experiments were also performed using a crystal with uncoated surfaces cut parallel at 29° , so light can enter the crystal at the Brewster angle, but alignment was more difficult while the output power was not larger. The crystal is held in a brass cylinder (coated with indium for thermal contact), which is placed in a metal block. No water cooling is used.

The ring cavity consists of two planoconcave mirrors $M1$ and $M2$ with a radius of curvature of 10 cm that have a 95% transmission for the pump light and two plane mirrors $M3$ and $M4$. The first three mirrors are highly reflecting at 1083 nm, while output coupler $M4$ transmits 7% of the infrared light. An LNA crystal normally fluoresces in a band around 1054 nm, but the ring cavity contains a Lyot filter to force the laser to work in a second band around 1082 nm. Other elements are an optical diode, consisting of a Faraday rotator in a strong permanent magnet and an antireflection-coated half-wave plate, and three uncoated glass etalons with a thickness of 0.1 mm, 1 mm, and 10 mm

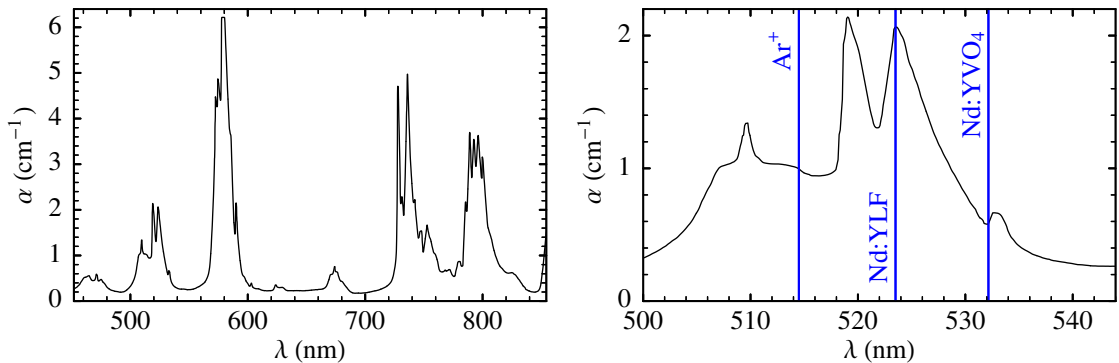


Figure 1.29. LNA absorption coefficient as a function of wavelength for light propagating along the crystallographic c axis [74]. To the right is a detail of the range around the wavelengths of the three pump lasers discussed in the main text. The vertical scale was originally the optical density in arbitrary units. Here it is calibrated using the two measured values, with an uncertainty of 10%.

for single-mode operation. The largest etalon is temperature stabilized, a few degrees above room temperature. The waist of the infrared laser beam in the crystal is 29 μm (the distance between points where the intensity is $e^{-1/2}$ times that on the axis). The pump laser is focused in the crystal by two lenses L1 (focal length $f = -15 \text{ cm}$), L2 ($f = +15 \text{ cm}$), and mirror M1 ($f = -19 \text{ cm}$), to a waist of 18 μm . The LNA laser is more stable if the beam diameter of the pump laser is somewhat smaller, while the output power stays equal: 250 mW at 4 W pump power. As the crystal absorbs only 2/3 of the pump light, an attempt was made to increase the output power by adding a mirror behind M2, reflecting the pump light back into the crystal. The output power increases by 30% as expected, but only at low pump power: at higher pump power the effect is smaller and the LNA laser becomes unstable. Hence this method is not used for experiments.

The laser frequency is locked in two stages. Cavity mirror M3 is mounted on a piezo-electric transducer (PZT), which changes the cavity length depending on the applied voltage. With a PI controller (built in-house) the cavity length is locked on the side of a fringe of a 750 MHz confocal Fabry-Perot interferometer (FPI). The length of the FPI is locked to the atomic transition at 1083 nm using saturation spectroscopy in a helium cell with an rf discharge [32]. From the saturated absorption signal an error signal is obtained with a lock-in amplifier (Ithaco Dynatrac 391A) and sent to a PI controller (see Fig. 1.30). The slow part of the error signal, mainly due to thermal drift, is extracted by low-passing the signal from the integrator. It is amplified and applied to one side of the PZT to which an FPI mirror is glued. An oscillator signal of 1 kHz is added to the total signal from the PI controller and the sum is applied directly to the other side of the PZT. This fast signal is not amplified so it can compensate noise produced in the high-voltage amplifier. Two Zener diodes keep the fast signal between -12 V and +12 V in case the PZT is accidentally earthed on the high voltage side.

The light used for optical molasses, probing, and (in early experiments) the slower comes from two DBR (distributed Bragg reflector) diode lasers (SDL-6702-H1), placed in an extended-cavity setup to reduce the line width from 3 MHz to less than 1 MHz.

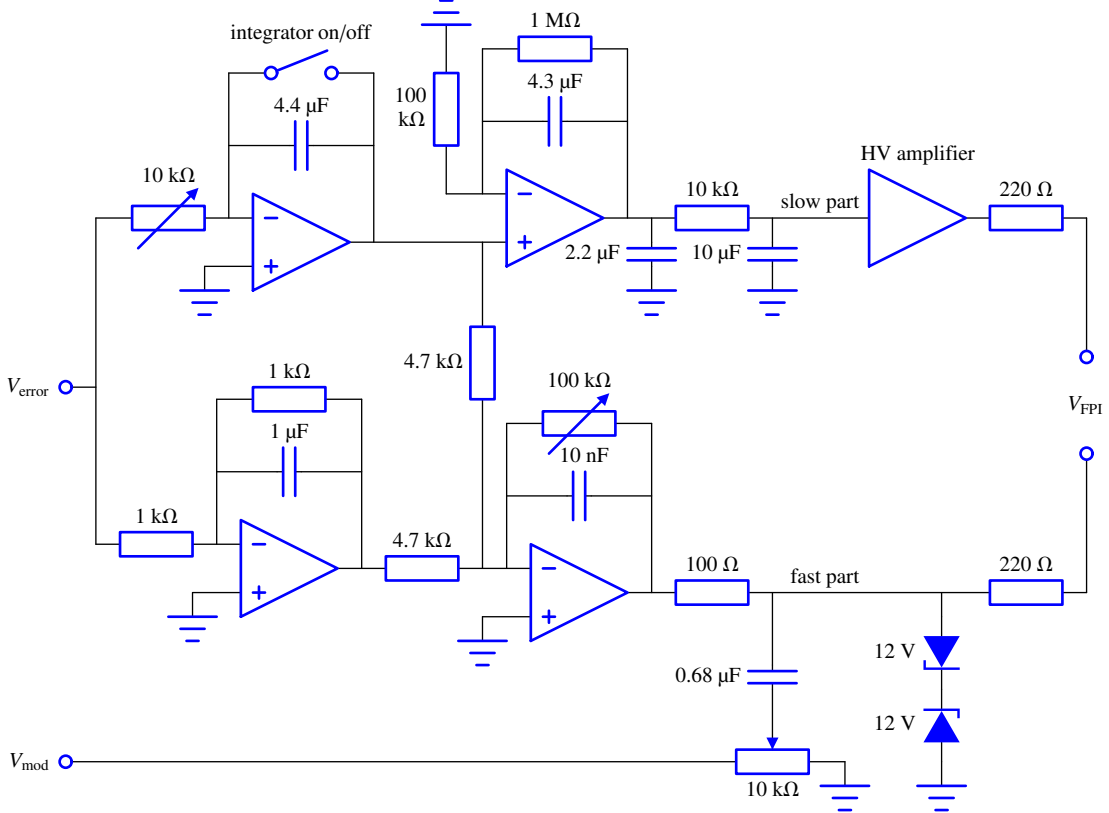


Figure 1.30. Electric circuit to lock the LNA laser.

Both lasers are locked to the 1083 nm transition using saturation spectroscopy, the molasses laser with a standard lock-in technique, the probe laser with rf-sideband locking. For spectroscopic applications the second laser is locked to a scanning FPI. Details are given in the thesis of Herschbach [32].

The line widths of the three lasers are determined in heterodyne beat experiments, in which for each laser pair power averages are taken of 50 beat note spectra over a period of 160 s. Due to technical noise the averaged spectra have a Gaussian shape. Hence the beat note width is assumed to be the root of the sum of squared laser line widths. According to these measurements the LNA laser has a FWHM line width of 0.16(10) MHz, the molasses laser 0.64(3) MHz, and the probe laser 0.56(3) MHz. At resonance the probe laser has a width of 0.43(5) MHz, but it is used at a detuning of 80 MHz, when the width is larger due to extra technical noise, although still negligible for absorption imaging.

1.9.2 Beam layout

The production of all laser beams is shown in Fig. 1.31. Four AOMs give frequency shifts of 250 MHz (A1, IntraAction ATM-250.3C2), 30 MHz to 50 MHz (A2, A3, IntraAction AOM-40R), and 80 MHz (A4, Neos Technologies N23080-1.06). Three of them are used to divide the light of the LNA laser into four possible beams: a 15 mW slower beam with a detuning of -250 MHz, a 45 mW MOT beam with a detuning of -35 MHz,

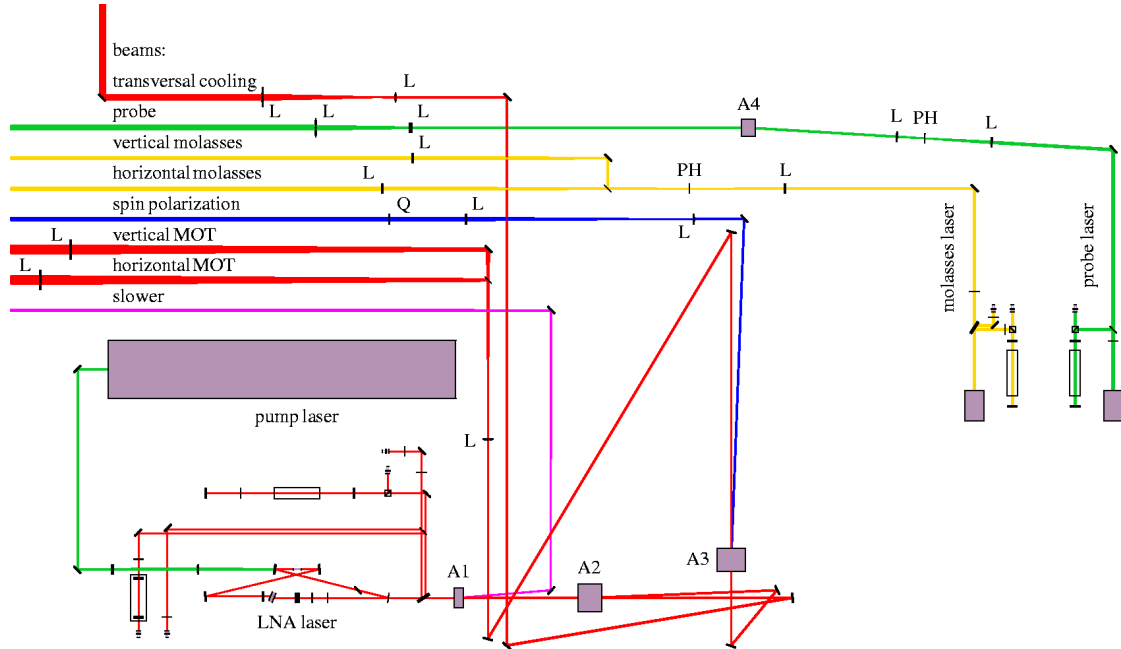


Figure 1.31. The optical table, with acousto-optic modulators A1–A4, lenses L, pinholes PH, and quarter-wave plate Q. Mirrors and beam splitters are not labelled, shutters are not shown.

a 10 mW spin-polarization beam with a detuning of +5 MHz, and a 190 mW transversal cooling beam at resonance. The fourth AOM is used as a fast switch of the probe beam; the AOM detuning is compensated by applying a magnetic field to the helium cell used for locking the probe laser. Beam expanders consisting of two lenses give beams the correct radii. For spatial filtering of the molasses and probe beams a pinhole is placed at the beam waist between the lenses. The slower, MOT, spin-polarization, and probe beams are switched with AOMs, while the molasses beam is switched with a mechanical shutter (Uniblitz LS2T2) behind the pinhole. A second shutter (home-made using a relay and a razor blade) between the beam expander lenses of the MOT beam is closed during spin polarization. Afterwards the light from the LNA laser is no longer needed and to avoid stray light in the cloverleaf trap the beam is blocked by a shutter just behind AOM A1 (Uniblitz LS6T2).

Figure 1.32 shows the beam layout at the trap chamber. For the MOT there are two beams, one horizontal and one vertical, which are retroreflected. For optical molasses the light is split into six separate beams of equal intensity; retroreflection is not possible due to the high absorption in the cloud. Quarter-wave plates with the correct orientation in the MOT, slower, spin-polarization, and (optionally) molasses beams change the polarization from linear to circular. The mirrors retroreflecting the MOT beams would change circularly polarized light from left-handed to right-handed and vice versa (the electric field vector keeps rotating in the same direction but the light propagates in the opposite direction). To keep the same polarization, in front of these mirrors quarter-wave plates are placed with an arbitrary orientation.

The MOT beams have a diameter of about 4 cm and a Gaussian intensity profile with

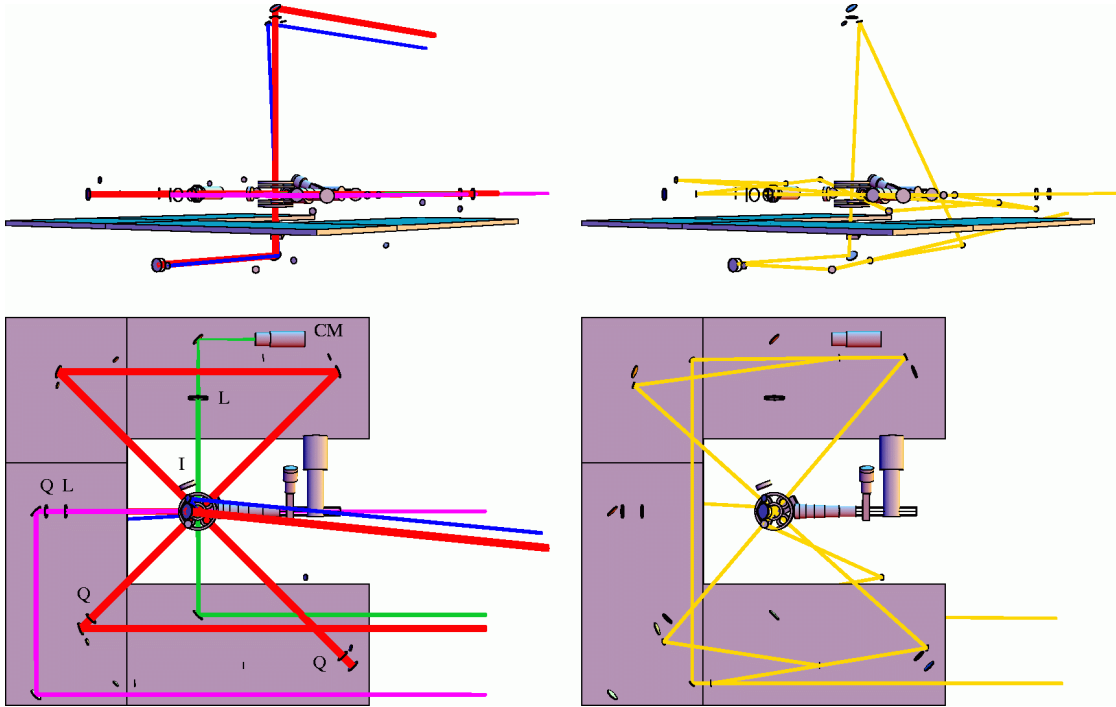


Figure 1.32. The setup around the trap (without the chamber itself). To the left a side and top view with all beams except for the molasses beams, to the right with only the molasses beams. Labelled are camera CM, ion detector I, lenses L, and quarter-wave plates Q.

an rms radius of 0.8 cm. The beam diameter needs to be large: if it is reduced to 3 cm or 2 cm there are 20% or 80% fewer atoms in the MOT cloud, respectively.

1.9.3 Imaging system

For imaging we use a Cohu 4710 camera, with a CCD chip consisting of 768×576 square pixels with sides of $8.4 \mu\text{m}$. The quantum efficiency is 0.15%, large enough to provide absorption images with a sufficient signal to noise ratio, even with a brief and low intensity probe pulse (see Figs. 6.7, 6.10, 6.11, 6.13, and 7.14). The cloud is imaged on the chip with a large convex lens (diameter 8 cm) and a camera lens (Philips LDH 6713/00) with focal lengths of +31 cm and +2.8 cm, respectively. The object distance to the first lens is 45 cm, the distance between the two lenses is 52 cm; the magnification is only 1/8, so the whole probe area is seen. This is necessary to image clouds from the MOT, which after an expansion time can fill the probe area. A near-infrared transmitting glass in front of the camera lens reduces visible background light, with a transmission of 84% for 1083 nm. The total transmission of the imaging system for probe light is 45%.

1.10 Experimental control

The experiment is controlled by a digital I/O card (Viewpoint Software Solutions DIO-128) with a digital signal processor. Using a LABVIEW program (from the AMOLF Institute, Amsterdam) this is loaded with a timetable of TTL triggers for every setup component corresponding to the experimental sequence of events. The timetable is executed with a resolution of 1 μ s, independent of the computer processor. The current supplies for the trap are set by an analogue output card (National Instruments AT-AO-6), which buffers the sequence of voltages corresponding to the current values. The digital I/O card supplies a trigger when the next set of values is to be given. The AOM drivers are switched on a time scale in the order of 1 μ s; the AOM power is set manually before the experiment. The mechanical shutters are switched on a millisecond time scale. Other switched components are the current switches, rf generator, oscilloscope, and frame grabber for the camera (Data Translation DT3152).

2

Determination of temperature and number of atoms

2.1 Introduction

One of the advantages of experiments with metastable helium is that atoms can not only be detected by absorption imaging, but also directly, with for instance a microchannel plate (MCP) detector. The two techniques are complementary: cloud size and absolute number of atoms can only be measured with absorption imaging, while temperature and relative amounts of atoms are more easily determined with an MCP detector. In cases where both methods can be used, the results are cross-checked. To account for differences, several complications have to be addressed. The trajectories between the trap and the MCP detector can be disturbed by magnetic field gradients and are in our case partly blocked by the setup. The theory of absorption imaging is examined in detail to consider the effects of the intensity, polarization, and wavelength of the light, the duration of probing, the state and temperature of the atoms, and the magnetic field they are in. Then this theory is applied to helium and the situation in our experiment. Finally, the number of atoms according to the MCP detector is calibrated.

2.2 Time-of-flight measurements

2.2.1 MCP detector

When a metastable helium atom hits a metal surface, an electron is released with high probability, due to the large internal energy of 20 eV. An MCP detector is a large collection of channels, each acting as electron multiplier: an avalanche of electrons is produced when an atom hits a channel. For stable signals two MCPs are used in series [102]. We use microchannel plates from Burle Electro-Optics[†], with an active area diameter of 2.0 cm and an open area ratio of 62%. The channels have a diameter of 10 μm . For the detection of ions a Chevron (3018MA) is used and for metastable atoms we have assembled two plates (S18-10-D) ourselves.

[†]Before July 1999 the Scientific Detector Products Group of Galileo Corporation.

After a trap has been switched off, He* atoms reaching the second detector produce a time-of-flight (TOF) signal. This is a voltage $V(t)$ as a function of time t , in our case measured over an effective resistance $R = 1 \text{ M}\Omega$. The number of atoms reaching the detector is the integral $N_{\text{MCP}} = \frac{1}{RC_1} \int V(t) dt$, where C_1 is the average charge produced by one atom hitting the detector. This constant is an effective gain, incorporating the real gain of the detector (at a given MCP voltage), the open area ratio, and the quantum efficiency for detection of one metastable helium atom. Using Monte-Carlo simulations the TOF signal shape as a function of temperature can be established. The same simulations also yield the fraction $F = N_{\text{MCP}}/N$ of the number of atoms N in the trap that hits the detector at a given temperature. We use absorption imaging to determine the absolute value of N (§2.3) and fit a corresponding TOF signal $V(t)$, yielding the calibration factor $NF/\int V(t) dt = 1/RC_1$. At 1450 V we have $C_1 = 4.5 \times 10^4 e$; at 1900 V it is 24 times larger. The gain is varied to keep the TOF signal smaller than 0.25 V, so that the MCP is not saturated. In plots of TOF signals the voltage is multiplied by the value of $1/RC_1$ appropriate to the MCP voltage in use (§2.3.7).

The MCP detector for metastable atoms is mounted below the trap; the distance between the trap centre and the centre of the detector is 17.8(3) cm vertically and 4.1(2) cm horizontally. In this position a vertical light beam with a diameter of at least 3 cm can be used for the MOT, while a straight path from the trap centre to the detector is not obstructed (Fig. 2.1). At low temperatures, however, the atoms can reach the detector only via a parabolic trajectory, in which case some of them will hit the setup. If the temperature is too low, all atoms miss the detector.

Only the experiments described in Chapters 6–7 have been performed using the geometry described here. The experiments of Chapters 3–5 were carried out using a simple MOT where the mechanical construction consisted of only two coils, with the detector placed closer to the cloud (at a position 6.3 cm vertically and 4.0 cm horizontally from the trap centre), imposing fewer geometrical constraints on the atomic trajectories [72].

2.2.2 Magnetic field gradients

At low temperatures the peak in the TOF signal arrives later than expected assuming simple ballistic trajectories: to fall 18 cm the atoms should require only 0.19 s, while we see a peak up to 0.21 s after release (see Fig. 2.6). The position of the detector was measured carefully using different methods and the trap is switched off too quickly to cause such a delay. Therefore the measured deviation is probably due to magnetic field gradients.

The force \mathbf{F} on a neutral atom with magnetic moment μ , exerted by a magnetic field \mathbf{B} is $\mathbf{F} = \nabla(\mu \cdot \mathbf{B}) = -\nabla(\Delta E)$, with Zeeman energy shift $\Delta E = 2\mu_B B$ in the case of He* atoms in Zeeman substate $m_J = +1$. Assuming most atoms stay in this substate, the force can be written as $\mathbf{F} = -2\mu_B \left(\frac{\partial B}{\partial x}, \frac{\partial B}{\partial y}, \frac{\partial B}{\partial z} \right)$. Calculations show that a field gradient of 0.070 G/cm along the whole trajectory is enough to explain the late arrival, corresponding to an increase of 1.2 G from the centre of the trap to the MCP. Other possibilities are, for instance, a total increase of only 0.15 G but concentrated in the first centimetre of the trajectory, or a 1.1 G increase between $z = -4.5$ cm and

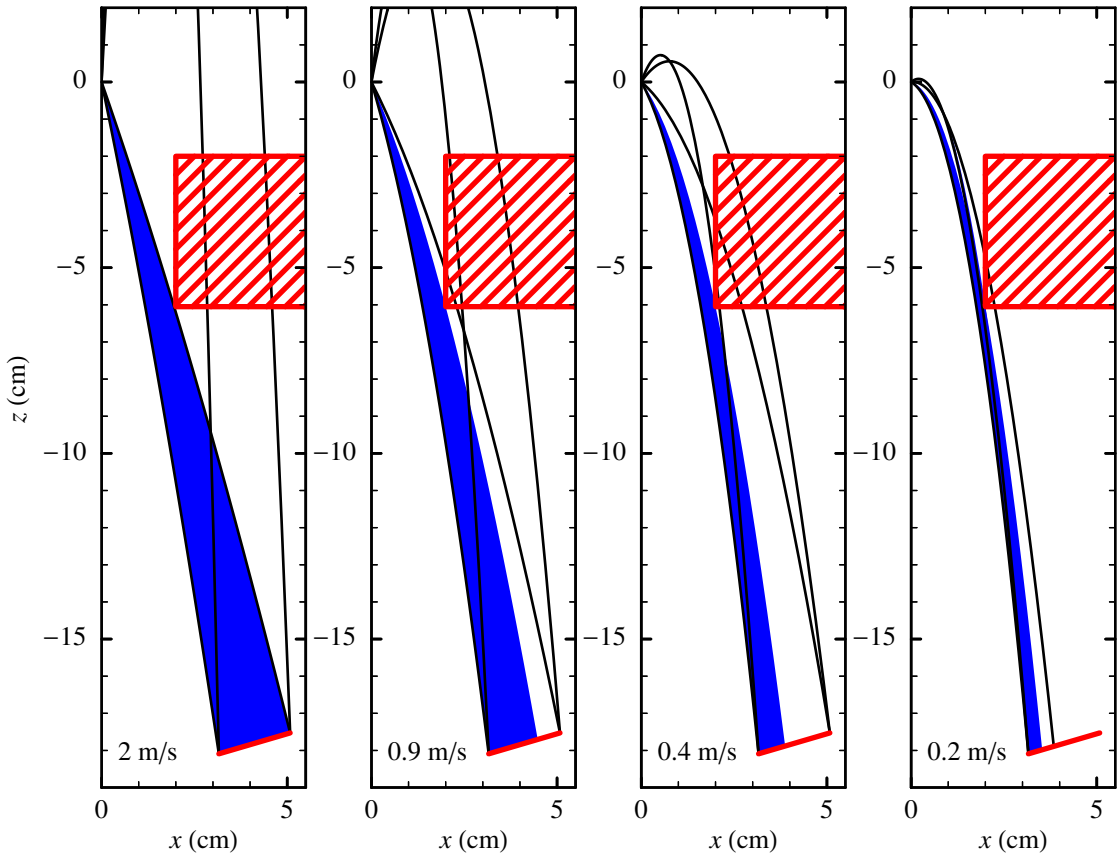


Figure 2.1. Atom trajectories in the vertical plane through the origin and the centre of the MCP detector (thick line at bottom right), when the total initial velocity has a given fixed value. Parabolic curves are trajectories to the outer edges of the detector or, if one of them cannot be reached, to a point as close as possible to that edge. The dark area consists of trajectories of atoms that actually reach the detector, without hitting the setup (hatched area) first. The situation is drawn for total velocities v that are the most probable speeds $\sqrt{2k_B T/m}$ for (from left to right) 1.0 mK, 0.2 mK, 0.04 mK, and 0.010 mK.

$z = -5.5$ cm, at the height of the lower axial coils. While the cloverleaf trap is on, the field gradients are largest at this last position, with values of the order of 300 G/cm (see Fig. 1.20). However, atoms with an initial velocity smaller than 0.5 m/s pass this region with a minimum velocity of 1.0 m/s and at least 65 ms after the trap has been switched off. The trapping field and eddy currents should be negligible at this time (see §1.8.3). The possibility of magnetization of the metal coil containers has been reduced by using paramagnetic steel. Hall probe measurements have shown the field around the trapping region due to magnetization to be smaller than the earth's magnetic field which, however, is large enough to cause the necessary gradients. On the other hand, at welds the steel regains the ability to be magnetized, so the gradients could be produced for instance at the edge of the setup that is closest to the trajectories of atoms reaching the MCP ($z = -6$ cm, $x = 2$ cm).

In TOF simulations there should be a region where the gravitational acceleration is

effectively smaller as a result of the added acceleration due to magnetic field gradients. Since we do not know where this region is and to simplify the simulations, we have kept the downward acceleration constant. Instead, the effect is simulated by a vertical offset velocity v_0 for the whole cloud. This means that the velocity components have a Gaussian distribution with an rms value of $\sqrt{k_B T/m}$, and a mean of 0 in the two horizontal directions, while vertically the mean is v_0 ; the offset velocity will be chosen such that low temperature TOF signals are simulated with the correct peak time. At high temperatures the same v_0 has little effect on the calculated signal, reflecting the small influence of the magnetic field gradients on the trajectories of fast atoms. The TOF signals for intermediate temperatures will then also be simulated correctly. In the MOT the field gradients are a factor of 5 smaller than in the cloverleaf trap, there are fewer problems with eddy currents, and the temperature is always high, so for corresponding TOF simulations we assume $v_0 = 0$.

2.2.3 Offset velocity

In Fig. 2.2 the horizontal and vertical velocity components, v_x and v_z respectively, are shown of atoms in the trap centre that hit the detector (dark area) and that would reach the detector if the setup were not in the way (light area). Dashed lines indicate the

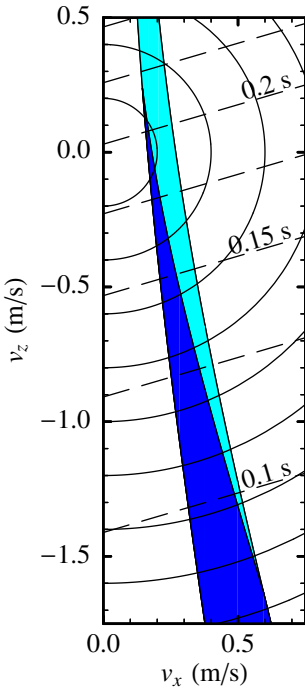


Figure 2.2. Range of velocity components that atoms at the centre must have to reach the He* detector (dark area). With values in the light area, atoms hit the setup before reaching the detector. Horizontal velocity component v_x is in the direction of the centre of the detector; horizontal component v_y perpendicular to this is zero. Circles constitute points with equal total velocity, dashed lines indicate travelling times to the plane of the detector.

time it takes to travel to the detector plane; with a larger v_z , i.e. if the starting velocity is directed more upward, atoms arrive later. An atom with $v_x = 0.15$ m/s and $v_z = 0.24$ m/s is the last one to be detected, 0.218 s after switching off the trap. Atoms with the same total velocity of 0.28 m/s but in an arbitrary direction arrive mostly after about 0.173 s. This corresponds in Fig. 2.2 to a circle around the origin intersecting the dark area in two places, with the largest intersection at earlier times. In general, although individual atoms can arrive after 0.2 s, the peak of a TOF signal comes before this time. However, if the atoms have a vertical offset velocity, which would look in the figure as an upward shift of the circular pattern, the TOF peak can come later: at 1 μK the peak is at 0.192 s without offset, at 0.206 s with $v_0 = 0.15$ m/s, and at 0.214 s with $v_0 = 0.3$ m/s.

To determine the effective offset velocity we can use the fact that the atoms need a minimum velocity $v_{\min} = 0.16$ m/s to reach the detector. The total energy of an atom in the trap cannot exceed the trap depth ε_t , so we will only detect atoms if the trap depth is at least $\frac{1}{2}mv_{\min}^2 = k_B(6 \mu\text{K})$. The temperature of the atoms is $\varepsilon_t/\eta k_B$, where the truncation parameter η is in the range $3 < \eta < 10$ with 6 as the most likely value (see §7.4.5). This means that the lowest temperature we can measure is 1 μK (between 0.6 μK and 2 μK). A TOF signal with a peak at 0.210 s corresponds to a temperature of 1 μK with $v_0 = 0.21$ m/s, and to one of the temperature limits if the offset velocity is between 0.18 m/s and 0.30 m/s. We will use $v_0 = 0.21$ m/s for TOF signals from the cloverleaf trap and $v_0 = 0$ for the magneto-optical and quadrupole trap, unless stated otherwise.

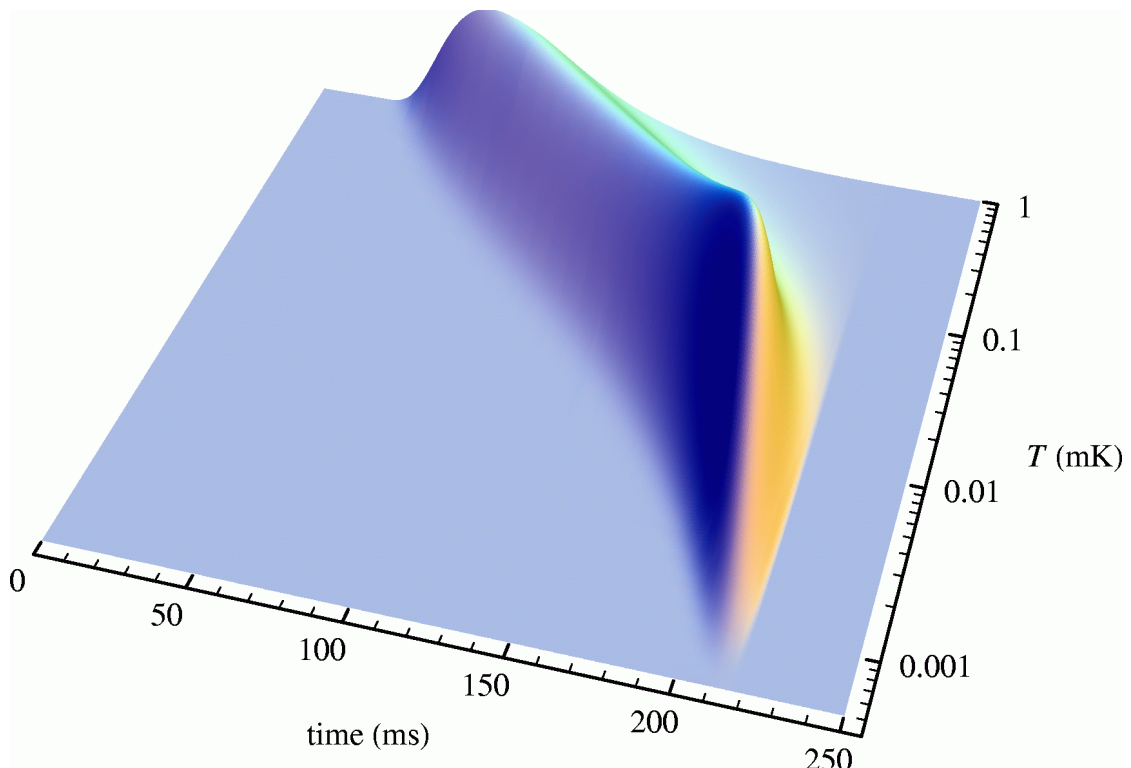


Figure 2.3. The expected signal on the He^* detector as a function of time and temperature, for a fixed number of atoms in the trap, with a vertical offset velocity of 0.21 m/s. This is the function with which TOF signals from the cloverleaf trap are fitted.

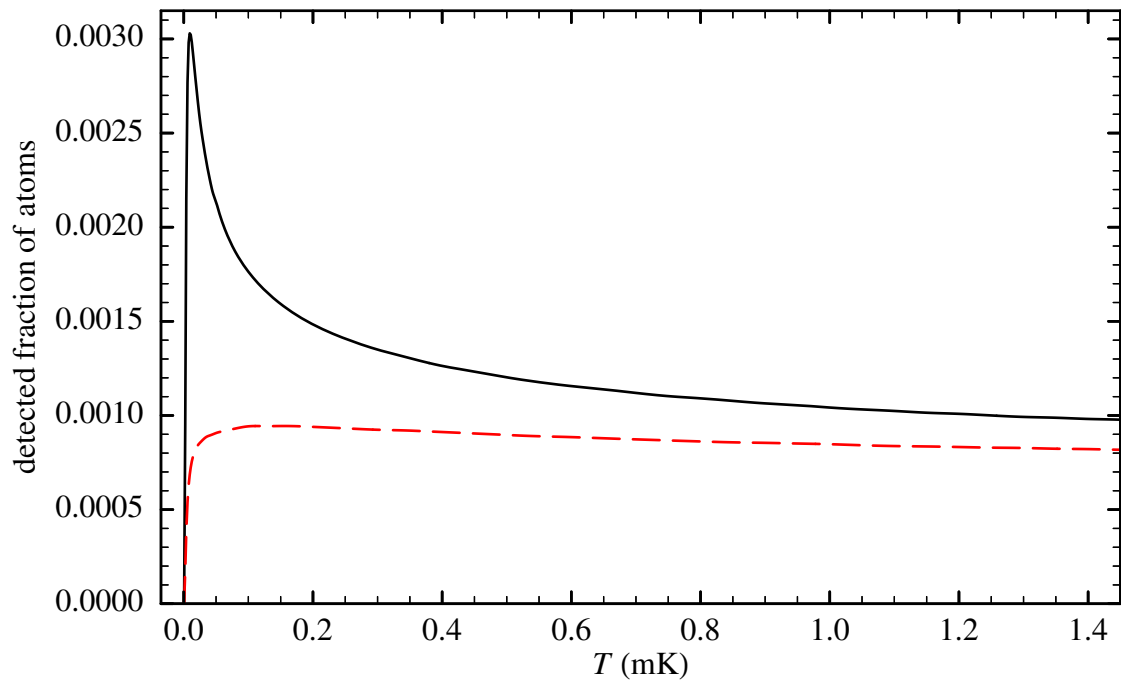


Figure 2.4. Fraction F of atoms in the trap reaching the He * detector, as a function of temperature. Solid curve is without offset velocity, dashed curve is with an upward offset velocity of 0.21 m/s, given to all atoms.

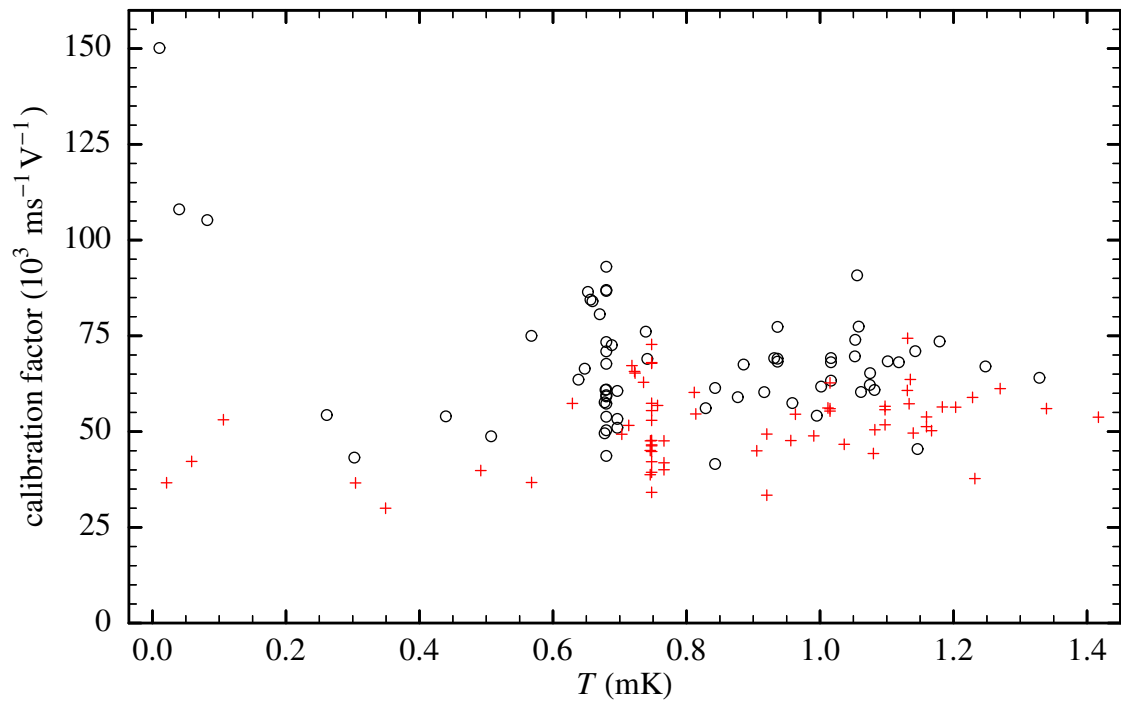


Figure 2.5. Measured calibration factor $1/RC_1$ as a function of temperature in the cloverleaf trap, without offset velocity (circles) and with a vertical offset velocity of 0.21 m/s (crosses).

Including an offset velocity only changes significantly the shape of the simulated TOF signal below 50 μK , making the peak wider, although not as wide as measured peaks (see Fig. 2.6). Fitted temperatures will be higher: 1 mK becomes 1.08 mK, 0.1 mK becomes 0.13 mK, 10 μK becomes 23 μK . Figure 2.3 shows the expected TOF signal as a function of temperature.

The offset velocity not only corrects the fitted temperature, but also the fraction of atoms falling on the detector (Fig. 2.4). In simulations without an offset velocity this fraction is much larger at about 10 μK than at high temperatures. This can be understood from Fig. 2.2: the fraction of a circle lying across the dark area is larger for smaller circles, especially when they start to intersect the dark area at two places. With a vertical offset velocity this no longer happens. The change in detected fraction has an effect on the calibration of the detector (Fig. 2.5). The apparent relative increase of the calibration factor below 0.2 mK is gone with an offset velocity, making the calibration more consistent. The absolute value of the calibration factor is discussed in §2.3.7.

By including an extra horizontal offset velocity, the fitted temperature changes only a little at any temperature (4% per 0.1 m/s at 20 μK , 0.8% per 0.1 m/s at 1 mK), so there is no need for inclusion. It would even make the calibration less consistent, because the number of atoms changes dramatically at low temperatures (38% per 0.1 m/s at 20 μK , 3% per 0.1 m/s at 1 mK). Therefore we use only a vertical offset velocity.

2.2.4 Examples of fits to TOF signals

In Figs. 2.1 and 2.2 the situation is given in two dimensions, but for the simulations a three-dimensional model is used, including the circular shape of the detector and the hole through which the atoms have to travel to reach the detector. The initial size of the atomic cloud is taken into account, although it has little effect on the TOF signal due to the large distance between the detector and the trap. Above 0.1 mK the simulated cloud has a Gaussian, spherical shape with an rms radius of 0.2 cm. Below this temperature we calculate the expected density profile (see §6.2.3) in our compressed cloverleaf trap, which is taken to be infinitely deep, and fit a Gaussian curve. Then, at 0.1 mK the vertical radius is still 0.2 cm, but the horizontal radius becomes 0.02 cm. The resulting TOF peak height is almost the same, but the tail at later times is reduced.

Figure 2.6 shows examples of TOF signals from the magneto-optical and cloverleaf trap, together with the temperature and number of atoms determined by fits. At high temperatures the fit is excellent, although in the cloverleaf trap there is an unexplained tail after 250 ms, when no atoms should be able to reach the detector. After 300 ms the signal suddenly drops to zero. At lower temperatures the measured TOF signal has a larger width than expected. This may be due to a spread in the magnetic field gradient the atoms encounter or, for instance, because the atoms have changed their Zeeman substate and we see a division into three groups of atoms. When the temperature has dropped to 1 μK , the number of atoms becomes difficult to determine, because the detected fraction of atoms is small and depends heavily on the temperature and assumed offset velocity (see Fig. 2.4). At 1 μK and for $v_0 = 0.21 \text{ m/s}$ the calculated fraction is 1.2×10^{-5} , but for instance at 2 μK it is 11 times larger. The number of atoms fitted in the bottom row of Fig. 2.6 is therefore unreliable.

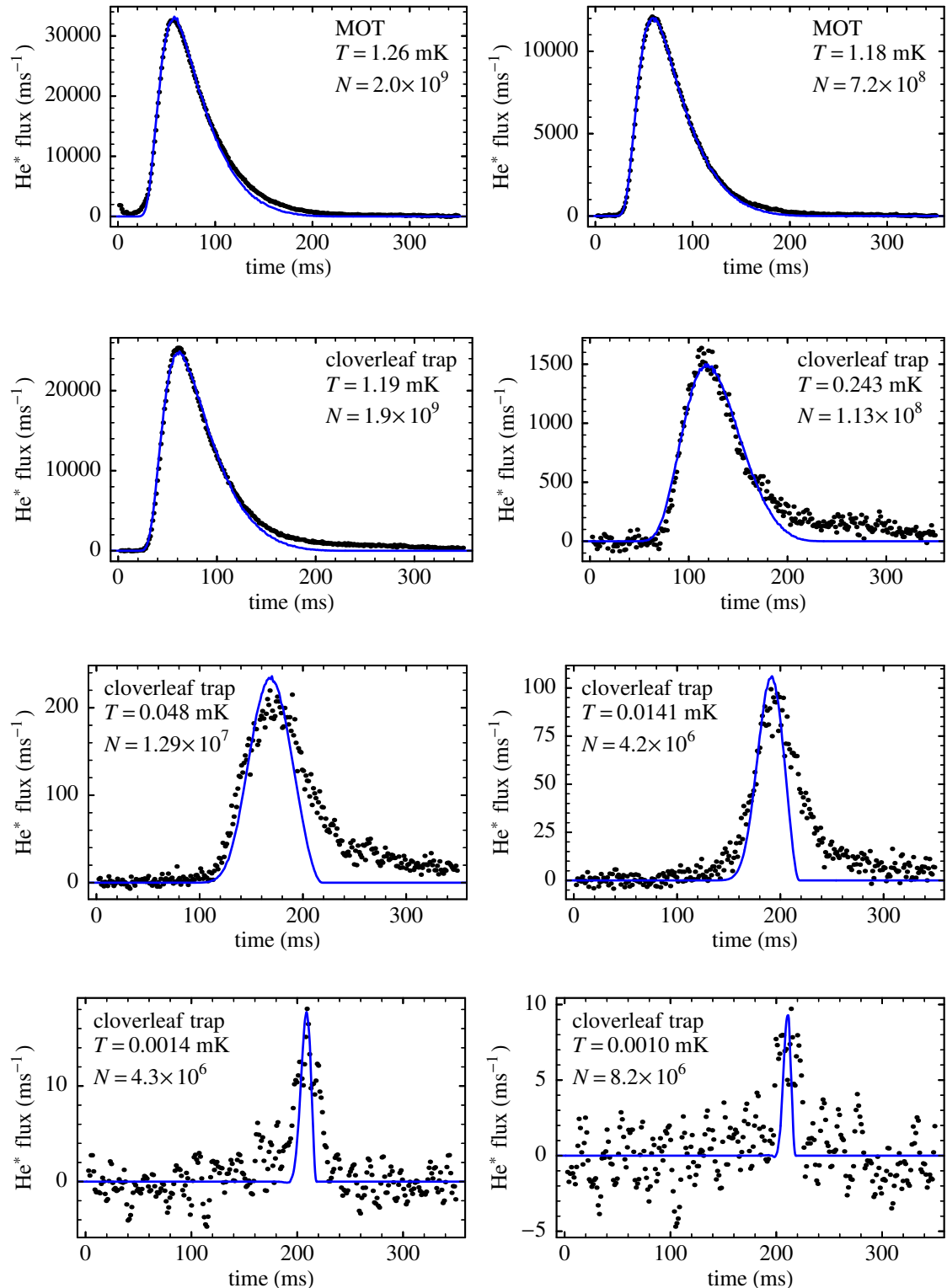


Figure 2.6. Number of metastable helium atoms per unit of time reaching the detector as a function of time: examples from the magneto-optical and cloverleaf trap. Solid curves are fits with time-of-flight simulations, from which temperature T and original number of atoms N in the trap are extracted.

If the detector were on a vertical line below the trap centre, the detected fraction would continually increase while the temperature decreases. The number of atoms falling on the detector would drop less during evaporative cooling (see §7.4.5), despite heavy trap loss. Due to the fact that a TOF signal is more peaked at lower temperatures, the signal *height* would even increase below a particular temperature (in our case 0.1 mK), an effect seen by Westbrook et al. [101]. With our detector at the current position, the signal height only decreases during evaporative cooling.

2.3 Absorption imaging

2.3.1 Introduction

A more general technique to determine the number of atoms is absorption imaging, whereby probe light at or near an atomic transition is sent through the cloud and the amount of absorption is examined. Not only can this technique be applied to any trapped element, there is also no need for calibration. However, in helium several complications occur due to its small atomic mass: the atoms are pushed by the probe beam, even at small intensities, and Doppler broadening has to be taken into account. In addition, the effects of light polarization and magnetic field have to be studied for an accurate determination of the number of atoms in our trap. Therefore we take a careful look at the theoretical treatment of absorption and include these extra elements. Section 2.3.2 is based on Hilborn [33], without neglecting stimulated emission. As far as possible the theory is kept independent of the precise nature of the transition, but for numerical examples the $2\ ^3S_1 - 2\ ^3P_2$ transition in helium at 1083 nm is used.

2.3.2 Two-level system

According to Lambert's law, the intensity I of a beam of light travelling in the $+\hat{x}$ direction through a medium with absorption coefficient α can be described by $dI/dx = -\alpha I$. When the absorption coefficient depends on frequency, the spectral irradiance $i(\omega)$ should be used, defined by $I = \int i(\omega) d\omega$. In this case Lambert's law becomes

$$\frac{di(\omega)}{dx} = -\alpha(\omega)i(\omega). \quad (2.1)$$

The frequency dependence of the absorption and emission processes can be expressed in terms of a line-shape function $g(\omega)$, normalized so that $\int_{-\infty}^{\infty} g(\omega) d\omega = 1$. If the spectral line is broadened by the effect of temperature (Doppler broadening) and/or collisions, $g(\omega)$ is the corresponding ensemble-averaged line shape.

Absorption and emission in the medium will be described in terms of Einstein A and B coefficients. First we take a two-level system, with N_1 atoms in lower level 1 with energy E_1 , and N_2 atoms in upper level 2 with energy E_2 . A broadband radiation field is present with energy density per unit angular frequency ρ . The transition rate for spontaneous emission from level 2 to level 1 is then $W_{21}^{sp} = A_{21}N_2$, and the transition rates for the induced processes of absorption and stimulated emission are $W_{12}^{ind} = B_{12}\rho N_1$

and $W_{21}^{\text{ind}} = B_{21}\rho N_2$, respectively. In general the relationships between the Einstein coefficients are $B_{21} = \frac{\pi^2 c^3}{\hbar \omega_{21}^3} A_{21}$ and $B_{12} = \frac{g_2}{g_1} B_{21}$, with $\omega_{21} = (E_2 - E_1)/\hbar$ the resonance frequency of the transition, g_1 and g_2 the degeneracy factors of the two levels, and \hbar Planck's constant divided by 2π .

In the case of nearly monochromatic radiation, ρ depends on frequency,

$$\rho(\omega) = i(\omega)/c \quad (2.2)$$

with c the speed of light, and we have to define an absorption rate due to radiation in the angular frequency range from ω to $\omega + d\omega$ as

$$w_{12}^{\text{ind}}(\omega) d\omega = b_{12}(\omega)\rho(\omega)N_1 d\omega, \quad (2.3)$$

with $b_{12}(\omega) = B_{12}g(\omega)$. Similarly, the stimulated emission rate becomes

$$w_{21}^{\text{ind}}(\omega) d\omega = b_{21}(\omega)\rho(\omega)N_2 d\omega, \quad (2.4)$$

with $b_{21}(\omega) = B_{21}g(\omega)$. The total power absorbed by the atoms in the frequency range from ω to $\omega + d\omega$ is then

$$-P = \hbar\omega[w_{12}^{\text{ind}}(\omega) - w_{21}^{\text{ind}}(\omega)] d\omega. \quad (2.5)$$

In volume element $dV = dx dy dz$ with dN_1 and dN_2 atoms in the lower and upper level, respectively, the incremental power absorbed is

$$-dP = [b_{12}(\omega) dN_1 - b_{21}(\omega) dN_2] \hbar\omega\rho(\omega) d\omega, \quad (2.6)$$

while the incremental power contained in the beam of light is

$$dP = i(\omega) d\omega dy dz. \quad (2.7)$$

Introducing local densities $n_1 = dN_1/dV$ and $n_2 = dN_2/dV$, Eq. (2.1) can be written as

$$\frac{di(\omega)}{dx} = -[b_{12}(\omega)n_1 - b_{21}(\omega)n_2]\hbar\omega\rho(\omega) = -(B_{12}n_1 - B_{21}n_2)\frac{\hbar\omega}{c}g(\omega)i(\omega). \quad (2.8)$$

At low intensities the upper level will have a negligible population and we get $\alpha(\omega) \approx B_{12}\frac{\hbar\omega}{c}g(\omega)n_1$: the absorption coefficient is directly proportional to the atomic density, as is stated by Beer's law. At higher intensities however, this law no longer holds. In contrast, Lambert's law always remains valid.

Generally the Einstein A coefficient, total decay rate, and line width are not the same. If a system consists of more than two levels, the total decay rate Γ_j from level j is given by a sum over the decay rates to all levels i with energies $E_i < E_j$. In general each decay rate consists of a radiative and a non-radiative part, but we will assume the non-radiative part can be neglected. The radiative decay rate for an atomic transition between levels j and i is its Einstein coefficient A_{ji} . The homogeneous FWHM transition line width is $\Gamma \equiv \Gamma_j + \Gamma_i$. Only when there is a single decay path from level 2, and the corresponding lower level 1 cannot decay (or with a negligible rate), as discussed here, $\Gamma = \Gamma_2 = A_{21}$.

2.3.3 Zeeman sublevels

If the two considered levels are degenerate, we can look at the system as a collection of transitions between $2J_2 + 1$ upper sublevels, labelled with their magnetic quantum number m_j , and $2J_1 + 1$ lower sublevels, labelled with m_i . The decay rate from m_j to m_i is a fraction $C_{ji} \equiv C_{m_j, m_i}$ of the total decay rate Γ , with $\sum_i C_{ji} = 1$. In terms of Clebsch-Gordan coefficients $\langle j_1 j_2 m_1 m_2 | j_1 j_2 jm \rangle$ we have for an electric dipole transition

$$C_{ji} = |\langle J_1 1 m_i (m_j - m_i) | J_1 1 J_2 m_j \rangle|^2, \quad (2.9)$$

with $\Delta m \equiv m_j - m_i = 0, \pm 1$ (see Fig. 2.7 for values of C_{ji} in the ${}^3P_2 - {}^3S_1$ case) [88].

Equation (2.8) becomes a sum of terms for every subtransition, with B_{21} and B_{12} replaced by $\frac{\pi^2 c^3}{\hbar \omega_{ji}^3} C_{ji} \Gamma$; as the degeneracy has been lifted by considering each sublevel separately, $b_{ji} = b_{ij}$. The line-shape functions $g_{ji}(\omega)$ can be assumed to be the same for all transitions, except for a possible shift if a magnetic field is present.

The induced transition rate between m_i and m_j for light characterized by unit polarization vector \hat{e} is proportional to

$$|\langle J_1 m_i | \hat{e} \cdot \mathbf{r} | J_2 m_j \rangle|^2 = \frac{4\pi}{3} |Y_1^{\Delta m}(\hat{e})|^2 |\langle J_1 m_i | r_q | J_2 m_j \rangle|^2, \quad (2.10)$$

with spherical harmonic $Y_1^{\Delta m}$, electric dipole moment $-e\mathbf{r}$, and r_q , the relevant spherical tensor component of \mathbf{r} [103]. Above we have assumed the light is unpolarized, so at this point b_{ji} is proportional to

$$\overline{|\langle J_1 m_i | \hat{e} \cdot \mathbf{r} | J_2 m_j \rangle|^2}$$

where the overbar indicates an average over all polarizations \hat{e} . If the polarization of the

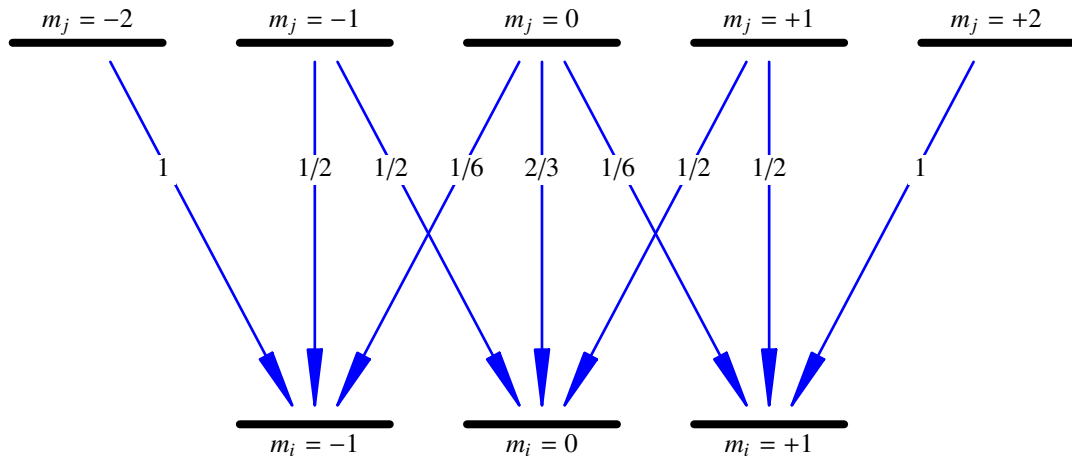


Figure 2.7. Value of C_{ji} for each subtransition $m_j \rightarrow m_i$ in an atom with ground state $J_1 = 1$ and excited state $J_2 = 2$. The value is zero for subtransitions that are not drawn.

light has a definite direction, b_{ji} has to be multiplied with a factor

$$\begin{aligned}\Theta_{ji}(\hat{\mathbf{e}}) &= \left| \langle J_1 m_i | \hat{\mathbf{e}} \cdot \mathbf{r} | J_2 m_j \rangle \right|^2 / \overline{\left| \langle J_1 m_i | \hat{\mathbf{e}} \cdot \mathbf{r} | J_2 m_j \rangle \right|^2} \\ &= \left| Y_1^{\Delta m}(\hat{\mathbf{e}}) \right|^2 / \overline{\left| Y_1^{\Delta m}(\hat{\mathbf{e}}) \right|^2} \\ &= 4\pi \left| Y_1^{\Delta m}(\hat{\mathbf{e}}) \right|^2,\end{aligned}\quad (2.11)$$

and b_{ji} becomes

$$b_{ji}(\omega) = \Theta_{ji} \frac{\pi^2 c^3 \Gamma}{\hbar \omega_{ji}^3} C_{ji} g_{ji}(\omega). \quad (2.12)$$

The polarization factor satisfies the equation

$$\frac{1}{2J_2 + 1} \sum_j \sum_i \Theta_{ji} C_{ji} = 1. \quad (2.13)$$

With $\hat{\mathbf{e}}$ expressed in terms of Cartesian coordinates as $\hat{\mathbf{e}} = a_1 \hat{\mathbf{x}} + a_2 \hat{\mathbf{y}} + a_3 \hat{\mathbf{z}}$ and the quantization axis in the $+\hat{\mathbf{z}}$ direction, the polarization factor is

$$\Theta_{ji}(\hat{\mathbf{e}}) = \begin{cases} 3|a_3|^2, & \Delta m = 0, \\ \frac{3}{2}|a_1 \pm ia_2|^2, & \Delta m = \pm 1. \end{cases} \quad (2.14)$$

Siegman [81] gives an alternative derivation for this factor.

On $\Delta m = 0$ transitions an atom (or a collection of aligned atoms) acts as a linearly oscillating electric dipole. If the light is linearly polarized with the electric field oscillating in a plane parallel to the $\hat{\mathbf{z}}$ direction ($\hat{\mathbf{e}} = \hat{\mathbf{z}}$), the light polarization matches the polarization of the transition, the atom is driven most effectively, and Θ_{ji} has the maximum value of 3. On $\Delta m = +1$ transitions the atom is a rotating dipole, for which the highest transition rate is reached with right-handed circularly polarized (RHCP) light propagating in the $+\hat{\mathbf{z}}$ direction, $\hat{\mathbf{e}} = (\hat{\mathbf{x}} - i\hat{\mathbf{y}})/\sqrt{2}$. Transitions with $\Delta m = -1$ are excited best with left-handed circularly polarized (LHCP) light in the same direction, $\hat{\mathbf{e}} = -(\hat{\mathbf{x}} + i\hat{\mathbf{y}})/\sqrt{2}$. If the light polarization does not match the polarization of the transition, only a component of the applied field is seen and Θ_{ji} is smaller, with a minimum of 0 (see Fig. 2.8 for examples).

If the polarization direction of the light is random compared to the quantization axis, either because the light is unpolarized or because a collection of atoms is *on average* randomly aligned (for instance when the degeneracy has not been broken),

$$\Theta_{ji} = 4\pi \overline{\left| Y_1^{\Delta m}(\hat{\mathbf{e}}) \right|^2} = 1, \quad \Delta m = 0, \pm 1; \hat{\mathbf{e}} \cdot \mathbf{r} \text{ random}. \quad (2.15)$$

In the second case, in effect, a third of the atoms are oriented along each axis. Then the light drives 1/3 of the atoms with $\Theta_{ji} = 3$ and the other 2/3 with $\Theta_{ji} = 0$. Averaged this means that all transitions have $\Theta_{ji} = 1$, whatever the polarization of the light.

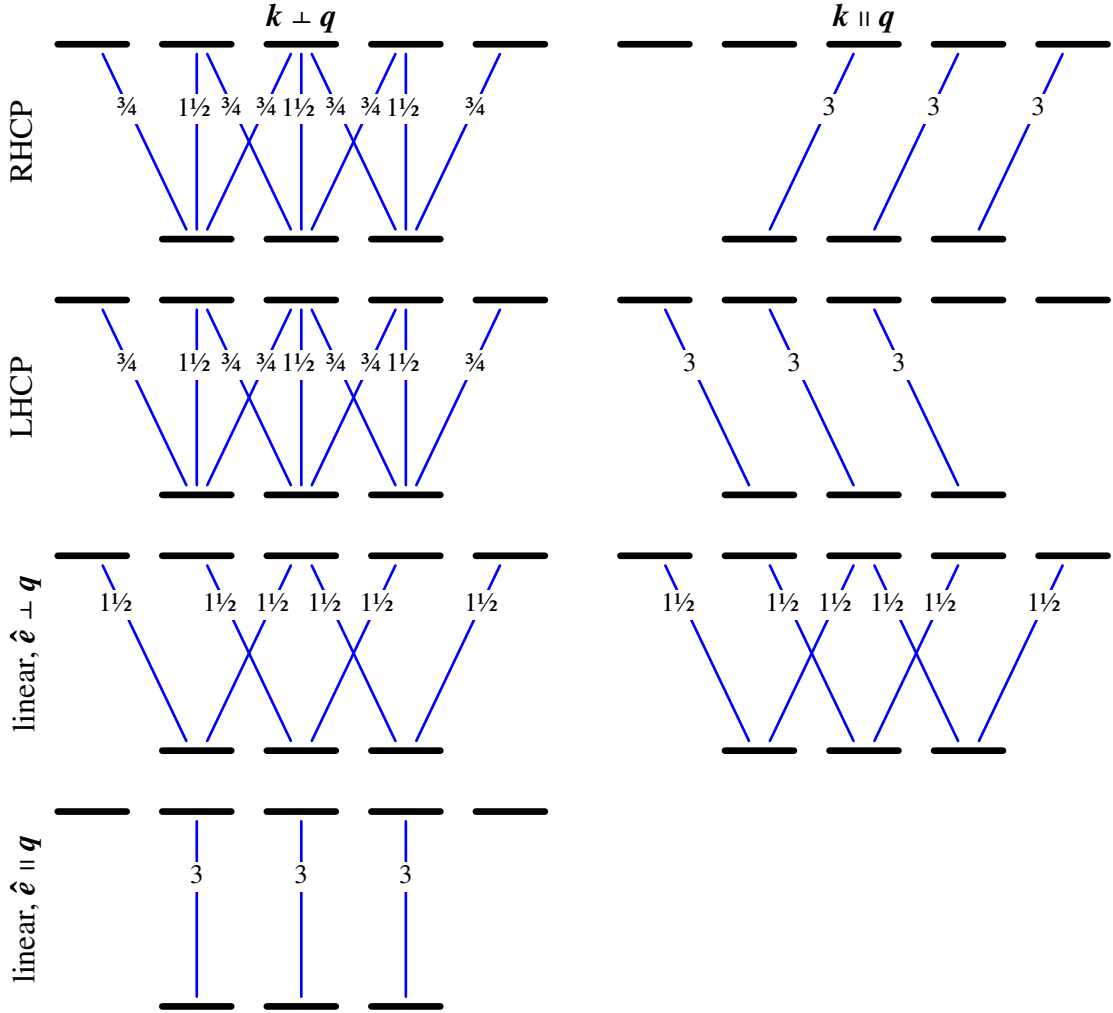


Figure 2.8. Value of polarization factor Θ_{ji} for each subtransition $m_j - m_i$ in an atom with ground state $J_1 = 1$ and excited state $J_2 = 2$, in different situations: light vector \mathbf{k} either perpendicular or parallel to quantization axis \mathbf{q} , while the light is either right-handed circularly polarized, left-handed circularly polarized, or linearly polarized, with polarization vector $\hat{\mathbf{e}}$ perpendicular or parallel to \mathbf{q} . Sublevels are labelled as in Fig. 2.7. The polarization factor is zero for subtransitions that are not drawn.

With Eq. (2.12) Lambert's law, Eq. (2.8), can be written as

$$\begin{aligned} \frac{di(\omega)}{dx} &= - \sum_j \sum_i [b_{ij}(\omega)n_i - b_{ji}(\omega)n_j] \hbar\omega_{ji}\rho(\omega) \\ &= - \sum_j \sum_i (n_i - n_j)\Theta_{ji} \frac{\pi^2 c^2 \Gamma}{\omega_{ji}^2} C_{ji} g_{ji}(\omega) i(\omega). \end{aligned} \quad (2.16)$$

Assuming all $g_{ji}(\omega)$ are peaked near ω_{21} , the factors ω_{ji} can be replaced by ω_{21} , and subsequently we drop the subscript. Introducing a line-shape factor

$$\chi_{ji} = \frac{\pi\Gamma}{2I} \int_{-\infty}^{\infty} g_{ji}(\omega) i(\omega) d\omega \quad (2.17)$$

and a saturation intensity

$$I_{\text{sat}} = \frac{\hbar\omega\pi\Gamma}{3\lambda^2} \quad (2.18)$$

with resonance wavelength λ , we obtain

$$\frac{\pi^2 c^2 \Gamma}{\omega^2} \int_{-\infty}^{\infty} g_{ji}(\omega) i(\omega) d\omega = \hbar\omega \frac{\Gamma}{2} \frac{I}{I_{\text{sat}}} \frac{1}{3} \chi_{ji} \quad (2.19)$$

and Lambert's law becomes after integration over frequency:

$$\frac{dI}{dx} = -\hbar\omega \frac{\Gamma}{2} \frac{I}{I_{\text{sat}}} \sum_j \sum_i (n_i - n_j) \frac{\Theta_{ji}}{3} C_{ji} \chi_{ji}. \quad (2.20)$$

At this point the saturation intensity is simply a constant associated with the transition.[†] For the transition in helium at 1083 nm it is 0.167 mW/cm². In literature the Rabi frequency Ω is often used, which can be defined in terms of the intensity by $I/I_{\text{sat}} = 2\Omega^2/\Gamma^2$.

All information about the line shape of the transition and the line width of the laser is contained in the factor χ_{ji} . In general χ_{ji} depends on temperature T , magnetic field B , laser line width γ_l , and laser detuning $\Delta = \omega_l - \omega_{21}$, with laser frequency ω_l . In a low-density gas, in the limit of low temperatures, $g_{ji}(\omega)$ has a Lorentz line shape with FWHM Γ . At higher temperatures Doppler broadening must be taken into account, and the line shape is integrated over a Maxwell-Boltzmann distribution of the atomic velocity in the light direction $v = c(\omega - \omega_{ji})/\omega_{ji}$:

$$\begin{aligned} g_{ji}(\omega) &= \frac{d}{\sqrt{\pi}} \int_{-\infty}^{\infty} \frac{\Gamma/2\pi}{(\omega - \omega')^2 + (\Gamma/2)^2} e^{-d^2(\omega' - \omega_{ji})^2} d\omega' \\ &= \frac{d}{\sqrt{\pi}} \text{Re} \left\{ \exp \left[-d^2 \left(i \frac{\Gamma}{2} + \omega - \omega_{ji} \right)^2 \right] \text{erfc} \left[d \left(\frac{\Gamma}{2} - i(\omega - \omega_{ji}) \right) \right] \right\} \end{aligned} \quad (2.21)$$

with $d = \frac{\lambda}{2\pi} \sqrt{\frac{m}{2k_B T}}$, mass m , complementary error function $\text{erfc}(z) = 1 - \frac{2}{\sqrt{\pi}} \int_0^z e^{-t^2} dt$, and

$$\int_{-\infty}^{\infty} \frac{y e^{-t^2}}{(x-t)^2 + y^2} dt = \pi \text{Re}[w(x+iy)], \quad x \text{ real}, y > 0, \quad (2.22)$$

with $w(z) = e^{-z^2} \text{erfc}(-iz)$ [2]. The influence of a magnetic field is to shift the line $g_{ji}(\omega)$ by an amount $\Delta_B = (g_j m_j - g_i m_i) \mu_B B / \hbar$, with Landé g factors. For the purpose of calculating χ_{ji} we can keep $g_{ji}(\omega)$ independent of B and instead shift the laser frequency. Then the laser has an effective detuning $\Delta' = \Delta - \Delta_B$, depending on the subtransition. The line-shape factor χ_{ji} only depends on the subtransition via Δ' : without magnetic field all χ_{ji} are the same. When $B = 0$ or when the subtransition dependence is not needed explicitly, we will suppress the subscripts of the line-shape factor.

[†]In a general multilevel system, Eqs. (2.20) and (2.17) are still correct if the saturation intensity is defined as $I_{\text{sat}} = \hbar\omega\pi\Gamma^2/3\lambda^2 A_{21}$.

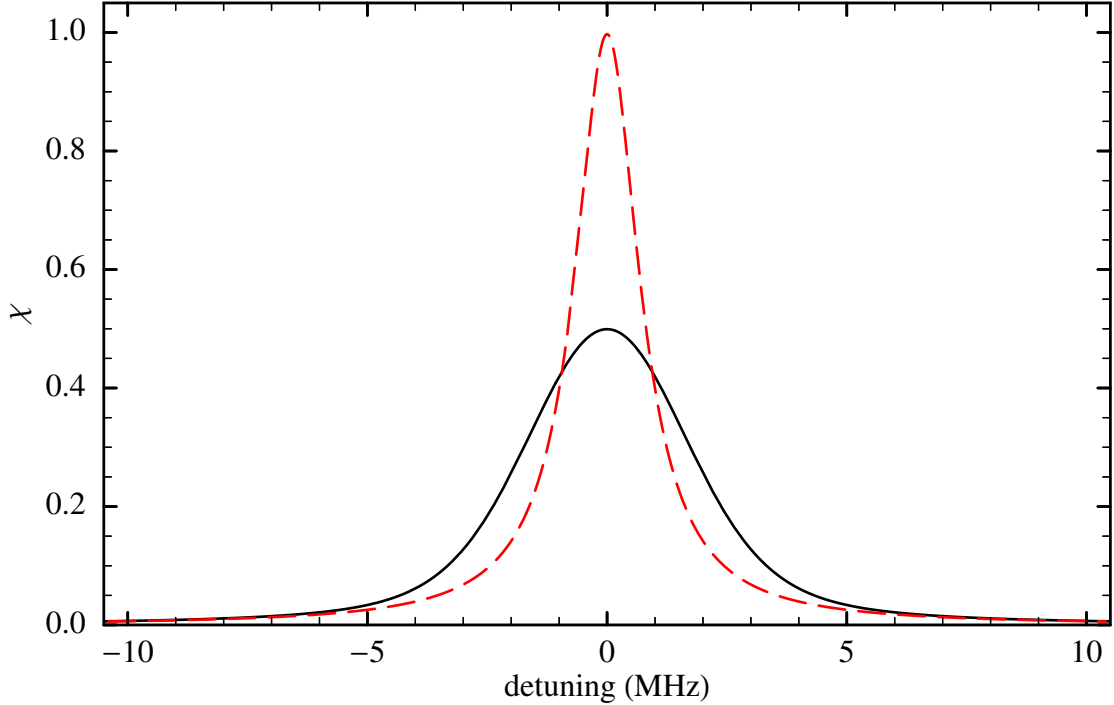


Figure 2.9. Line-shape factor χ as a function of detuning $\Delta'/2\pi$ for the transition used for absorption in helium, at a temperature of 1 mK (solid curve) and 1 μK (dashed curve). A negligible laser line width is assumed.

The factor χ has been normalized so it has a value of unity in the simplest case of a transition with a natural Lorentz line shape and the laser, with a negligible line width, at resonance:

$$\lim_{\substack{T \rightarrow 0 \\ \gamma_l \rightarrow 0 \\ \Delta' \rightarrow 0}} \chi = 1. \quad (2.23)$$

With a detuning and a Lorentz laser line width γ_l (FWHM), respectively, χ becomes

$$\lim_{\substack{T \rightarrow 0 \\ \gamma_l \rightarrow 0}} \chi = \frac{1}{1 + (2\Delta'/\Gamma)^2}, \quad (2.24)$$

$$\lim_{T \rightarrow 0} \chi = \frac{\Gamma(\Gamma + \gamma_l)}{(\Gamma + \gamma_l)^2 + 4\Delta'^2}. \quad (2.25)$$

In case of only Doppler broadening we get

$$\begin{aligned} \lim_{\gamma_l \rightarrow 0} \chi &= \frac{\pi\Gamma}{2} g_{ji}(\omega_l - \Delta_B) \\ &= d \frac{\Gamma}{2} \sqrt{\pi} \operatorname{Re} \left\{ \exp \left[-d^2 \left(i \frac{\Gamma}{2} + \Delta' \right)^2 \right] \operatorname{erfc} \left[d \left(\frac{\Gamma}{2} - i\Delta' \right) \right] \right\}. \end{aligned} \quad (2.26)$$

The same result is reached by directly averaging Eq. (2.24) over a Maxwell-Boltzmann distribution with Δ' replaced by $\Delta' - \frac{2\pi}{\lambda}v$. At $\Delta' = 0$ the line-shape factor becomes simply

$$\lim_{\substack{\gamma_i \rightarrow 0 \\ \Delta' \rightarrow 0}} \chi = \sqrt{\pi} u \exp(u^2) \operatorname{erfc}(u), \quad (2.27)$$

with $u = \frac{\lambda\Gamma}{4\pi} \sqrt{\frac{m}{2k_B T}}$. In the most general case χ has to be calculated numerically. Figure 2.9 shows χ for the transition at 1083 nm in helium which, according to Eq. (2.26), is the same as transition line shape g_{ji} in scaled units. Due to the small mass of helium and the small natural line width of $\Gamma/2\pi = 1.6$ MHz, Doppler broadening cannot be neglected in the magneto-optical and magnetic trap at temperatures of about 1 mK: then the FWHM line width becomes 4.1 MHz. In rubidium, using the transition at 780 nm with a natural line width of 6 MHz, $\chi = 0.98$ at resonance at 1 mK, while temperatures are much lower in corresponding traps.

2.3.4 Effective saturation intensity

To simplify equations later on, Eq. (2.20) can be written as

$$\frac{dI}{dx} = -\hbar\omega \frac{\Gamma}{2} \frac{I}{I'_{\text{sat}}} (\sum_i n_i - \sum_j n_j), \quad (2.28)$$

with effective saturation intensity

$$I'_{\text{sat}} \equiv \frac{\sum_i n_i - \sum_j n_j}{\sum_j \sum_i \frac{\Theta_{ji}}{3} C_{ji} \chi_{ji} (n_i - n_j)} I_{\text{sat}}. \quad (2.29)$$

Population densities n_i and n_j are governed by rate equations. First we give these equations for populations N_i and N_j :

$$\begin{aligned} \frac{dN_i}{dt} &= \sum_j \left(-W_{ij}^{\text{ind}} + W_{ji}^{\text{ind}} + W_{ji}^{\text{sp}} \right), \\ \frac{dN_j}{dt} &= \sum_i \left(W_{ij}^{\text{ind}} - W_{ji}^{\text{ind}} - W_{ji}^{\text{sp}} \right), \end{aligned} \quad (2.30)$$

with $\sum_i N_i + \sum_j N_j = N$ and transition rates

$$\begin{aligned} W_{ji}^{\text{ind}} &= \int w_{ji}^{\text{ind}}(\omega) d\omega = N_j \int b_{ji}(\omega) \rho(\omega) d\omega = N_j \frac{\Gamma}{2} \frac{I}{I'_{\text{sat}}} \frac{\Theta_{ji}}{3} C_{ji} \chi_{ji}, \\ W_{ij}^{\text{ind}} &= W_{ji}^{\text{ind}} N_i / N_j, \\ W_{ji}^{\text{sp}} &= \Gamma C_{ji} N_j. \end{aligned} \quad (2.31)$$

Replacing populations by population densities, the rate equations become:

$$\begin{aligned} \frac{dn_i}{dt} &= \sum_j \left(\frac{\Gamma}{2} \frac{I}{I'_{\text{sat}}} \frac{\Theta_{ji}}{3} C_{ji} \chi_{ji} (-n_i + n_j) + \Gamma C_{ji} n_j \right), \\ \frac{dn_j}{dt} &= \sum_i \left(\frac{\Gamma}{2} \frac{I}{I'_{\text{sat}}} \frac{\Theta_{ji}}{3} C_{ji} \chi_{ji} (n_i - n_j) \right) - \Gamma n_j, \end{aligned} \quad (2.32)$$

with

$$\sum_i n_i + \sum_j n_j = n. \quad (2.33)$$

However, they are only valid if coherences between the transitions can be neglected. This is the case when the time rate of change of the populations is smaller than $\Gamma/2$ [81] and when the transitions do not share common upper or lower sublevels, i.e. when all excited transitions have the same Δm , with a value of either -1 , 0 , or 1 . Polarization factor Θ_{ji} will only have values of either 0 or 3 . Coherences are also lost if a magnetic field shifts the transitions so much that the distance between substates is larger than the transition or laser line width: only one transition can then be excited.

For situations conforming to these restrictions, the intensity of the probe light as a function of position and time is described by Eqs. (2.28), (2.29), (2.32), and (2.33). At two stages of probing these equations can be simplified by eliminating population densities n_i and n_j in favour of total population density n : the moment at which the light is switched on and when steady state is reached.

Steady state

By definition, in steady state $dn_j/dt = 0$. Equation (2.29) for the effective saturation intensity can then be written as

$$I'_{\text{sat}}/I = \frac{\sum_i n_i - \sum_j n_j}{2 \sum_j n_j}. \quad (2.34)$$

If an intensity $I = I'_{\text{sat}}$ is used, this leads to $\sum_i n_i = 3 \sum_j n_j$: at this intensity in steady state, a quarter of the atoms is in the upper state (half of the maximum population), whatever the temperature, laser detuning, or laser line width. Here we ignore situations in which all atoms are optically pumped to one or more dark states, where they no longer interact with the light. By rearranging Eq. (2.34) as

$$\sum_i n_i - \sum_j n_j = \frac{\sum_i n_i + \sum_j n_j}{1 + I/I'_{\text{sat}}}, \quad (2.35)$$

Eq. (2.28) reduces in steady state to

$$\frac{dI}{dx} = -\hbar\omega \frac{\Gamma}{2} n \frac{I/I'_{\text{sat}}}{1 + I/I'_{\text{sat}}}. \quad (2.36)$$

The reduction in intensity $-dI$ is the number of atoms $n dx dy dz$ times the average absorption rate per atom $\frac{1}{2}\Gamma(I/I'_{\text{sat}})/(1 + I/I'_{\text{sat}})$ times the energy of a photon $\hbar\omega$ divided by area $dy dz$. The value of I'_{sat} is found by solving the rate equations. When all χ_{ji} are the same or when only one subtransition is involved, the effective saturation intensity is expressed as

$$I'_{\text{sat}} = f I_{\text{sat}} / \chi, \quad (2.37)$$

with rational number f .[†]

[†]For instance Herschbach [32] defines the saturation intensity itself as $f I_{\text{sat}}$.

For $J_2 = J_1 + 1$ with $\Delta m = \pm 1$ (when $J_1 = 0$ also with $\Delta m = 0$), all atoms are pumped into one lower sublevel m_i and one upper sublevel m_j , and there is only one relevant transition left, with $C_{ji} = 1$ and $\Theta_{ji} = 3$. The population of sublevel m_j is

$$n_j = \frac{1}{2} \frac{\chi_{ji} I / I_{\text{sat}}}{1 + \chi_{ji} I / I_{\text{sat}}} n, \quad (2.38)$$

and $f = 1$. This means that in the textbook case when the temperature, laser detuning, and laser line width can be neglected and only one lower sublevel is involved, $I'_{\text{sat}} = I_{\text{sat}}$.

With fixed Δm , the only other cases where atoms in steady state keep interacting with the light are for $\Delta m = 0$, when either $J_2 \geq J_1$ and both angular momenta are half-integers, or $J_2 > J_1$ and both angular momenta are integers. For example with $J_1 = 1$ and $J_2 = 2$, $I'_{\text{sat}} = \frac{1}{10} \left(\frac{4}{\chi_{-1-1}} + \frac{9}{\chi_{00}} + \frac{4}{\chi_{11}} \right) I_{\text{sat}}$; without magnetic field this reduces to Eq. (2.37) with $f = 17/10$. For the determination of f , an alternative to solving rate equations is given by Gao [25], valid for the pure $\Delta m = 0$ case without magnetic field:

$$f = 1 \left/ \left(\sum_{m'=-J_1}^{J_1} w_{m'} C_{m',m'} \right) \right., \quad (2.39)$$

with

$$w_m = \xi_m \left/ \left(\sum_{m'=-J_1}^{J_1} \xi_{m'} \right) \right., \quad (2.40)$$

$$\xi_m = \begin{cases} \left(\prod_{m'=1-m}^{J_1} C_{m',m'} C_{m',m'-1} \right) \left(\prod_{m''=1+m}^{J_1} C_{m'',m''} C_{m'',m''-1} \right), & |m| < J_1, \\ \prod_{m'=1-J_1}^{J_1} C_{m',m'} C_{m',m'-1}, & |m| = J_1. \end{cases} \quad (2.41)$$

The population densities of the lower sublevels are given by

$$n_i = \frac{w_i}{2} \frac{2 + C_{ii} f I / I'_{\text{sat}}}{1 + I / I'_{\text{sat}}} n. \quad (2.42)$$

The population densities of the upper sublevels with $|m_j| \leq J_1$ are

$$n_j = \frac{w_j}{2} \frac{C_{jj} f I / I'_{\text{sat}}}{1 + I / I'_{\text{sat}}} n; \quad (2.43)$$

if $J_2 > J_1$, the population densities in $|m_j| = J_2$ are 0. For the example $J_1 = 1$ and $J_2 = 2$: $w_0 = 9/17$ and $w_{\pm 1} = 4/17$.

Power broadening, the apparent broadening of a transition by the use of a high intensity, is automatically included in the effective saturation intensity. For instance when $I'_{\text{sat}} = I_{\text{sat}}/\chi$ and $\chi = 1/[1 + (2\Delta/\Gamma)^2]$,

$$\frac{dI}{dx} \propto \frac{I/I'_{\text{sat}}}{1 + I/I'_{\text{sat}}} = \frac{I/I_{\text{sat}}}{1 + I/I_{\text{sat}} + (2\Delta/\Gamma)^2} = \frac{I/I_{\text{sat}}}{1 + I/I_{\text{sat}}} \frac{1}{1 + (2\Delta/\Gamma')^2} \quad (2.44)$$

with $\Gamma' = \Gamma\sqrt{1+I/I_{\text{sat}}}$; the detuning dependence of the absorption is a Lorentz curve with a width that is larger than the natural line width.

Pereira dos Santos et al. [64] have developed an absorption model for a standing wave configuration in steady state, without magnetic field, and $f = 1$. The probe consists of two independent beams with intensities I_+ and I_- going in the $+\hat{x}$ and $-\hat{x}$ directions, respectively, one of which is directed towards a camera. The differential equations for the intensities can be written as

$$\frac{dI_{\pm}}{dx} = -\hbar\omega\frac{\Gamma}{4}n\left(1 - \frac{1 \pm \frac{I_- - I_+}{I'_{\text{sat}}}}{\left[1 + 2\frac{I_- + I_+}{I'_{\text{sat}}} + \left(\frac{I_- - I_+}{I'_{\text{sat}}}\right)^2\right]^{1/2}}\right), \quad (2.45)$$

which reduces to Eq. (2.36) when $I_+ = I$ and $I_- = 0$.

Initial state

At the moment the light is switched on, all $n_j = 0$ and Eq. (2.28) leads to

$$\frac{dI}{dx} = -\hbar\omega\frac{\Gamma}{2}n\frac{I}{I'_{\text{sat}}}. \quad (2.46)$$

As in steady state, the effective saturation intensity is given by Eq. (2.37) when all involved line-shape factors χ_{ji} have the same value. If initially all population densities n_i are equal (which means that the atoms are randomly aligned) and all χ_{ji} are equal (when the levels are degenerate), Eqs. (2.29) and (2.13) lead to a factor $f = 3(2J_1 + 1)/(2J_2 + 1)$ for any light polarization. If, on the other hand, all atoms are in one sublevel m_i , then $f = 1/C_{ji}$ for fixed Δm . Only if a closed transition is excited ($C_{ji} = 1$), do the atoms stay in the same sublevel and is the effective saturation intensity the same as in steady state. For spin-polarized atoms on a transition with $J_1 = 1$ and $J_2 = 2$ for instance, a factor $f = 2$ is found at the start of probing with $\Delta m = 0$.

When all population densities n_i are the same and there is no magnetic field, the atoms do not have a preferred direction, so the polarization of the light does not matter

Table 2.1. Effective saturation intensity $I'_{\text{sat}} = fI_{\text{sat}}/\chi$ depending on situation. In steady state, $\Delta m = 0$, without field: f given by Eq. (2.39).

	initial state	steady state
spin-polarized atoms and closed transition	$f = 1$	$f = 1$
spin-polarized atoms and other transitions	Δm fixed: $f = 1/C_{ji}$ Δm random: $f = 3\frac{2J_1 + 1}{2J_2 + 1}$ and Eq. (2.48)	
equal n_i	$f = 3\frac{2J_1 + 1}{2J_2 + 1}$ with field: Eq. (2.47)	

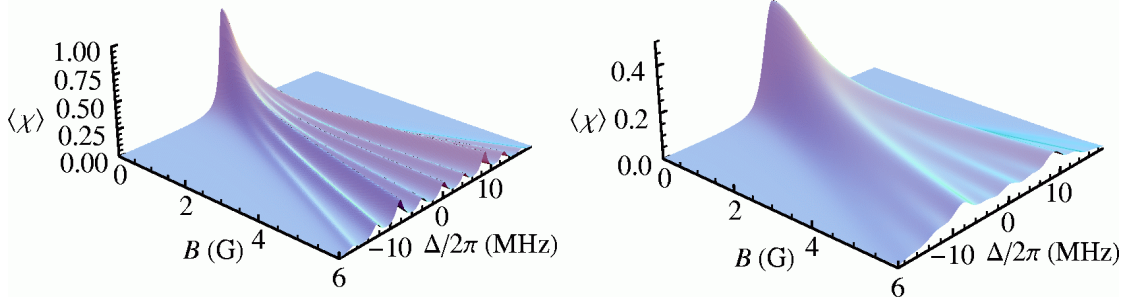


Figure 2.10. Average line-shape factor $\langle \chi \rangle$ as a function of detuning and field for the transition at 1083 nm in helium when the light is randomly polarized, in the low-temperature limit (left plot) and at 1 mK (right plot).

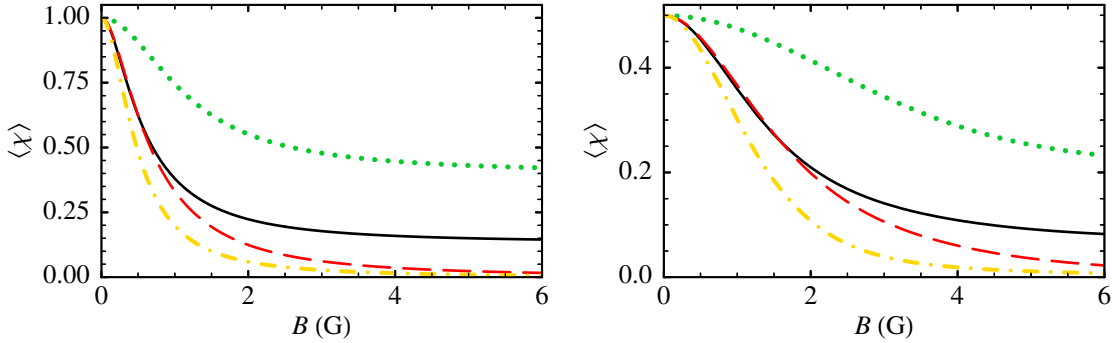


Figure 2.11. Average line-shape factor $\langle \chi \rangle$ as a function of field when the probe laser is resonant with the helium transition at 1083 nm and the polarization is random (solid curves), linear (dotted curves), or circular (dot-dashed curves), with randomly aligned atoms. The dashed curves are drawn for random light polarization and spin-polarized atoms. The left plot is valid in the low-temperature limit, the right plot at 1 mK.

at the moment the light is switched on. However, once the light is on, the polarized beam breaks the degeneracy, the population densities n_i will change, and the effective saturation intensity will depend on the polarization. The quantization axis can be chosen arbitrarily, but for ease of calculation it is simplest to use for linearly polarized light the polarization direction, and for circularly polarized light the direction in which the light travels. If there is a magnetic field in a particular direction, the polarization matters even in the beginning of the light pulse: although the populations are equal and independent of the chosen quantization axis, the shifts of the possible transitions are in practice defined with the quantization axis parallel to the magnetic field. Equation (2.29) then leads to an effective saturation intensity $I'_{\text{sat}} = 3 \frac{2J_1+1}{2J_2+1} I_{\text{sat}} / \langle \chi \rangle$ with weighted average

$$\langle \chi \rangle = \frac{1}{2J_2 + 1} \sum_j \sum_i \Theta_{ji} C_{ji} \chi_{ji} \quad (2.47)$$

[see Eq. (2.13)]. Figure 2.10 shows an example of $\langle \chi \rangle$ as a function of detuning and field when the light is randomly polarized. At high fields the splitting into all possible transitions is visible. The curve turns into Fig. 2.9 at zero field. The effect of the polarization of the probe light, resonant on the same transition, on $\langle \chi \rangle$ is shown in

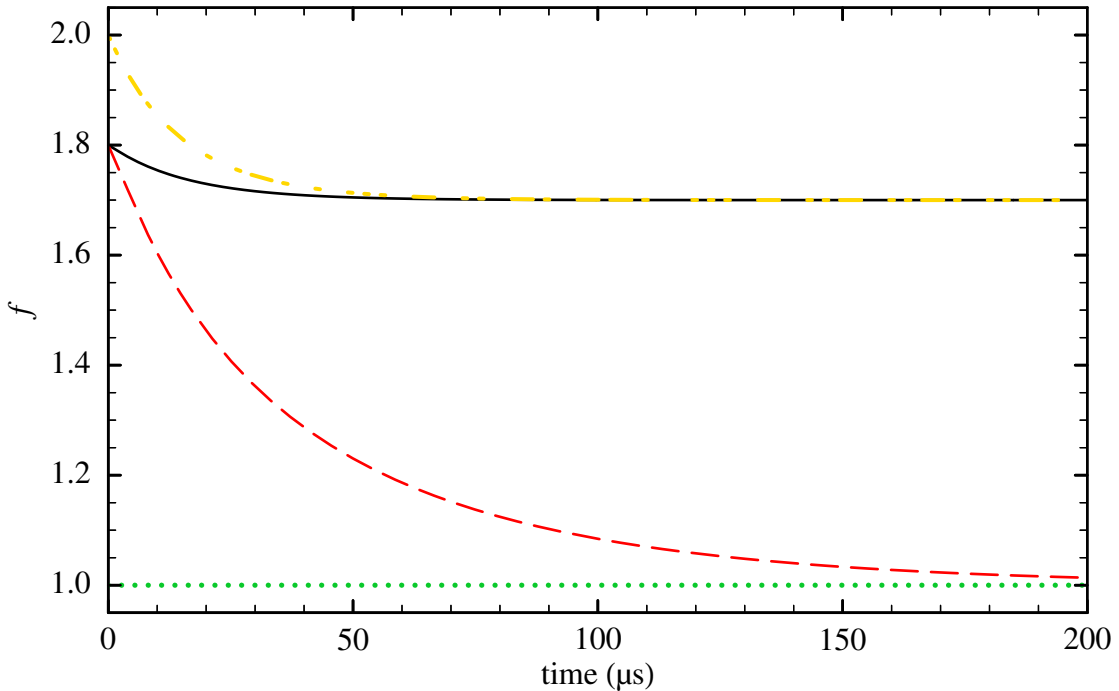


Figure 2.12. Effective saturation intensity in units of I_{sat}/χ as a function of time after a laser beam is switched on in a cloud of atoms, in four situations: light circularly polarized and atoms randomly polarized (dashed curve) or spin-polarized (dotted curve); light linearly polarized and atoms randomly polarized (solid curve) or spin-polarized (dot-dashed curve). Calculated for the $2^3S_1 - 2^3P_2$ transition in helium at 1083 nm, without magnetic field, at 1 mK, for a laser with negligible line width, no detuning, and an intensity of $0.05I_{\text{sat}} = 8 \mu\text{W/cm}^2$.

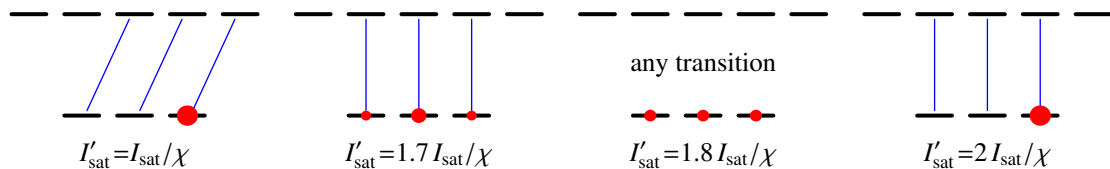


Figure 2.13. Effective saturation intensity in several situations for $J_1 = 1$ and $J_2 = 2$ without magnetic field as mentioned in the main text. Area of dots is proportional to the population of the corresponding sublevel. The two situations to the left are in steady state.

Fig. 2.11. Differences depend mainly on whether or not the transition between $m_i = 0$ and $m_j = 0$ can be excited, which is the only one without a Zeeman shift. Also plotted is the case of randomly polarized resonant light when all atoms are in the highest m_i state, with

$$\langle \chi \rangle = \frac{2J_1 + 1}{2J_2 + 1} \sum_{m_j} C_{m_j, J_1} \chi_{m_j, J_1}. \quad (2.48)$$

Only when the field is large enough to split the three possible transitions does $\langle \chi \rangle$ deviate significantly from the case when also other substates are populated. Most notably,

the line-shape factor can go to zero, whereas a non-zero minimum is reached for equal populations, which is for this example, in the limit of low temperatures, 2/15.

All situations discussed are summarized in Table 2.1. Figure 2.12 shows the effective saturation intensity according to Eq. (2.29) as a function of time for the transition between $J_1 = 1$ and $J_2 = 2$ with negligible magnetic field (see also Fig. 2.13). If the atoms are randomly oriented and the light has any circular polarization (dashed curve), f changes from 18/10 at the moment when the light is switched on, to 1 in steady state, because all atoms will be pumped into the $m_i = \pm 1$ state; if the light is linearly polarized (solid curve), f only changes from 18/10 to 17/10. If the atoms are already all in the $m_i = \pm 1$ state according to the quantization axis defined by the light beam that is to come, and the light has the appropriate circular polarization to keep them in this state (dotted curve), then $f = 1$ at all times; if the light is linearly polarized (dot-dashed curve), f starts at 2 and decreases to 17/10.

2.3.5 Transmission in practice

A probe beam with intensity $I_{\text{in}}(y, z)$ travelling in the $+\hat{x}$ direction, through a cloud of atoms with position-dependent density $n(x, y, z)$ centred around the origin, will have an intensity $I_{\text{out}}(y, z)$ on the other side. This intensity is, in steady state, after solving differential equation Eq. (2.36) with intensity $I(x)$ and density $n(x, y, z)$ dependent on position:

$$I_{\text{out}} = I'_{\text{sat}} W \left(\frac{I_{\text{in}}}{I'_{\text{sat}}} \exp \left(\frac{I_{\text{in}}}{I'_{\text{sat}}} - \hbar\omega \frac{\Gamma}{2} \frac{1}{I'_{\text{sat}}} \int n(x, y, z) dx \right) \right), \quad (2.49)$$

with Lambert's W -function $W(z)$ (also called product logarithm) satisfying $W(z)e^{W(z)} = z$. To give an example of the use of Lambert's W -function: the solution of $\ln(x) = 1/x$ is $x = 1/W(1)$. Equation (2.49) can also be expressed as

$$\int n(x, y, z) dx = \frac{2}{\hbar\omega\Gamma} \left[I_{\text{in}} - I_{\text{out}} - I'_{\text{sat}} \ln \left(\frac{I_{\text{out}}}{I_{\text{in}}} \right) \right]. \quad (2.50)$$

It is possible to use the exact form Eq. (2.49) and an arbitrary intensity, but the high- and low-intensity limits are simpler:

$$I_{\text{out}} = I_{\text{in}} - \hbar\omega \frac{\Gamma}{2} \int n(x, y, z) dx, \quad I_{\text{out}} \gg I'_{\text{sat}}, \quad (2.51)$$

$$I_{\text{out}} = I_{\text{in}} \exp \left(-\hbar\omega \frac{\Gamma}{2} \frac{1}{I'_{\text{sat}}} \int n(x, y, z) dx \right), \quad I_{\text{in}} \ll I'_{\text{sat}}, \quad (2.52)$$

or, stated as expressions for the integrated density:

$$\int n(x, y, z) dx = \frac{2}{\hbar\omega\Gamma} (I_{\text{in}} - I_{\text{out}}), \quad I_{\text{out}} \gg I'_{\text{sat}}, \quad (2.53)$$

$$\int n(x, y, z) dx = -\frac{2}{\hbar\omega\Gamma} I'_{\text{sat}} \ln \left(\frac{I_{\text{out}}}{I_{\text{in}}} \right), \quad I_{\text{in}} \ll I'_{\text{sat}}. \quad (2.54)$$

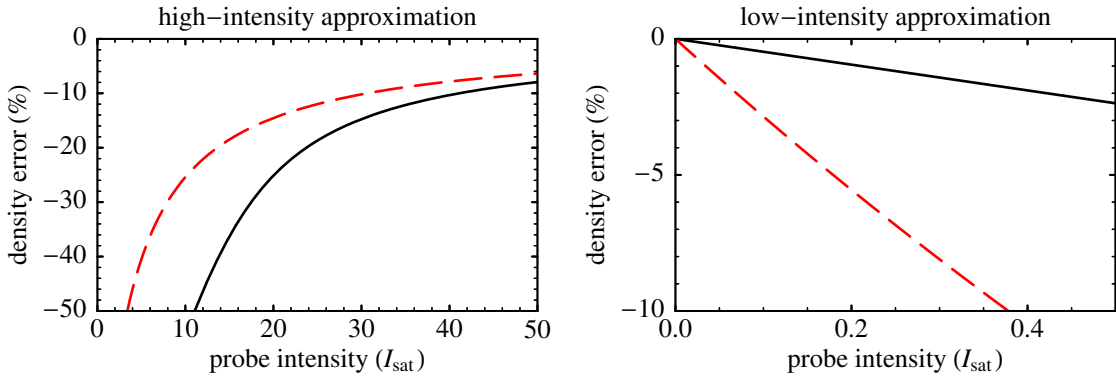


Figure 2.14. Relative error in the integrated density when using the high- or low-intensity approximation as a function of probe intensity. Calculated for a typical high density (solid curves) and in the limit of a low density (dashed curves). See main text for numerical details.

Equation (2.52) is often written as $I_{\text{out}} = I_{\text{in}} e^{-D}$, with optical density

$$D(y, z) = \sigma_a \int n(x, y, z) dx \quad (2.55)$$

and absorption cross section

$$\sigma_a = \hbar \omega \frac{\Gamma}{2} \frac{1}{I'_{\text{sat}}} = \frac{3\lambda^2 \chi}{2\pi f}. \quad (2.56)$$

Factors χ and f are defined by Eq. (2.17) and (2.37), respectively. Values for many situations are given by Eqs. (2.23)–(2.27) and Table 2.1, respectively.

Equations (2.49)–(2.54) have been derived from the steady state differential equation (2.36). For the start of probing, Eq. (2.46) should be solved. However, since this is the same equation as Eq. (2.36) with $I \ll I'_{\text{sat}}$, we can use any equation for the steady state in the low-intensity limit also for the initial state with arbitrary intensity. The value of the effective saturation intensity is usually different.

Figure 2.14 shows the relative error in the integrated density (and therefore in the number of atoms) when using the high- or low-intensity approximation, for two He^{*} clouds at 1 mK: in the low-density limit and for a high-density MOT cloud (Gaussian shaped, with rms radius $\sigma_x = 0.3$ cm and central density $5 \times 10^9 \text{ cm}^{-3}$). In all cases a linearly polarized laser at resonance with negligible line width is assumed, without magnetic field ($\chi = 0.50$, $I'_{\text{sat}} = 3.4I_{\text{sat}}$).

To calculate the low-density limit we use the fact that $\ln(I_{\text{out}}/I_{\text{in}}) \approx I_{\text{out}}/I_{\text{in}} - 1$ when $I_{\text{out}} \approx I_{\text{in}}$. This results in an absolute density error for the high-intensity approximation of at least $I'_{\text{sat}}/(I_{\text{in}} + I'_{\text{sat}})$ and for the low-intensity approximation of at most $I_{\text{in}}/(I_{\text{in}} + I'_{\text{sat}})$. In the situation described above, the error in the high-intensity approximation is large: even at an intensity of $50I_{\text{sat}}$ the density is still underestimated by at least 6%, while there is only 39% absorption for the MOT cloud. In the low-intensity approximation the error is much smaller: at an intensity of $0.05I_{\text{sat}}$ the density is underestimated by at most 1.4% and for the MOT cloud by only 0.2%, while there is 99.8% absorption.

This means one can probe a cloud with fewer atoms, after a long expansion time and still have high contrast. Another advantage of the low-intensity approximation is that only the transmittance $I_{\text{out}}/I_{\text{in}}$ is needed and not the absolute value of the probe intensity, which in practice may vary from day to day.

A third reason to use low intensities is that the cloud is disturbed less, which is an important consideration especially with helium atoms. After every absorption the velocity v of an atom in the direction of the light beam is increased by the recoil velocity $v_{\text{rec}} = \hbar k/m$ ($k = 2\pi/\lambda$); for helium at 1083 nm $v_{\text{rec}} = 0.092$ m/s. Heating caused by the subsequent emission in transversal directions will not be discussed here. After α absorptions the extra Doppler detuning is $-\alpha k v_{\text{rec}}$. Assuming that from the start the atoms are distributed among the sublevels as in steady state, the average absorption rate for one atom is

$$\frac{d\alpha}{dt} = \frac{\Gamma}{2} \frac{I/I'_{\text{sat}}}{1 + I/I'_{\text{sat}}} \quad (2.57)$$

with line-shape factor χ given by Eq. (2.24) and effective detuning $\Delta' = \Delta - \alpha k v_{\text{rec}}$ when the atom is initially at rest (neglecting laser line width and magnetic field). The resulting expression is

$$\frac{d\alpha}{dt} = \frac{\Gamma}{2} \frac{\kappa}{1 + \kappa + \frac{4}{\Gamma^2} (\Delta - \alpha \hbar k^2/m)^2}, \quad (2.58)$$

with $\kappa = I/fI_{\text{sat}}$. The average time before n photons have been absorbed is $t = \sum_{\alpha=0}^{n-1} dt/d\alpha$. Leaving out negligible terms, the motion of the atom can be described using the velocity $v = nv_{\text{rec}}$ as a parameter [4]:

$$t \approx 2 \frac{mv}{\hbar k \Gamma \kappa} \left[1 + \kappa + \frac{4}{\Gamma^2} \left(\frac{1}{3} k^2 v^2 - kv\Delta + \Delta^2 \right) \right]. \quad (2.59)$$

The corresponding displacement $x(v)$ is [4]

$$x \approx \frac{mv^2}{\hbar k \Gamma \kappa} \left[1 + \kappa + \frac{2}{\Gamma^2} \left(k^2 v^2 - \frac{8}{3} kv\Delta + 2\Delta^2 \right) \right] \quad (2.60)$$

and the absorption rate

$$\frac{d\alpha}{dt} = \frac{\Gamma}{2} \frac{\kappa}{1 + \kappa + \frac{4}{\Gamma^2} (\Delta - kv)^2}. \quad (2.61)$$

If the atom has an initial velocity v_0 , the following substitutions should be made: $\Delta \rightarrow \Delta - kv_0$ and $v \rightarrow v - v_0$.

For a cloud of atoms at a given temperature, Eqs. (2.59)–(2.61) can be solved numerically for a distribution of initial velocities. With a short light pulse, one can also use Eq. (2.57) with the Doppler broadened version Eq. (2.26) for χ and zero initial velocity. For a low intensity of $0.05I_{\text{sat}}$ the average number of absorbed photons as a function of time is shown in Fig. 2.15, together with the average absorption rate. Experimentally we use this intensity for 50 μs . At the end of the light pulse, the absorption rate has dropped just 5% at 1 mK. At lower temperatures the rate decreases up to 30% after absorption of at most 6 photons, so in this case a shorter pulse or lower intensity would be better. Using a medium intensity of $1I_{\text{sat}}$ for 50 μs a helium atom absorbs up to 31 photons and

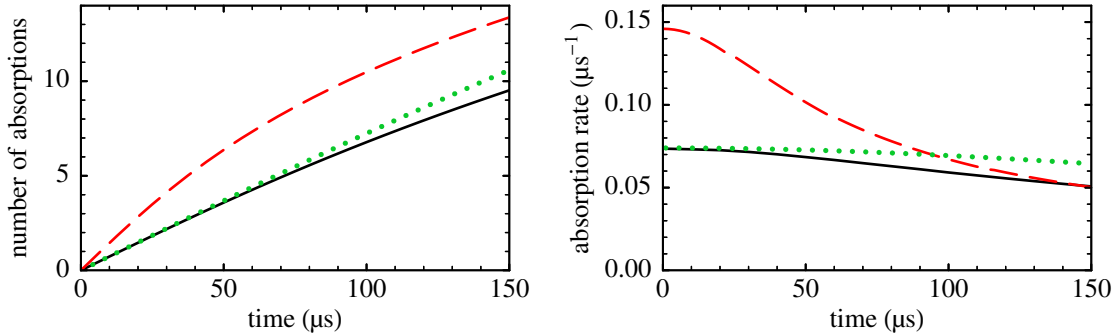


Figure 2.15. Average number of absorptions per atom and (its time derivative) the average absorption rate, as a function of time after switching on resonant and linearly polarized probe light with an intensity of $0.05I_{\text{sat}}$, with steady state populations, at 1 mK (solid curves) and in the low-temperature limit (dashed curves). The dotted curves are according to the model where only the mean of the velocity distribution changes, for the case of 1 mK.

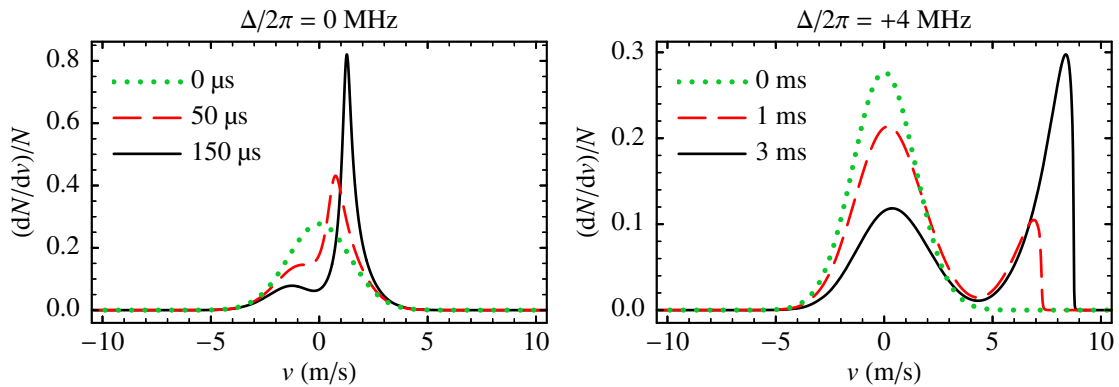


Figure 2.16. Normalized velocity distribution at different times after switching on linearly polarized probe light with an intensity of $0.05I_{\text{sat}}$, with steady state populations, at 1 mK. In the left plot the laser is at resonance, corresponding to the situation in Fig. 2.15. In the right plot the detuning is 4 MHz to the blue, for which atoms with a velocity of $v = \Delta/k = 4.3$ m/s are resonant.

the absorption rate drops 87%; to keep effects on the rate as small as they are at our low intensity, the light pulse would have to be 5 μs, which is an impractically short time.

The simple model in which a Doppler broadened line profile is assumed to shift to the red by the continuing absorption without altering shape is only correct for a limited time (dotted curves in Fig. 2.15). This is because the velocity distribution changes dramatically, especially at blue laser detuning (Fig. 2.16). Consider one atom initially at rest. At the moment blue-detuned light is switched on, the absorption rate is small. While the velocity of the atom increases, from the point of view of the atom the light frequency shifts to the red, towards resonance, and the absorption rate grows. If the light stays on long enough, the rate goes down again once the Doppler shift becomes larger than the detuning. A simple extrapolation to a cloud of atoms would mean that the transmittance can reach a minimum after a long time, if the detuning is large enough.

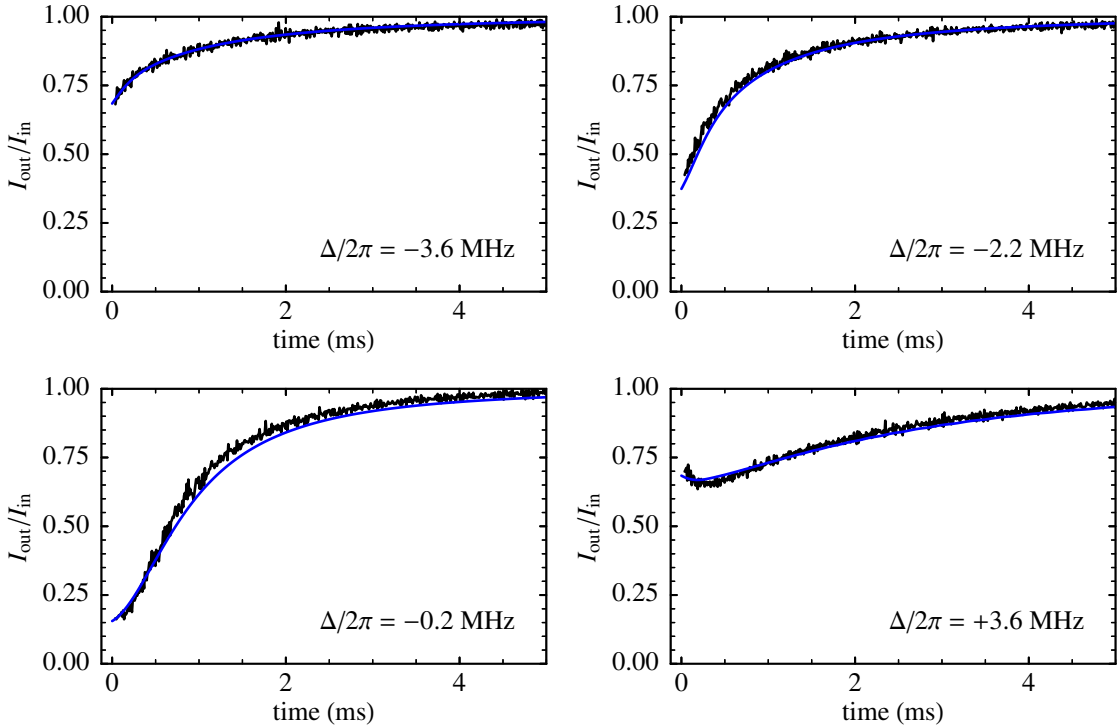


Figure 2.17. Experimental transmittance through a cloud of atoms as a function of time after probing starts, for different detunings, together with theoretical curves according to the model given in the main text.

However, atoms already moving away from the light source when the light is switched on pass through resonance earlier than other atoms. For higher temperatures this results in a velocity distribution with two peaks and the absence of a pronounced minimum in the transmittance. In Fig. 2.17 the experimental transmittance is shown as a function of the time t the light is on, for several laser detunings. The cloud of N atoms with a temperature of 1.3 mK originates from the MOT, which has been switched off 3 ms before $t = 0$. The transmittance, measured with a photodiode behind the centre of the cloud, is explained well by simulating the behaviour of N_{calc} atoms along the x axis with a Gaussian initial velocity distribution. Assuming a Gaussian shaped cloud, the output intensity is given by Eq. (2.52) with the following replacement:

$$\int \frac{n(x, 0, 0, t)}{I'_{\text{sat}}(x, t)} dx \rightarrow \frac{1}{2\pi\sigma_y(t)\sigma_z(t)} \frac{N}{N_{\text{calc}}} \sum_i^N \frac{1}{I'_{\text{sat}}(i, t)}, \quad (2.62)$$

with transversal rms radii σ_y and σ_z . These radii are time dependent to include expansion of the cloud, which would also take place without light. Heating has a small effect compared to the temperature without probing and is not taken into account. Each of the N_{calc} atoms stays therefore on the x axis, but the density decreases. Close to resonance and at the start of the light pulse the absorption is high enough to influence the absorption rate of atoms further away from the light source. Therefore a position-dependent intensity is used. Atoms passing through resonance and reaching high velocities are pushed 2 cm in 5 ms.

In the MOT, atoms are aligned randomly. Not only are all three Zeeman substates populated at every position, but the quadrupole field is also pointing in all directions. At the start of probing, when the trap has been off for at least 1 ms, the field has become so small that the effective saturation intensity is given by $I'_{\text{sat}} = 1.8I_{\text{sat}}/\chi$ for any light polarization, with χ given by Eq. (2.26). However, the factor 1.8 decreases in time by an amount dependent upon the polarization (see Fig. 2.13). Therefore it is better to use linearly polarized light, for which the change (to 1.7) is smallest. This should result in a small rise of absorption. However, there should also be a drop in absorption because the atoms get pushed by the light (see Fig. 2.15). Over 50 μs (the period for absorption imaging) both effects are small and since they cancel each other out at least partly, both are neglected; measurements with the probe laser at resonance show that the transmittance does not change during this time.

The top left plot in Fig. 2.18 shows the transmittance at $t = 0$ as a function of detuning for the same data set. The fitted function is $I_{\text{out}}/I_{\text{in}} = \exp(-c/I'_{\text{sat}}(\Delta, T, B))$ with fit parameter $c = \hbar\omega \frac{\Gamma}{2} \frac{N}{2\pi\sigma_z \alpha_z}$. The temperature T is determined from a corresponding TOF signal and the magnetic field B is either another fit parameter (solid curve) or set to zero (dashed curve). For the MOT the best fit is without a field, so both curves are the same. The value of parameter c from this fit is used for all theoretical curves in Fig. 2.17. The fact that the experimental curves, shown again in the top right plot of Fig. 2.18, are well explained by the model, is also an indication that the magnetic field has a negligible influence on the transmittance.

For the cloverleaf trap the situation is different. The trapping field is pointing in more or less every direction (see Fig. 1.19), but only the $m_i = 1$ state is populated at any position, using the direction of the local magnetic field as quantization axis. Once the trap is switched off, the radial field dies down with a principal decay time of 65 μs , leaving only an axial field during probing, after at least 1 ms. First, this means magnetic field gradients can be neglected, so cloud size information from absorption is correct. Second, in the whole trap area the field points in one direction during probing, so the atoms are aligned, assuming they could follow the field changes during switch-off. However, although the probe light travels in a radial direction, we cannot ensure that linearly polarized light excites only $\Delta m = 0$ transitions: due to the combination of a constant background field and a decreasing axial field, the direction changes as a function of time (see Fig. 1.27). For calculations at $t = 0$ we approximate this situation with randomly polarized light, so the effective saturation intensity is $I'_{\text{sat}} = 1.8I_{\text{sat}}/\langle\chi\rangle$ with $\langle\chi\rangle$ given by Eq. (2.48). At later times this approach does not work, as will be shown below.

Fitting the transmittance at $t = 0$ as a function of detuning for the cloverleaf trap in the same way as for the MOT (Fig. 2.18), the best result is reached assuming a field of about 0.8 G. As this is an indirect way of measuring the field, by determining the broadening of an already Doppler broadened line, the field magnitude may not be accurate. More important is the fact that the same value is obtained at different temperatures and with different polarizations of the light: when the magnetic field makes an arbitrary angle with the polarization vector, all transitions can be made and the effect is the same as with random light polarization, whatever the exact polarization. The fits with field are slightly asymmetric because, when all the atoms are in the $m_i = 1$ state and random

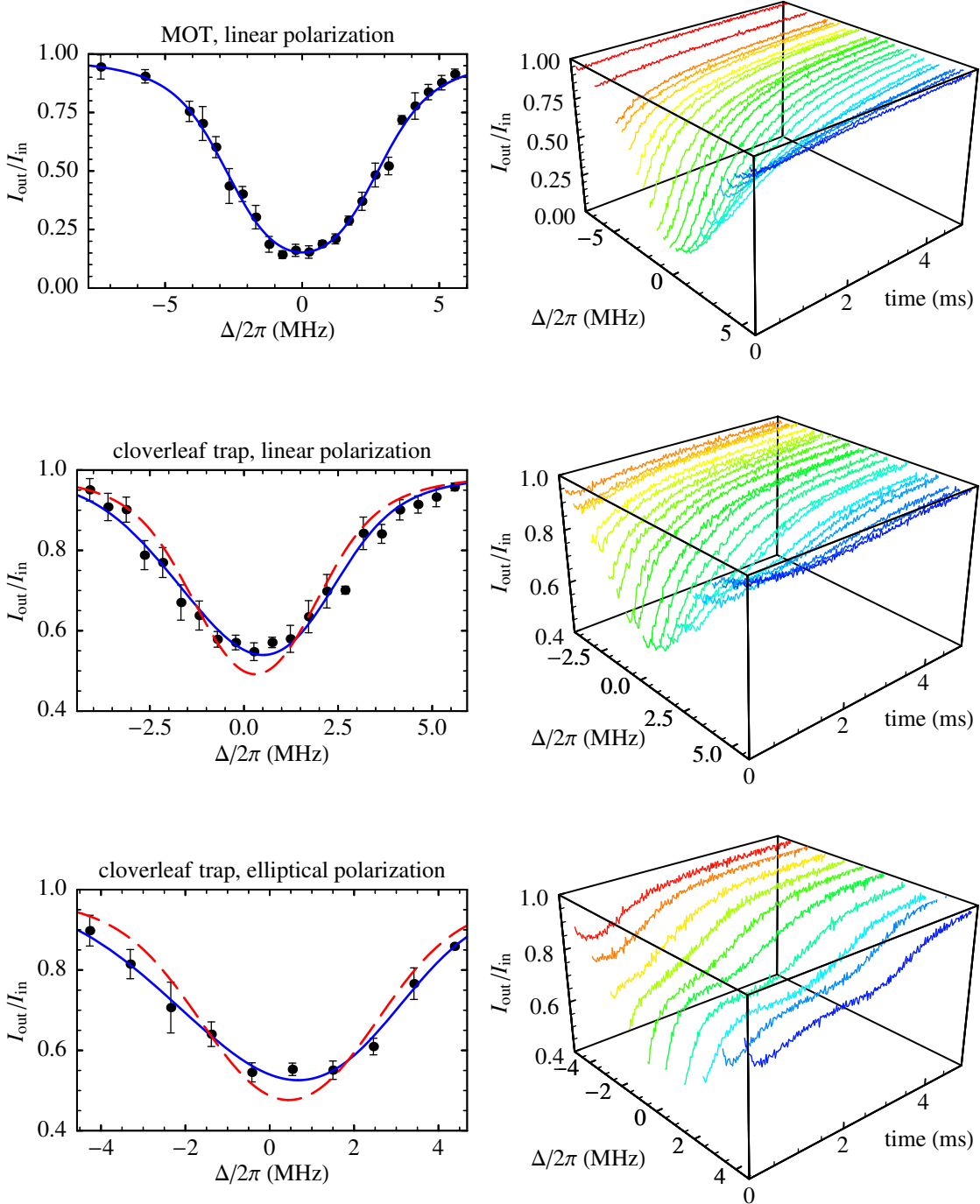


Figure 2.18. Transmittance as a function of probe detuning in three situations, at the start of probing (left column) and as a function of time from this moment (right column). Fits in the left column are either with the magnetic field parameter left free (solid curves) or set to zero (dashed curves). The trap is switched off 3 ms or 1 ms beforehand in case of the magneto-optical or cloverleaf trap, respectively. Top row: cloud of atoms from the magneto-optical trap with a temperature $T = 1.3$ mK, probed with linearly polarized light; middle row: cloverleaf trap, $T = 0.7$ mK, linear polarization; bottom row: cloverleaf trap, $T = 1.2$ mK, elliptical polarization.

polarization is used, the possible transitions are towards $m_j = 0, 1, 2$ with Zeeman shifts of $-2, -1/2, +1$ times $\mu_B B/\hbar$ and weights 1, 3, 6, respectively. In the figure, the position of resonance is given according to the fit with magnetic field. The asymmetry is not clear from the measured points, but becomes obvious when an extra field is applied.

The polarization of the probe light we normally use can be characterized by the Stokes vector $S = (1, -0.5, -0.87, 0)$: linear polarization making an angle of 30° with the vertical direction [80]. The light has a degree of polarization of at least 99%. In the bottom row of Fig. 2.18 the polarization is given by $S = (1, 0, -0.87, -0.5)$: elliptical polarization where the long axis makes an angle of 45° with the vertical direction and the length ratio of the long and short axis is 3.7. The difference between the two polarization states is not large, but the effect on the transmittance at later times is pronounced (right column of Fig. 2.18). Apparently at later times the coherences between the possible transitions cannot be neglected if there is a magnetic field present. In the MOT case the transmittance curves are the same for different light polarizations.

2.3.6 Fitting absorption images

Usually the cloud is assumed to have a Gaussian shape

$$n(x, y, z) = n_0 \exp\left(-\frac{x^2}{2\sigma_x^2}\right) \exp\left(-\frac{y^2}{2\sigma_y^2}\right) \exp\left(-\frac{z^2}{2\sigma_z^2}\right) \quad (2.63)$$

with central density n_0 , vertical (axial) rms radius σ_z , and two horizontal (radial) rms radii σ_x and σ_y . The last two are taken to be equal. To extract the number of atoms in the cloud and the cloud size, three pictures need to be taken: a raw absorption image $I_{\text{abs}}(y, z)$ of the cloud; a probe image $I_{\text{prb}}(y, z)$ under the same conditions but without the cloud; and a background image $I_{\text{bgr}}(y, z)$ without probe light. The transmittance is then

$$\frac{I_{\text{out}}(y, z)}{I_{\text{in}}(y, z)} = \frac{I_{\text{abs}}(y, z) - I_{\text{bgr}}(y, z)}{I_{\text{prb}}(y, z) - I_{\text{bgr}}(y, z)}. \quad (2.64)$$

As the probe light has a low intensity and is on for a short period, Eq. (2.52) applies. The function

$$\frac{I_{\text{out}}(y, z)}{I_{\text{in}}(y, z)} = \exp\left[-\hbar\omega \frac{\Gamma}{2} \frac{1}{I'_{\text{sat}}} \frac{N}{2\pi\sigma_y\sigma_z} \exp\left(-\frac{(y - y_0)^2}{2\sigma_y^2}\right) \exp\left(-\frac{(z - z_0)^2}{2\sigma_z^2}\right)\right] \quad (2.65)$$

is fitted to the transmission image, where $n_0 = N/[(2\pi)^{3/2}\sigma_x\sigma_y\sigma_z]$ is used. There are therefore five fit parameters: centre of the cloud (y_0, z_0) , rms radii σ_y and σ_z , and number of atoms N .

In our measurements the noise in the three raw images is independent of intensity, so the error in the transmission image is everywhere the same. This means that every pixel can have the same weight in the least-squares fit. If first the logarithm were taken of every value in the transmission image, to fit the simpler Eq. (2.54), the error would be larger where the transmittance is lower, yielding an incorrect fit.

The advantage of fitting the full image instead of two perpendicular lines through the centre of the cloud is that all information contained in the image is used. In a rectangular image the pixels in the corners contribute little information but may influence the fit because there are so many of them. Therefore a circular area of pixels is used for the fit. This has the added advantage that the circular probe is used more economically. However, there are still more pixels far away from the centre than in the cloud. In images where the background is not very smooth or the contrast is low, the fit can become better by first performing an unweighted fit to find the centre of the cloud and then a fit where each pixel has a weight $1/r$, with r the pixel distance to the centre (maximum weight 1). Then each circle of pixels around the centre has an equal weight, which is the two-dimensional version of the two-line fit mentioned above.

We have assumed that probe light is either absorbed by the cloud or transmitted in exactly the same direction. However, when the light is not resonant and the cloud has a large density, lensing may occur, which leads to systematic errors in the determination of the cloud size and therefore of the number of atoms. More specifically, the probe light is given a phase shift

$$\varphi = -\hbar\omega \frac{\Delta/2}{I'_{\text{sat}}} \int n \, dx = -D \frac{\Delta}{\Gamma}, \quad (2.66)$$

but if $|\varphi| \leq \pi/2$, refraction can be neglected [38]. In our experiments the number of atoms is always determined with resonant probe light, so lensing is not an issue.

2.3.7 Calibration of MCP detector

Now that the absolute number of atoms in a cloud can be established with absorption imaging, the MCP detector is calibrated. As described in §2.2.1, a TOF signal $V(t)$ on this detector corresponds to a number of atoms in the cloud

$$N = \frac{1}{F} N_{\text{MCP}} = \frac{1}{F} \frac{1}{RC_1} \int V(t) \, dt, \quad (2.67)$$

with N_{MCP} the number of atoms actually falling on the detector, being a fraction F of the total number of atoms, and $1/RC_1$ a calibration factor, valid for a given MCP voltage.

By fitting a Monte-Carlo function, the temperature and the fraction F are determined. By using N from absorption imaging, the calibration factor is the absolute number of atoms according to imaging divided by the relative number of atoms according to the corresponding TOF signal. Figure 2.19 shows the calibration factor for a collection of measurements in the magneto-optical, cloverleaf, and quadrupole trap, in chronological order, assuming for absorption imaging that there is no magnetic field. The calibration factor should in principle be one value, independent of time or the type of trap, although a range of values can be seen.

First, the points are divided into three periods. This can be explained by the fact that at $t = 80$ days the MCP voltage supply was replaced, and although care was taken to check whether the two supplies gave the same high voltage, there obviously was a difference. At $t = 350$ days the MCP voltage was too high during alignment of molasses,

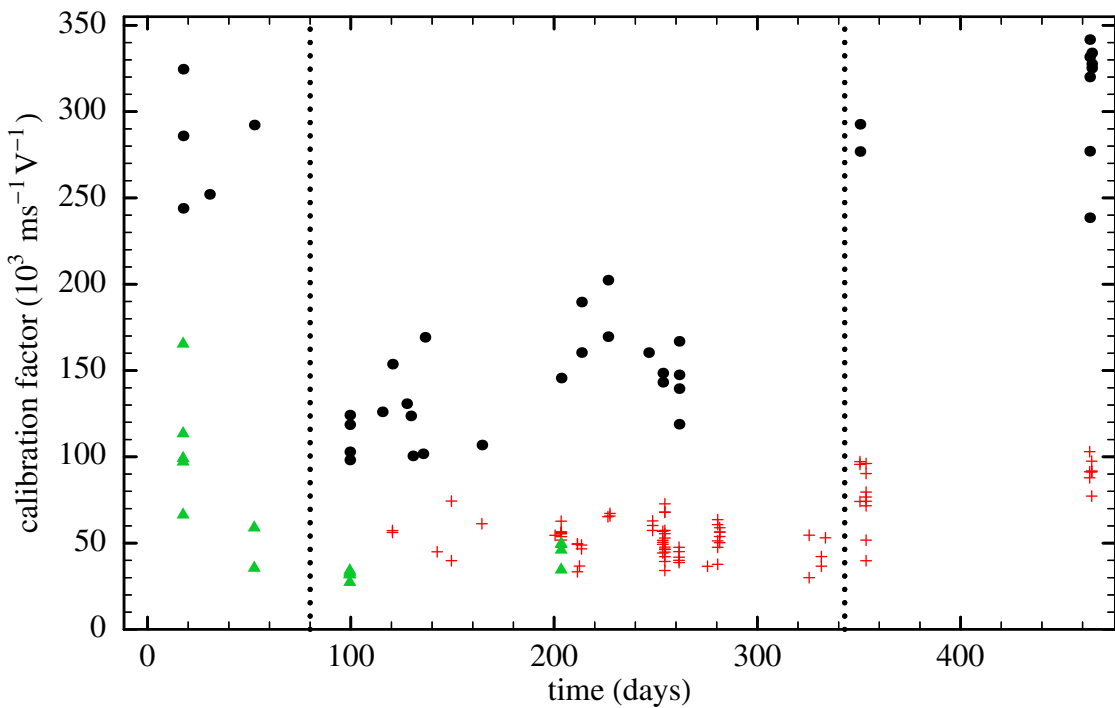


Figure 2.19. Measured calibration factor $1/RC_1$ at an MCP voltage of 1450 V as a function of lab time in the magneto-optical trap (circles), cloverleaf trap (crosses), and quadrupole trap (triangles), assuming no influence from a magnetic field. Dotted lines indicate separation into different periods.

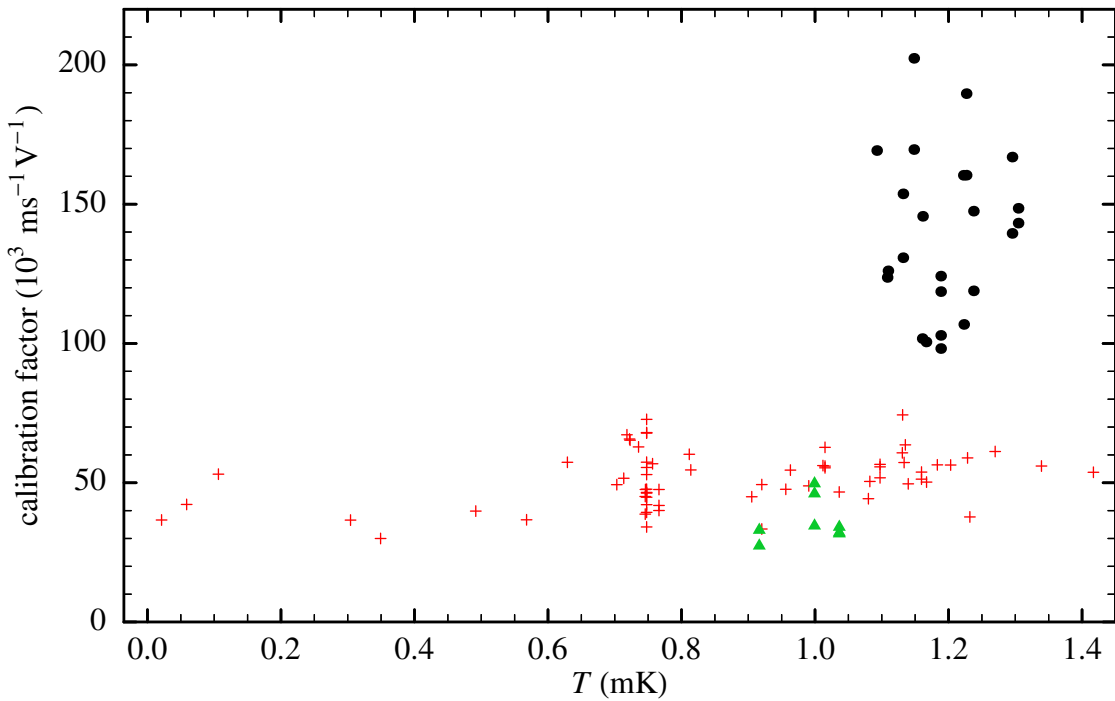


Figure 2.20. Measured calibration factor $1/RC_1$ as a function of cloud temperature. Plotted are all points in the central period of Fig. 2.19, in the same way.

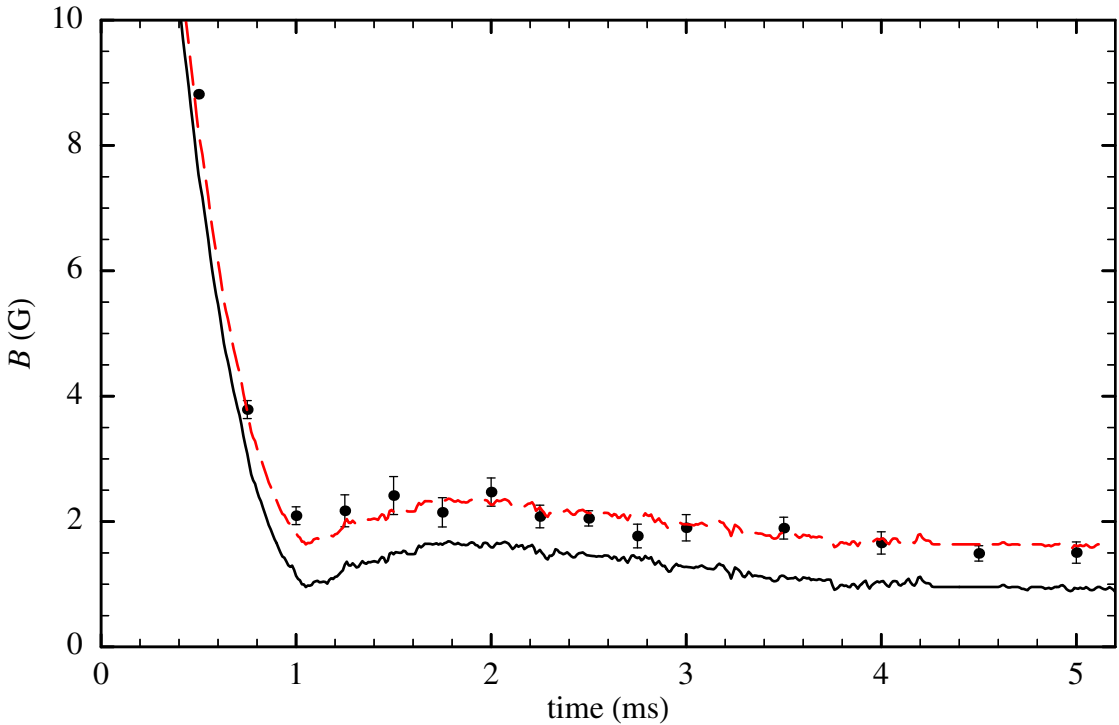


Figure 2.21. Magnetic field as a function of time since switching off the cloverleaf trap, measured with a Hall probe (solid curve) and predicted from absorption imaging and the MCP calibration (points). The dashed curve is the same as the solid curve but with an offset of 0.68 G, to fit the points.

causing the detector to saturate and in the process to deteriorate. However, during the period in between these dates, the calibration factor stayed constant, as can be seen especially from the crosses in the cloverleaf trap. Apparently the MCP detector does not age significantly as long as the signal is kept small. Here it should be noted that the same MCPs were already in use at $t = -1172$ days.

Second, the calibration factor seems to depend on the trap type. This means that either F or N in Eq. (2.67) is trap dependent: either the detected fraction is larger in a magnetic trap than in a MOT, or in a magnetic trap the number of atoms according to absorption imaging is too small. There is no hidden temperature dependence of F due to incorrect Monte-Carlo simulations for the TOF signal. This is shown in Fig. 2.20, where the measurements in the central period are rearranged as a function of temperature. The tacit assumption that atoms in any Zeeman state can reach the detector, not just those in the $m_J = 0$ state, remains valid: it is unlikely that more atoms are transferred to this field-insensitive state while the cloverleaf trap is switched off than are already present in the MOT. The detected fraction has to be independent of the magnetic field shape, or the quadrupole trap data would have the same mean apparent calibration factor as the magneto-optical trap data. This leaves the effect of the absolute magnetic field on the number of atoms. As was already reported in §2.3.5, during absorption imaging of clouds from the MOT there is no field, while there is a field in the case of the cloverleaf trap. More evidence is given in Fig. 2.21. A cloud of atoms from the cloverleaf trap is

imaged with different delays between switching off the trap and probing. Also some TOF signals are taken and the number of atoms is determined, assuming the calibration factor from the MOT measurements is correct. Then the magnetic field is calculated, necessary to get the same number of atoms from the images. As in §2.3.5, the assumption is that the atoms are aligned and that the resonant probe light has an effectively random polarization. The points in the figure are the calculated magnetic field as a function of the time of probing. The error bars include only the contribution from the spread in (central) absorption in each set of images; the size of the cloud as a function of time is taken from a fit (see Fig. 6.12). The point at $t = 0.5$ ms has no error bars, because only an average of the set of images could be fitted reliably. There is only 4% absorption at the centre of the cloud, while at $t = 0.75$ ms and $t = 1$ ms the absorption increases to 23% and 50%, respectively. Without a field it would have been 90% at $t = 0.5$ ms. If we were to assume that the atoms are aligned randomly, there could not be less than 26% absorption (see Fig. 2.11). The solid curve is the field as measured with a Hall probe (see §1.8.3), which exhibits the time dependence needed to explain the difference in calibration factors, except for an absolute field offset. The dashed curve is the measured field plus 0.68 G, fitting well to the points. The Hall probe measurement was only done in two dimensions, so the difference between the two curves could be due to a background field component in the horizontal direction that was not measured, although it is larger than expected. The field magnitude is not consistent with the measurement of the transmittance as a function of detuning (Fig. 2.18), which yields a lower value of about 0.8 G at $t = 1$ ms. However, this discrepancy is not an issue for the MCP calibration; we can simply use the MOT measurements, where we assume the field has no effect. According to Hall probe measurements, the field during MOT cloud imaging is about 0.5 G which, according to our model, would increase the calibration factor by 8%.

The calibration factor at an MCP voltage of 1450 V, according to the MOT data set in the central period, is $1/RC_1 = 1.40(29) \times 10^5 \text{ ms}^{-1}\text{V}^{-1}$. The uncertainty in the average is 4%, but there will be day to day fluctuations due to variations in the experimental situation, for instance the exact MCP voltage. Therefore the stated error bar is the standard deviation in the values of 20% (the same value is also found in the cloverleaf trap data set). We assume that this includes the possible increase due to a small field and a contribution of 1% due to the FWHM line width of the probe laser of 0.56 MHz.

3

Large numbers of cold He* atoms in a MOT

Adapted from: P. J. J. Tol, N. Herschbach, E. A. Hessels, W. Hogervorst, and W. Vassen, *Phys. Rev. A* **60**, R761 (1999).

3.1 Introduction

Since the first report of Bose-Einstein condensation (BEC) in Rb, condensates of other alkali-metal atoms, Na and Li, and recently also H have been realized [3, 8, 9, 14, 22]. Metastable triplet helium (He*) is another interesting candidate. It is a light atom with good theoretical access, its mean-field interaction term is large, and two isotopes exist, obeying different quantum statistics: ⁴He (boson) and ³He (fermion). Until recently, however, a major obstacle appeared to be that a magneto-optical trap (MOT) cannot be loaded with more than $\sim 10^6$ atoms because losses due to Penning ionization, $\text{He}^* + \text{He}^* \rightarrow \text{He} + \text{He}^+ + e^-$ (or $\rightarrow \text{He}_2^+ + e^-$), limit densities to $\sim 10^9 \text{ cm}^{-3}$. To overcome this problem, we have developed a large-sized, far-red-detuned helium MOT, in which we loaded a large number of He* atoms. These atoms will be transferred into a magnetic trap, where they will be spin-polarized. This will strongly suppress Penning ionization [19], and compression to much higher densities will become feasible. Evaporative cooling is expected to be an efficient process in spin-polarized triplet helium, because of a calculated large positive scattering length a [19], a large ratio of elastic to inelastic collisions [19], and a high collision rate. The Penning ionization loss mechanism results in decay products that can be detected easily, providing a direct probe for the density. This will substantially simplify diagnostics during evaporative cooling and provide an extra tool to investigate the transition to BEC.

Several groups have published data on the loading of a MOT with He* atoms, but with particle numbers $< 10^6$ in a trap with a diameter $< 2 \text{ mm}$ [5, 39, 53]. In a preliminary experiment [71] we already succeeded in trapping $\sim 10^7$ atoms. For BEC experiments, however, more than 10^8 cold atoms are typically required. In this chapter we present results on a MOT containing a cloud with a FWHM diameter of 7 mm and up to 1.5×10^9 atoms. In our MOT the laser beams are intense, far-red-detuned, and have a large diameter. The trap is positioned close to the exit of a Zeeman slower. This has the advantage that transverse spreading of the atomic beam is less important and more

atoms can be captured. Here we report on the full characterization of this MOT. Penning ionization loss rates were measured and are compared with reported results, where recently a large discrepancy was pointed out [53].

3.2 Setup

Our setup consists of a liquid-nitrogen-cooled He^{*} source, connected to a transverse cooling section, where the He^{*} atoms are collimated and deflected, a two-part Zeeman slower, and a UHV chamber containing the MOT. The laser-cooling transition used is 2 ³S₁ – 2 ³P₂ at 1083 nm [natural line width $\Gamma/2\pi = 1.6$ MHz; saturation intensity $I_{\text{sat}} = 0.167$ mW/cm² for the cycling transition]. For a detailed description of the setup we refer to earlier papers on the source and collimation section [70] and on the Zeeman slower and MOT [71], combined and modified for the present experiment.

The atomic beam is collimated vertically using the curved-wavefront technique [70]. A slightly convergent laser beam is sent from above through the transverse cooling section and retroreflected. In the horizontal direction the geometry is similar. Here half of the retroreflecting mirror is blocked, so that atoms are collimated in the first half and deflected over an angle of 1° in the second half. This separates the metastable beam from the ground-state atoms. A knife-edge is placed just outside the beam of collimated metastable atoms, and a 3 mm inner diameter tube is mounted in the geometric shadow of this knife-edge. It blocks ground-state atoms, whereas He^{*} atoms curve around the knife-edge and enter the tube. With a tube instead of a diaphragm a better vacuum is achieved in our beam line.

The 230 mW output power of a Nd:LaMgAl₁₁O₁₉ (LNA) laser (pumped by 4 W from a Spectra-Physics Millennia solid-state laser at 532 nm) is split into two and used for the transverse cooling and MOT laser beams. For the slower beam, a diode laser (SDL-6702-H1) is used. To investigate the dependence of cloud parameters on detuning Δ , experiments were performed close to optimum performance at $\Delta = -35$ MHz and -44 MHz, which is about -25Γ [71]. Experimental details are given in Table 3.1.

To detect metastables and ions escaping from the trap independently we use two double microchannel plate (MCP) detectors, positioned about 7 cm from the centre of

Table 3.1. Experimental details.

Slower	Laser detuning	-250 MHz
	Intensity	60 mW/cm ²
MOT	Laser detuning	-35, -44 MHz
	1/e ² beam diameter	4 cm
	Horizontal intensity I_ρ	5 mW/cm ²
	Vertical intensity I_z	1.4 mW/cm ²
	Total intensity I_{tot}	24 mW/cm ²
	Field gradient $\frac{\partial B}{\partial z} = 2 \frac{\partial B}{\partial \rho}$	20 G/cm

the trap. One has an exposed negative voltage on its front plate and thus attracts all of the ions produced in the trap, while the other has a grounded grid in front and detects only metastable atoms that exit the trap in its direction. An absolute calibration of the MCPs is not required.

3.3 Absorption measurements

The fluorescence of trapped atoms is monitored with a standard video camera, despite its low sensitivity at 1083 nm. However, for an accurate determination of the size of the cloud and its central density n_0 (and thus the absolute number of atoms), we measured the relative absorption of a probe beam in the cloud with a photodiode. The linearly polarized probe laser ($\Delta = 0$, $I = 0.04fI_{\text{sat}}$, with $fI_{\text{sat}} = 0.30 \text{ mW/cm}^2$ assuming equal population of all magnetic sublevels M of the 2^3S_1 state in the trap) is sent through the cloud at least 0.5 ms after the MOT coils and laser beams, and the last part of the Zeeman slower, have been turned off. This delay is necessary to ensure that residual magnetic fields can be neglected; the MOT is turned off within 20 μs , whereas eddy currents limit the switch-off time of the slower magnet to 0.5 ms. During the first 60 μs , absorption, which at trap centre amounts to 80%, is constant. Thereafter radiation pressure pushes the atoms out of resonance and absorption decreases.

At both detunings the cloud has a Gaussian density distribution. With a central density n_0 and an rms radius σ_ρ (σ_z) in the horizontal (vertical) direction, the number of atoms in the cloud is $N = n_0 V$, with volume $V = (2\pi)^{3/2} \sigma_\rho^2 \sigma_z$ (68% of the atoms are within V). The experimental results are given in Table 3.2. The values are corrected for the expansion of the cloud during the delay between turning off the MOT and turning on the probe beam. The temperature of the cloud, which is needed to model this expansion, is determined in two ways. First, we turn off the MOT and fit the time-of-flight signal on our metastables detector with a Maxwell-Boltzmann distribution. We find temperatures close to 1 mK. Second, and more accurately, the temperature is determined from the absorption measurements using different delays before switching on the probe beam. From the ballistic expansion of the cloud we can infer the rms velocity, in principle

Table 3.2. Typical experimental results. Errors correspond to one standard deviation.

Detuning	-35 MHz	-44 MHz
Temperature T (mK)	1.12(11)	1.18(17) horizontal 1.38(25) vertical
Horizontal radius σ_ρ (cm)	0.157(8)	0.235(12)
Vertical radius σ_z (cm)	0.306(15)	0.371(19)
Volume V (cm ³)	0.12(1)	0.32(4)
Number of atoms N	$4.8(5) \times 10^8$	$7.5(8) \times 10^8$
Central density n_0 (cm ⁻³)	$4.1(6) \times 10^9$	$2.3(3) \times 10^9$
Decay rate βn_0 (s ⁻¹)	21.3(14)	8.8(6)

independently in the horizontal and vertical directions. We observe, however, a statistically marginal 0.2 mK difference for the two directions. The best results for n_0 and N are $n_0 = 4.5 \times 10^9 \text{ cm}^{-3}$ (at -35 MHz) and $N = 1.5 \times 10^9$ (at -44 MHz), with typical results for N being a factor of 2 lower.

The cloud is elongated in the vertical direction. The aspect ratio σ_z/σ_ρ varied from 1.9 at -35 MHz to 1.6 at -44 MHz. Assuming thermal equilibrium, the spring constants in the radial and vertical directions k_ρ and k_z are related via $k_B T = k_\rho \langle \rho^2 \rangle = k_z \langle z^2 \rangle$, and therefore $\sigma_z/\sigma_\rho = \sqrt{k_\rho/k_z}$. The spring constant in each direction can be calculated with a two-level-atom model when intensity and field gradients are known [48, 78], resulting in aspect ratios of 1.3 and sizes that are about 40% too small. A more elaborate numerical model for He^{*}, incorporating Zeeman sublevels and their populations, slightly improves the comparison. A three-dimensional Monte Carlo simulation predicts a 50% temperature difference between the ρ and z directions (around 1.0 mK) and the correct aspect ratio for the clouds, but it still predicts sizes that are 35% smaller than those measured. When the force due to reabsorption of photons is taken into account, the calculated size increases only a few percent, as the central density is relatively small and the detuning of the light very large [97]. The gas is not unpolarized everywhere; at a radius of 2 mm, the populations of the $M = -1, 0$, and $+1$ sublevels can differ by 30%.

3.4 Decay experiments

The two-body loss rate coefficient β in the trap due to collisions between metastable helium atoms is determined from the trap decay when the loading is interrupted by simultaneously blocking the deceleration laser and the light entering the deflection zone. For a Gaussian density profile the total losses in the trap as a function of time t then are [5]

$$\frac{dn_0(t)}{dt} = -\alpha n_0(t) - \frac{\beta}{2\sqrt{2}} n_0^2(t), \quad (3.1)$$

with α the loss rate for collisions between He^{*} and background atoms and β defined via $dn/dt = -\alpha n - \beta n^2$. The ion current φ on the MCP then becomes

$$\varphi(t) = V \left(\varepsilon_a \alpha n_0(t) + \frac{\varepsilon_b \beta}{4\sqrt{2}} n_0^2(t) \right) + B, \quad (3.2)$$

where B is a constant background signal and ε_a (ε_b) are the efficiencies with which ions are produced and detected for losses due to background and two-body collisions, respectively. Collisions that do not yield ions but induce trap losses include those with ground-state helium atoms, resulting in a reduced ε_a , and radiative escape [87], which may decrease ε_b .

The total loss rate coefficient β is a function of MOT laser-beam intensities and detuning at a given temperature. In our MOT the density and β are both high enough and the

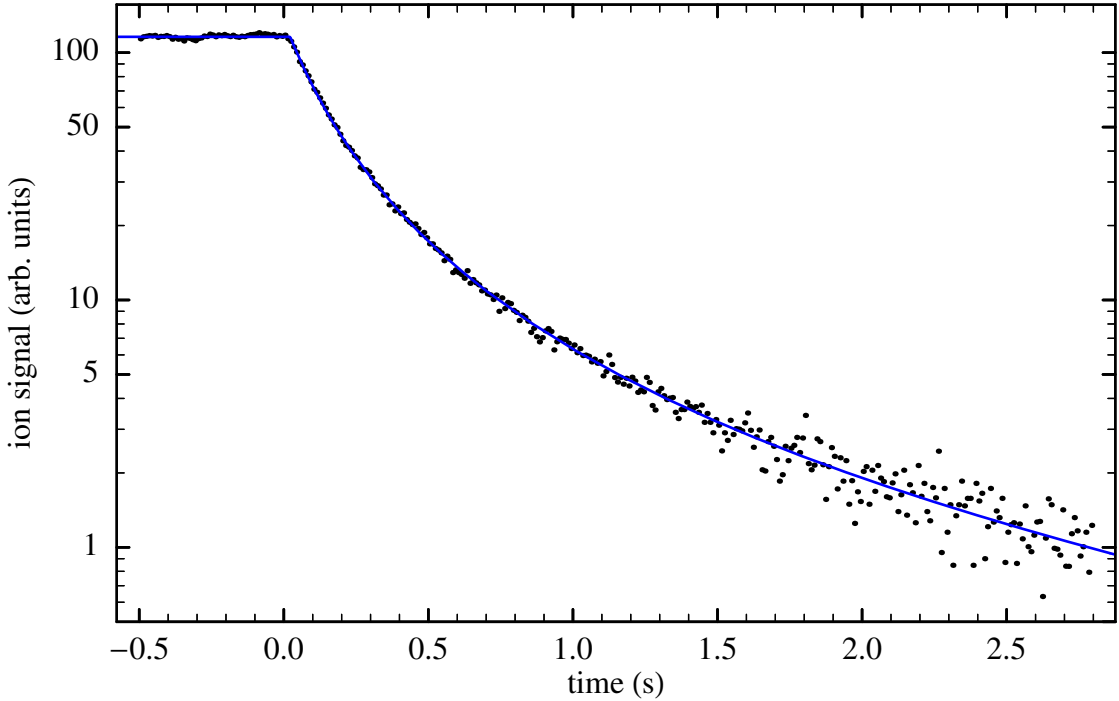


Figure 3.1. Nonexponential trap decay after loading stopped at $t = 0$ for a trap with $\beta n_0 = 9.4 \text{ s}^{-1}$.

background pressure low enough (about 1×10^{-9} mbar) to neglect the loss rate α . Solving Eqs. (3.1) and (3.2) leads to an ion signal that decreases in time after $t = 0$ when the loading is stopped as

$$\varphi(t) = \sqrt{2}\varepsilon_b V n_0(0) \frac{\beta n_0(0)}{\left[2\sqrt{2} + \beta n_0(0)t\right]^2} + B. \quad (3.3)$$

This shows that to deduce β the central density must be well known. An example of such a highly nonexponential decay curve is shown in Fig. 3.1.

At $t = 0$ those atoms that were just captured still take about 10 ms to spiral into the trap centre. When Eq. (3.3) is fitted to the measured decay, points near $t = 0$ are not used and a parameter t_0 is used in the fits. A fitted curve is also included in Fig. 3.1 and perfect agreement with experimental data is obtained. Using n_0 from the absorption measurements we find $\beta = 5.3(9) \times 10^{-9} \text{ cm}^3/\text{s}$ at $\Delta = -35 \text{ MHz}$ and $\beta = 3.7(6) \times 10^{-9} \text{ cm}^3/\text{s}$ at $\Delta = -44 \text{ MHz}$. The uncertainty in the density is the main contribution to the experimental error. This low loss rate at large detunings is one of the reasons for the large number of atoms in our trap, another being the high trap-loading rate of $\beta n_0 N / 2\sqrt{2} = 5 \times 10^9 \text{ s}^{-1}$. Compared with a He^{*} flux entering the slower of 10^{11} s^{-1} [70], this shows that as many as 5% of the atoms entering the Zeeman slower are decelerated and captured in the trap.

3.5 Loss rates

3.5.1 Radiative escape

When the MOT is on we measure a constant flux of 4×10^8 metastable atoms per second escaping from the trap. We attribute these losses to radiative escape in optical collisions [87], where absorption of a photon followed by fluorescence produces two fast metastable atoms. Compared to Penning ionization the radiative escape process for He* is expected to be insignificant, due to the long lifetime of the $2\ ^3P$ state [53]. At both our detunings (-35 MHz and -44 MHz) the measured radiative escape loss rate was indeed small: $\beta_{\text{re}} \approx 1.3 \times 10^{-10}$ cm³/s, which is about 3% of the total β .

3.5.2 Loss rate without light

In the absence of light, losses are caused only by ionizing S-S collisions. The commonly used rate constant $K_{\text{SS}} = \beta_{\text{off}}/2$ is measured, relative to the β when the trap lasers are on, by switching off the MOT laser and the deceleration laser for 100 μ s each 0.2 s. The ion currents φ_{on} and φ_{off} for the situations with the MOT light on and off are given by Eq. (3.2), where $\beta_{\text{off}} = 2K_{\text{SS}}$ in the case of φ_{off} . We define a signal ratio S :

$$S = \frac{\varphi_{\text{off}} - B}{\varphi_{\text{on}} - \varphi_{\text{off}}} = \frac{4\sqrt{2}\frac{\varepsilon_a}{\varepsilon_b}\alpha}{\beta - 2K_{\text{SS}}} \frac{1}{n_0} + \frac{2K_{\text{SS}}}{\beta - 2K_{\text{SS}}}, \quad (3.4)$$

which is proportional to n_0^{-1} for constant MOT-laser intensity and detuning. Here, α/n_0 may not be negligible compared to K_{SS} . We could not measure α directly. However, by measuring S as a function of $1/n_0$ we can extrapolate to higher density, where α/n_0 is small, to determine the ratio β/K_{SS} . The results of such measurements are collected in Fig. 3.2. The horizontal scale is not the same for both detunings: at -35 MHz the density was much higher and the first term in Eq. (3.4) is almost negligible. The straight lines are fits of Eq. (3.4) to the experimental points, yielding the value $K_{\text{SS}} = 1.3(2) \times 10^{-10}$ cm³/s. Mastwijk et al. [53] reported a measured value of $2.7(12) \times 10^{-10}$ cm³/s; their value, however, is an upper limit due to the presence of off-resonance light.

Theoretical estimates for the rate constant for ionizing collisions of unpolarized atoms have also been published. Julienne et al. [36] obtain $K_{\text{SS}} \geq 5 \times 10^{-10}$ cm³/s in the $T \rightarrow 0$ limit and $K_{\text{SS}} \leq 10^{-9}$ cm³/s for the unitarity limit at 30 μ K. Mastwijk et al. [53] calculated $K_{\text{SS}} = 7.3 \times 10^{-11}$ cm³/s at 1 mK using more recent potential curves. Our experimental value of $1.3(2) \times 10^{-10}$ cm³/s is twice as large as this last value.

3.5.3 Loss rate with light

To compare our loss rate coefficients with the trap light on, with contradictory results reported in literature, we performed a second series of measurements to determine the dependence of β on detuning. During a 100 μ s MOT-off interval each 0.1 s, a linearly polarized 1083 nm laser beam is sent through the trap region ($I = 24$ mW/cm², the same as in the MOT). The detuning from resonance is varied in steps of 0.8 MHz from

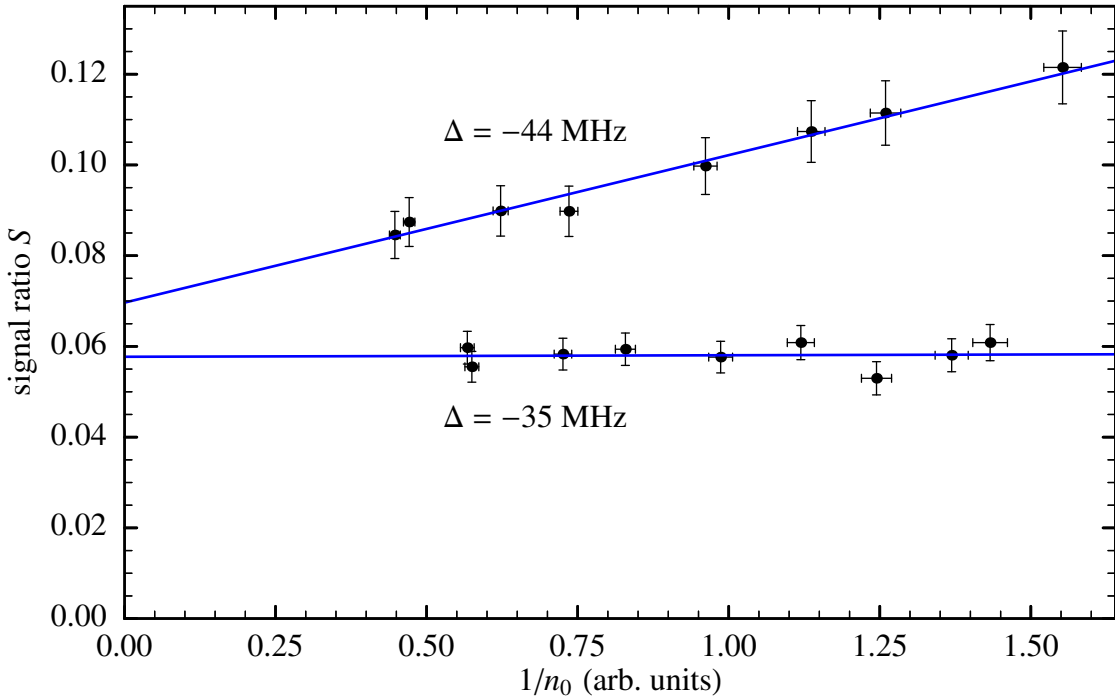


Figure 3.2. Signal ratio S of Eq. (3.4) as a function of $1/n_0$ for two MOT detunings.

-2 GHz to +1 GHz. In this MOT-off interval we detect all ions and fast metastables escaping from the trap. At $\Delta \approx -5$ MHz we find a maximum in the ion production rate. The losses of fast metastables due to radiative escape contribute at the few percent level for all detunings. From the absolute values at -35 MHz and -44 MHz we deduce $\beta_{\max} = 1.3(3) \times 10^{-8} \text{ cm}^3/\text{s}$. Bardou et al. [5] in Paris measured the total loss rate coefficient from their MOT at $\Delta \approx -5$ MHz and at the same intensity.[†] They report $\beta = 7 \times 10^{-8} \text{ cm}^3/\text{s}$ with a factor of 4 uncertainty; this value is somewhat larger but in reasonable agreement with our value. Browaeys et al. [10] in Orsay find at $\Delta = -8$ MHz but at twice our intensity a loss rate of $\beta = 3 \times 10^{-8} \text{ cm}^3/\text{s}$ with an uncertainty of a factor of 2, which also agrees with our value. Mastwijk et al. [53] in Utrecht measured the ion production rate β as a function of detuning by scanning their MOT-laser frequency quickly from -350 MHz to resonance. They observed a broad maximum near -10 MHz, also at twice our intensity, and extract $\beta = 1.9(8) \times 10^{-9} \text{ cm}^3/\text{s}$. This value is a factor of 7 smaller than our result, although a larger value is expected at higher intensity. The interpretation of the Utrecht group relies on model calculations of the trap size, which we find to be correct only within a factor of 2; as the third power of the trap size is needed to determine β , this may explain part of the discrepancy. In addition, we noticed a much stronger dependence of β on detuning for $|\Delta| < 20$ MHz; this may be due to the large repetition rate used in the Utrecht experiment.

Mastwijk et al. [53] also obtain a theoretical value for the ion production rate in optical collisions at small detunings: $\beta = 4 \times 10^{-9} \text{ cm}^3/\text{s}$. This value is a factor of 3

[†]In Refs. [5] and [53] a rate constant K_{SP} is used. At small detuning, where the atomic populations of the 2^3S_1 and 2^3P_2 states are approximately 50%, $K_{\text{SP}} \approx \beta$.

smaller than our experimental value.

3.6 Conclusions

We conclude that model calculations of rate constants for Penning ionization with and without light do not agree with our experimental results. Despite the fact that the loss rate in a far-red-detuned He^{*} MOT is much higher than in an alkali-metal MOT, we achieve particle numbers comparable to those in alkali-metal MOTs used to reach BEC. Prospects for further cooling and compression appear to be excellent. We therefore anticipate that Bose-Einstein condensation in triplet helium may be achieved in the near future.

4

Suppression of Penning ionization by spin polarization of cold He^{*} atoms

Adapted from: N. Herschbach, P. J. J. Tol, W. Hogervorst, and W. Vassen, *Phys. Rev. A* **61**, 050702(R) (2000).

4.1 Introduction

The internal energy of a metastable triplet helium atom He($2\ ^3S_1$) (He^{*}) of 19.8 eV is sufficient to ionize most atoms and molecules. The reaction products of this Penning ionization are the ionized atom or molecule, an electron, and a ground-state helium atom He($1\ ^1S_0$). When the collision partner is another He^{*} atom the reaction products are a He⁺($1\ ^2S_{1/2}$) ion, an electron, and a ground-state helium atom; or with a few percent probability [58], a He₂⁺ ion and an electron (associative ionization). In an unpolarized He^{*} gas pair collisions occur within the quasimolecular symmetries $^1\Sigma_g^+$, $^3\Sigma_u^+$ or $^5\Sigma_g^+$ with total spin 0, 1, and 2, respectively. The rate constant K_{SS} for Penning ionization in this case is large. For totally spin-polarized atoms, which can collide only in a $^5\Sigma_g^+$ potential, the ionization process is forbidden as the total spin of the products of the ionization reaction is at most 1. A reduction of the Penning ionization rate in collisions between He^{*} atoms was demonstrated around 1970 in the flowing afterglow of helium discharges by measuring the electron density while optically pumping the atoms with circularly polarized 1.08 μm light from helium lamps. In ^4He (^3He) a reduction in the electron production rate of 5% (0.6%) at a degree of spin polarization of 15% (8%) was observed [34, 75].

If the cross section for ionizing collisions in a totally spin-polarized He^{*} gas is small enough such that high densities ($10^{12}\ \text{cm}^{-3}$) can be achieved, and if the ratio of elastic to inelastic collision rate is favourable for effective evaporative cooling, then He^{*} is a promising candidate for an experiment on Bose-Einstein condensation in a dilute gas. A theoretical investigation of the decay kinetics of a trapped, spin-polarized He^{*} gas revealed that, for densities $< 10^{13}\ \text{cm}^{-3}$, where three-body losses are not yet important, the main inelastic processes are spin relaxation and relaxation-induced ionization, which are induced by the spin-dipole interaction in pair collisions. In low magnetic fields ($B < 100\ \text{G}$) and at temperatures $T < 10\ \text{mK}$ the calculations predict relaxation-induced

ionization to be the dominant process, with a rate constant $K_{\text{ss}}^{\uparrow\uparrow} \sim 10^{-14} \text{ cm}^3/\text{s}$, four orders of magnitude smaller than in the unpolarized case. This indicates that the ratio of elastic to inelastic collision rate can be large over the relevant ranges of temperature and magnetic fields, so that the prospects for evaporative cooling are promising [19, 79, 95].

Experiments concerning the suppression of Penning ionization in the spin-polarized gas compared with the unpolarized case have not advanced substantially since the 1970s. In this chapter we discuss an experiment that demonstrates in a straightforward way the suppression of Penning ionization in an ultracold gas of He^{*} when the atoms are spin-polarized. It yields an experimental upper bound for the ionization rate constant in the spin-polarized case. We use the atomic cloud released from a magneto-optical trap (MOT), which is more advantageous compared with the techniques applied in former experiments and leads to improved sensitivity. First, the low temperature (1 mK) ensures pure s-wave scattering, and collisions cannot occur in the ${}^3\Sigma_u^+$ potential, which otherwise is also an efficient ionization channel. Second, when loading the MOT from a pure He^{*} atomic beam, under ultrahigh vacuum (UHV) conditions, there are no sources of ions and electrons other than Penning ionization in pair collisions and, to a lesser degree, Penning ionization of background molecules. As a result the detection sensitivity of Penning ionization is substantially increased. Furthermore, by optical pumping with a narrow bandwidth laser close to 100% spin polarization can be achieved.

4.2 Experiment

We load a MOT with atoms from an intense and pure He^{*} beam after deceleration in a two-part Zeeman slower. The He^{*} beam is produced in a liquid-nitrogen-cooled dc-discharge source. In a transversal cooling section based on the curved-wavefront technique the He^{*} beam is collimated and deflected such that ground-state atoms, charged particles, and uv photons from the source are geometrically blocked. The loading rate of the MOT is $5 \times 10^9 \text{ s}^{-1}$ and typically the trap contains about 1×10^9 He^{*} atoms with a central density of $4 \times 10^9 \text{ cm}^{-3}$ and a temperature of 1 mK. For further details on these parts of the setup we refer to Chapter 3 and references therein. The fringe magnetic field of the end of the Zeeman slower is overlapping with the quadrupole field of the MOT such that the centre of the trap is displaced by about 3 mm from the zero point of the quadrupole field. Thus, when we switch off the MOT, including its quadrupole field, the atomic cloud is left in the fringe field of the Zeeman slower, which has a strength of about 3 G. The homogeneity of this small field is good enough to reach a high degree of spin polarization with optical pumping. For this we use a 1083 nm diode laser (SDL-6702-H1) in an extended-cavity geometry with sub-MHz bandwidth and absolute frequency stability. This laser beam is aligned collinearly with the Zeeman slower and is switched on with an acousto-optic modulator for about 20 μs . We produce circularly polarized light using a polarizer and a $\lambda/4$ plate in front of the entrance window of the UHV chamber. This window will finally limit the degree of circular polarization that can be achieved. A laser intensity of about 15 mW/cm² is used (saturation intensity 0.167 mW/cm²). For optical pumping the laser is tuned to a frequency close to the $2 \ {}^3S_1 - 2 \ {}^3P_2$ atomic transition, optimized such that efficient spin polarization is

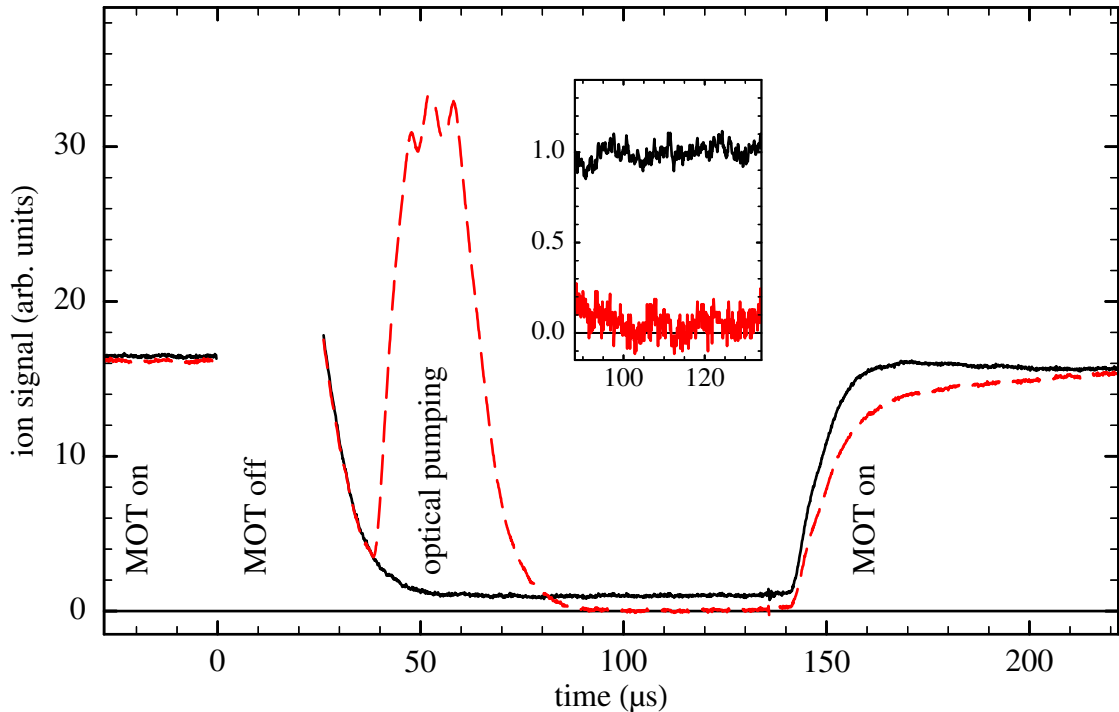


Figure 4.1. Ion signal with optical pumping (dashed curve) and without optical pumping (solid curve). The ion signal is electronically averaged over 10 μs . Just after the switching-off of the MOT coils the signal is disturbed by the induction pulse and is therefore not shown. The inset shows a magnification of that part of the curves where the suppression of Penning ionization occurs.

reached. Ions produced by Penning ionization are detected with a double microchannel plate (MCP) detector positioned about 7 cm from the atomic cloud. The exposed negative high voltage on its front plate attracts all positive ions produced in the atomic cloud.

In the MOT optical collisions in the trap laser light cause an enhancement of the Penning and associative ionization processes leading to a large ionization rate constant β that depends on the detuning and total laser intensity used for the trap. For the MOT used in this experiment $\beta \approx 5 \times 10^{-9} \text{ cm}^3/\text{s}$. In the absence of light a decrease in the ionization rate constant to $\beta = 2K_{\text{SS}} = 2.6(4) \times 10^{-10} \text{ cm}^3/\text{s}$ was found (§3.5.2). From the rate equations for absorption in the MOT we deduce that the steady-state populations of the Zeeman substates of He^{*} are all close to 1/3 in the centre of the atomic cloud, but gradually deviate from this value with increasing distance from the centre. Accounting for this deviation a $K_{\text{SS}}^{\text{eq}} = 1.8(4) \times 10^{-10} \text{ cm}^3/\text{s}$ for the case of equal populations of the magnetic substates is inferred.

In Fig. 4.1 the ion signal is plotted once with and once without the optical pumping pulse. In the curve without optical pumping, the ion signal drops down to the value for collisions in an unpolarized cloud, when the MOT laser is switched off. With optical pumping the ion signal drops significantly below this level: the decrease of the ion signal relative to the unpolarized case is at least a factor of 20. For both helicities of the light

pulse equal suppression factors are measured. The displayed curves are averages over about 350 cycles, each taking a few seconds in order to start always with an equilibrated MOT. As the MOT magnetic field is switched off rapidly (5 μs exponential decay time) and the trap is off only for 150 μs the decrease of the density of the released atomic cloud by ballistic expansion is negligible. This is demonstrated by the fact that, when the MOT is switched on again, the ion signal rapidly regains a level near its value at the beginning of the cycle. The ion signal takes somewhat longer to reach its final value when the MOT is switched on again in the case with optical pumping. This can be explained from the different populations of the Zeeman substates in both cases. The short duration of the laser pulse ensures that effects of the radiation pressure force on the density distribution of the atoms are negligibly small. The increase in ion signal during the optical pumping laser pulse is caused by the ionization enhancement in optical collisions.

4.3 Discussion of results

For an atomic cloud with Gaussian density distribution and central density n_0 , the ion current φ measured on the MCP detector can be written as [5]

$$\varphi = V \left(\varepsilon_a \alpha n_0 + \frac{\varepsilon_b \beta}{4\sqrt{2}} n_0^2 \right), \quad (4.1)$$

where α is the loss rate due to collisions with background molecules, β the loss rate coefficient for pair collisions, and V an effective volume (§3.3). In Eq. (4.1) ε_a and ε_b are the efficiencies for ion production and detection for losses due to background and pair collisions, respectively. Collisions that do not yield ions but induce trap losses include those with ground-state helium atoms, resulting in a reduced ε_a , and radiative escape, which may decrease ε_b , but only in the MOT situation.

For dark collisions in an atomic cloud the ionization rate coefficient β can be written as a sum of the contributions of all symmetries in which collisions occur: $\beta = \beta_{1\Sigma} + \beta_{3\Sigma} + \beta_{5\Sigma}$. Actually, the gas temperature of 1 mK is sufficiently low to assume pure s-wave scattering: the relative probability for p-wave scattering is $\ll 1\%$. Thus pair collisions with ${}^3\Sigma$ symmetry are highly improbable as they can only occur with an odd total orbital momentum quantum number. The contribution to the ionization rate from collisions occurring in the ${}^5\Sigma$ symmetry is predicted to be small ($\sim 10^{-14} \text{ cm}^3/\text{s}$) and lies beyond the sensitivity of the present experiment. Thus the ionization rate coefficient β in an atomic cloud with fractional populations ρ_{-1} , ρ_0 , and ρ_1 for the magnetic substates $|M\rangle$ ($M = -1, 0, +1$) is given by

$$\beta \approx \beta_{1\Sigma} = 18K_{\text{SS}}^{\text{eq}} \frac{1}{3} (2\rho_{-1}\rho_1 + \rho_0^2). \quad (4.2)$$

This expression is obtained by averaging the projection operator on the $|{}^1\Sigma\rangle$ quasi-molecular state ($|{}^1\Sigma\rangle = [|{-1}\rangle|{+1}\rangle + |{+1}\rangle|{-1}\rangle - |0\rangle|0\rangle]/\sqrt{3}$) over an arbitrary distribution of populations (ρ_{-1} , ρ_0 , ρ_1). The factor $18K_{\text{SS}}^{\text{eq}}$ ensures that $\beta = 2K_{\text{SS}}^{\text{eq}}$ for $\rho_{-1} = \rho_0 = \rho_1 = 1/3$. The dark collision rate constant for Penning ionization takes its maximum, $\beta = 6K_{\text{SS}}^{\text{eq}}$, when $\rho_0 = 1$ and vanishes for either $\rho_{-1} = 1$ or $\rho_1 = 1$.

The ionization signal after optical pumping is very small and is close to the detection limit of our experiment. This signal is averaged over time in the interval shown in the inset of Fig. 4.1. An average of 5% of the ionization signal of the unpolarized cloud is found with an rms deviation of similar size. However, it cannot be concluded that the suppression of Penning ionization in a totally spin-polarized sample will be only a factor of 20 compared with the unpolarized case. The residual signal may be due to Penning ionization of molecules from the background gas (typical pressure 5×10^{-10} mbar). From measurements of the ionization signal as a function of the atomic density (§3.5.2) we estimate that this contribution indeed is approximately 5% of the ionization signal from the dark unpolarized atomic cloud. In addition, spin polarization is not perfect. From Eq. (4.2) we deduce that at least 88% of the atoms must be in a single magnetic substate with $|M| = 1$ to observe a suppression by a factor of 20. This appears realistic; we did not particularly try to determine the degree of spin polarization by a different method. An additional contribution to the signal could stem from fast metastable atoms escaping from the MOT while it is switched on. From an earlier calibration of this flux of metastables (§3.5.1) we conclude that this contribution can be neglected.

To summarize, we deduce from the observed suppression an upper bound $K_{\text{SS}}^{\uparrow\uparrow} < 6 \times 10^{-12} \text{ cm}^3/\text{s}$ for the ionization rate constant for spin-polarized He*. This value is obtained dividing the previously measured rate constant for the unpolarized case $K_{\text{SS}} = 1.3 \times 10^{-10} \text{ cm}^3/\text{s}$ (§3.5.2) by the observed suppression factor.

4.4 Outlook

To increase the sensitivity to Penning ionization in pair collisions of spin-polarized He* atoms it is feasible, prior to the optical pumping, to compress the trapped atomic cloud by increasing the gradient of the magnetic field and/or decreasing the laser detuning of the MOT. Furthermore, by selectively detecting He⁺ ions with mass-spectrometric techniques the measured signal will be free of background molecular ions. However, despite these improvements, the imperfect spin polarization and the relatively small atomic density will hamper a precise determination of the ionization rate constant in such an experiment. To ensure perfect spin polarization the cloud released from the MOT can be recaptured in a magnetic trap. A quadrupole trap is advantageous as it can be operated with the same coils used for the MOT, if an appropriate gradient of the field can be reached [60]. In this trap, spin polarization is locally provided everywhere, except for the centre of the trap, where the field vanishes. In a magnetic trap the ions can be collected over a longer time, and from the time dependence of the decay of the trap it is possible to discriminate between losses due to pair collisions and those stemming from collisions with background gas. We indeed recapture close to 1/3 of the atoms in a quadrupole trap after reducing the temperature of the cloud in a Doppler molasses down to 0.2 mK. Measuring the trap decay we found no evidence for a deviation from the exponential behaviour characteristic of collisions with molecules of the background gas. However, the density of 10^9 cm^{-3} reached at that point in our experiment is too small for a significant loss contribution from pair collisions. To reduce the upper bound for $K_{\text{SS}}^{\uparrow\uparrow}$ below the measured value of $6 \times 10^{-12} \text{ cm}^3/\text{s}$ a central density larger than 10^{10} cm^{-3} is

required in a quadrupole trap. In a Ioffe quadrupole trap the cloud has a Gaussian density profile and Eq. (4.1) can be used to estimate that for $(\varepsilon_a/\varepsilon_b)\alpha \approx 0.01 \text{ s}^{-1}$ (inferred from measurements in the MOT, Fig. 3.2) a central density of 10^{12} cm^{-3} is required in order to observe clearly on an ion detector the loss contribution of pair collisions with the predicted small value of $\beta^{\uparrow\uparrow}$. This higher density can be reached by compression in the trap. Ongoing experiments in this direction have to show whether $\beta^{\uparrow\uparrow}$ is sufficiently small to allow for effective evaporative cooling and the realization of Bose-Einstein condensation.

5

Photoassociation spectroscopy of cold He^{*} atoms

Adapted from: N. Herschbach, P. J. J. Tol, W. Vassen, W. Hogervorst, G. Woestenenk, J. W. Thomsen, P. van der Straten, and A. Niehaus, *Phys. Rev. Lett.* **84**, 1874 (2000).

5.1 Introduction

Photoassociation spectroscopy of cold atoms is a new and powerful technique to investigate long-range interactions between atoms [50, 86]. Experiments in alkali-atom traps have revealed precise information on the long-range part of molecular potentials. This has resulted in the precise determination of s-wave scattering lengths for these systems, of high interest for studies of Bose-Einstein condensation in dilute trapped gases [1, 26, 89]. In these experiments a probe laser beam is sent through a cloud of cold atoms in a trap and the trap loss as a function of the laser frequency is detected. When the laser frequency is tuned to a photoassociative resonance, trap losses increase through the process of radiative escape or the formation of molecules, which are not trapped [86]. In some cases the excited molecules can also be photoionized by absorption of a second photon and the produced ions can be detected with high efficiency [50].

In view of this success it is worthwhile to consider whether the same method can be applied to cold rare gas metastables. Especially in the case of metastable He(2 ³S) atoms (He^{*}), the detailed information that can be obtained on the long-range interactions of collision systems in ground and photoexcited states is of fundamental interest. Metastable rare gas systems differ from alkali systems mainly by the possibility of Penning ionization occurring at small internuclear distances. If the lifetime of a molecule formed by photoassociation is short compared with a vibrational period, photoassociation resonances will not occur. For He^{*} atoms, close collisions in the molecular ¹Σ_g⁺ or ³Σ_u⁺ potentials have ionization probability close to unity [58], which means that a vibrational level structure is absent in these potentials. An ionization rate constant of $1.3 \times 10^{-10} \text{ cm}^3/\text{s}$ in laser-cooled unpolarized He^{*} atomic clouds (§3.5.2) is attributed to these collisions. For the ⁵Σ_g⁺ potential, however, the ionization probability is reduced by orders of magnitude [19] due to the total spin conservation selection rule and therefore vibrational levels can exist in this potential. It is to be expected that, for the molecular

potentials relevant for the photoassociation process, i.e., potentials that asymptotically belong to He(2 ³S)-He(2 ³P), the situation at small internuclear distances is equivalent: the singlet and triplet states decay with high probability, while the quintet states are stable. However, the fine-structure interaction implies the possibility of spin mixing at large distances. It is thus an open question how this mixing affects the formation and detection of photoassociated molecules. An earlier measurement of the ion rate as a function of the detuning did not show any vibrational resonances [53]. However, this measurement was aimed at a determination of the general shape of the ion rate curve and does not exclude the existence of such resonances due to insufficient statistics. In this chapter we demonstrate that photoassociation spectroscopy is indeed possible on the He(2 ³S)-He(2 ³P) system.

5.2 Photoassociation experiments

5.2.1 Setups

To study photoassociation of He^{*} below the 2 ³S – 2 ³P₂ asymptote, experiments have been carried out in Amsterdam and Utrecht using two different setups. Although the techniques used in both setups are similar, the two experiments focus on different aspects of the photoassociation process. In the Amsterdam experiment the dependence of the rate constant for ionization on the probe laser detuning is measured over 2 GHz around resonance, whereas in the Utrecht experiment photoassociation at larger detunings is studied. In principle, the effects of the probe laser on the cloud of cold atoms should be small, such that the detected signal is directly proportional to the rate of photoassociation. However, at high laser intensity the probe laser will always perturb the cloud close to resonance. In the case of He^{*} this is a large effect due to its small mass.

Both experimental setups use a cooled dc-discharge source of He^{*} atoms. The He^{*} atoms are decelerated with a Zeeman slowing technique and loaded into a magneto-optical trap (MOT). In the Utrecht experiment typically 5×10^6 atoms are trapped in a cloud with a diameter of about 1 mm. In Amsterdam the MOT contains typically 1×10^9 atoms (§3.3). In both experiments the temperature is 1 mK and the atom density around $5 \times 10^9 \text{ cm}^{-3}$. The probe lasers are DBR (distributed Bragg reflector) diode lasers used free running in Utrecht, whereas in Amsterdam an extended cavity and frequency locking to a Fabry-Perot interferometer (FPI) are used. Relative frequency calibration is obtained from FPI markers and saturation spectroscopy in an rf-discharge cell yields an absolute frequency reference. Positive ions produced by Penning ionization are detected with a microchannel plate (MCP) detector at negative high voltage, whereas He^{*} atoms released from the trap can be measured with a second MCP detector at ground potential. This enables time-of-flight determination of temperatures as well as measurement of fast neutral atoms escaping from the trap (radiative escape).

5.2.2 Ion rate at small detunings

To measure the rate constant for ionization at relatively small detunings the experiment in Amsterdam is performed in a pulsed way such that the probe laser always sees an

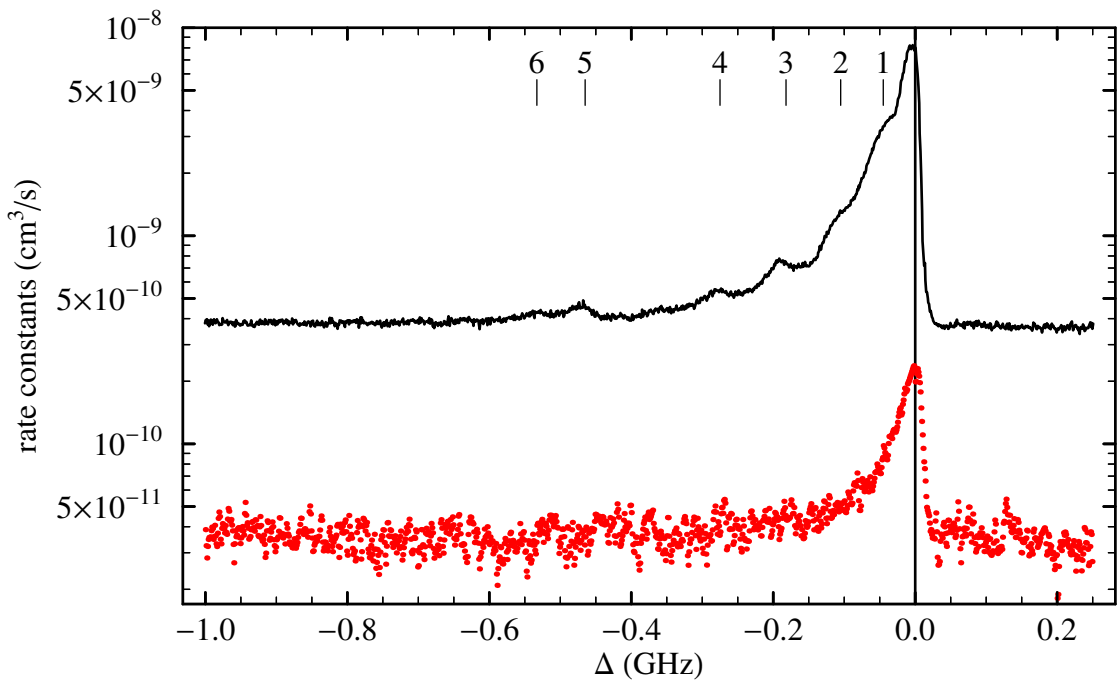


Figure 5.1. Rate constants for ionization (solid curve) and for radiative escape (dotted curve) as a function of the detuning Δ of the probe laser. Both are measured with circularly polarized light. The radiative escape signal for $\Delta < -0.25$ GHz and $\Delta > 0.020$ GHz is a constant background of slow atoms released during the trapping phase against which the signal of the faster atoms is measured.

atomic cloud with the same characteristics. The probe laser and the trapping laser are switched with acousto-optic modulators. The MOT is loaded for 0.1 s and then switched off for 130 μ s. During this trap-off time interval the probe laser is switched on for 60 μ s and the ion current on an MCP is collected using a gated boxcar averager. Repetition rates below 10 Hz are necessary to ensure equilibration of the MOT before the next cycle. It turned out that the damping time constant of the MOT, around 10 ms in this case, is the relevant timescale to prevent cumulative effects from successive probe laser pulses, as observed with a video camera from the fluorescence of the trap. The intensity of the probe laser is about 14 mW/cm² ($\approx 90 I_{\text{sat}}$, $I_{\text{sat}} = 0.167$ mW/cm² being the saturation intensity). At higher intensities perturbation of the atomic cloud by the probe laser cannot be neglected around the atomic resonance. About 10 spectra were added to average out possible instabilities of the MOT. The calibration of the measured ion currents was done with respect to the MOT values previously calibrated (Chapter 3).

The resulting rate constant for ionization is plotted on a logarithmic scale as a function of probe laser detuning in Fig. 5.1. Its accuracy is estimated to be better than 50%. The contribution of Penning ionization of background molecules to the measured ion currents is estimated to be smaller than 9×10^{-11} cm³/s. The peaks in this curve, which are attributed to photoassociation resonances, are clearly visible. Choosing circular instead of linear polarization for the probe beam did not produce a significant difference in the spectrum. The peak structure only became slightly more pronounced when the magnet of the MOT was switched off, thus removing Zeeman broadening by the trap field. To determine the peak positions a steeply increasing but smooth curve is subtrac-

ted such that fitting could be done against a constant background. Peak positions are numbered and collected in Table 5.1 and indicated in Fig. 5.1.

The blue detuning part of the spectrum is interesting for the effect of optical shielding. Although our experimental conditions are similar to those in Xe^{*}, where for blue detuning a factor of 8 suppression of Penning ionization was observed [96], the ion signal in our case did not decrease below the level of S-S collisions (see Fig. 5.1).

5.2.3 Ion rate at large detunings

In the Utrecht experiment photoassociation resonances up to detunings of -20 GHz are observed. The measurement is pulsed by modulating the trapping laser frequency. During the trapping phase the MOT laser operates at the trapping frequency and during the probe phase at a detuning of -600 MHz, which is sufficiently large to avoid enhancement of the ionization by the trapping laser. The repetition rate is 25 kHz and the duty cycle 50% , which was chosen such that the MOT does not expand appreciably during the probe phase. A gate to the counter is opened only in the probing phase, so only ions produced by the probe laser are measured together with ions produced in the probe phase by collisions with the background gas or He^{*} atoms. To verify the stability of the MOT, the ion signal in the trap phase is monitored. A typical scan takes 100 s and for the spectrum a few scans are summed. In Fig. 5.2 two typical spectra using circularly polarized light with different saturation parameters are shown. The dotted line indicates the region where the MOT is perturbed by the probe laser. A structure of pronounced peaks overlaps the overall trend of ionization observed earlier by Mastwijk et al. [53]. The width of the peaks is in the order of 10 MHz for low intensities and increases with increasing intensity. Peaks up to a frequency of -21 GHz were measured and are collected in Table 5.1. For the largest detunings the intensity of the probe laser is $2.1 \times 10^5 I_{\text{sat}}$, and then the probe laser perturbs the MOT already at a detuning of -5 GHz. The positions of the peaks found in both experiments agree within their uncertainty.

5.2.4 Radiative decay

Photoassociation can also be observed by detecting trap loss via radiative decay and He^{*} atoms are favourable in this respect as they can directly be detected with an MCP. The results for small detunings are shown in Fig. 5.1 as well, where the rate constant can be compared on an absolute scale with the rate constant for Penning ionization. The behaviour of both signals is comparable but in the radiative decay signal no pronounced peaks can be resolved. This is probably due to the poorer signal-to-noise ratio resulting from a 40 times smaller escape rate compared to the ionization rate and a small detection fraction. From the time the metastables take to reach the MCP we can deduce that 75% of these atoms are produced with high velocities in the range (650 to 2500) m/s independent of the detuning of the laser. We can conclude that radiative decay contributes at most 2.5% to the total loss rate constant at these detunings.

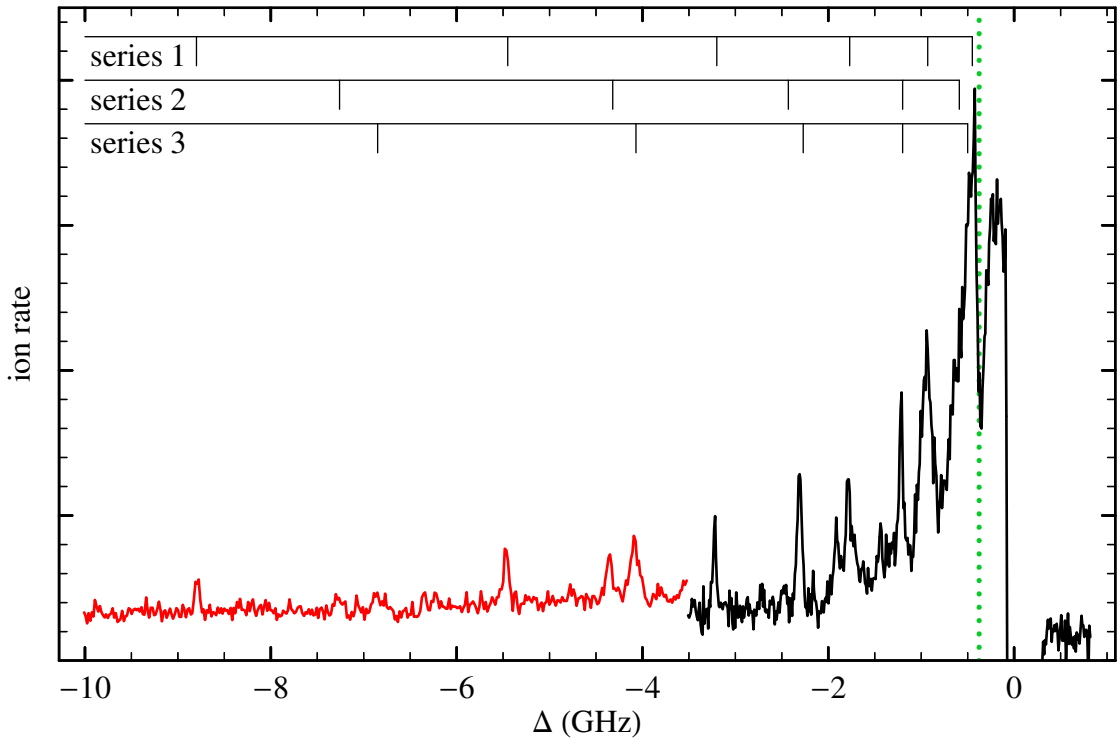


Figure 5.2. Photoassociation spectrum of He^{*} as a function of the detuning Δ of the probe laser. For the left side of the spectrum (from -10 GHz to -3.5 GHz) the probe laser intensity is $1.2 \times 10^5 I_{\text{sat}}$ and for the right side (from -3.5 GHz to 0 GHz) $7.5 \times 10^4 I_{\text{sat}}$. The assignment of the states to vibrational series is indicated at the top.

5.3 Analysis of photoassociation spectra

To interpret the peak structure in the ion rate, we have carried out an analysis of the peak positions. The peak separation increases with increasing detuning from atomic resonance, which is a clear indication of a vibrational spectrum. Identification of the different peaks is more complicated compared to the alkali systems, since there is no hyperfine interaction, which often causes structures that indicate the symmetry of the state [49]. Furthermore, the temperature of the sample is well below the limit for pure s-wave scattering, and there is no rotational progression visible. Therefore the separation between the peaks, and to a lesser degree the strength and width of the peaks, is the only information that can be used to identify a series of vibrational peaks.

In a first attempt to identify the different vibrational series, we have used the LeRoy and Bernstein analysis for the positions of the vibrational states in a long-range C_n/R^n potential [46, 85]. For the $2\ ^3S - 2\ ^3P$ asymptotes the long-range potential is determined by the dipole-dipole interaction C_3/R^3 , where C_3 is proportional to the lifetime τ of the excited $2\ ^3P$ state. In the absence of the fine structure [Hund's case (a)] there are two sets of attractive potentials, namely ${}^{1,5}\Sigma_u^+$, ${}^3\Sigma_g^+$ with $C_3 = -12.80$ a.u. and ${}^{1,5}\Pi_g$, ${}^3\Pi_u$ with $C_3 = -6.40$ a.u. However, due to the fine-structure interaction these potentials are strongly mixed and the resulting C_3 coefficients depend on the molecular symmetry for Hund's case (c). We have fitted the LeRoy-Bernstein formula to the peaks which form

Table 5.1. Detunings Δ of the probe laser from the $2\ ^3P_2$ atomic resonance at which photoassociation peaks are observed. The peaks are labelled from small to large detunings and, if possible, a tentative assignment is made. Peak positions $n = 1$ to 9 are measured in Amsterdam (uncertainty 3 MHz), 2 to 25 in Utrecht (uncertainty 20 MHz). Very weak peaks are given in parentheses.

n	$-\Delta$ (GHz)	series	n	$-\Delta$ (GHz)	series	n	$-\Delta$ (GHz)	series	
1	0.045	10	1.77	1	18	6.85	3
2	0.105	0.11	2	11	1.91	...	19	7.26	2
3	0.182	0.19	...	12	2.27	3	20	8.80	1
4	0.275	0.27	2	13	2.43	2	(21)	10.73	3
5	0.465	0.45	1	14	3.20	1	(22)	11.43	2
6	0.533	0.50	3	15	4.07	3	23	13.67	1
7	0.622	0.59	2	16	4.32	2	(24)	20.11	...
8	0.996	0.93	1	17	5.45	1	(25)	21.01	...
9	1.287	1.20	2,3						

a vibrational progression. We find three series with $C_3 = -8.35$, -7.62 , and -8.00 a.u., respectively. The assignment of the peaks to a particular vibrational series is indicated in Table 5.1.[†]

To analyse the spectrum further we have calculated the long-range Hund's case (c) potentials connected to the $2\ ^3S - 2\ ^3P_{0,1,2}$ asymptotes including fine-structure interaction, similar to the Movre-Pichler analysis [57] for the alkali systems. The resulting potential curves are shown in Fig. 5.3. There are in total 34 potentials, of which 9 are both attractive and connected to the $2\ ^3S - 2\ ^3P_2$ asymptote. Because of avoided crossings between potential curves of the same symmetry connected to different asymptotes the potentials can be approximated by C_3/R^3 with a fixed C_3 coefficient only at very long range ($>1000a_0$) and intermediate range [$(20$ to $100)a_0$]. Since we probe vibrational states with outer turning point in the range $(100$ to $500)a_0$, the C_3 coefficients we found above are only average values, which depend on the range of detunings for the states included in the fitting procedure.

In order to calculate the vibrational states in the Hund's case (c) potentials, we have employed the method of accumulated phase, which was first described by Moerdijk

[†]After publication, the Utrecht values were found to be incorrect due to a calibration error, with shifts of up to 270 MHz from detunings measured later by Léonard [45], which have an uncertainty of 15 MHz. By applying the function $1.065\Delta - (0.116\Delta)^3 - (0.102\Delta)^4$ to the Utrecht values, Léonard's values are reproduced within 27 MHz. The Amsterdam values agree with Léonard's measurements, except for peak 6, where the difference is 23 MHz. Léonard's assignment to series is the same (with peak 9 belonging to series 3), except that peak 6 is assigned to a fourth series, together with unassigned peak 11. He has not measured further than -14 GHz, but peak 23 fits better in the fourth series. Correcting the energy positions and assignments in this way, our measurements yield C_3 coefficients for the four series of -9.66 , -8.37 , -8.55 , and -8.80 a.u., respectively. The corrected data support Léonard's conclusion: series 2 & 3 and 1 & 4 probably belong to the 1_u and 2_u potentials, respectively, that are coupled at short range to the $5\Sigma_u^+$ state.

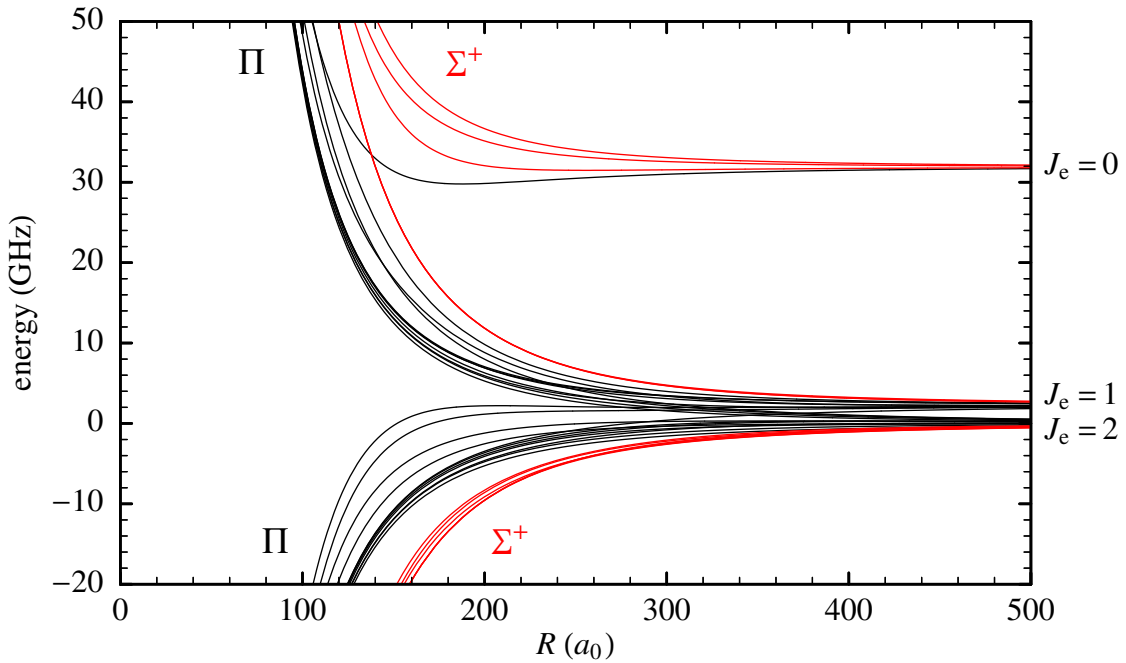


Figure 5.3. Long-range potential curves for the Hund's case (c) states connected to the $2^3S - 2^3P_{0,1,2}$ asymptotes. The mixing between the states is stretched out over the range (100 to 1000) a_0 .

et al. [55]. In this analysis the effect of the potential at small internuclear distance is reflected only in the total accumulated phase φ_0 at a matching distance R_0 and it is assumed that this phase is independent of the energy of the state. The wave function in the outer region is then integrated inwards for a certain energy using the known long-range potential. When the phase of the wave function in the outer region matches the phase φ_0 in the inner region, there is a resonance for that energy.

From our analysis we can conclude that energy positions of series 1 and 3 can be calculated using either a 0_u^+ or a 1_u potential. Since the two potentials are both connected at small range to $^{1,5}\Sigma_u^+$ and their long-range C_3 coefficients are nearly equal (-4.64 and -6.00 a.u., respectively), we cannot conclude with absolute certainty from the analysis, which potential belongs to which series. However, because the states in both potentials have large quintet character (> 80%), they will only weakly Penning ionize. Therefore it is to be expected that in these potentials vibrational states can be excited.

To give a physical reason why the excitation of vibrational states can lead to an increased ionization rate, we note that during the vibration of the molecule the system always crosses the region where the fine-structure interaction becomes comparable to the C_3/R^3 interaction. In this region singlet, triplet, and quintet states mix, and this mixing causes a transfer of amplitude of the quintet state, which is not ionized, to the singlet and triplet states, which can subsequently lead to ionization. This mixing, which depends on the binding energy of the state, is probably not very efficient, since otherwise no well-resolved vibrational structure would be observed. This possibly also accounts for the fact that below -20 GHz we are not able to observe vibrational states, if the excitation of these states is outside the region where the mixing takes place.

Finally, recent theoretical and experimental efforts to determine the absolute rate constant for Penning ionization led to an unsatisfactory disagreement between experimental and theoretical results [10, 40, 53, 90]. In the theoretical model [53] it is assumed that all potential curves contribute to the rate constant and an average is made over all states. Since we have identified the potentials that are responsible for the vibrational structure, this can be taken into account, leading to a better agreement between theory and experiment.

5.4 Conclusion

To conclude, we have demonstrated that photoassociation spectroscopy of metastable triplet helium atoms is possible. This represents a significant improvement in the accessibility of the collisional interactions of this system, which might stimulate further investigations of the underlying long-range interaction potentials. In particular, a spectroscopic determination of the s-wave scattering length may become possible.

6

The three traps

6.1 Introduction

In this chapter experimental data are presented on He* clouds in the magneto-optical, quadrupole, and cloverleaf trap, as well as on the effect of optical molasses and spin polarization between loading from one type of trap to another. For an accurate description of the density distribution in the traps, several aspects have to be taken into account: the different force fields in the three traps, the trap depth, the cloud expansion after a trap is switched off, and the integration in one direction by probing. Hence, before discussing experiments (§§6.3–6.6), a theoretical description of the density distribution is given (§6.2).

6.2 Density distribution

6.2.1 Density in the traps

The density distribution $n(\mathbf{r})$ of a cloud of N atoms with temperature T in a trapping potential $U(\mathbf{r})$ is in thermal equilibrium

$$n(\mathbf{r}) = n_0 \exp\left[-\frac{U(\mathbf{r})}{k_B T}\right], \quad (6.1)$$

with central density $n_0 = n(0)$, assuming the potential minimum is at $\mathbf{r} = 0$, with $U(0) = 0$. Three examples are considered. In a harmonic potential $U(r) = \beta r^2$, the density distribution is Gaussian with rms radius $\sigma = \sqrt{k_B T / 2\beta}$. If the potential is not spherically symmetric and the cloud has different rms radii σ_x , σ_y , and σ_z along the three Cartesian axes, the density distribution becomes

$$n_G(x, y, z) = \frac{N}{(2\pi)^{3/2} \sigma_x \sigma_y \sigma_z} \exp\left(-\frac{x^2}{2\sigma_x^2}\right) \exp\left(-\frac{y^2}{2\sigma_y^2}\right) \exp\left(-\frac{z^2}{2\sigma_z^2}\right). \quad (6.2)$$

This is the usual approximation for a cloud in a magneto-optical trap.

In a linear potential $U(\mathbf{r}) = \alpha |\mathbf{r}|$, the atoms form an exponentially cusped or Laplace distribution with $\sigma = \sqrt{2} k_B T / \alpha$ (solid curve in left plot of Fig. 6.1). Our quadrupole

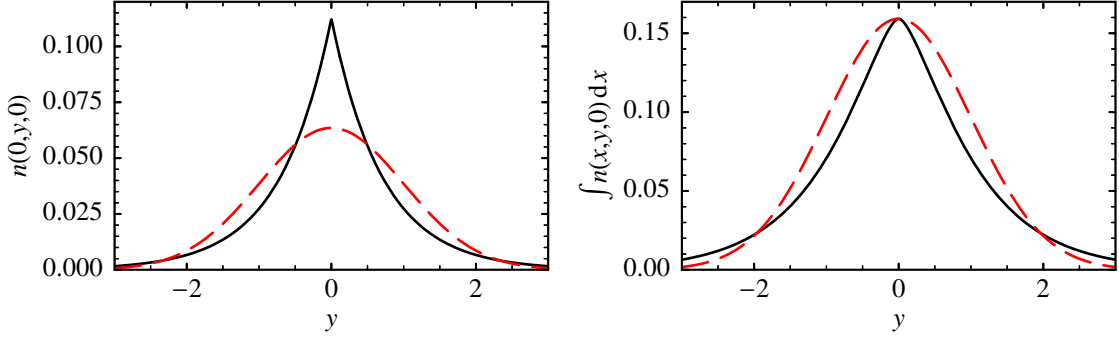


Figure 6.1. The density distribution itself (left plot) and integrated over x (right plot) along the y axis, when the cloud is described by a Gaussian function (dashed curves) or a Laplace function (solid curves). All rms radii are 1 and $N = 1$.

trap is an example of this, with $U(x, y, z) = \alpha(x^2 + y^2 + 4z^2)^{1/2}$. In the general case where all three radii are different, the density distribution is

$$n_L(x, y, z) = \frac{N}{2\sqrt{2}\pi\sigma_x\sigma_y\sigma_z} \exp\left[-\sqrt{2\left(\frac{x^2}{\sigma_x^2} + \frac{y^2}{\sigma_y^2} + \frac{z^2}{\sigma_z^2}\right)}\right]. \quad (6.3)$$

The trapping potential of an Ioffe quadrupole trap, of which the cloverleaf trap is an example, can be approximated by

$$U(x, y, z) = \sqrt{\alpha^2(x^2 + y^2) + (U_0 + \beta z^2)^2} - U_0. \quad (6.4)$$

The shape of the corresponding density distribution depends on the potential minimum: if $U_0 \gg k_B T$, the potential can be approximated by

$$U(x, y, z) \approx \frac{\alpha^2}{2U_0}(x^2 + y^2) + \beta z^2, \quad (6.5)$$

and the distribution is Gaussian; if $U_0 \ll k_B T$, the potential is linear in the xy plane and harmonic along the z axis,

$$U_{sL}(x, y, z) = \sqrt{\alpha^2(x^2 + y^2) + (\beta z^2)^2}, \quad (6.6)$$

and the density has a semi-Laplace distribution

$$n_{sL}(x, y, z) = \frac{\sqrt{2}N}{3\pi^{3/2}\sigma_x\sigma_y\sigma_z} \exp\left[-\sqrt{2\left(\frac{x^2}{\sigma_x^2} + \frac{y^2}{\sigma_y^2}\right) + \frac{z^4}{4\sigma_z^4}}\right]. \quad (6.7)$$

In absorption imaging the density is integrated over x (right plot of Fig. 6.1 and Fig. 6.2). To calculate this column density we use ($a > 0$):

$$\int_{-\infty}^{\infty} \exp[-a(s^2 + t^2)] ds = \sqrt{\pi/a} \exp(-at^2), \quad (6.8)$$

$$\int_{-\infty}^{\infty} \exp[-a\sqrt{s^2 + t^2}] ds = \begin{cases} 2|t|K_1(a|t|), & t \neq 0, \\ 2/a, & t = 0, \end{cases} \quad (6.9)$$

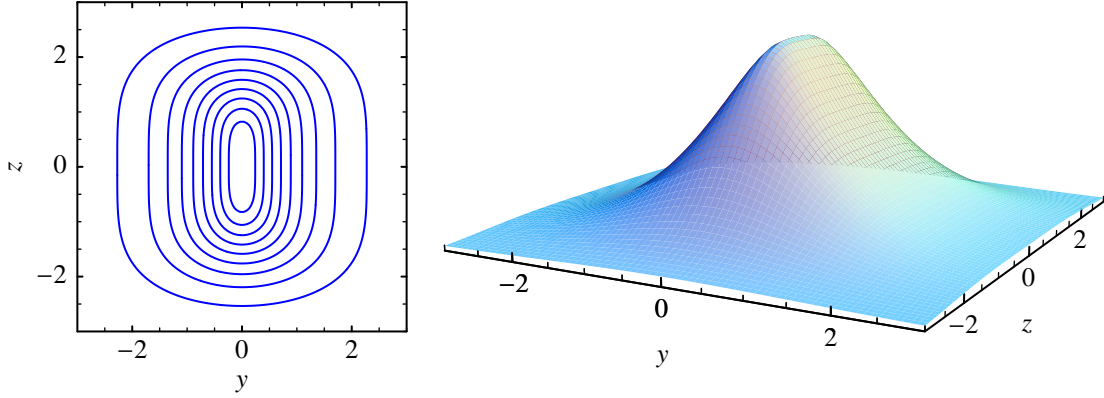


Figure 6.2. The integrated semi-Laplace distribution with $\sigma_y = \sigma_z = 1$, shown in two ways. In the contour plot lines are drawn at 10%, 20%, ..., 90% of the maximum value.

with modified Bessel function K_τ [98]. Using the fact that

$$e^{-u} = \sqrt{2u/\pi} K_{1/2}(u), \quad u > 0, \quad (6.10)$$

the density with or without integration in one dimension can be given in terms of the standard generalized symmetric Laplace distribution ($\tau > 0$)

$$\mathcal{L}(\tau, u) = \begin{cases} \frac{\sqrt{2/\pi}}{\Gamma(\tau + 1/2)} \left(\frac{|u|}{\sqrt{2}} \right)^\tau K_\tau(\sqrt{2}|u|), & u \neq 0, \\ \frac{\Gamma(\tau)}{\sqrt{2\pi} \Gamma(\tau + 1/2)}, & u = 0, \end{cases} \quad (6.11)$$

$$\int_{-\infty}^{\infty} \mathcal{L}(\tau, a\sqrt{s^2 + t^2}) ds = \frac{\mathcal{L}(\tau + 1/2, at)}{a\mathcal{L}(\tau + 1/2, 0)}, \quad (6.12)$$

with Euler gamma function Γ (for the value at $u = 0$ we use $\lim_{v \rightarrow 0} v^\tau K_\tau(v) = \Gamma(\tau) 2^{\tau-1}$ with fixed $\tau > 0$). The Gaussian, Laplace, and semi-Laplace distributions are expressed as:

$$n_G(x, y, z) = \frac{N}{2\pi^{3/2} \sigma_x \sigma_y \sigma_z} \mathcal{L}\left\{ \frac{1}{2}, \frac{1}{2\sqrt{2}} \left[\left(\frac{x}{\sigma_x} \right)^2 + \left(\frac{y}{\sigma_y} \right)^2 + \left(\frac{z}{\sigma_z} \right)^2 \right] \right\}, \quad (6.13)$$

$$n_L(x, y, z) = \frac{N}{2\pi \sigma_x \sigma_y \sigma_z} \mathcal{L}\left\{ \frac{1}{2}, \sqrt{\left(\frac{x}{\sigma_x} \right)^2 + \left(\frac{y}{\sigma_y} \right)^2 + \left(\frac{z}{\sigma_z} \right)^2} \right\}, \quad (6.14)$$

$$n_{sL}(x, y, z) = \frac{2N}{3\pi^{3/2} \sigma_x \sigma_y \sigma_z} \mathcal{L}\left\{ \frac{1}{2}, \sqrt{\left(\frac{x}{\sigma_x} \right)^2 + \left(\frac{y}{\sigma_y} \right)^2 + \frac{1}{8} \left(\frac{z}{\sigma_z} \right)^4} \right\}. \quad (6.15)$$

These densities, integrated in the x direction, are

$$\int n_G(x, y, z) dx = \frac{N}{\sqrt{2} \pi \sigma_y \sigma_z} \mathcal{L} \left\{ \frac{1}{2}, \frac{1}{2\sqrt{2}} \left[\left(\frac{y}{\sigma_y} \right)^2 + \left(\frac{z}{\sigma_z} \right)^2 \right] \right\}, \quad (6.16)$$

$$\int n_L(x, y, z) dx = \frac{N}{2\sqrt{2} \sigma_y \sigma_z} \mathcal{L} \left\{ 1, \sqrt{\left(\frac{y}{\sigma_y} \right)^2 + \left(\frac{z}{\sigma_z} \right)^2} \right\}, \quad (6.17)$$

$$\int n_{sL}(x, y, z) dx = \frac{\sqrt{2/\pi} N}{3\sigma_y \sigma_z} \mathcal{L} \left\{ 1, \sqrt{\left(\frac{y}{\sigma_y} \right)^2 + \frac{1}{8} \left(\frac{z}{\sigma_z} \right)^4} \right\}. \quad (6.18)$$

6.2.2 Density after expansion

Absorption imaging takes place after the trap is switched off and the magnetic field has become sufficiently weak. During this time a helium cloud expands significantly, especially at high temperatures. Neglecting gravity, the position \mathbf{r} of an atom with velocity \mathbf{v} at time t is given by $\mathbf{r} = \mathbf{r}_0 + \mathbf{v}t$, where \mathbf{r}_0 is the position at time $t = 0$. Assuming the cloud has a density distribution $n(\mathbf{r}_0)$ in the trap and a Maxwell-Boltzmann velocity distribution $\mathcal{M}(\mathbf{v}) d^3 v$ with

$$\mathcal{M}(\mathbf{v}) = \left(\frac{m}{2\pi k_B T} \right)^{3/2} \exp \left(-\frac{m|\mathbf{v}|^2}{2k_B T} \right), \quad (6.19)$$

the density distribution after expansion is

$$n(\mathbf{r}, t) = \int n(\mathbf{r}_0) \mathcal{M}(\mathbf{v}) d^3 v = \frac{1}{t^3} \int n(\mathbf{r}_0) \mathcal{M} \left(\frac{\mathbf{r} - \mathbf{r}_0}{t} \right) d^3 r_0 = \int n(\mathbf{r}_0) \mathcal{K}(\mathbf{r} - \mathbf{r}_0) d^3 r_0, \quad (6.20)$$

with $\mathcal{K}(\mathbf{r}) = \exp(-r^2/\xi)/(\pi\xi)^{3/2}$ and $\xi = 2t^2 k_B T/m$.

For a Gaussian distribution with rms radii σ_x , σ_y , and σ_z at $t = 0$, the density distribution becomes

$$\begin{aligned} n_G(x, y, z, t) &= \frac{N}{\sigma_x \sigma_y \sigma_z} \left(\frac{1}{2\pi^2 \xi} \right)^{3/2} \int \exp \left[-\frac{x_0^2}{2\sigma_x^2} - \frac{1}{\xi} (x - x_0)^2 \right] dx_0 \\ &\times \int \exp \left[-\frac{y_0^2}{2\sigma_y^2} - \frac{1}{\xi} (y - y_0)^2 \right] dy_0 \int \exp \left[-\frac{z_0^2}{2\sigma_z^2} - \frac{1}{\xi} (z - z_0)^2 \right] dz_0. \end{aligned} \quad (6.21)$$

The integral over x_0 is

$$\int_{-\infty}^{\infty} \exp \left[-\frac{x_0^2}{2\sigma_x^2} - \frac{1}{\xi} (x - x_0)^2 \right] dx_0 = \frac{\sqrt{2\pi\xi} \sigma_x}{\sqrt{\xi + 2\sigma_x^2}} \exp \left(-\frac{x^2}{\xi + 2\sigma_x^2} \right). \quad (6.22)$$

The integrations over y_0 and z_0 give similar results. It turns out that the density distribution stays Gaussian during expansion, with rms radii

$$\sigma_i(t) = \sqrt{\sigma_i^2(0) + \xi/2} = \sqrt{\sigma_i^2(0) + t^2 k_B T/m}. \quad (6.23)$$

The Laplace distribution has a more complicated behaviour in time:

$$n_L(x, y, z, t) = \frac{N}{2\pi^{5/2}\sigma_x\sigma_y\sigma_z\xi^{3/2}} \int_{-\infty}^{\infty} \int_{-\infty}^{\infty} \int_{-\infty}^{\infty} \mathcal{L}\left[\frac{1}{2}, \sqrt{\left(\frac{x_0}{\sigma_x}\right)^2 + \left(\frac{y_0}{\sigma_y}\right)^2 + \left(\frac{z_0}{\sigma_z}\right)^2}\right] \times \exp\left\{-\frac{1}{\xi}\left[(x - x_0)^2 + (y - y_0)^2 + (z - z_0)^2\right]\right\} dx_0 dy_0 dz_0. \quad (6.24)$$

With the help of [98]

$$K_{\tau}(v) = \frac{1}{2}\left(\frac{v}{2}\right)^{\tau} \int_0^{\infty} r^{-\tau-1} \exp\left(-r - \frac{v^2}{4r}\right) dr, \quad v > 0, \quad (6.25)$$

replacing $v = \sqrt{2}u$ and $r = u^2/s^2$, we can write the generalized Laplace distribution as

$$\mathcal{L}(\tau, u) = \frac{\sqrt{2/\pi}}{\Gamma(\tau + 1/2)} \int_0^{\infty} \frac{1}{s}\left(\frac{s^2}{2}\right)^{\tau} \exp\left(-\frac{s^2}{2} - \frac{u^2}{s^2}\right) ds. \quad (6.26)$$

Then we get

$$n_L(x, y, z, t) = \frac{N}{2\pi^3\sigma_x\sigma_y\sigma_z\xi^{3/2}} \int_0^{\infty} \exp\left(-\frac{s^2}{2}\right) B(x)B(y)B(z) ds, \quad (6.27)$$

with

$$B(w) = \int_{-\infty}^{\infty} \exp\left[-\frac{1}{s^2}\left(\frac{w_0}{\sigma_w}\right)^2 - \frac{1}{\xi}(w - w_0)^2\right] dw_0 = \frac{s\sqrt{\pi\xi}\sigma_w}{\sqrt{\xi + s^2\sigma_w^2}} \exp\left(-\frac{w^2}{\xi + s^2\sigma_w^2}\right). \quad (6.28)$$

For absorption imaging the integral over x is $\int_{-\infty}^{\infty} B(x) dx = s\pi\sqrt{\xi}\sigma_x$. The density distribution at later times, integrated in the x direction is then

$$\int n_L(x, y, z, t) dx = \frac{N}{2\pi} \int_0^{\infty} \frac{s^3}{\sqrt{(\xi + s^2\sigma_y^2)(\xi + s^2\sigma_z^2)}} \exp\left(-\frac{s^2}{2} - \frac{y^2}{\xi + s^2\sigma_y^2} - \frac{z^2}{\xi + s^2\sigma_z^2}\right) ds. \quad (6.29)$$

The remaining integrals over s are done numerically.

In the case of the semi-Laplace distribution, also the integral over z cannot be solved analytically, which renders the calculation after expansion impractical. We could approximate the semi-Laplace distribution with

$$n'_{sL}(x, y, z) = \frac{N}{\sqrt{2\pi^3}\sigma_x\sigma_y\sigma_z} \exp\left\{-\sqrt{2\left[\left(\frac{x}{\sigma_x}\right)^2 + \left(\frac{y}{\sigma_y}\right)^2\right]} - \frac{z^2}{2\sigma_z^2}\right\}, \quad (6.30)$$

corresponding to a potential

$$U'_{sL}(x, y, z) = \alpha\sqrt{x^2 + y^2} + \beta z^2, \quad (6.31)$$

which is accurate on the axes. Then the density after expansion is given by

$$\begin{aligned} n'_{\text{sL}}(x, y, z, t) &= \frac{\sqrt{2}N}{\pi^2 \sqrt{\xi + 2\sigma_z^2}} \exp\left(-\frac{z^2}{\xi + 2\sigma_z^2}\right) \\ &\times \int_0^\infty \frac{s^2}{\sqrt{(\xi + s^2\sigma_x^2)(\xi + s^2\sigma_y^2)}} \exp\left(-\frac{s^2}{2} - \frac{x^2}{\xi + s^2\sigma_x^2} - \frac{y^2}{\xi + s^2\sigma_y^2}\right) ds \quad (6.32) \end{aligned}$$

and integrated along the x direction

$$\begin{aligned} \int n'_{\text{sL}}(x, y, z, t) dx &= \frac{\sqrt{2}N}{\pi^{3/2} \sqrt{\xi + 2\sigma_z^2}} \exp\left(-\frac{z^2}{\xi + 2\sigma_z^2}\right) \\ &\times \int_0^\infty \frac{s^2}{\sqrt{\xi + s^2\sigma_y^2}} \exp\left(-\frac{s^2}{2} - \frac{y^2}{\xi + s^2\sigma_y^2}\right) ds. \quad (6.33) \end{aligned}$$

However, the semi-Laplace distribution is used only to describe the cloud in the cloverleaf trap, for which we have to assume already that the potential minimum U_0 is negligible. For the density distribution after expansion it is therefore more accurate to calculate the distribution in the potential given by Eq. (6.4) and to do the convolution in Eq. (6.20) numerically. Two corrections can then be included: gravitational sag and the effect of a finite trap depth.

6.2.3 Density in magnetic traps with finite depth

The trapping potential due to a magnetic field $B(\mathbf{r})$ with (local) minimum B_0 is given by $U(\mathbf{r}) = 2\mu_B[B(\mathbf{r}) - B_0]$. The factor 2 is the product of the Landé g factor and magnetic quantum number of the state we use (3S_1 , $m_J = 1$). As discussed earlier, the potential of the cloverleaf trap can be approximated by Eq. (6.4), with minimum potential energy $U_0 = 2\mu_B B_0$. However, at low temperatures the gravitational potential energy mgz , with mass m and gravitational acceleration g in the $-\hat{z}$ direction, becomes important. Adding this contribution, the trapping potential becomes

$$U(x, y, z) = \sqrt{\alpha^2(x^2 + y^2) + (2\mu_B B_0 + \beta z^2)^2} + mgz - U_0, \quad (6.34)$$

with

$$U_0 = 2\mu_B B_0 - \frac{m^2 g^2}{4\beta}. \quad (6.35)$$

The potential minimum sags to position $z = -mg/2\beta$ with $x = y = 0$. In the magneto-optical and quadrupole traps the temperature is never low enough to notice this effect. As a reminder, the potential in the quadrupole trap is $U(x, y, z) = \alpha(x^2 + y^2 + 4z^2)^{1/2}$.

According to Luiten et al. [52] the atoms in a magnetic trap with a finite depth are described well by a Boltzmann energy distribution that is truncated at an energy equal to the trap depth. The phase-space distribution is assumed to be only a function of the energy of the atoms. At low temperatures this is the case if there are many elastic

collisions between the atoms. At higher temperatures in the cloverleaf trap, the atoms occupy a part of space large enough that higher-order terms of the potential break the axial symmetry of Eq. (6.34) and the motion of the atoms becomes ergodic even without collisions. For the quadrupole trap, where this is not the case, the model will only be a rough approximation. Below a summary is given of the equations needed to calculate the density distribution in a magnetic trap [52].

The (thermal) density distribution in an infinitely deep trap is

$$n_{\infty}(\mathbf{r}) = n_0 \exp\left[-\frac{U(\mathbf{r})}{k_B T}\right]. \quad (6.36)$$

When only atoms with an energy smaller than ε_t are trapped, the density distribution becomes

$$n(\mathbf{r}) = P\left(\frac{3}{2}, \kappa\right) n_{\infty}(\mathbf{r}), \quad (6.37)$$

with incomplete gamma function P and

$$\kappa(\mathbf{r}) = \begin{cases} \frac{\varepsilon_t - U(\mathbf{r})}{k_B T}, & U(\mathbf{r}) \leq \varepsilon_t, \\ 0, & U(\mathbf{r}) > \varepsilon_t. \end{cases} \quad (6.38)$$

In this truncated Boltzmann distribution T is still called the temperature, although strictly speaking a thermodynamic temperature is not defined for a nonequilibrium distribution. The central density is given by $n(0) = P\left(\frac{3}{2}, \kappa\right) n_0$; the parameter n_0 is equal to the central density only in the limit of infinite trap depth. It is defined by

$$n_0 = N/V_e, \quad (6.39)$$

with number of trapped atoms N and reference volume V_e , which is equal to the effective volume $N/n(0)$ in the limit of a deep trap. In general the reference volume is given by

$$V_e = \Lambda^3 \zeta, \quad (6.40)$$

with thermal de Broglie wavelength

$$\Lambda = \sqrt{\frac{2\pi\hbar^2}{mk_B T}} \quad (6.41)$$

and trap-dependent single-atom partition function ζ ,

$$\text{cloverleaf trap: } \begin{cases} \zeta = \zeta_{\infty}^0 \left[P(4, \eta) + \frac{2}{3} \frac{U_0}{k_B T} P(3, \eta) \right], \\ \zeta_{\infty}^0 = 6A_{IQ}(k_B T)^4, \\ A_{IQ} = m^{3/2} / (4\sqrt{2\beta} \alpha^2 \hbar^3), \end{cases} \quad (6.42)$$

$$\text{quadrupole trap: } \begin{cases} \zeta = \zeta_{\infty} P\left(\frac{9}{2}, \eta\right), \\ \zeta_{\infty} = \sqrt{2/\pi} m^{3/2} (k_B T)^{9/2} / (\alpha^3 \hbar^3), \end{cases} \quad (6.43)$$

where the gravitational sag is neglected. Finally truncation parameter

$$\eta = \frac{\varepsilon_t}{k_B T} \quad (6.44)$$

is used in any magnetic trap. Although n_0 is not the central density and a thermodynamic temperature cannot be given for this nonequilibrium distribution, the (central) phase-space density (or degeneracy parameter) is still $n_0 \Lambda^3$.

The incomplete gamma function P can be given in terms of the incomplete gamma function Γ as

$$P(a, \eta) = 1 - \frac{\Gamma(a, \eta)}{\Gamma(a, 0)} = \frac{\int_0^\eta t^{a-1} e^{-t} dt}{\int_0^\infty t^{a-1} e^{-t} dt}. \quad (6.45)$$

Extreme values are $P(a, 0) = 0$ and $P(a, \infty) = 1$. A useful recursion relation is

$$P(a + 1, \eta) = P(a, \eta) - \frac{\eta^a e^{-\eta}}{\Gamma(a + 1)}, \quad (6.46)$$

with Euler gamma function $\Gamma(z) \equiv \Gamma(z, 0)$. For integer a , $\Gamma(a + 1) = a!$ and for half-integer a , $\Gamma(a + 1) = \sqrt{\pi/2}(2a)!!/2^a$. With the help of $P(0, \eta) = 1$ and $P(1/2, \eta) = \text{erf } \sqrt{\eta}$ we can write

$$P(a, \eta) = \begin{cases} 1 - e^{-\eta} \sum_{k=0}^{a-1} \frac{\eta^k}{k!}, & \text{integer } a, \\ \text{erf}(\sqrt{\eta}) - \sqrt{\frac{2}{\pi}} e^{-\eta} \sum_{k=1/2}^{a-1} \frac{(2\eta)^k}{(2k)!!}, & \text{half-integer } a, \end{cases} \quad (6.47)$$

with error function $\text{erf}(z) = \frac{2}{\sqrt{\pi}} \int_0^z e^{-t^2} dt$. We will also need the derivative with respect to η :

$$\frac{\partial P(a, \eta)}{\partial \eta} = P(a - 1, \eta) - P(a, \eta). \quad (6.48)$$

6.3 Magneto-optical trap

6.3.1 Characteristics

The experiments in Chapters 3–5 were carried out in a setup with two magnetic field coils. For magnetic trapping these were replaced by the cloverleaf setup with twelve coils. The new MOT uses the pair of small axial coils. The typical loading rate has become $2 \times 10^{10} \text{ s}^{-1}$ and the maximum number of atoms is now trapped at gradients of $\partial B / \partial z = 2\partial B / \partial \rho = 12.1 \text{ G/cm}$, at a lower light intensity: 45 mW of the LNA laser beam is sent to the trap chamber, where the horizontal beams have each an intensity of $I_{\text{horz}} = 2.0 \text{ mW/cm}^2$ and the vertical beams $I_{\text{vert}} = 1.3 \text{ mW/cm}^2$, in total $I = 11 \text{ mW/cm}^2$. The detuning is still 35 MHz to the red. Figure 6.3 shows the number of atoms and temperature as a function of the total MOT intensity. If the intensity is above an optimum and getting higher, the number of atoms decreases and the temperature increases. At

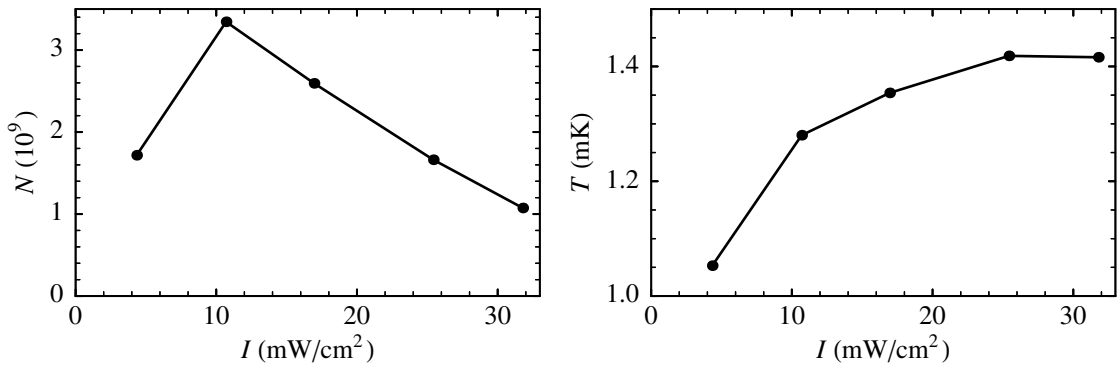


Figure 6.3. Number of atoms and temperature in the MOT as a function of total MOT intensity.

constant intensity the temperature increases with the number of atoms: if the temperature is 1.34 mK in the ‘standard’ MOT, the temperature drops to 1.14 mK when only 1/8 of the normal number of atoms is captured by changing the loading rate.

The ratio of the field gradients is fixed. Therefore the ratio of the horizontal and vertical intensities determines the aspect ratio of the cloud, which is chosen to be compatible with the cloverleaf trap in order to trap magnetically a maximum number of atoms. The absolute size of the cloud is examined in fluorescence while the trap is still on, and in absorption after the trap has been switched off.

6.3.2 Fluorescence imaging

The advantage of fluorescence imaging is that the cloud is seen *in situ*, but the number of atoms cannot be determined accurately, as the amount of fluorescence depends not only on the number of atoms, but also on the laser intensity, which may vary from day to day. Despite central densities of up to 10^{10} cm⁻³, the fluorescence is found to depend linearly on the number of atoms, and it is also proportional to the intensity, as long as the intensity is not too high (Fig. 6.4). This means that fluorescence does not give a false impression of the cloud shape. The number of emitted photons per atom is calculated by dividing the integral of the fluorescence by the number of atoms according to TOF signals. As the camera is calibrated and taking into account that only 0.09% of the fluorescence is directed towards the camera, the fluorescence is given in absolute numbers. According to theory, the average absorption rate per atom is $\frac{1}{2}\Gamma(I/I'_{\text{sat}})/(1 + I/I'_{\text{sat}})$ with effective saturation intensity $I'_{\text{sat}} = fI_{\text{sat}}/\chi$ (see §2.3.4). At a detuning of $\Delta/2\pi = 35$ MHz, the influence of Doppler broadening is not significant and χ is given by Eq. (2.24), assuming the influence of the magnetic field can be neglected. If the average light polarization is random, $f = 1.8$. However, this last approximation is too simple: the effect of six beams is not the same as the effect of one beam with the sum of the intensities [64, 92]. The f -values at the two occurrences of f in the equation for the average absorption rate may even be different. The measured data are consistent with the model if $f = 3.3$. The value is of limited interest, because the calibration of the camera is only used for Fig. 6.4.

Figure 6.5 shows a fluorescence image of the cloud and a Gaussian fit. If at constant

intensity the loading rate is increased, the cloud shows a small increase in size (Fig. 6.6). Figure 6.3 suggests that the best total intensity is 11 mW/cm^2 , because of the maximum number of atoms at a relatively low temperature. However, Fig. 6.6 shows that the cloud is then relatively large. The highest central density can be found at 25 mW/cm^2 , where

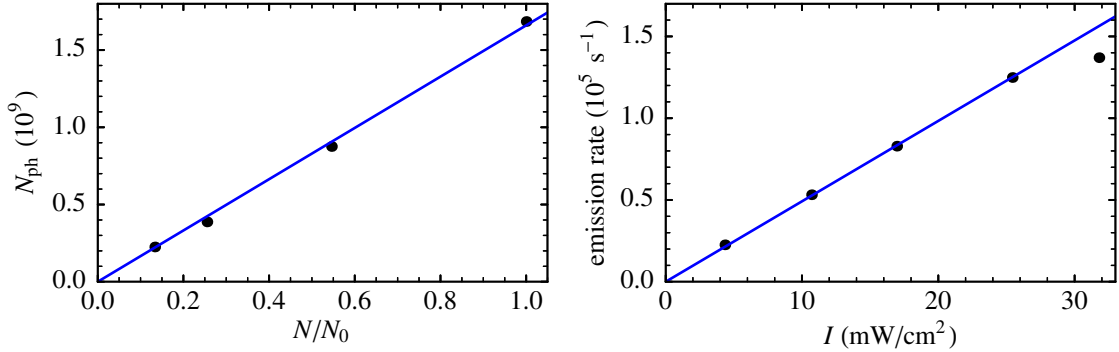


Figure 6.4. Left plot: number of detected fluorescence photons imaged in 20 ms as a function of the number of atoms N in the MOT, scaled with the number of atoms N_0 trapped under typical loading conditions. Right plot: measured fluorescence emission rate per atom as a function of total MOT intensity. Curves are linear fits.

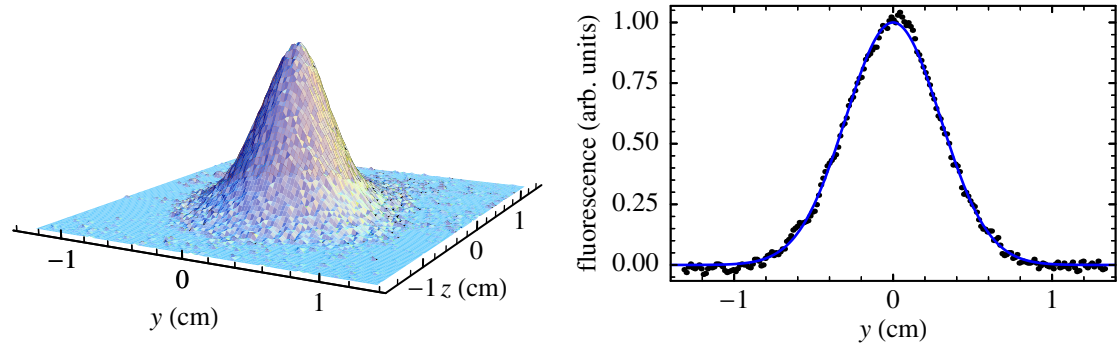


Figure 6.5. Fluorescence image of a MOT cloud at $I = 11 \text{ mW/cm}^2$, with a horizontal cross section through the centre. The curve is a Gaussian fit to the whole cloud.

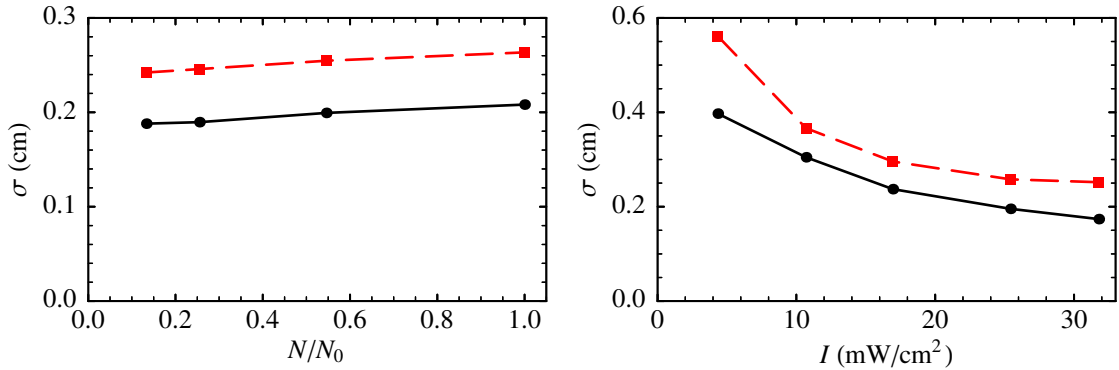


Figure 6.6. Gaussian rms radius as a function of scaled number of atoms in the MOT (left) and as a function of total MOT intensity (right). Dots are horizontal radii, squares are vertical radii.

it is 70% larger than at 11 mW/cm^2 . The optimum for loading the magnetic trap is somewhere in between.

6.3.3 Absorption imaging

With absorption imaging the number of atoms is determined without calibration (see §2.3). The MOT is switched off and after a delay a resonant $50 \mu\text{s}$ probe pulse is applied. The resulting image is fitted as described in §2.3.6 assuming the cloud has a Gaussian density distribution. The delay is 1 ms to let the magnetic field decay to a negligible level. If the optical density is large enough to absorb almost all probe light, the determination of the number of atoms can become inaccurate. In this case the delay is extended so the cloud expands more before probing (Fig. 6.7).

Using a range of delays, the dynamics of the expansion are studied. According to the fits the cloud does not move during expansion; the standard deviation in the position of the centre of the cloud is 4% of the rms radius in either direction. Figure 6.8 shows the radii as a function of expansion time t before probing. Points at $t = 0$ are determined

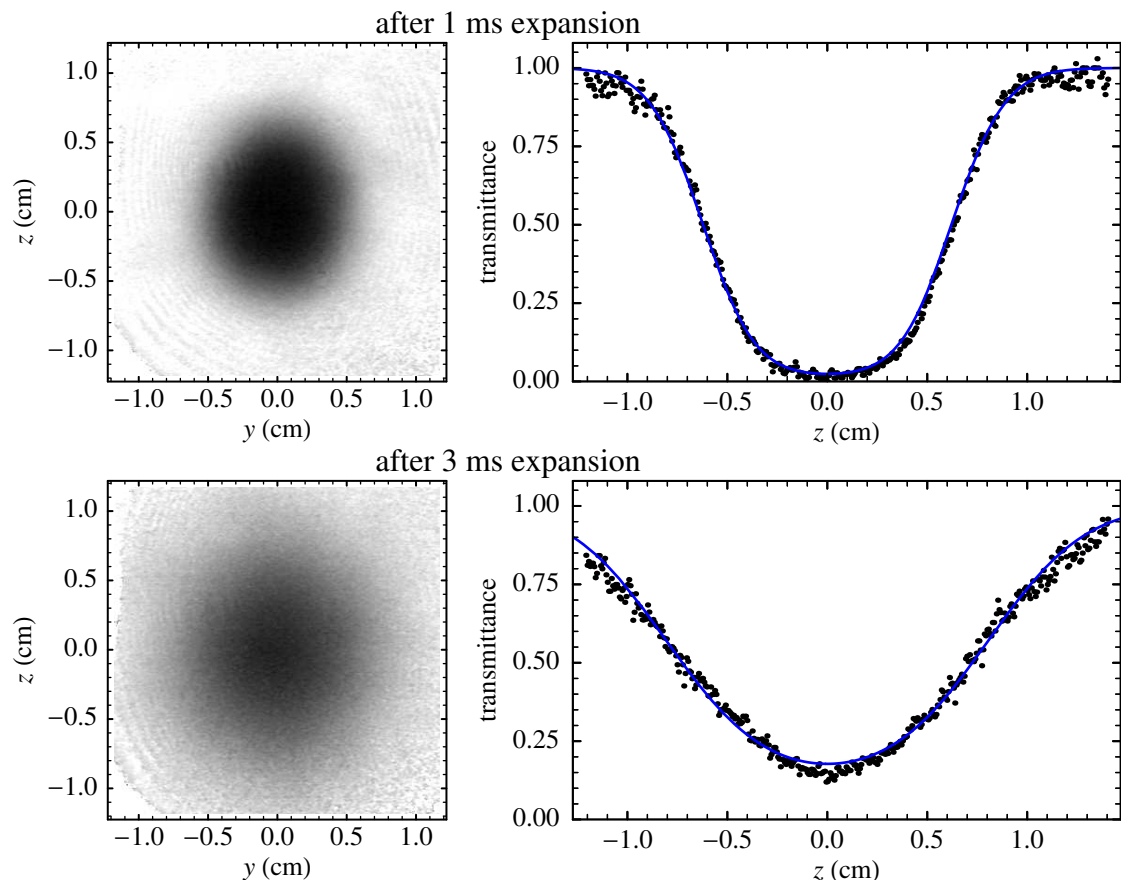


Figure 6.7. Absorption images of a MOT cloud with 1.5×10^9 atoms, taken 1 ms (top) and 3 ms (bottom) after switching off the trap. Also shown are vertical cross sections through the centre of the cloud, where the curves are fits assuming a Gaussian shaped cloud.

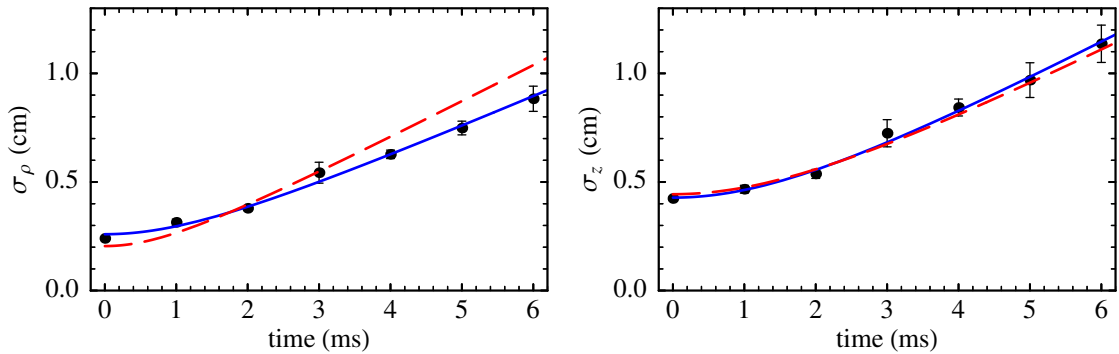


Figure 6.8. Gaussian rms radius as a function of expansion time after the MOT is switched off, in the horizontal direction (left plot) and vertical direction (right plot). Solid curves are fits with both the radius at the start and the temperature as free parameters, dashed curves are fits with the temperature fixed at the value according to TOF measurements.

with fluorescence imaging. Fitting Eq. (6.23) to the radii, with the radius at $t = 0$ and the temperature as parameters (solid curves), the temperature is horizontally 0.98 mK and vertically 1.51 mK. The MCP detector is mounted almost vertically below the trap, so if the temperature is not the same in the two directions, the temperature determined from TOF signals should agree with that in the vertical direction. In this case the TOF temperature is 1.38 mK, and fitting with this value fixed (dashed curves) is compatible with the error bars of the vertical radii. The temperature is probably 30% lower in the horizontal direction because the laser intensity of the horizontal beams is 50% higher and the cooling force therefore different.

The temperature anisotropy may imply that the detected fraction of a MOT cloud on the MCP detector is larger than simulations with a uniform temperature indicate, because the cloud expands less than expected. This has no influence on the number of atoms in the MOT, as this is determined with absorption imaging. Correction for the temperature anisotropy would increase the number of atoms in the cloverleaf trap, making the numbers given in this thesis a conservative estimate. However, they cannot be much larger, as the capture efficiency from the MOT to the cloverleaf trap is already 90% (after spin polarization). An uncertainty in the number of atoms in the cloverleaf trap due to the detected fraction is already given when calculating the uncertainty in the cloverleaf temperature: for this the offset velocity v_0 is varied in TOF simulations (§2.2.3), which also changes the detected fraction.

6.4 Optical molasses and spin polarization

To load the atoms from the MOT into the cloverleaf trap, the temperature needs to be lowered, because the cloverleaf trap has a lower trap depth. By optical pumping the atoms are spin-polarized as well to allow all of them to be captured instead of only the fraction that is in the $m = +1$ magnetic sublevel.

Optical molasses should in principle be applied while no magnetic field is present.

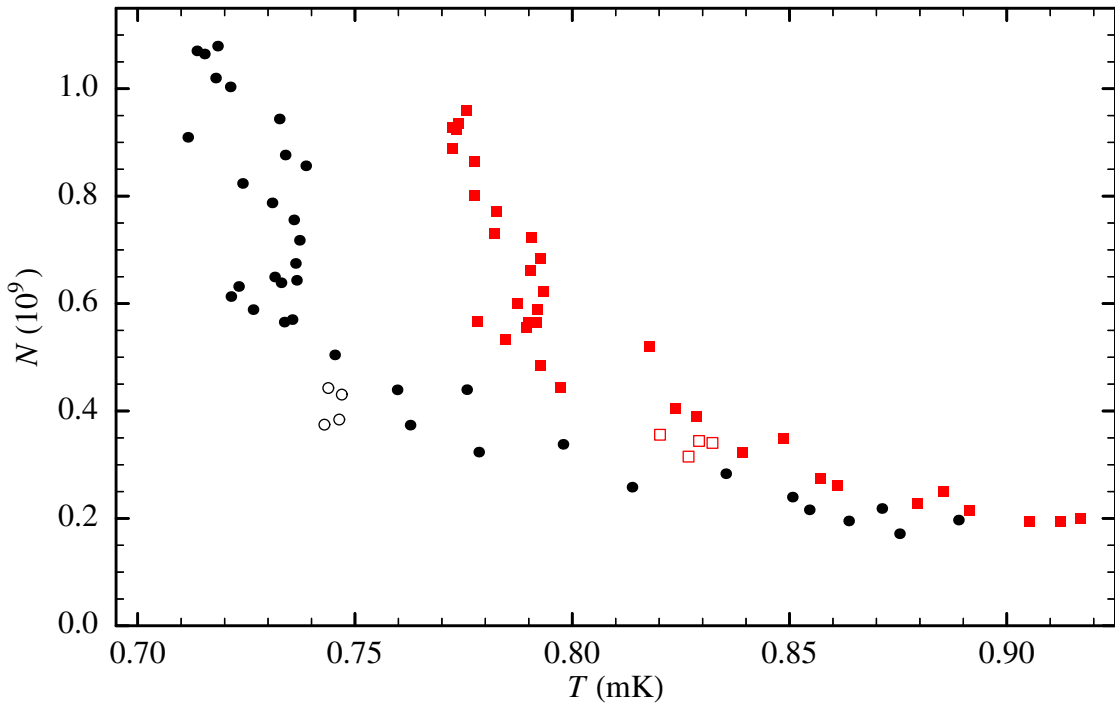


Figure 6.9. Number of atoms and temperature in the cloverleaf trap after 5 s trapping, depending on molasses and spin polarization. Molasses beams are linearly polarized, the light polarization of the spin-polarization beam is varied by rotating an inserted quarter-wave plate in intervals of 5° over a 180° range. Dots – with molasses, squares – without molasses, closed symbols – with spin polarization, open symbols – without spin polarization.

Therefore we wait 1 ms after the MOT is switched off, before turning on the molasses beams for 1 ms. The six separate molasses beams are usually 2Γ detuned to the red at an intensity of about $0.4I_{\text{sat}}$ per beam. To compensate for intensity imbalances, a magnetic field is added of about 0.8 G, mainly in the vertical direction, produced by three extra sets of large coils, which are kept on during all experiments. The temperature decreases to about 0.4 mK. Theory and further direct experimental results are discussed by Herschbach [32].

After molasses, just before the cloverleaf trap is switched on, spin polarization is applied with a retroreflected laser beam in the vertical direction, which is the direction of the magnetic field in the centre when the trap is on. During the 50 μ s light pulse (with an intensity of $10I_{\text{sat}}$) a small magnetic field pulse is applied to break the degeneracy. The field is directed upward, while the beam goes down left-handed circularly polarized, to make $\Delta m = +1$ transitions. The light is detuned 5 MHz to the blue, resonant with the central $\Delta m = +1$ transition at 2.5 G. However, the largest effect is measured at 0.8 G, possibly to reduce the probability of $\Delta m = -1$ and $\Delta m = 0$ transitions when the alignment is not perfect.

Figure 6.9 shows the effect of both molasses and spin polarization on the temperature and number of atoms after the cloverleaf trap is on for 5 s. During this measurement the lifetime was 10.5 s, implying 60% more atoms at the start of trapping. The light

polarization of the spin-polarization beam is varied by rotating a quarter-wave plate in the beam, which has not only an effect on the number of atoms, but also on the temperature. Apparently these beams not only change the state of the atoms, but also cool them. Using only molasses (from open squares to open circles), the temperature of 0.83 mK drops a mere 0.08 mK and the number of atoms increases 20%. Applying only spin polarization (from open squares to closed squares at top left) increases the number of atoms by a factor of 2.8 and lowers the temperature 0.05 mK. With both molasses and spin polarization (from open squares to closed circles at top left), we have 3.2 times the number of atoms at a 0.11 mK lower temperature than without any extra beams. The highest density is also reached in the top left corner of the figure.

6.5 Quadrupole trap

Before discussing the cloverleaf trap, some measurements in a quadrupole trap are described. Either the MOT is switched off, followed by possible molasses and spin polarization, before switching on again the same coils, or the current is simply ramped up to the desired current while the MOT light is turned off. A drawback of the second method is that it takes some time to change the current. Spin polarization should not work in a quadrupole, as the magnetic field does not point in one particular direction, but applying the spin-polarization beam after molasses before loading the strongest trap increases the number of trapped atoms by 90% and cools them by 0.14 mK to 1.01 mK. This is another indication that this beam does not simply change the atomic state.

The density distribution in the quadrupole trap is assumed to be thermalized. This was checked with Monte-Carlo simulations of a cloud of atoms with a Gaussian position and velocity distribution that is captured in an infinitely deep quadrupole trap where no collisions take place. After 0.1 s the cloud has already reached a steady state, with a density distribution which is nearly exponential and a velocity distribution which is nearly Gaussian. The deviation cannot be seen in absorption imaging and will be even smaller if there are elastic collisions. When the trap has a finite depth, the distribution can be calculated as described in §6.2.3. However, in our trap the truncation parameter $\eta > 7$, which makes the trap deep enough to assume a perfect Laplace distribution with rms radii $2\sigma_z = \sigma_\rho = \sqrt{2}k_B T/\alpha$, with $\alpha = 2\mu_B \partial B / \partial \rho$.

In a weak quadrupole trap ($\partial B / \partial z = 2\partial B / \partial \rho = 18$ G/cm) clouds are observed with a temperature of 0.3 mK and rms radii as expected from theory: 0.20 cm in the vertical direction and twice that in the horizontal direction, with a standard deviation of 20% in the fitted values. Figure 6.10 shows an absorption image of a cloud trapped for 1 s, taken 1 ms after the trap has been switched off. The solid curve in the vertical cross section through the centre is the result of a fit of the whole image with Eq. (2.52), where $\int n(x, y, z) dx$ is given by the expression for an integrated Laplace distribution after expansion, Eq. (6.29). For the dashed curve a Gaussian distribution is assumed, showing that after expansion of the cloud and integration in the probe direction, the two distributions cannot be distinguished.

In the strongest quadrupole trap ($\partial B / \partial z = 58$ G/cm) the most atoms are trapped: according to TOF measurements 5×10^8 atoms with molasses but without ‘spin polariza-

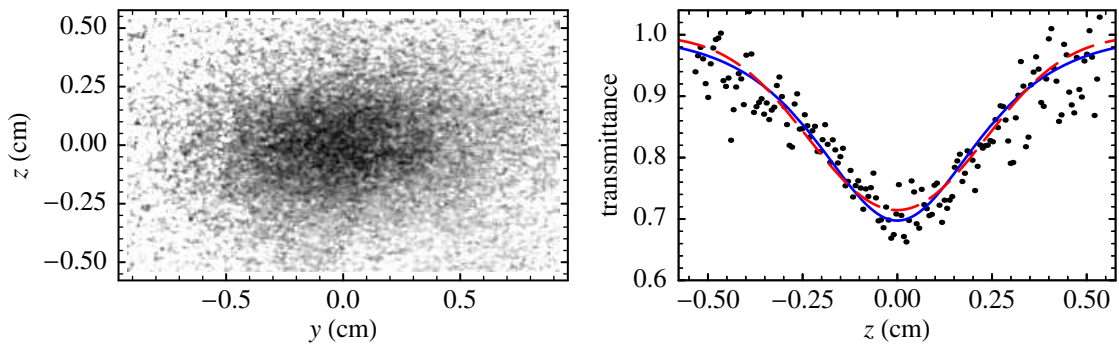


Figure 6.10. Absorption image and vertical cross section through the centre of a cloud in the weak quadrupole trap, after molasses (no spin polarization), with 2.0×10^8 atoms according to a TOF measurement. The fits in the cross section assume either a Laplace distribution (solid curve) or a Gaussian distribution (dashed curve) in the trap.

tion', at 1.0 mK. However, the clouds appear to have radii that are 60% of the theoretical value (0.18 cm vertically), again with a standard deviation of 20%. The difference is due to remaining field gradients during absorption imaging: in a volume with a radius of 0.5 cm around the trap centre, the measured field has extreme values that are 4 G apart when the quadrupole trap is 1 ms off. After 2 ms the difference has only gone down to 2 G. If the cloud is probed much later, it has expanded too much for an accurate determination of the original radii in the trap.

As has been discussed in §2.3.5, field gradients are negligible after switching off the cloverleaf trap. Another, more fundamental, reason why the cloverleaf trap is to be preferred, is that Majorana spin flips around the zero field minimum in the quadrupole trap cause atom loss, preventing the formation of a dense cold cloud. Even at high temperatures the lifetime in the quadrupole trap is considerably smaller than in the cloverleaf trap [32].

6.6 Cloverleaf trap

6.6.1 Loading

To keep phase-space density as high as possible when loading the cloverleaf trap, the cloud of atoms must have the same shape in the cloverleaf trap as before it is switched on, with the same temperature. However, the MOT cloud is large and gets larger during expansion: there is 2.5 ms between switching off the MOT and switching on the cloverleaf trap, to allow time for molasses. It takes another 1 ms before the trap currents have risen sufficiently. This means the cloverleaf trap parameters α and β would have to be very small for the cloud to keep the same size, with a high B_0 for a Gaussian shape. Unfortunately, the trap depth is then too small to load all atoms in the trap. Therefore the confinement is made stronger than for adiabatic loading, at the cost of a higher temperature.

If the cloud is compressed while the MOT is still on, by increasing the magnetic field gradient and laser intensity, the effect on the central density after loading into the

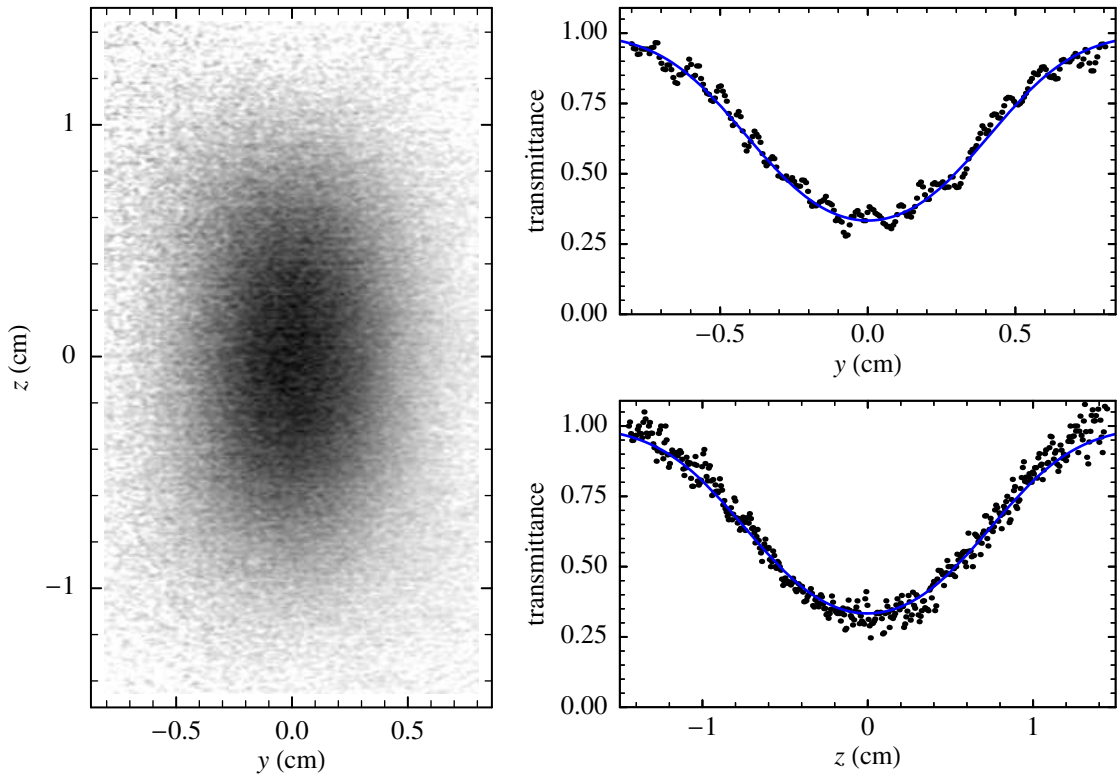


Figure 6.11. Absorption image taken 1 ms after switching off the cloverleaf trap used for loading, with two cross sections through the centre. After 2 s trapping the cloud consists of 2.1×10^9 atoms. The fit in the cross sections assumes a Gaussian density distribution.

cloverleaf trap is marginal, because the expansion makes a large contribution to the cloud size. Molasses brings down the temperature so the expansion becomes slower, but the effect is not large enough to be able to load the cloverleaf trap adiabatically.

The cloverleaf trap, optimized on central density, is given by parameters $\alpha/2\mu_B = 37$ G/cm, $\beta/2\mu_B = 10.9$ G/cm², $B_0 = 8.6$ G, and a trap depth of 26 G (3.4 mK). The harmonic part is characterized by trap frequencies $\omega_\rho/2\pi = 105$ Hz and $\omega_z/2\pi = 39$ Hz, gravitational sag is 0.016 cm. Although the trap is not quite harmonic in the whole region where the atoms are located, B_0 is sufficiently high to give the cloud an almost Gaussian shape (Fig. 6.11). The temperature increases from 0.4 mK right after molasses to 0.7 mK in the trap. In §7.4.1 it will be shown that the remaining fraction of atoms is given by $\zeta(\eta)/\zeta(\infty)$, assuming pure spilling of atoms without a change of the temperature. This fraction is at least 80% for $T \leq 0.7$ mK, agreeing with the measured fraction of 90% (after spin polarization).

The standard deviation in the position of the cloud is 4% of the rms radius in either direction, the same as in the MOT. The rms radii as a function of expansion time after trapping for 2 s are shown in Fig. 6.12. Error bars indicate the standard deviation in the fitted values. At $t < 1$ ms, the remaining magnetic field is not small enough for accurate imaging, which is obvious from the images because the absorption is much smaller than at $t \geq 1$ ms (see §2.3.7). The cloud at $t = 0.5$ ms could only be seen after averaging,

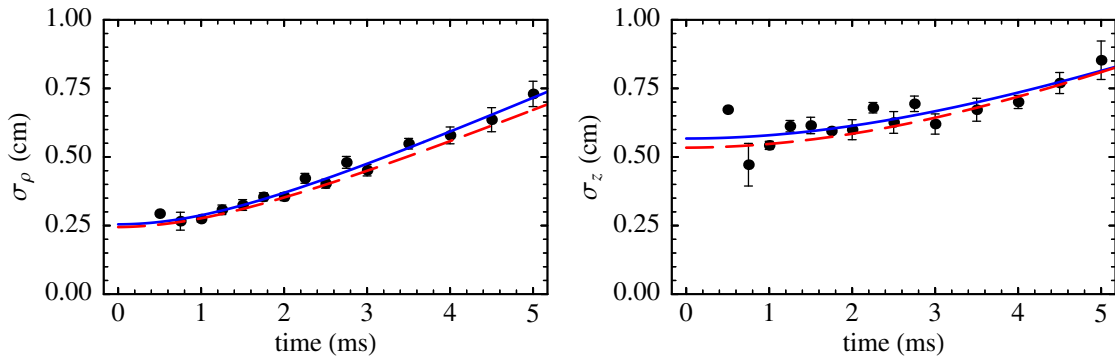


Figure 6.12. Gaussian rms radius as a function of expansion time after the cloverleaf trap is switched off, in the horizontal direction (left plot) and vertical direction (right plot). Solid curves are fits assuming Gaussian expansion with both the radius at the start and the temperature as free parameters; dashed curves are predictions according to theory with the temperature according to TOF measurements.

which is why no error bars are given. Using only the radii for $t \geq 1$ ms, solid curves are fits with the radius in the trap and the temperature as parameters, similar to Fig. 6.8. The fitted temperature is 0.86 mK horizontally and 0.66 mK vertically. This difference may be due to insufficient thermalization, as it is not noticed after 5 s trapping time. Perhaps there is no real difference and the discrepancy is caused by the uncertainty in the data; if both sets of radii are fitted with the same temperature (not shown), its value is 0.79 mK, close to the TOF temperature of 0.75 mK. The theoretical radii at $t = 0$ are 0.24 cm horizontally and 0.53 cm vertically; the radii extrapolated from the fits are only 4% and 6% larger, respectively. Curves with the theoretical cloud size in the trap (§6.2.3) and the temperature from TOF signals, i.e. without fit parameters, agree well with the measured data. Although the cloud is almost Gaussian in the trap, according to the model there are small deviations that remain even after longer expansion times. This happens primarily in the vertical direction, where the size is not much increased by the expansion. Therefore the theoretical cloud is integrated in the probe direction and fitted with a Gauss. At later times first a numerical convolution is applied with a Maxwell-Boltzmann velocity distribution, as described in §6.2.2.

6.6.2 Compression

After the atoms are loaded into the cloverleaf trap, the cloud is compressed to increase the elastic collision rate, which is necessary for efficient evaporative cooling. The magnetic confinement is increased until the strongest field configuration is reached: $a/2\mu_B = 69$ G/cm, $\beta/2\mu_B = 13.9$ G/cm², $B_0 = 0.5$ G, and a trap depth of 47 G (6.4 mK). The harmonic part is then characterized by trap frequencies $\omega_\rho/2\pi = 853$ Hz and $\omega_z/2\pi = 44$ Hz, gravitational sag is 0.013 cm (with a vertical ρ axis the sag would have been 0.34 μm).

Before compression the temperature is 0.75 mK. Under instantaneous compression the kinetic energy of the atoms and their distribution stay momentarily constant, while the potential energy increases. Using the general expression for the total internal energy

of the trapped atoms [52]

$$E = \frac{12 P(5, \eta) + 6 \frac{U_0}{k_B T} P(4, \eta)}{3 P(4, \eta) + 2 \frac{U_0}{k_B T} P(3, \eta)} N k_B T, \quad (6.49)$$

the total energy after compression is

$$E_f = E_i + \int [U_f(\mathbf{r}) - U_i(\mathbf{r})] n_i(\mathbf{r}) d^3 r, \quad (6.50)$$

where indices i and f denote the initial and final situation, respectively. When Eq. (6.49) is solved with this new total energy, the temperature increases to 1.23 mK after instantaneous compression. Experimentally the same value is found when the trap currents are changed in one step.

The other extreme is adiabatic compression, where the entropy S stays constant (as long as N is constant). It is given by [67]

$$S = N k_B \left(1 + \frac{E}{N k_B T} - \ln n_0 \Lambda^3 \right), \quad (6.51)$$

which can be rewritten with Eqs. (6.39) and (6.40) as

$$\frac{S}{N k_B} + \ln N - 1 = \frac{E}{N k_B T} + \ln \zeta = \text{constant}. \quad (6.52)$$

Calculating this constant before compression and solving the equation for T afterwards yields a temperature of only 0.96 mK after adiabatic compression. The phase-space density increases by a factor of 2.3. However, this means the compression has to be slow compared to the elastic collision rate, which is initially 3 s^{-1} averaged over the cloud (calculated in §7.3.3). As the trap lifetime is only about 10 s and the trap depth is small at the start, the density would increase less than desired due to atom loss. Therefore the optimum tempo lies between the two scenarios: the trap currents are changed linearly in 20 steps of 25 ms, starting immediately after the atoms are loaded into the trap. This result was found by maximizing the optical density 2 s after compression. The delay is needed to bring the cloud near equilibrium. Although the temperature becomes 1.20 mK, close to the instantaneous-compression limit, the collision rate still doubles to 6 s^{-1} . With 1.8×10^9 atoms in the trap, the central density in the trap increases from $4 \times 10^9 \text{ cm}^{-3}$ to $1.0 \times 10^{10} \text{ cm}^{-3}$. The phase-space density increases by 40% to 1.6×10^{-7} , of which 6% is due to the fact that more atoms are kept in the trap.

As the radial confinement is much stronger than the axial confinement, the cloud becomes elongated by compression: the density while the atoms are still in the trap has a FWHM of 0.2 cm horizontally and 1.4 cm vertically. Figure 6.13 shows an example of a cloud in the compressed cloverleaf trap with 2.6×10^9 atoms. The solid curves in the cross sections are the result of a numerical convolution of the theoretical density distribution in the trap with a Maxwell-Boltzmann velocity distribution during expansion, where the cloud size is determined by the field: the only fit parameters are the number of atoms and the central position. Only for this image the actual magnetic field is used,

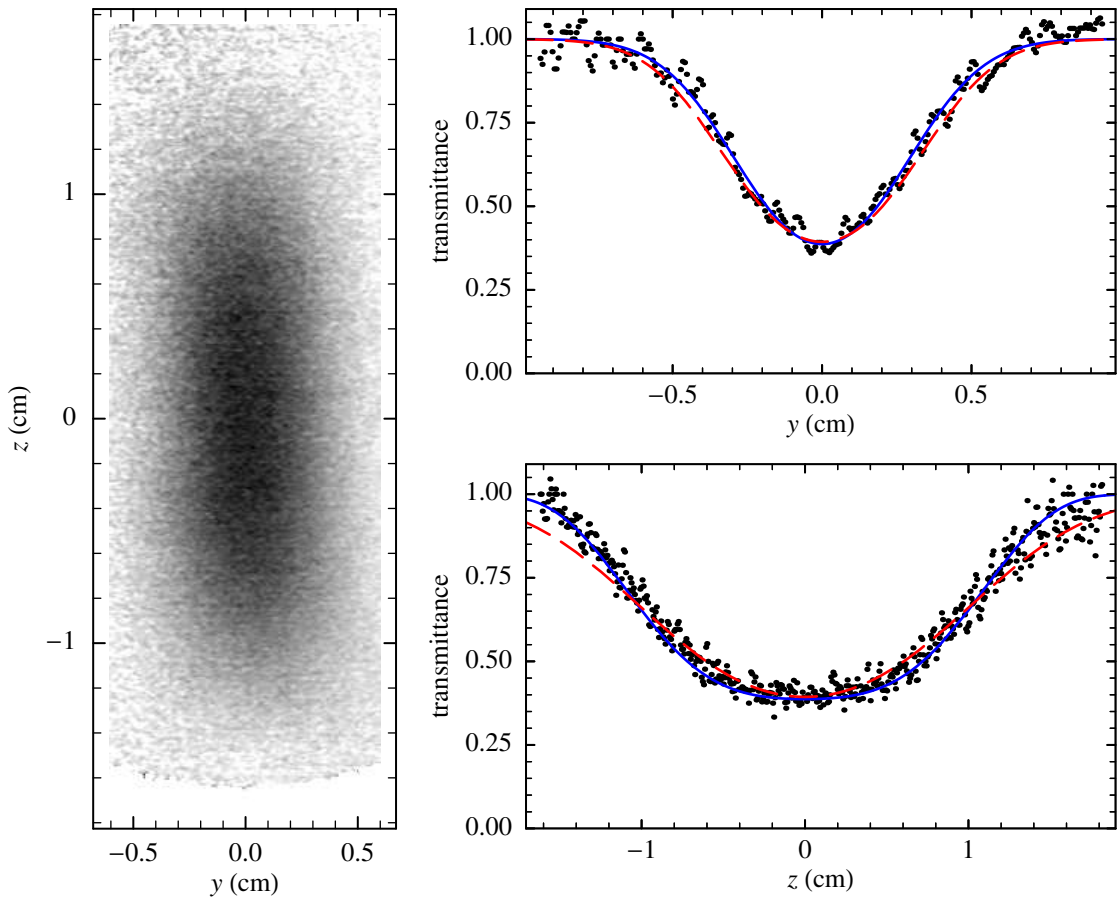


Figure 6.13. Absorption image taken 1 ms after switching off the compressed cloverleaf trap, with two cross sections through the centre. After 0.5 s compression and 1 s further trapping the cloud consists of 2.6×10^9 atoms. The fits in the cross sections assume either the predicted distribution (solid curves) or a Gaussian distribution (dashed curves).

not the approximation given by Eq. (6.34); the cloud is large enough to show deviations between the two methods for calculating the field, although the general shape does not change. A Gaussian fit including two extra parameters for the radii (dashed curves) describes the data less well, especially in the vertical wings. This is seen more clearly when comparing two-dimensional contour plots of the column density in the experiment and according to the two models mentioned above (Fig. 6.14). It may seem surprising that the cloud appears to be less Gaussian in the vertical direction, as the model predicts an exact Gaussian distribution along the z axis. In imaging, however, the radial dependence is important, because the vertical cross section shows the transmittance of all atoms in the xz plane. Usually a cloud becomes more Gaussian after expansion, particularly when the temperature is as high as 1.2 mK, but due to the large aspect ratio the cloud expands more horizontally. Figure 6.14 includes a contour plot of the column density in the trap, showing that the aspect ratio changes significantly before probing. At lower temperatures the cloud becomes smaller and a larger part is confined to the harmonic region of the trap. Therefore the density distribution approaches a Gaussian

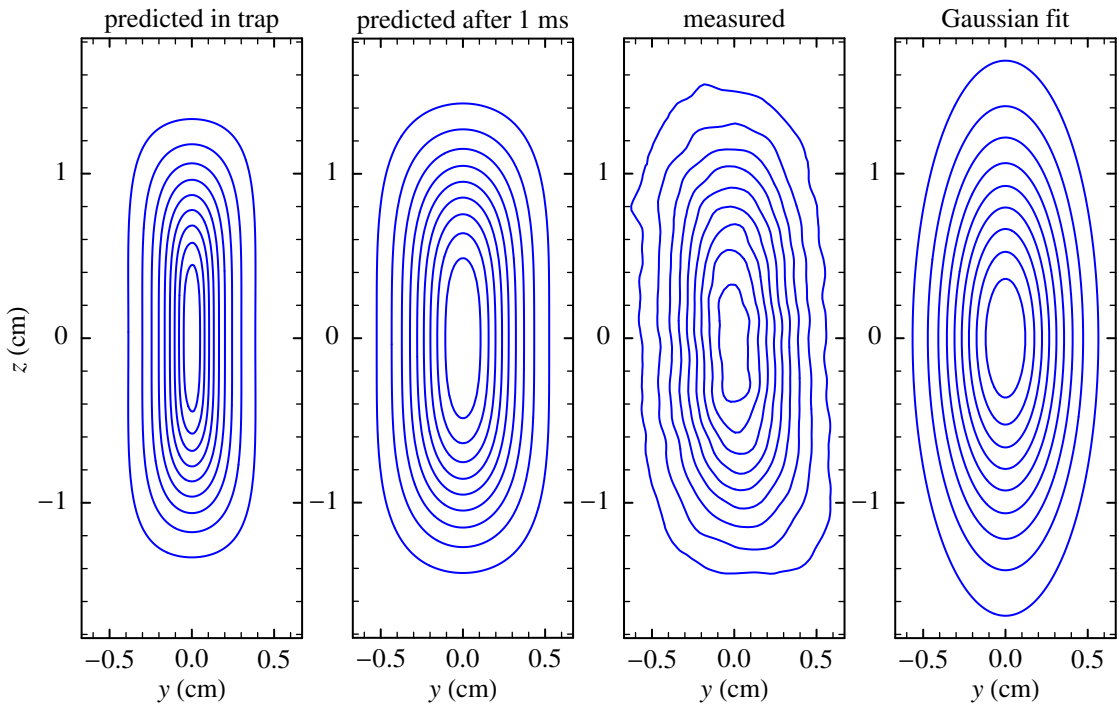


Figure 6.14. The density distribution in the compressed cloverleaf trap, integrated in the x direction. From left to right, the theoretical column density in the trap and after 1 ms expansion, the column density from the experimental absorption image (the negative logarithm of the transmittance), and a Gaussian fit to the experimental column density. Contours every 10% of the maximum column density.

shape during evaporative cooling. More details are given in the next chapter, where the size as a function of temperature is discussed.

7

Evaporative cooling

7.1 Introduction

A powerful method to increase the phase-space density of a dilute trapped gas is evaporative cooling: while the energy of the atoms is redistributed by elastic collisions, the atoms acquiring energies larger than the trap depth are expelled from the trap. This significantly reduces the average energy per trapped atom whereas only a relatively small number of atoms is lost. In forced evaporative cooling, the trap depth is gradually lowered, during which cooling increases the density and the elastic collision rate, accelerating evaporation.

First, an important parameter in this process is introduced: the scattering length. In the case of spin-polarized He* it can be determined theoretically, because the potential in which these atoms collide has been calculated. Then a model is given for evaporative cooling, taken from literature, but adapted for experiments with He* to incorporate an elastic scattering cross section depending on energy. Finally, the cooling experiments are described. The scattering length is fitted using the model and compared with the theoretical value.

7.2 Scattering length

The introduction and determination of the scattering length for two colliding atoms starts with the radial Schrödinger equation,

$$\left[-\frac{\hbar^2}{2\mu} \frac{d^2}{dr^2} + \frac{\hbar^2 l(l+1)}{2\mu r^2} + V(r) - E \right] u_l(r) = 0, \quad (7.1)$$

where $u_l(r)/r$ is the radial wave function for angular momentum quantum number l as a function of internuclear separation r , $V(r)$ is the interaction potential, total energy $E = \hbar^2 k^2 / 2\mu$, and μ is the reduced mass. To keep the wave function finite everywhere, $u_l(0) = 0$. The slope of u_l at the origin is determined by the normalization of the wave function. At large r the solution has the form [54]

$$u_l \sim \frac{1}{k} \left[A_l \sin \left(kr - l \frac{\pi}{2} \right) - B_l \cos \left(kr - l \frac{\pi}{2} \right) \right]. \quad (7.2)$$

The ratio of A_l and B_l can be defined by $B_l/A_l = -\tan \delta_l$, where δ_l is an energy-dependent phase shift. Then

$$u_l \sim \frac{A_l}{\cos \delta_l} \frac{1}{k} \sin(kr - l\frac{\pi}{2} + \delta_l) \quad (7.3)$$

and the phase shift is calculated by fitting this asymptotic form to the long-range part of the numerical solution of Eq. (7.1). Then the elastic scattering cross section [99]

$$\sigma(k) = \frac{4\pi}{k^2} \sum_{l=0}^{\infty} (2l+1) \sin^2 \delta_l \quad (7.4)$$

is also known.

For p waves ($l = 1$) the effective potential

$$\frac{\hbar^2}{2\mu} \frac{l(l+1)}{r^2} + V(r)$$

has a barrier with a height of 6.7×10^{-3} cm $^{-1}$ (10 mK) at $r = 78a_0$. At 1 mK the probability for an atom to have a larger relative energy than this barrier is only 2.5×10^{-4} . Therefore collisions in our experiments (between He* atoms in any atomic state) always occur in the s-wave regime ($l = 0$). For potentials $V(r) \propto r^{-s}$ at large r and with $s > 5$, the following expansion is valid:

$$k \cot \delta_0 = -\frac{1}{a} + \frac{1}{2} r_e k^2 + O(k^4), \quad (7.5)$$

where the constants are defined as scattering length a and effective range r_e ; the s-wave phase shift has the property $\lim_{k \rightarrow 0} \delta_0/k = -a$. Setting normalization constant $A_0 = -a^{-1} \cos \delta_0$, the radial eigenfunction becomes at long distances

$$u_0(r) \sim -\frac{\sin(kr + \delta_0)}{ka} \quad (7.6)$$

and when the energy becomes small $u_0(r) \sim 1 - r/a \equiv v_0(r)$. This means that to calculate the scattering length, all one has to do is solve numerically the equation

$$\left[-\frac{\hbar^2}{2\mu} \frac{d^2}{dr^2} + V(r) \right] u_0(r) = 0 \quad (7.7)$$

with $u_0(0) = 0$ and $u'_0(0)$ an arbitrary number, and fit a straight line to the long-range part of the solution. The extrapolated line will cross the r axis at $r = a$ (Fig. 7.1). The effective range of the potential is calculated with [28]

$$r_e = 2 \int_0^\infty [v_0^2(r) - u_0^2(r)] dr, \quad (7.8)$$

when $u_0(r)$ is normalized as described above, i.e. $v_0(0) = 1$. If Eq. (7.7) cannot be solved accurately for large separations, it is possible to correct a and r_e with a method given by Jamieson et al. [35].

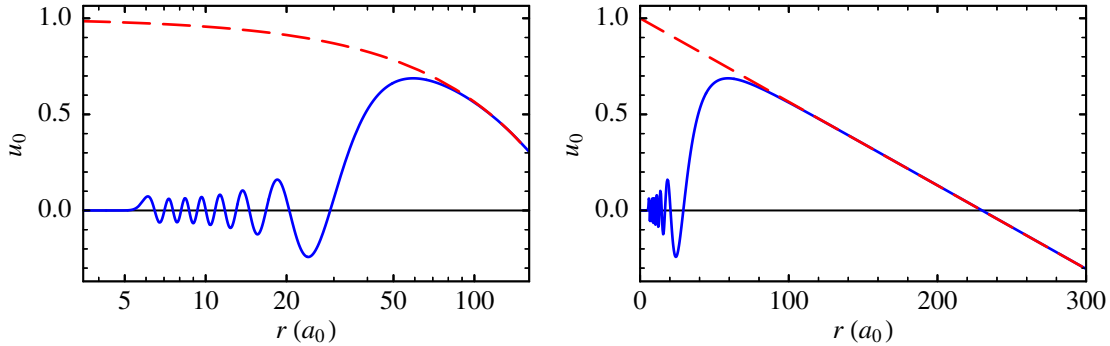


Figure 7.1. The scaled radial eigenfunction as a function of the internuclear separation (solid curves) and extrapolated linearly from the long-range part (dashed curves), for $E = 0$. A logarithmic as well as a linear scale is used to show the inner and outer part of the eigenfunction more clearly.

In the s-wave regime, the elastic scattering cross section, including a factor 2 for identical particles, is

$$\sigma = \frac{8\pi}{k^2} \sin^2 \delta_0 = \frac{8\pi}{k^2} \frac{1}{1 + \cot^2 \delta_0}. \quad (7.9)$$

For potentials with leading long-range term $-C_6/r^6$, the s-wave phase shift is given accurately by $k \cot \delta_0 = \frac{1}{2}r_e k^2 - 1/a$ if $k \ll (\hbar^2/\mu C_6)^{1/4}$ [21]. Then the cross section can be written as

$$\sigma \approx \frac{8\pi a^2}{k^2 a^2 + \left(\frac{1}{2}ar_e k^2 - 1\right)^2}. \quad (7.10)$$

In the limit of small k , $\sigma \rightarrow 8\pi a^2$. For larger k , the s-wave phase shift and the cross section can no longer be given in terms of the scattering length and effective range, and the numerical calculation should be used. In general there are a number of negative energy values for which the eigenfunction strongly vanishes at large distances. The states described by such eigenfunctions are said to be bound (see §5.1). In cases where the binding energy E_b of the highest state is small, the connection between the scattering length, effective range, and this binding energy is

$$\frac{1}{a} \approx k_b - \frac{1}{2}r_e k_b^2, \quad (7.11)$$

with $\hbar k_b = \sqrt{2\mu E_b}$.

The short-range part of the ${}^5\Sigma_g^+$ potential for collisions in spin-polarized He*, shown in Fig. 7.2, has been calculated in 1994 by Stärck and Meyer (SM) [83] and more accurately in 2002 by Gadéa, Leininger, and Dickinson (GLD) [24]. The depth of the potential has not changed much: the GLD dissociation energy is $(1045.1 \pm 1) \text{ cm}^{-1}$, 0.7 cm^{-1} smaller than the SM value. This is because the SM potential used a midpoint dummy basis set to improve the range near the equilibrium separation at $r = 7.34a_0$. However, the potential at larger separations is more important for the determination of the scattering length, and there the two potentials differ more. The largest difference is at $r = 11.3a_0$, where the GLD energy is 2.0 cm^{-1} higher. The least-bound level is very sensitive to

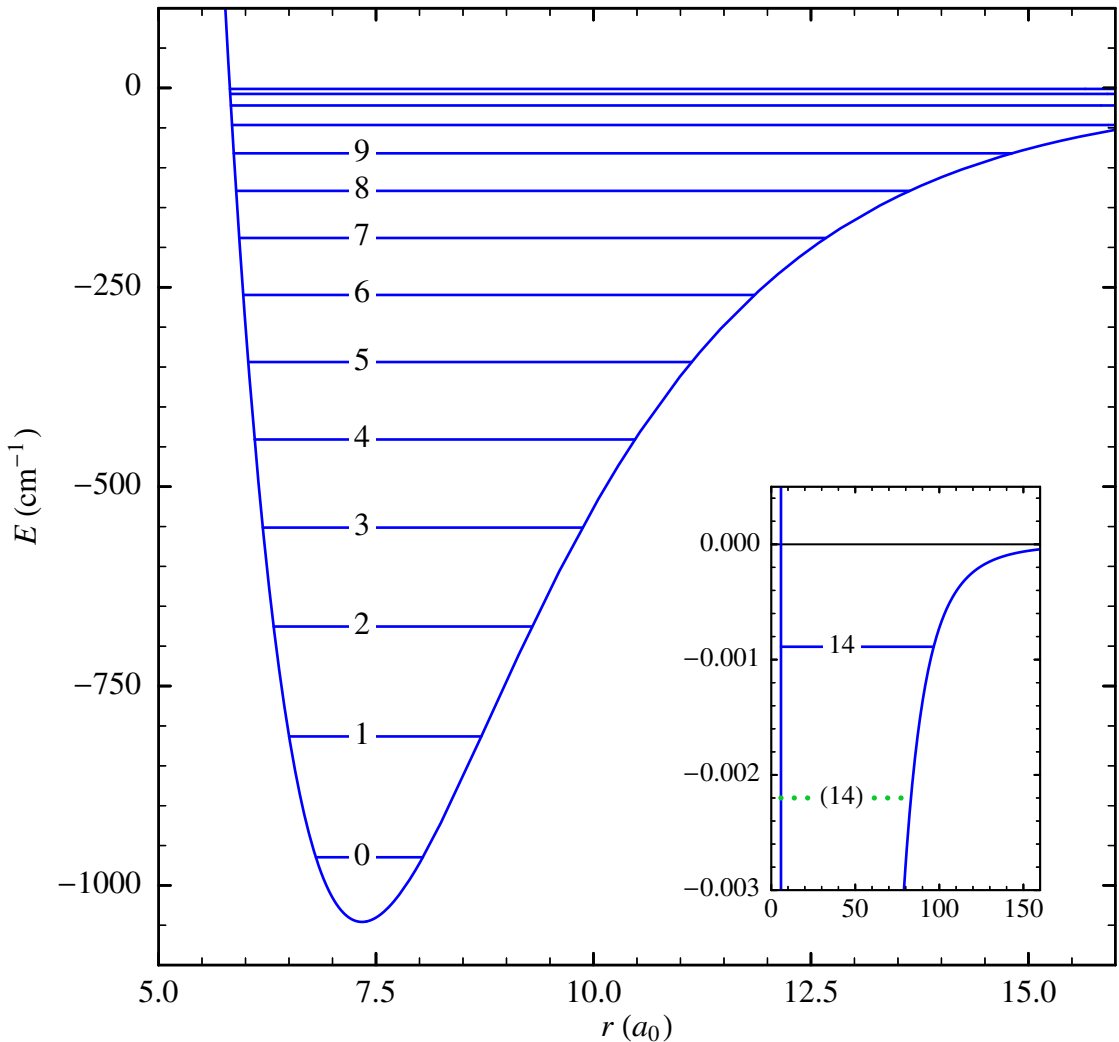


Figure 7.2. The interaction energy as a function of internuclear separation for the lowest ${}^5\Sigma_g^+$ state of He_2 , together with the 15 bound rotationless vibrational states. On this scale the difference between the calculations cannot be distinguished. The weakest bound state is shown in the inset, for the SM potential (dotted line) and the revised GLD potential (solid line).

these changes: in the SM potential it had a binding energy of $2.2 \times 10^{-3} \text{ cm}^{-1}$, in the GLD potential this reduced to $0.9 \times 10^{-3} \text{ cm}^{-1}$.

According to the SM potential, the scattering length a for ${}^4\text{He}$ is $+157a_0$. Gadéa et al. use a cubic spline through their *ab initio* points for small r and the potential function

$$V(r) = -\frac{C_6}{r^6} - \frac{C_8}{r^8} - \frac{C_{10}}{r^{10}} \quad (7.12)$$

for large r , with coefficients determined by Yan and Babb (YB): $C_6 = 3276.6800(3)$ a.u., $C_8 = 210\,566.55(6)$ a.u., and $C_{10} = 21\,786\,760(5)$ a.u. [105]. This reference also gives a version of Eq. (7.12) including retardation effects, but the influence on a is negligible. The way the two parts are connected does affect the value of the scattering length.

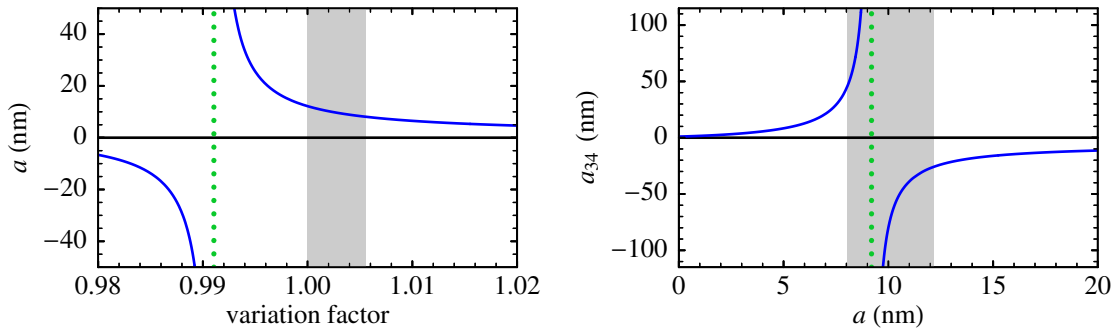


Figure 7.3. Left plot: the ${}^4\text{He} - {}^4\text{He}$ scattering length as a function of a factor with which the revised GLD potential is multiplied. Right plot: the ${}^3\text{He} - {}^4\text{He}$ scattering length versus the ${}^4\text{He} - {}^4\text{He}$ scattering length when varying the potential. Dotted lines mark the transition between negative and positive scattering length ranges. Shaded areas indicate probable ranges.

Initially the join was at $r = 20a_0$ with the C_{10} coefficient fitted for a smooth transition, resulting in $a = +291a_0$ [24]. However, C_{10} then became a factor of 5 smaller than the YB value. A better connection of the two parts was later made by using the original YB value while adapting the spline, using *ab initio* points at $r \leq 18a_0$ together with points at $r/a_0 = 19, 20, 21, 22, 23$ according to the long-range form [16]. Actually, for a smoother result, the energy values are multiplied by r^6 before the spline is applied. This spline, divided by r^6 , is used at $r \leq 23a_0$, and Eq. (7.12) at $r > 23a_0$. The revised GLD potential (used here) yields a scattering length of $+230a_0$. Table 7.1 summarizes the values of a , r_e , and E_b for both the SM and the revised GLD potential.

A lower bound for the scattering length was found by making the GLD potential deeper. The lowest values within the error bars of the *ab initio* points are used, while keeping the same long-range part and method of joining [16]. The result is $152 < a/a_0 < 230$, where the actual value is probably closer to the upper bound. Figure 7.3 shows the scattering length as a function of a scaling factor with which the short-range potential is multiplied, i.e. the relative error in all *ab initio* points is assumed to be equal.

The lower bound of $152a_0$ corresponds to a scaling factor of 1.0056. Using this scaled potential, the range of possible values for the effective range is $64 < r_e/a_0 < 74$.

The cross section is given by Eq. (7.10) when $k \ll 0.017a_0^{-1}$. To get an idea of the corresponding temperature range, the collision energy averaged over a thermal velocity distribution is used: $\langle \hbar^2 k^2/m \rangle = \frac{3}{2}k_B T$. Replacing k^2 by $\langle k^2 \rangle$, Eq. (7.10) is valid for

Table 7.1. Scattering length, effective range, and energy of least bound state according to the potentials mentioned in the main text.

potential	a/a_0	a/nm	r_e/a_0	r_e/nm	E_b/cm^{-1}	E_b/MHz
Stärck and Meyer [83]	157	8.3	65	3.4	2.2×10^{-3}	66
Gadéa et al. [16, 24]	230	12.2	74	3.9	0.9×10^{-3}	27

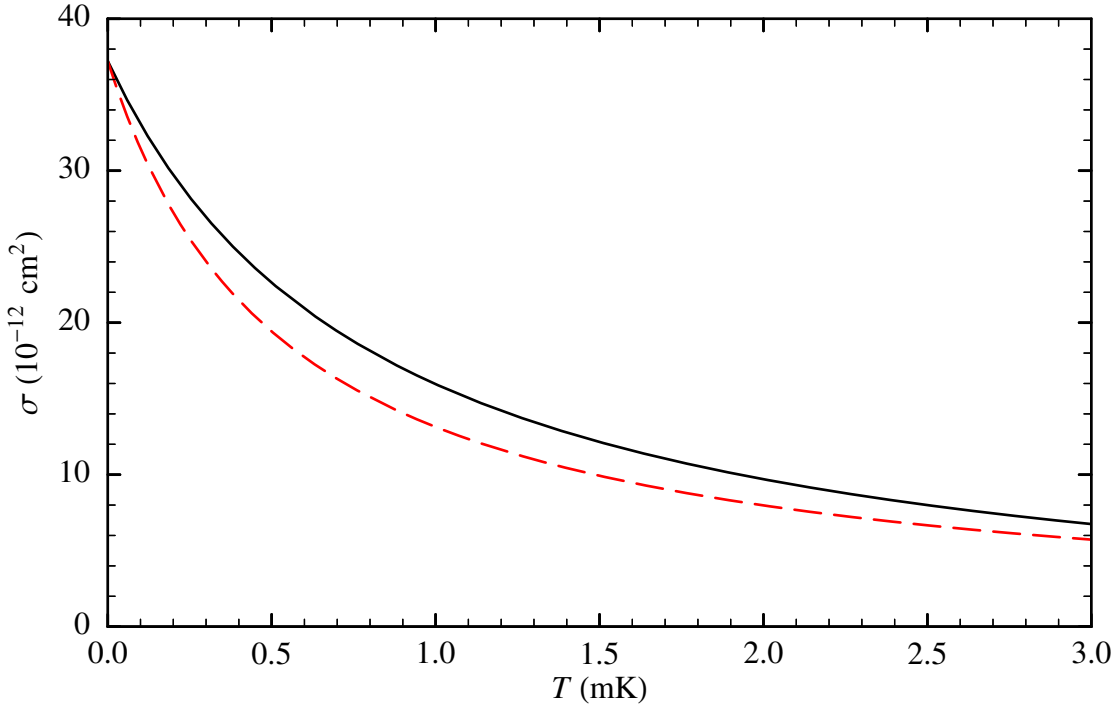


Figure 7.4. Cross section as a function of temperature according to Eq. (7.13) with $a = 230a_0$ and $r_e = 74a_0$ (solid curve) and setting $r_e = 0$ (dashed curve).

$T \ll 8$ mK and can be written as

$$\sigma(T) \approx \frac{8\pi a^2}{\frac{T}{T_0} + \left(\frac{r_e}{2a} \frac{T}{T_0} - 1\right)^2}, \quad (7.13)$$

with temperature $T_0 = 2\hbar^2/(3k_B ma^2)$ characterizing the range where the energy dependence of the cross section is important ($T_0 = 0.55$ mK when $a = 230a_0$). The solid curve in Fig. 7.4 shows $\sigma(T)$ according to this equation, although in the temperature range shown it is indistinguishable from the numerically calculated cross section. The effective range in this potential is small enough to be neglected (dashed curve), bearing in mind that the uncertainty in the scattering length is large. Then the cross section becomes $\sigma \approx 8\pi a^2/(k^2 a^2 + 1)$.

The scattering length a_{34} for elastic collisions between ${}^3\text{He}$ and ${}^4\text{He}$ can be calculated with the same potential used for ${}^4\text{He} - {}^4\text{He}$, with the corresponding reduced mass: in the Born-Oppenheimer approximation the potential does not depend on the particular isotope. Differences between mass-dependent adiabatic corrections can be neglected [16]. According to the most probable potential, there are 13 bound levels for ${}^3\text{He} - {}^4\text{He}$ scattering. However, with a scaling factor of only 1.0035 (when $a = 174a_0$), an extra bound level appears (Fig. 7.3). Therefore the scattering length has certainly a large magnitude and probably a negative sign: $a_{34} < -488a_0$ or $a_{34} > 865a_0$ [16]. The effective range is $88 < r_{e34}/a_0 < 108$ according to the scaled potential.

7.3 Theoretical description of cooling experiments

7.3.1 Trap depth defined by rf

The cloverleaf trap has a finite depth, defined by the saddle points. To vary the trap depth an rf field is applied to induce atomic transitions to an untrapped magnetic substate. The magnetic field $B(\mathbf{r})$ in which a He^* atom is resonant with the rf with frequency ω_{rf} is given by $\hbar\omega_{\text{rf}} = 2\mu_B B(\mathbf{r})$. If this field is lower than the trap barrier, it defines a new trap depth ε_t . If ε_t is kept constant (plain evaporation), evaporation peters out once the most energetic atoms have left the trap. If the trap is gradually made shallower (forced evaporation), by sweeping the frequency from a high to a low value, evaporation proceeds at an adjustable rate. Before giving more details, ε_t is defined when rf power is used. In the cloverleaf trap the rf is resonant at positions (ρ, z) for which

$$\hbar\omega_{\text{rf}} = \sqrt{\alpha^2\rho^2 + (2\mu_B B_0 + \beta z^2)^2}, \quad (7.14)$$

along the ρ axis at

$$\rho_{\text{res}} = \pm \sqrt{(\hbar\omega_{\text{rf}})^2 - (2\mu_B B_0)^2}/\alpha \quad (7.15)$$

and along the z axis at

$$z_{\text{res}} = \pm \sqrt{(\hbar\omega_{\text{rf}} - 2\mu_B B_0)/\beta}. \quad (7.16)$$

The potential energy at these points is different if gravitational sag is included:

$$U(\rho_{\text{res}}, 0) = \hbar\omega_{\text{rf}} - U_0, \quad (7.17)$$

$$U(0, z_{\text{res}}) = \hbar\omega_{\text{rf}} - U_0 + mgz_{\text{res}}, \quad (7.18)$$

where Eqs. (6.34) and (6.35) have been used. The trap depth is defined by the lowest of these potentials, at the bottom of the trap:

$$\varepsilon_t = \hbar\omega_{\text{rf}} - U_0 - mg|z_{\text{res}}|. \quad (7.19)$$

Gravity is only important when the trap depth is small; at high frequencies the trap depth is given by the difference of the rf energy and the minimum magnetic field energy, $\varepsilon_t \approx \hbar\omega_{\text{rf}} - 2\mu_B B_0$.

7.3.2 Evaporative cooling model

The behaviour of a cloud of atoms during an rf sweep is simulated with the model of Luiten et al. [52] and Pinkse et al. [67]. What follows is a continuation of the section on the density distribution in a trap with finite depth (§6.2.3). Again, equations from references are given without derivation. The version of the model described here assumes that every atom with an energy greater than the trap depth ε_t leaves the trap, so-called three-dimensional evaporation. Their trajectories should bring these atoms sufficiently

fast to the exit area of the trap (one of the saddle points or, when an rf field is applied, positions where the rf field is resonant with the magnetic field), so they are removed without first colliding with another atom. A third assumption is that collisions occur in the s-wave regime. The model as described in the references restricts the validity further to the low-temperature limit, where the elastic scattering cross section is energy independent. Here the theory will be adapted to include energy dependence.

At the start, N atoms at temperature T are contained in a trap with depth ε_t determined by the magnetic field configuration. After a time step of negligible duration the rf power is turned on: the rf frequency, the time dependence of which is here known beforehand, determines a new truncation energy ε_t . Then in small steps (for our situation 10 ms) the loss of atoms and energy due to inelastic collisions, trap changes (spilling), and evaporation is determined, as discussed below. The temperature is found by numerically solving the equation for the total energy of the trapped atoms, Eq. (6.49) with $\eta = \varepsilon_t/k_B T$. If experimentally an extra heating rate is found, for instance due to instability of the power supplies, this can be added separately. The calculation is stopped when either no atoms are left or when BEC is achieved. In the last case the phase-space density is $n_0 \Lambda^3 \geq g_{3/2}(1) \approx 2.6$, with polylogarithm function $g_n(z) = \sum_{k=1}^{\infty} z^k/k^n$.

The references describing the model do not give all loss rates in a suitable form, so first some intermediate equations are given and the energy density is derived. Trapped atoms have energy

$$\varepsilon(\mathbf{r}, \mathbf{p}) = U(\mathbf{r}) + p^2/2m. \quad (7.20)$$

The number of atoms with energy between ε and $\varepsilon + d\varepsilon$ is $\rho(\varepsilon)f(\varepsilon)d\varepsilon$, with phase-space distribution

$$f(\varepsilon) = n_0 \Lambda^3 \exp\left(-\frac{\varepsilon}{k_B T}\right) \quad (7.21)$$

and (in the cloverleaf trap) an energy density of states

$$\rho(\varepsilon) = A_{IQ}(\varepsilon^3 + 2U_0\varepsilon^2). \quad (7.22)$$

The phase-space distribution can be given as a function of \mathbf{r} and \mathbf{p} via Eq. (7.20) and is normalized so that the total number of trapped atoms is

$$N = \frac{1}{(2\pi\hbar)^3} \iint f(\mathbf{r}, \mathbf{p}) d^3r d^3p, \quad (7.23)$$

where the integration is done over the volume in phase space where $\varepsilon \leq \varepsilon_t$. The density is given by

$$\begin{aligned} n(\mathbf{r}) &= \frac{1}{(2\pi\hbar)^3} \int f(\mathbf{r}, \mathbf{p}) d^3p \\ &= \frac{n_0 \Lambda^3}{(2\pi\hbar)^3} \int_0^{\sqrt{2m(\varepsilon_t - U)}} \exp\left(-\frac{U + p^2/2m}{k_B T}\right) 4\pi p^2 dp \\ &= P\left(\frac{3}{2}, \kappa\right) n_0 \exp\left(-\frac{U}{k_B T}\right). \end{aligned} \quad (7.24)$$

Similarly, the energy density is

$$\begin{aligned} e(\mathbf{r}) &= \frac{1}{(2\pi\hbar)^3} \int \varepsilon(\mathbf{r}, \mathbf{p}) f(\mathbf{r}, \mathbf{p}) d^3 p \\ &= [\frac{3}{2}k_B T P(\frac{5}{2}, \kappa) + U P(\frac{3}{2}, \kappa)] n_0 \exp\left(-\frac{U}{k_B T}\right). \end{aligned} \quad (7.25)$$

Inelastic collisions

Three types of inelastic collisions are included: collisions between trapped atoms and background gas atoms, and two-body and three-body collisions among trapped atoms. Corresponding atom loss rates are

$$\dot{N}_{\text{bgr}} = -\frac{1}{\tau} \int n(\mathbf{r}) d^3 r = -N/\tau, \quad (7.26)$$

$$\dot{N}_{2b} = -G \int n^2(\mathbf{r}) d^3 r, \quad (7.27)$$

$$\dot{N}_{3b} = -L \int n^3(\mathbf{r}) d^3 r, \quad (7.28)$$

respectively; corresponding energy loss rates are

$$\dot{E}_{\text{bgr}} = -\frac{1}{\tau} \int e(\mathbf{r}) d^3 r = -E/\tau, \quad (7.29)$$

$$\dot{E}_{2b} = -G \int e(\mathbf{r}) n(\mathbf{r}) d^3 r, \quad (7.30)$$

$$\dot{E}_{3b} = -L \int e(\mathbf{r}) n^2(\mathbf{r}) d^3 r, \quad (7.31)$$

respectively. An overdot denotes a derivative with respect to time. The integrals have to be calculated numerically for every time step. The constant τ is the lifetime of the trap, determined experimentally.

For spin-polarized He* the two-body loss rate constant G has been determined theoretically. Fedichev et al. [19] have calculated that, for $T < 0.1$ mK, G depends only on magnetic field. The maximum value is 6×10^{-13} cm³/s at 750 G, but as the contribution of two-body collisions is more significant towards the end of the sweep when the cloud is concentrated at the centre, the value for $B \leq 10$ G, which is $G = 3 \times 10^{-14}$ cm³/s, can be used. Venturi et al. [95] later determined a value of 2×10^{-14} cm³/s with an uncertainty of a factor of 2 down to 1 μK, which is consistent with experiments [65, 77, 82].

For the three-body loss rate constant we use $L = 11.6\hbar a^4/m$, with scattering length a [20]. Later calculations have shown that the numerical factor has a value between 0 and 204 [6].[†] However, the most accurate experimental value for this factor in the case of spin-polarized He* is 9_{-6}^{+11} [77, 82].

[†]This is valid for any system with a large scattering length, in any magnetic field.

Spilling

When the trap shape or depth is changed, the eigenstates of the trapping potential with highest energies can become unbound. Atoms in these states are spilled from the trap. This process does not depend on collisions; when the potential is changed only by lowering the truncation energy ε_t , spilling does not alter parameters T and n_0 [67]. After instantaneous lowering of the trap depth from ε_t to ε'_t , the change in the number of atoms due to spilling is $\Delta N_\theta = - \int_{\varepsilon'_t}^{\varepsilon_t} \rho(\varepsilon) f(\varepsilon) d\varepsilon$ and the corresponding change in energy is $\Delta E_\theta = - \int_{\varepsilon'_t}^{\varepsilon_t} \varepsilon \rho(\varepsilon) f(\varepsilon) d\varepsilon$. With $n_0 \Lambda^3 = N/\zeta$ and Eq. (6.42), integration yields

$$\Delta N_\theta = -N \left[1 - \frac{3P(4, \eta') + 2\frac{U_0}{k_B T} P(3, \eta')}{3P(4, \eta) + 2\frac{U_0}{k_B T} P(3, \eta)} \right] = -N \left[1 - \frac{\zeta(\eta')}{\zeta(\eta)} \right], \quad (7.32)$$

$$\Delta E_\theta = -N k_B T \frac{12P(5, \eta) + 6\frac{U_0}{k_B T} P(4, \eta) - 12P(5, \eta') - 6\frac{U_0}{k_B T} P(4, \eta')}{3P(4, \eta) + 2\frac{U_0}{k_B T} P(3, \eta)}, \quad (7.33)$$

where $\eta' = \varepsilon'_t/k_B T \leq \eta$; the values of N and T are those before the step takes place.

Evaporation

After an elastic collision of two trapped atoms with energy $\varepsilon < \varepsilon_t$, one atom may have an energy $\varepsilon_t < \varepsilon < 2\varepsilon_t$ and leave the trap. After this thermal escape, or evaporation, the average energy per atom has decreased. The atom and energy loss rates due to evaporation are

$$\dot{N}_{ev} = -\sqrt{\frac{8k_B T}{\pi m}} n_0^2 \sigma e^{-\eta} V_{ev}, \quad (7.34)$$

$$\dot{E}_{ev} = \dot{N}_{ev} \left(\eta + \frac{W_{ev}}{V_{ev}} \right) k_B T, \quad (7.35)$$

with effective volumes for evaporation

$$V_{ev} = \Lambda^3 \zeta_\infty^0 \left\{ \left(1 + \frac{2}{3} \frac{U_0}{k_B T} \right) [\eta - \sum_{i=1}^4 P(i, \eta)] - P(5, \eta) \right\}, \quad (7.36)$$

$$W_{ev} = \Lambda^3 \zeta_\infty^0 \left\{ \left(1 + \frac{2}{3} \frac{U_0}{k_B T} \right) [\eta - \sum_{i=1}^5 P(i, \eta)] - P(6, \eta) \right\}, \quad (7.37)$$

and elastic scattering cross section σ . The model has been developed for an energy-independent cross section $\sigma = 8\pi a^2$. However, during evaporation of He* the temperature is too high for this assumption. Next, a simple approximation is presented that works at higher temperatures: Eqs. (7.34) and (7.35) with σ replaced by an effective cross section

$$\sigma_{eff} \approx 8\pi a^2 [\xi - \xi^2 e^\xi \Gamma(0, \xi)], \quad (7.38)$$

where $\xi = 3\hbar^2/(\varepsilon_t m a^2)$.

7.3.3 Incorporation of an energy-dependent cross section

In our experiment the temperature at the start of the rf sweep is about 1 mK, where the dependence of the elastic scattering cross section σ on the relative velocity of the colliding atoms cannot be neglected. For the derivation of atom loss rate \dot{N}_{ev} and energy loss rate \dot{E}_{ev} with an energy-dependent cross section σ , Luiten's derivation [51] is adapted. The elastic collision event rate Γ_c , which is the number of collisions per second occurring in the whole cloud, is also derived. The average collision rate per atom is $2\Gamma_c/N$. This rate is not needed in the sweep simulation, but it is an interesting quantity, related to the atom loss rate \dot{N}_{ev} , which is the collision event rate under the condition that afterwards one of the atoms has enough energy to leave the trap.

Collision event rate

First the collision rate in the case of an (untruncated) Boltzmann velocity distribution is examined. The two-body elastic collision event rate is

$$\Gamma_c = \int \frac{1}{2} n(\mathbf{r})^2 \langle \sigma v_r \rangle d^3 r, \quad (7.39)$$

where the rate coefficient $\langle \sigma v_r \rangle$ is the product of the cross section σ and the relative velocity v_r of the colliding pair of atoms, averaged over the thermal velocity distribution

$$\frac{1}{2\sqrt{\pi}} \left(\frac{m}{k_B T} \right)^{3/2} v_r^2 \exp\left(-\frac{mv_r^2}{4k_B T}\right) dv_r.$$

Assuming the rate coefficient does not depend on position due to the magnetic field, the collision event rate can be written as

$$\Gamma_c = \frac{N V_{2e}}{2 V_e} n_0 \langle \sigma v_r \rangle \quad (7.40)$$

and the average collision rate per atom as $(V_{2e}/V_e)n_0\langle \sigma v_r \rangle$, with

$$V_e = \int \frac{n(\mathbf{r})}{n_0} d^3 r = N/n_0, \quad (7.41)$$

$$V_{2e} = \int \left(\frac{n(\mathbf{r})}{n_0} \right)^2 d^3 r. \quad (7.42)$$

For a Gaussian shaped density distribution $V_{2e}/V_e = 1/\sqrt{8}$. The collision rate at position \mathbf{r} is $n(\mathbf{r})\langle \sigma v_r \rangle$. Using the approximation $\sigma = 8\pi a^2/(k^2 a^2 + 1)$ with thermal wave vector $k = mv_r/2\hbar$, we get

$$\langle \sigma v_r \rangle = 8\pi a^2 \langle v_r \rangle [\xi_c - \xi_c^2 e^{\xi_c} \Gamma(0, \xi_c)], \quad (7.43)$$

with $\xi_c = \hbar^2/(a^2 m k_B T)$ and average relative velocity $\langle v_r \rangle = 4\sqrt{k_B T/\pi m}$. Figure 7.5 shows the quantity in square brackets and the temperature dependence of the rate coefficient. In the low-temperature limit $\lim_{\xi \rightarrow \infty} [\xi - \xi^2 e^\xi \Gamma(0, \xi)] = 1$.

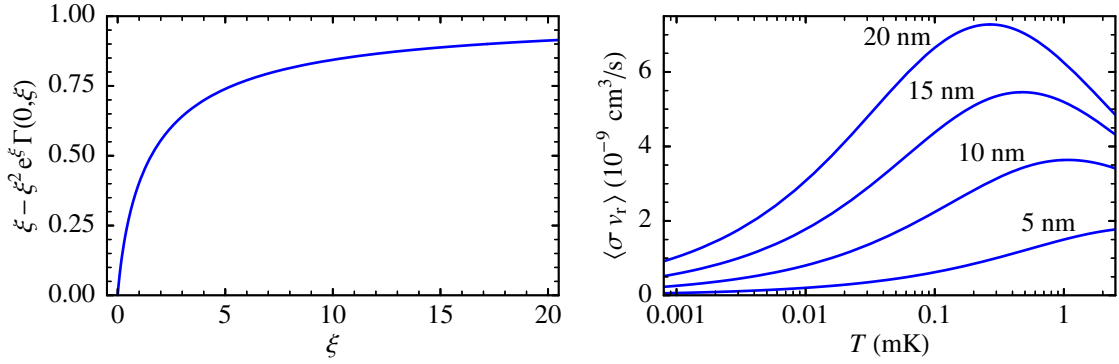


Figure 7.5. Factor $\langle\sigma v_r\rangle/(8\pi a^2 \langle v_r \rangle)$ as a function of ξ , and the rate coefficient as a function of temperature for He* assuming four different values for the scattering length a .

For a truncated Boltzmann distribution the collision event rate can be written as

$$\Gamma_c = \frac{1}{2m(2\pi\hbar)^6} \iiint \sigma(|\mathbf{p}_2 - \mathbf{p}_1|) |\mathbf{p}_2 - \mathbf{p}_1| f(\mathbf{r}, \mathbf{p}_1) f(\mathbf{r}, \mathbf{p}_2) d^3 p_1 d^3 p_2 d^3 r. \quad (7.44)$$

The integration is over all $(\mathbf{r}, \mathbf{p}_i)$ with $U(\mathbf{r}) + p_i^2/2m \leq \varepsilon_t$ for both $i = 1$ and $i = 2$. A more convenient coordinate system uses the average momentum $\mathbf{P} = (\mathbf{p}_1 + \mathbf{p}_2)/2$ and relative momentum $\mathbf{q} = \mathbf{p}_2 - \mathbf{p}_1$, with angle θ between \mathbf{P} and \mathbf{q} , and azimuthal angle φ . With the Jacobian $d^3 p_1 d^3 p_2 = d^3 P d^3 q$, we get

$$\Gamma_c = \frac{n_0^2 \Lambda^6}{2m(2\pi\hbar)^6} \int e^{-2U/k_B T} \int \sigma(q) q e^{-q^2/4mk_B T} \int e^{-P^2/mk_B T} d^3 P d^3 q d^3 r, \quad (7.45)$$

where the integration range is now given by

$$P^2 + \frac{q^2}{4} + Pq|\cos\theta| \leq 2m[\varepsilon_t - U(\mathbf{r})]. \quad (7.46)$$

To eliminate the angle dependence, the integrand is multiplied by the fraction F of colliding pairs at position \mathbf{r} for fixed P and q that are part of the truncated Boltzmann distribution:

$$F = \frac{1}{4\pi} \int_0^{2\pi} \int \sin\theta d\theta d\varphi, \quad (7.47)$$

where the integration over θ is restricted by condition (7.46). The result is

$$F = \frac{Q^2 - P^2 - q^2/4}{Pq}, \quad (7.48)$$

with $Q = \sqrt{2m[\varepsilon_t - U(\mathbf{r})]}$ the maximum momentum an atom can have at position \mathbf{r} without leaving the trap. This fraction has to be restricted to the physical range between 0 and 1. For $P > (Q^2 - q^2/4)^{1/2}$ at least one of the colliding atoms would have more momentum than is possible at position \mathbf{r} and the fraction is 0. For $0 < P < Q - q/2$ all

angles θ are possible and the fraction is 1. The integration over \mathbf{P} is therefore divided into two parts:

$$\Gamma_c = \frac{n_0^2 \Lambda^6}{2m(2\pi\hbar)^6} \int e^{-2U/k_B T} \int_0^{2Q} \sigma(q) q e^{-q^2/4mk_B T} \\ \times \left(\int_0^{Q-q/2} e^{-P^2/mk_B T} d^3 P + \int_{Q-q/2}^{\sqrt{Q^2-q^2/4}} F e^{-P^2/mk_B T} d^3 P \right) d^3 q d^3 r. \quad (7.49)$$

For a trapping potential

$$U(\mathbf{r}) = \sqrt{\alpha^2(x^2 + y^2) + (U_0 + \beta z^2)^2} - U_0 \quad (7.50)$$

the integration over position can be made one dimensional [52] using

$$\int \mathcal{F}[U(\mathbf{r})] d^3 r = \frac{4\pi}{\alpha^2 \sqrt{\beta}} \int_0^{\varepsilon_t} \sqrt{U(U + U_0)} \mathcal{F}(U) dU. \quad (7.51)$$

Introducing the scaled variables $\lambda = q/\sqrt{mk_B T}$ and $\kappa = (\varepsilon_t - U)/k_B T$ and the scaled constant $\eta = \varepsilon_t/k_B T$, the collision event rate after integration over \mathbf{P} becomes

$$\Gamma_c = \frac{n_0^2 e^{-2\eta}}{\alpha^2 \sqrt{\beta m}} (k_B T)^3 \int_0^\eta \int_0^{\sqrt{8\kappa}} \sigma(\lambda) \sqrt{\eta - \kappa} \left(\eta - \kappa + \frac{U_0}{k_B T} \right) \lambda^2 \\ \times \left[2 - 2 \exp\left(\sqrt{2\kappa}\lambda - \frac{1}{2}\lambda^2\right) + \sqrt{\pi} \lambda \exp\left(2\kappa - \frac{1}{4}\lambda^2\right) \operatorname{erf}\left(\sqrt{2\kappa} - \frac{1}{2}\lambda\right) \right] d\lambda d\kappa. \quad (7.52)$$

For an energy-dependent cross section σ with $\hbar k = q/2$ this equation has to be integrated numerically. For a constant cross section, after integration over λ , the expression for Γ_c contains terms

$$\int_0^\eta (\eta - \kappa)^x e^{l\kappa} \operatorname{erfc} \sqrt{l\kappa} d\kappa = \Gamma(x+1) e^{l\eta} [P(x+1, l\eta) - P(x + \frac{3}{2}, l\eta)] / l^{x+1} \quad (7.53)$$

and

$$\int_0^\eta (\eta - \kappa)^x \kappa e^{\kappa} \operatorname{erfc} \sqrt{\kappa} d\kappa = \Gamma(x+1) e^\eta \{ (\eta+1) [P(x+2, \eta) - P(x + \frac{7}{2}, \eta)] \\ - \frac{3}{2} P(x + \frac{5}{2}, \eta) - (x+2) P(x+3, \eta) + (x + \frac{7}{2}) P(x + \frac{9}{2}, \eta) \}, \quad (7.54)$$

with complementary error function $\operatorname{erfc}(z) = 1 - \operatorname{erf}(z)$, which has the property [2]

$$e^\kappa \operatorname{erfc} \sqrt{\kappa} = \frac{\sqrt{\kappa}}{\pi} \int_0^\infty \frac{e^{-t}}{\sqrt{t(t+\kappa)}} dt. \quad (7.55)$$

The collision event rate for constant σ becomes

$$\Gamma_c = \frac{1}{2\sqrt{2}} n_0^2 \sigma \sqrt{\frac{k_B T}{\pi m}} \Lambda^3 \zeta_\infty \left\{ 1 + \frac{4}{3} \frac{U_0}{k_B T} - 8 e^{-\eta} \left(\eta - 1 + \frac{2}{3} \frac{U_0}{k_B T} \eta \right) \right. \\ \left. + \frac{1}{3} e^{-2\eta} \left[\eta^4 + 4\eta^3 + 6\eta^2 - 6\eta - 27 + \frac{4}{3} \frac{U_0}{k_B T} (2\eta^3 + 6\eta^2 + 6\eta - 3) \right] \right\}. \quad (7.56)$$

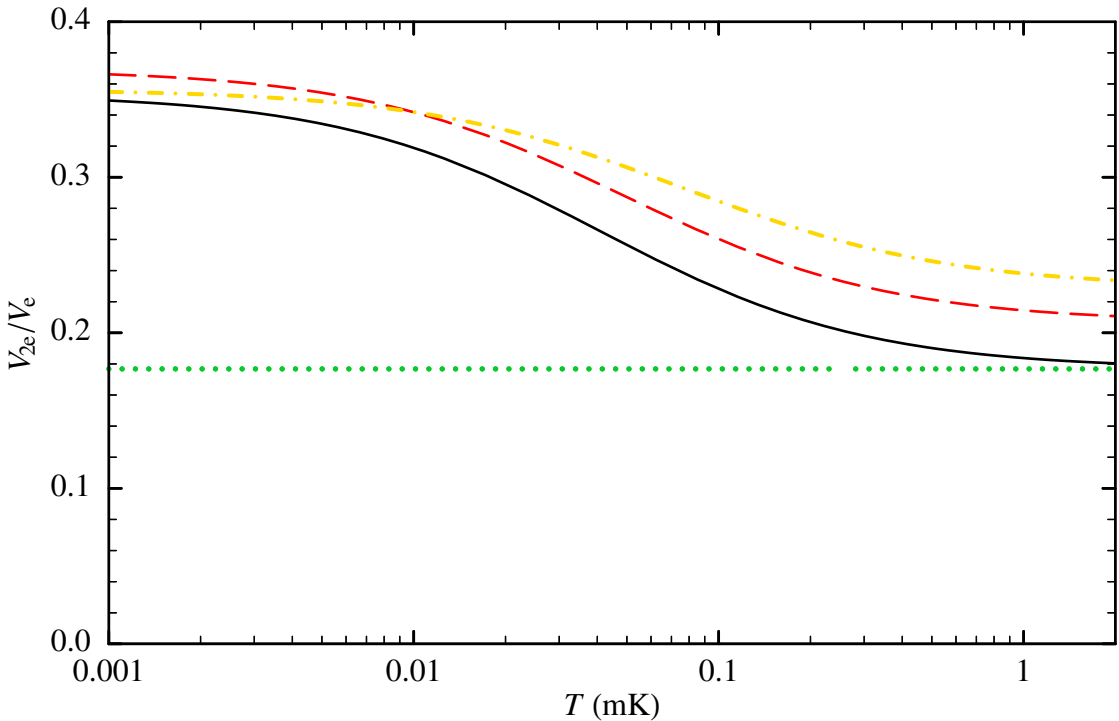


Figure 7.6. Volume ratio V_{2e}/V_e as a function of temperature, for $\eta = \infty$ (solid curve), $\eta = 5$ (dashed curve), and $\eta = 2.5$ (dot-dashed curve). A curve for $\eta = 10$ would almost coincide with the curve for $\eta = \infty$. The dotted line is valid for $U_0 = 0$ and $\eta = \infty$.

When σ is energy dependent, Γ_c needs to be calculated numerically. However, in the limit of large η the velocity distribution becomes thermal, and Eq. (7.52) is expected to produce the same result as Eq. (7.40). For common values of η and a cross section given by $\sigma = 8\pi a^2/(k^2 a^2 + 1)$, Eqs. (7.40) and (7.43) can be used as an approximation: comparing exact numerical calculations of $\Gamma_c / (\frac{N}{2} \frac{V_{2e}}{V_e} n_0)$ with the rate coefficient as given by Eq. (7.43), at $\eta = 10$ the deviations are smaller than 0.1% and at $\eta = 5$ smaller than 6% (for $m < 100$ u, $|a| < 100$ nm, $U_0/\mu_B < 100$ G, $T < 5$ mK). The ratio V_{2e}/V_e depends on $U_0/k_B T$ and η . For $U_0 = 0$ and infinite η , $V_{2e}/V_e = 1/\sqrt{32}$. Figure 7.6 shows this ratio as a function of temperature in our situation ($B_0 = 0.46$ G) for several values of η .

Evaporation rates

The collision event rate Γ_c was given by Eq. (7.45), with constraints on the integration range incorporated by a factor F in the integrand. The atom loss rate \dot{N}_{ev} is given by the same equation, but with an extra factor for the fraction of collisions for which afterwards one of the atoms has enough energy to leave the trap. Since P and q are the same before and after collisions and all scattering angles θ' have equal probability in the s-wave regime, this factor is $(1 - F)$. In the case of the collision event rate, the integration over P had to be divided into two parts [see Eq. (7.49)]. Here only one part is left, as the integrand including $F(1 - F)$ with $F = 1$ is zero. The atom loss rate due to evaporation

becomes

$$\begin{aligned} \dot{N}_{\text{ev}} = & -\frac{4\pi n_0^2 \Lambda^6}{\alpha^2 \sqrt{\beta} 2m(2\pi\hbar)^6} \int_0^{\varepsilon_t} \sqrt{U}(U + U_0) e^{-2U/k_B T} \int_0^{2Q} \sigma(q) 4\pi q^3 e^{-q^2/4mk_B T} \\ & \times \int_{Q-q/2}^{\sqrt{Q^2-q^2/4}} F(1-F) 4\pi P^2 e^{-P^2/mk_B T} dP dq dU, \end{aligned} \quad (7.57)$$

and after integration over P ,

$$\begin{aligned} \dot{N}_{\text{ev}} = & -\frac{n_0^2 e^{-2\eta}}{8\alpha^2 \sqrt{\beta m}} (k_B T)^3 \int_0^\eta \int_0^{\sqrt{8\kappa}} \sigma(\lambda) \sqrt{\eta-\kappa} \left(\eta - \kappa + \frac{U_0}{k_B T} \right) \lambda \\ & \times \left\{ -2[\lambda(2+\lambda^2-8\kappa) + 2\sqrt{2\kappa}(6+\lambda^2-8\kappa)] \exp(\sqrt{2\kappa}\lambda - \frac{1}{2}\lambda^2) \right. \\ & + 2[8\lambda + \sqrt{8\kappa-\lambda^2}(6+\lambda^2-8\kappa)] - \sqrt{\pi}[12+4\lambda^2+\lambda^4-16(2+\lambda^2)\kappa+64\kappa^2] \\ & \left. \times \exp(2\kappa - \frac{1}{4}\lambda^2) [\operatorname{erf}(\sqrt{2\kappa - \frac{1}{4}\lambda^2}) - \operatorname{erf}(\sqrt{2\kappa} - \frac{1}{2}\lambda)] \right\} d\lambda d\kappa. \end{aligned} \quad (7.58)$$

For the energy loss rate \dot{E}_{ev} there is an extra factor in the integrand for the energy of the lost atom,

$$\varepsilon_4 = U + \frac{1}{2m} \left(P^2 + \frac{q^2}{4} + Pq|\cos\theta'|\right). \quad (7.59)$$

This means \dot{E}_{ev} is given by Eq. (7.57) with the factor $(1-F)$ replaced by

$$G = \frac{1}{4\pi} \int_0^{2\pi} \int \varepsilon_4 \sin\theta' d\theta' d\varphi' \quad (7.60)$$

where the integration range is given by $\varepsilon_4 > \varepsilon_t$. After integration over θ' and φ' we get

$$G = (1-F) \left[\varepsilon_t + \frac{(2P+q)^2 - 4Q^2}{16m} \right]. \quad (7.61)$$

The energy loss rate after integration over P becomes

$$\begin{aligned} \dot{E}_{\text{ev}} = & \varepsilon_t \dot{N}_{\text{ev}} - \frac{n_0^2 e^{-2\eta}}{128\alpha^2 \sqrt{\beta m}} (k_B T)^4 \int_0^\eta \int_0^{\sqrt{8\kappa}} \sigma(\lambda) \sqrt{\eta-\kappa} \left(\eta - \kappa + \frac{U_0}{k_B T} \right) \lambda \\ & \times \left\{ 256\lambda + 2\sqrt{8\kappa-\lambda^2} [60 + \lambda^4 - 16\lambda^2(\kappa-2) + 64\kappa(\kappa-1)] \right. \\ & - 2\{\lambda^5 + 2\lambda^4\sqrt{2\kappa} - 4\lambda^3(4\kappa-3) - 16\lambda^2\sqrt{2\kappa}(2\kappa-1) \\ & + \lambda[68 + 32\kappa(2\kappa-3)] + 8\sqrt{2\kappa}[15 + 16\kappa(\kappa-1)]\} \exp(\sqrt{2\kappa}\lambda - \frac{1}{2}\lambda^2) \\ & - \sqrt{\pi}(\lambda^6 - 2\lambda^4(12\kappa-7) + 4\lambda^2[21 + 8\kappa(6\kappa-5)] + 8\{15 - 4\kappa[9 + 4\kappa(4\kappa-3)]\}) \\ & \left. \times \exp(2\kappa - \frac{1}{4}\lambda^2) [\operatorname{erf}(\sqrt{2\kappa - \frac{1}{4}\lambda^2}) - \operatorname{erf}(\sqrt{2\kappa} - \frac{1}{2}\lambda)] \right\} d\lambda d\kappa. \end{aligned} \quad (7.62)$$

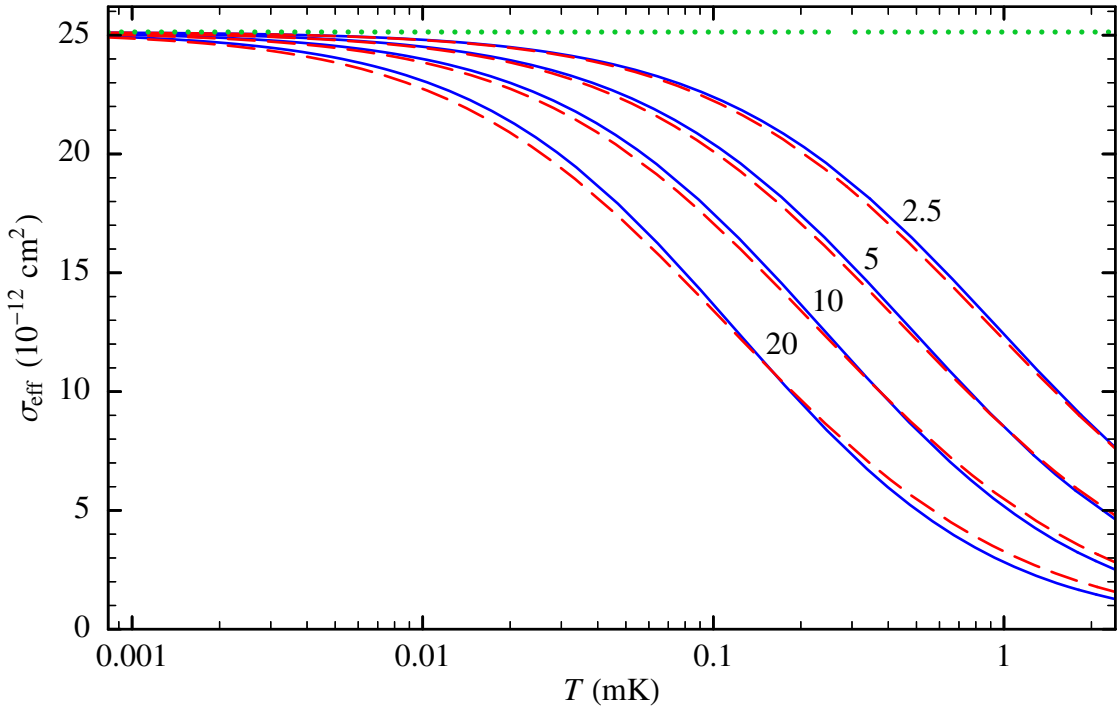


Figure 7.7. Effective cross section as a function of temperature for $m = 4 \text{ u}$, $a = 10 \text{ nm}$, $B_0 = 0.46 \text{ G}$, and four values of η (solid curves), together with the approximation (dashed curves). The dotted line is the low-temperature limit.

When σ is a constant, Eqs. (7.58) and (7.62) reduce after integration to Eqs. (7.34) and (7.35), respectively. When σ is energy dependent, the expressions for \dot{N}_{ev} and \dot{E}_{ev} have to be integrated numerically. However, when the cross section can be given in terms of the scattering length and (optionally) the effective range, approximations exist. First an effective cross section σ_{eff} is introduced, which will give the correct value of \dot{N}_{ev} if $\sigma = \sigma_{\text{eff}}$ in Eq. (7.34). When the cross section is given by $\sigma = 8\pi a^2/(k^2 a^2 + 1)$, the effective cross section can be approximated by a variation of Eq. (7.43):

$$\sigma_{\text{eff}} \approx 8\pi a^2 [\xi_{\text{ev}} - \xi_{\text{ev}}^2 e^{\xi_{\text{ev}}} \Gamma(0, \xi_{\text{ev}})], \quad (7.63)$$

where

$$\xi_{\text{ev}} = \frac{3}{\eta} \frac{\hbar^2}{m k_B T a^2} = \frac{3\hbar^2}{\varepsilon_t m a^2}. \quad (7.64)$$

In this approximation, found by trial and error, the effective cross section depends on temperature only via the trap depth. Figure 7.7 shows σ_{eff} and its approximation as a function of temperature in our situation for $a = 10 \text{ nm}$ and several values of η . Clearly, $\sigma_{\text{eff}}(T)$ does not approach an asymptote at high η . In general ($m < 100 \text{ u}$, $|a| < 100 \text{ nm}$, $U_0/\mu_B < 100 \text{ G}$, $T < 5 \text{ mK}$, $2 < \eta < 25$) the absolute difference between σ_{eff} and its approximation is less than 3% of the low-temperature limit $8\pi a^2$, shown as a dotted line in Fig. 7.7. The energy loss rate can still be calculated with Eq. (7.35), even though the effective volumes are not correct: the relative error in $\dot{E}_{\text{ev}}/\dot{N}_{\text{ev}}$ is less than 2%.

When the cross section is given by Eq. (7.10), the following approximation can be

used:

$$\sigma_{\text{eff}} \approx \frac{8\pi a^2}{\frac{3/2}{\xi_{\text{ev}}} + \left(\frac{r_e}{2a} \frac{3/2}{\xi_{\text{ev}}} - 1 \right)^2}, \quad (7.65)$$

which is Eq. (7.13) with T_0 multiplied by $3/\eta$. For the same parameter ranges as the previous approximation and $0 < r_e/a < 1$, the absolute difference between this approximation and the exact σ_{eff} is at most 9% of the low-temperature limit, while the relative error in $\dot{E}_{\text{ev}}/\dot{N}_{\text{ev}}$ is less than 7%. Here Eq. (7.63) will be used, because for spin-polarized He* the effective range can be neglected in the determination of the scattering length (see §7.2).

7.4 Rf experiments

7.4.1 Spilling

In order to check whether the rf system works at all frequencies, the rf is turned on at full power (16 W) for 0.5 s at a fixed frequency, causing spilling. Next, to be able to interpret TOF signals correctly, we wait for 1 s for thermalization, before switching off the trap. The fraction of atoms remaining in the trap as a function of frequency is given in Fig. 7.8. Below 40 MHz 0.5 s rf time is not long enough to remove all hot atoms, so for those points the rf is on for 5 s. Below 6.4 MHz the rf energy is smaller than U_0 , and atoms are no longer removed. According to Eq. (7.32) the fraction of atoms left in the

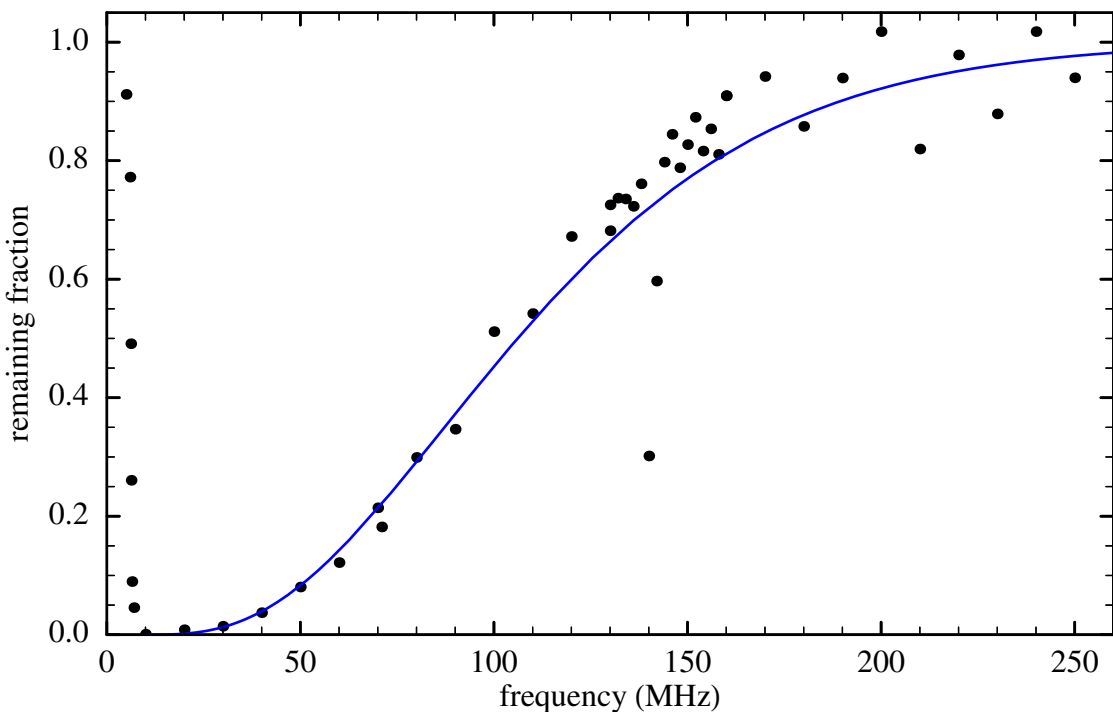


Figure 7.8. Remaining fraction of atoms as a function of rf frequency, together with a theoretical prediction.

trap when going instantaneously from η to η' is $\zeta(\eta')/\xi(\eta)$. In the cloverleaf trap, using Eq. (6.42), this is a fraction

$$\frac{3 P(4, \eta') + 2 \frac{U_0}{k_B T} P(3, \eta')}{3 P(4, \eta) + 2 \frac{U_0}{k_B T} P(3, \eta)}.$$

In this experiment the magnetic field at the saddle points corresponds to an rf frequency of 143 MHz, but the figure shows that atoms are also removed when the frequency is higher. Atoms probably do not come close enough to the saddle points to be removed efficiently (see Fig. 1.17). Hence for the theoretical curve in Fig. 7.8 a thermal distribution is assumed before the rf is turned on ($\eta = \infty$); there are no fit parameters.

The rf power is large enough to affect power supply switches: the dip at 140 MHz is caused by a malfunctioning of the power supply for the slower compensation coils. By moving this supply half a meter away and putting iron coils around the current leads, the dip disappeared. We measured the same curve as a function of rf power, and down to 5 W the remaining fraction does not change much. We usually work at 10 W, so the rf transition is still saturated while there is less chance of resonance problems.

7.4.2 Plain evaporation

Plain evaporation, losing atoms at constant ε_t , can be examined by keeping the rf power on for a longer period than 0.5 s. Figure 7.9 shows the temperature and number of atoms as a function of the rf time, with rf frequencies of 125 MHz and 100 MHz. To compensate for the effect of trap decay (here $\tau = 10$ s), we wait before turning on the rf so the total period is 11 s. The trap is switched off 0.5 s after the rf power is turned off.

In the case of plain evaporation, i.e. when the trap shape and depth are kept constant, there is no spilling and the change in temperature \dot{T} can be calculated directly with

$$C\dot{T} = \dot{E}_{ev} - E\dot{N}_{ev}/N, \quad (7.66)$$

with heat capacity $C = (\partial E / \partial T)_{N, \varepsilon_t, U_0}$ [67]. For the cloverleaf trap the heat capacity can be written as

$$C = 12Nk_B \left\{ 15P(4, \eta)P(6, \eta) - 12P(5, \eta)^2 + \frac{U_0}{k_B T} [10P(3, \eta)P(6, \eta) - 6P(4, \eta)P(5, \eta)] \right. \\ \left. + \left(\frac{U_0}{k_B T} \right)^2 [4P(3, \eta)P(5, \eta) - 3P(4, \eta)^2] \right\} / \left\{ 3P(4, \eta) + 2 \frac{U_0}{k_B T} P(3, \eta) \right\}^2. \quad (7.67)$$

Neglecting two- and three-body losses, the change in number of atoms is $\dot{N} = \dot{N}_{ev} + \dot{N}_{bgr}$. The experimental temperature decrease is best fitted with a small scattering length, $a = 2.8$ nm (solid curves), which according to Eq. (7.43) leads to a rate coefficient of 6×10^{-10} cm³/s. However, the number of atoms is better described by a higher value; dashed curves are drawn for 10 nm, when the rate coefficient is 4×10^{-9} cm³/s. Instead of measuring a decreasing number of atoms during rf, Browaeys et al. [11] examine the increasing number of atoms occupying the truncated part of the energy distribution after the rf power is turned off. At a similar density and temperature, they

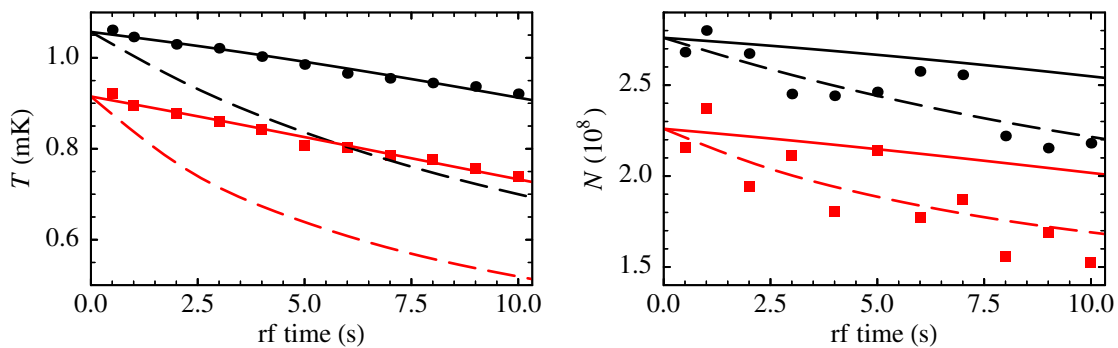


Figure 7.9. Temperature and number of atoms as a function of the time rf power is on, for 125 MHz (dots) and 100 MHz (squares). Curves are theoretical calculations for $a = 2.8$ nm (solid curves) and 10 nm (dashed curves).

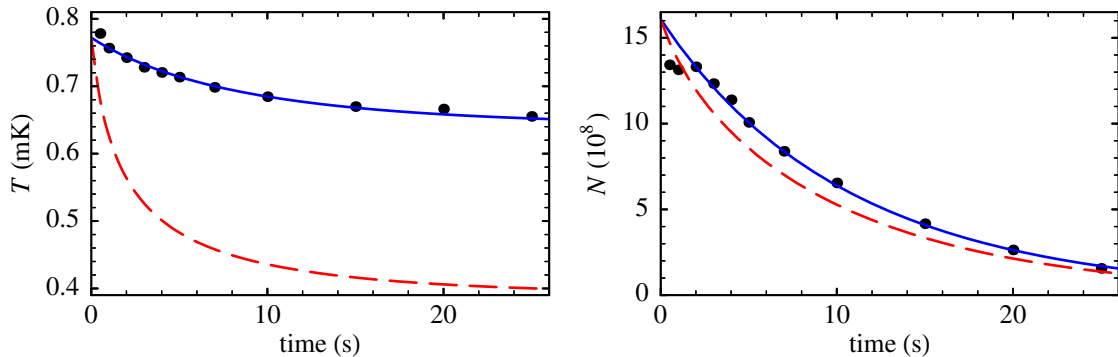


Figure 7.10. Temperature and number of atoms as a function of the time the cloverleaf trap is on. Solid curves are fits assuming $a = 2$ nm, with the lifetime and starting values for T and N as parameters. Dashed curves are calculations with the same parameter values and $a = 10$ nm.

find a rate coefficient of $5 \times 10^{-9} \text{ cm}^3/\text{s}$ to within a factor of 3. Maybe the temperature decrease is smaller than expected, because the collision rate is only between 2 and 4 per second (averaged over the whole cloud, with $a = 10$ nm), while the model assumes fast thermalization.

Plain evaporation can also be seen without rf, if the trap depth is low compared to the temperature. This is the case in the uncompressed trap, where initially $\eta = 4.5$. Figure 7.10 shows the temperature and number of atoms as a function of time. For the solid curves the scattering length is taken to be 2 nm, again very small. The decay time due to background collisions is 11.8 s and evaporation shortens it to 11.0 s.

The trap depth is assumed to be defined by the lowest saddle points in the potential, but if the effective depth is larger, as in the case of the spilling experiment, evaporation is more difficult and the scattering length needs to be made larger to explain the data. If for instance the trap is 60% deeper, we have $a = 10$ nm. However, this is a large increase and the collision rate is the same as in the previous experiment, so the conditions for the model are probably not met sufficiently in these situations.

7.4.3 Potential minimum

The field minimum at the centre must be known accurately in order to use the theoretical model effectively. It depends on the currents through the two sets of axial coils. In practice the maximum current is sent through the large coils and the current through the small coils is lowered (see §1.8.2). This last current is first set coarsely by choosing the resistance of the bypasses of the small coils, then fine-tuned by adding current from an additional small power supply. Measuring the central field directly with a Hall probe or flux-gate probe is not as accurate as using rf. The spilling experiment described earlier (Fig. 7.8) is an example: the frequency where all atoms are thrown out of the trap corresponds to the field minimum. However, it is difficult to remove all hot atoms with a fixed frequency. It is better to use an rf sweep ending at a particular low frequency, during which evaporation brings down the temperature. The end frequency is kept for several seconds before the rf is turned off. Instead of lowering the end frequency in a given trap, the end frequency is kept fixed and the field minimum is raised by increasing the current. For three end frequencies, Fig. 7.11 shows the number of atoms still reaching the detector after such sweeps as a function of current. The theoretical dependence is complicated, but a linear response seems a good approximation. Extrapolation of each series gives the current at which the central field corresponds to the known end frequency. By linear interpolation of these three combinations the central field at any

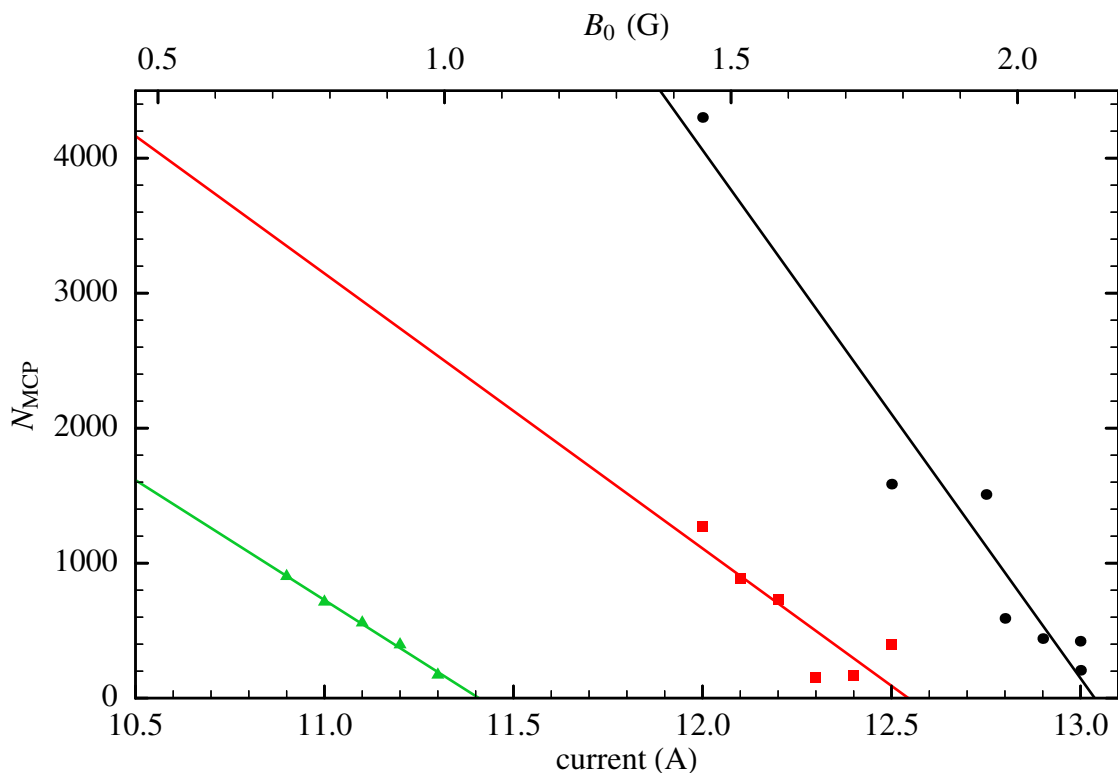


Figure 7.11. Detected number of atoms as a function of current of the additional power supply, after sweeps to 6 MHz (dots), 5 MHz (squares), and 3 MHz (triangles). Lines are linear fits to each set of points. The top axis indicates the calculated B_0 .

current, shown on the top axis, is determined. Actually, because the MCP detector is not under the centre of the trap, no atoms are detected already when the trap depth is smaller than 46 mG (6 μ K), leading to a small overestimation of B_0 (see §2.2.3).

The temperature in these measurements is too low for an accurate determination of the detected fraction, so instead of the number of atoms in the trap the number reaching the detector is plotted. The arrival times related to the TOF peak are among the latest we ever found. Two of them, corresponding to the points in Fig. 7.11 at 13.0 A, are shown at the bottom of Fig. 2.6. As the expected signal deviates significantly from what is actually detected, a Gaussian fit is used for N_{MCP} in Fig. 7.11.

According to measurements with a current probe, 17% of the current goes through the bypasses. With the knowledge from the rf measurements above this value is corrected to 20%, which will include corrections for the exact shape and position of the coils. In this and later experiments the trap is on for about 20 s. Although the coils and bypass resistors are connected to the same cooling system, small differences in heating during this period lead to a decreasing B_0 . When the trap is switched on for the first time the coils and resistors undergo a relatively large temperature change, but after the first cycle both parts heat up slowly and equally, so the central field is reproducible, with a drop of less than 0.1 G over the last 10 s. For stable operation in the following experiments we only went down with B_0 to a value of 0.5(1) G. If it were possible and necessary to determine B_0 more accurately, the influence of the rf power on the potential should be taken into account.

7.4.4 Tempo of forced evaporation

Forced evaporation is usually done by lowering the trap depth almost exponentially. In §7.4.6 the optimum time dependence for our situation according to theory is discussed. The simplest type of sweep the rf generator is capable of is decreasing the frequency in time steps of at least 50 ms with frequency steps of either a fixed size, leading to a linear sweep, or a fixed percentage, resulting in an exponential sweep (without offset). Experimentally, for a limited sweep to 15 MHz (~ 0.1 mK), the best results are obtained for an exponential sweep with smallest time steps, as expected. The same time dependence is kept at lower frequencies, although the optimum sweep will deviate in the final stage of cooling.

To determine the best exponential decay time τ_{rf} of the rf frequency, ideally the frequency range is broken up into several parts and each part is optimized separately, but this could not be implemented easily. That is why we start every time at the same frequency of 120 MHz and sweep to one of three end values: 50 MHz, 15 MHz, or 5 MHz. Figures 7.12 and 7.13 show the temperature, number of atoms, and elastic collision rate per atom after such ramps as a function of τ_{rf} . Optimizing on temperature alone, the best sweep would be as slow as possible, but then the number of atoms would be smaller than necessary due to trap decay. The collision rate depends on both quantities and is therefore a better parameter to optimize. In Fig. 7.13 a parabola is fitted to the two series with lowest end frequencies, resulting in the same optimum: $\tau_{\text{rf}} = 5.7$ s (0.87% frequency change per 50 ms time step). As the dependency on rf decay time is stronger for lower end frequencies, this means that an optimization in consecutive parts would

probably result in the same tempo, at least down to 5 MHz. For historical reasons we have chosen $\tau_{\text{rf}} = 5.0$ s (steps of 1%), which is close to the optimum. The rf should start in principle at the frequency corresponding to the trap barrier field, in this case 136 MHz. However, results are only very weakly dependent on the start frequency and seem to be slightly better at lower frequencies. Therefore we skip the first 0.6 s and start at 120 MHz.

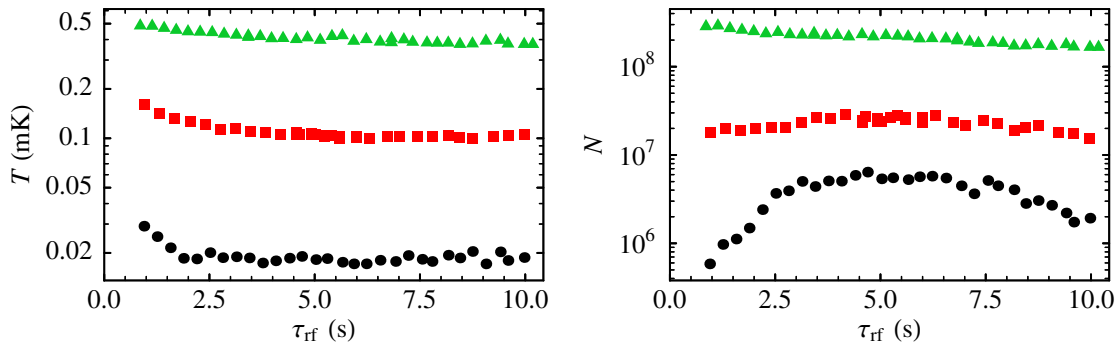


Figure 7.12. Temperature and number of atoms as a function of rf frequency decay constant, for sweeps to 5 MHz (dots), 15 MHz (squares), and 50 MHz (triangles).

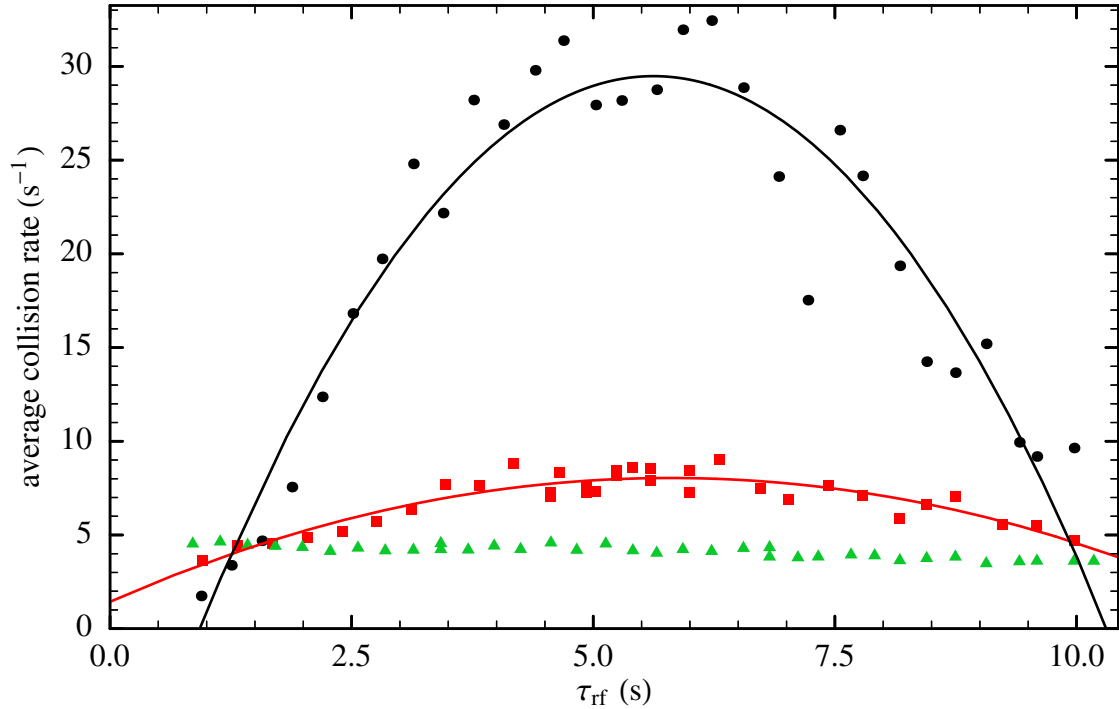


Figure 7.13. Collision rate averaged over the cloud as a function of rf frequency decay constant, for sweeps to 5 MHz (dots), 15 MHz (squares), and 50 MHz (triangles). Parabolic fits show the maximum in two cases.

7.4.5 Sweep

During a sweep starting at 120 MHz with an exponential time constant of 5.0 s, the progress of the temperature and number of atoms is followed both in absorption imaging and with the He* MCP detector. A series of images taken after 1 ms expansion is shown in Fig. 7.14. To emphasize the change in cloud size, maximum absorption within each image is rendered black. The central absorption varies from 62% in the leftmost image to 14% in the rightmost image. The smallest cloud contains $9(4) \times 10^6$ atoms at a temperature of $23(3) \mu\text{K}$. Figure 7.15 displays the horizontal and vertical rms radii as a function of temperature according to Gaussian fits of clouds as shown in Fig. 7.14. Vertical error bars indicate the standard deviation in the fitted radii, horizontal bars correspond to the range of temperatures if the offset velocity v_0 , used in TOF simulations (§2.2.3), varies between 0.18 m/s and 0.30 m/s (default value 0.21 m/s). When fitting TOF signals, the truncation of the energy distribution is not taken into account, which could lead to an underestimation of the temperature.

When the cloud is still in the trap, the shape is not really Gaussian; only below 17 μK will the rms radii calculated with a harmonic approximation of the trap deviate by less than 10% from the exact solution. For the theoretical shape therefore the density distribution given in §6.2.3 is used. The 1 ms expansion is taken into account by performing a numerical convolution with a Maxwell-Boltzmann velocity distribution, as described in §6.2.2. For a correct comparison with the experimental radii, the new distribution is integrated in one direction and fitted with a Gaussian curve. The resulting rms radii are connected with lines in Fig. 7.15. The radii are larger than expected, especially in the horizontal plane, resulting in a density that is half of the predicted value. This may be explained by the truncation of the energy distribution, or by a time lag between a change

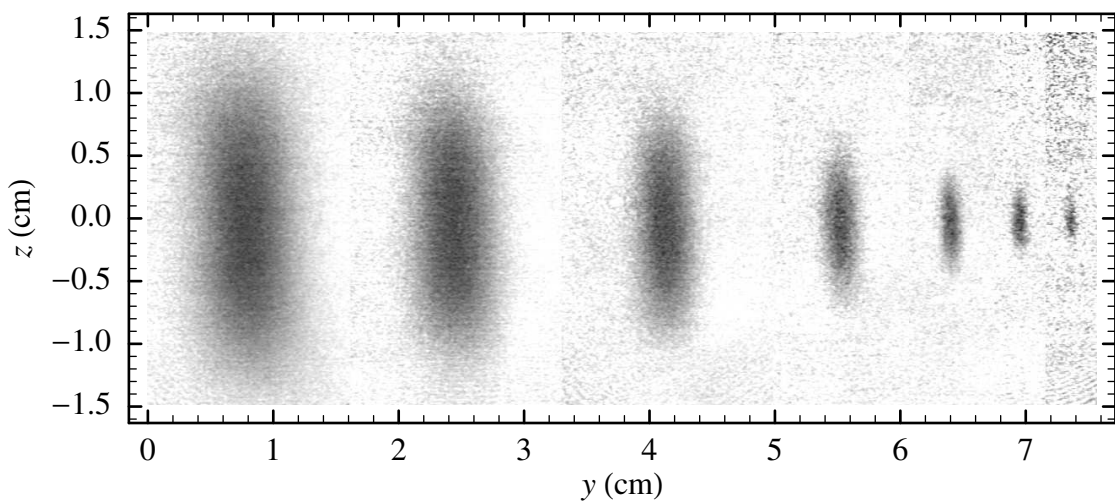


Figure 7.14. Collection of absorption images taken 1 ms after the cloverleaf trap is switched off, at various stages during an rf sweep. From left to right, just before rf is turned on, at 100 MHz, 65 MHz, 35 MHz, 15 MHz, 10 MHz, and 5 MHz. Each image is an average of about five realizations.

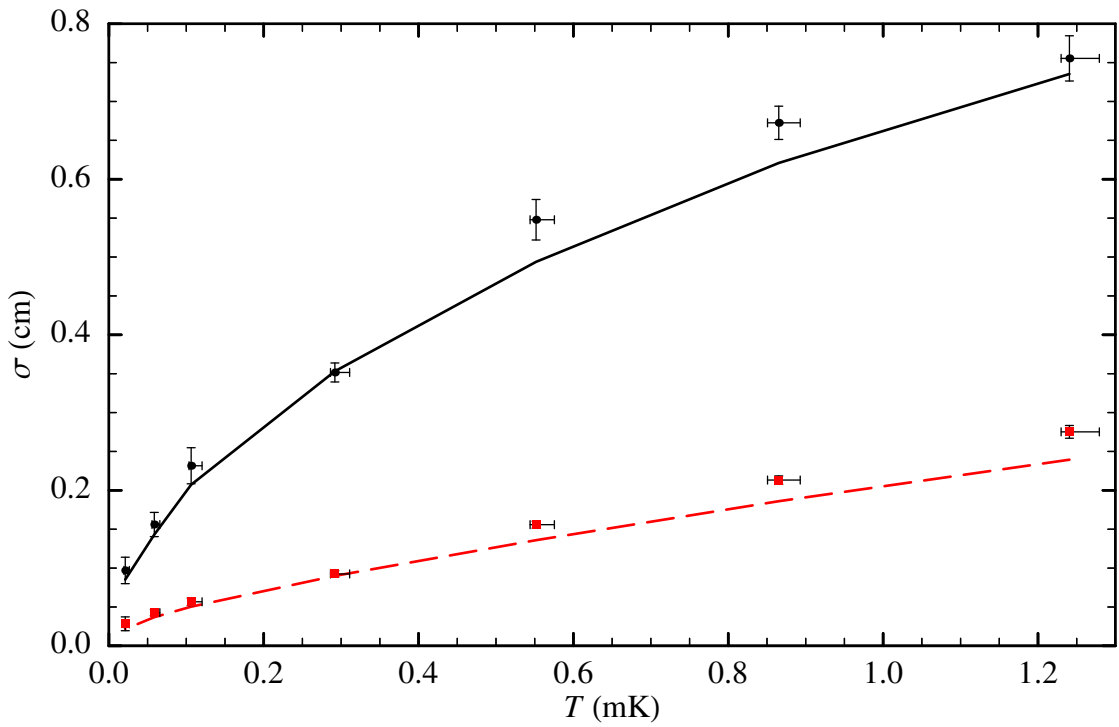


Figure 7.15. The rms radii taken from Gaussian fits to images as given in Fig. 7.14, as a function of temperature. Dots and solid curve are vertical radii, squares and dashed curve are horizontal radii. Curves connect theoretical expectation values, as discussed in the main text.

of trap depth and getting closer to steady state at a smaller cloud size: the sweep has to be executed rather fast, due to a limited trap lifetime of 12.5 s. In any case, for theoretical calculations the actual size during the sweep is required. A first-order correction of the modelled density distribution is to multiply trap parameters α and β with factors that are kept constant during the sweep. These are $f_\alpha = 0.74(9)$ and $f_\beta = 0.89(5)$, respectively, where the uncertainty includes the variation in the measured radii and the range of offset velocities. In §7.4.6 a confirmation will be given that this adaptation produces a better description of the cloud.

Figure 7.16 shows the temperature and number of atoms as a function of time since the start of the rf sweep. Each point is the result of a TOF measurement after the sweep is interrupted by turning off the rf power and the trap at the same time. The TOF signals after 0 s, 7 s, 13 s, and 17 s are shown in the central four plots of Fig. 2.6. Error bars in this and later figures are given as a grey band, including the 20% standard deviation in the calibration of the number of atoms according to the MCP detector (§2.3.7) and including the uncertainty in the temperature, which is characterized by a variation of the offset velocity $0.18 < v_0/(\text{m/s}) < 0.30$. The indirect effect of the temperature error on the number of atoms is automatically taken into account. In subsequent figures correction factors f_α and f_β for the theoretical cloud size are used, with appropriate values depending on v_0 . The uncertainty in these factors will form a third component of the error bar. The line is a theoretical calculation, assuming the scattering length

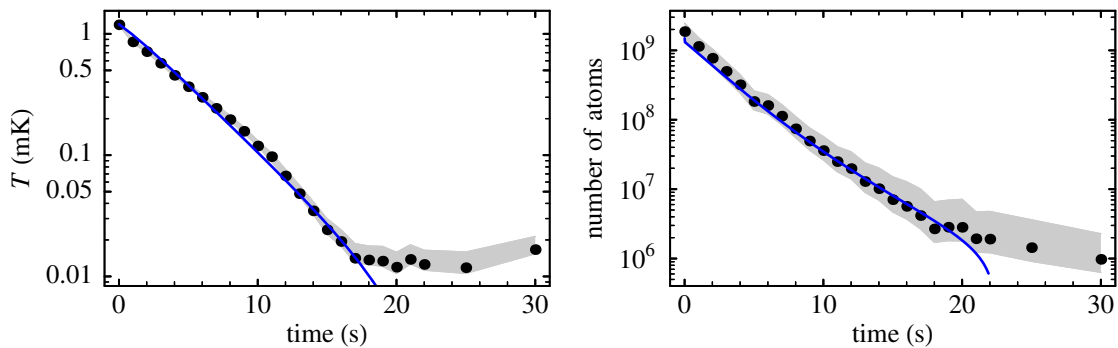


Figure 7.16. Temperature and number of atoms as a function of rf time during a sweep. Each point corresponds to an average of about eight realizations. The grey bands show the possible values due to uncertainty in the detector calibration and in the temperature. The curve is a simulation with $a = 10 \text{ nm}$.

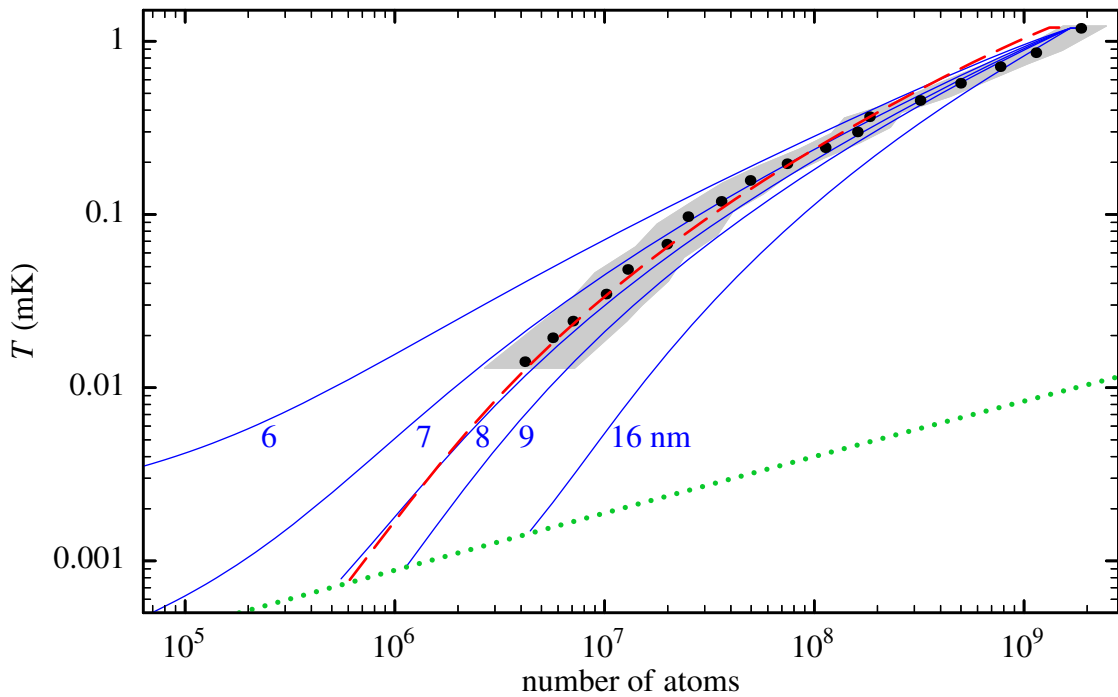


Figure 7.17. Temperature versus number of atoms during the sweep. Solid curves are theoretical calculations starting from $t = 0$ with the scattering length given by the curve label. The dashed curve is a simulation fitted to $\lg T$ and $\lg N$ with $a = 10 \text{ nm}$. The dotted line indicates the BEC transition for $\eta = \infty$. The grey band is used as in Fig. 7.16.

is 10 nm. The trap lifetime is measured to be 12.5 s, the measured heating rate of $0.7 \mu\text{K}/\text{s}$ is neglected, and the trap minimum is 0.5 G. Correction factors f_α and f_β for $v_0 = 0.21 \text{ m/s}$ are included, so $\alpha/2\mu_B = 51 \text{ G/cm}$ and $\beta/2\mu_B = 12.4 \text{ G/cm}^2$.

Due to an unexpected feature of the rf generator, below 7 MHz the rf power drops in the mode we had to use, dwindling to zero below 4 MHz. This means the rf is effectively turned off after 17 s, the temperature stays constant, and the number of atoms

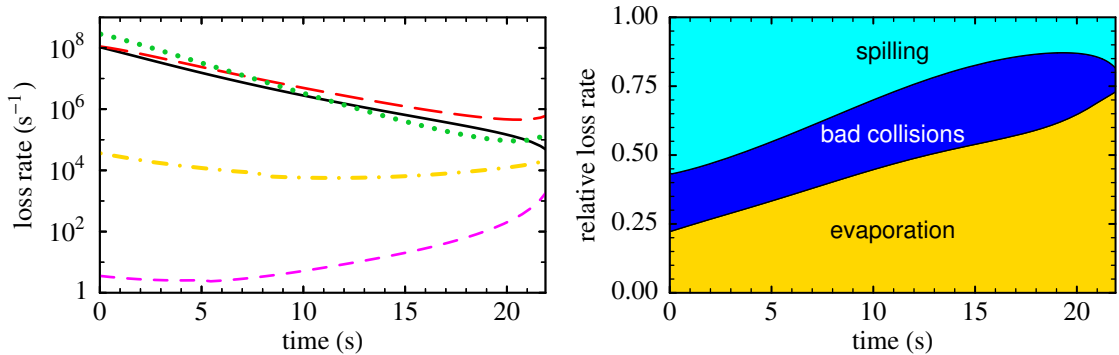


Figure 7.18. Absolute and relative atom loss rates due to background collisions \dot{N}_{bgr} (solid curve), evaporation \dot{N}_{ev} (long-dashed curve), spilling \dot{N}_θ (dotted curve), two-body collisions $\dot{N}_{2\text{b}}$ (dot-dashed curve), and three-body collisions $\dot{N}_{3\text{b}}$ (small-dashed curve), as a function of sweep time. In the right plot the three loss rates due to bad inelastic collisions are summed. This is according to the simulation with $a = 10 \text{ nm}$.

decreases only because of background collisions.[†] To see whether BEC would have been possible if the rf power continued to work, in Fig. 7.17 the points for times $0 \leq t/\text{s} \leq 17$ are given with the temperature plotted versus the number of atoms. The dotted line is the BEC transition (for $\eta = \infty$). Solid curves are sweeps simulated for several values of the scattering length, starting from the experimental values $T = 1.19 \text{ mK}$ and $N = 1.9 \times 10^9$ just before the rf is turned on. The theoretical sweep coming closest to the experimental values at $t = 17 \text{ s}$ assumes a scattering length of 8 nm. However, this method discards the points in between and assumes that all experimental stages of evaporation are equally well described by the model, which is not the case. For instance, turning on the rf is not modelled well, as the experimental temperature at $t = 1 \text{ s}$ is lower than expected (see Fig. 7.16). Later the number of atoms decreases faster than theory predicts, but at the end the 8 nm curve catches up. The dashed curve in Fig. 7.17 shows an alternative calculation, assuming a larger scattering length of 10 nm, but with 20% fewer atoms at the start. It fits better to the temperature and the number of atoms at $t \geq 5 \text{ s}$. Therefore this calculation is shown as an example in previous and following figures. Below the best value of the scattering length is determined by examining each 1 s interval separately.

According to the model, if the scattering length is larger than 7 nm, BEC should have been achievable. However, the model assumes three-dimensional evaporation: every atom with $\varepsilon > \varepsilon_t$ leaves the trap immediately. Due to gravitational sag, an atom moving in the $z = 0$ plane actually needs slightly more energy to be removed: $U(\rho_{\text{res}}, 0) = \varepsilon_t + mg|z_{\text{res}}|$. As the average energy of an evaporated atom is $\dot{E}_{\text{ev}}/\dot{N}_{\text{ev}} = \varepsilon_t + (W_{\text{ev}}/V_{\text{ev}})k_B T$, evaporation in this plane starts to become less efficient when $mg|z_{\text{res}}| > (W_{\text{ev}}/V_{\text{ev}})k_B T$, which in our case happens below $18 \mu\text{K}$. The evaporation gets one dimensional, the temperature will decrease more slowly, and BEC is harder to achieve [67].

The five atom loss rates used in the model are plotted as a function of time in Fig. 7.18, for the theoretical sweep with $a = 10 \text{ nm}$. According to this sweep, the

[†]In the spilling experiment $B_0 = 3.4 \text{ G}$, so there no problems arise.

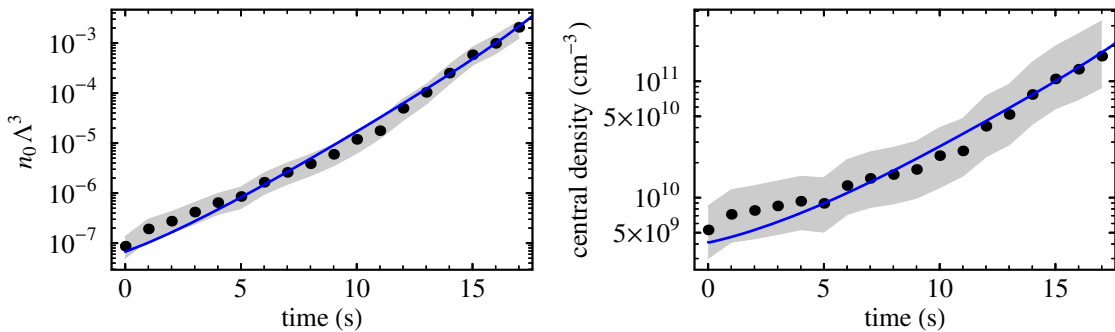


Figure 7.19. Phase-space density and central density as a function of sweep time. The curve is the simulation with $a = 10 \text{ nm}$; the grey bands indicate the error due to uncertainty in the number of atoms, temperature, and cloud size.

contribution of two- and three-body collisions is at most 3% and 0.2%, respectively, at the onset of BEC, which is theoretically after 22 s. At the start of the sweep the dominant loss process is spilling, because the frequency is decreased relatively fast. If the sweep took longer, spilling loss would be reduced in favour of evaporation loss, but this would be advantageous only if the trap lifetime were larger. For instance, if the sweep tempo and the trap decay rate were halved, the contribution of evaporation loss at the start would already increase from 22% to 36%. The figure shows that in the present situation an exponentially decreasing rf frequency goes unnecessarily fast towards the end: the spilling contribution increases in the last seconds.

The phase-space density reached in this sweep is $2.0(7) \times 10^{-3}$ (Fig. 7.19). In the experiment to find the potential minimum (Fig. 7.11) the phase-space density was probably higher. There the rf sweep was almost the same (start at 120 MHz, exponential decay time 5.7 s), but ending for instance at 6 MHz in a trap with $B_0 = 2.1 \text{ G}$ (TOF signal in Fig. 2.6, bottom right). This means the power drop of the rf generator at low frequencies was avoided. In this case the temperature was $1 \mu\text{K}$ (see §2.2.3), when BEC is reached theoretically with at least 6.6×10^6 atoms. According to the fit 8.2×10^6 atoms remained, but if the TOF signal corresponds to $2 \mu\text{K}$, the number of atoms was a factor of 11 smaller and the phase-space density 0.04. A lower number is more likely, judging by the trend at higher temperatures, and the error in the determination may be larger. Simulations show that BEC cannot be achieved with a high potential minimum, as the central density is too small.

The central density and phase-space density as a function of time during the sweep discussed here exhibit a slope change after 11 s, which is not seen in simulations with any value of the scattering length. A possible explanation may be that it takes some time before evaporative cooling works according to the model. In the plain evaporation experiments at high temperature this was the case because the elastic collision rate $R = 2\Gamma_c/N$ was not large enough for fast thermalization. Here, however, the collision rate at the start is at the centre 20 s^{-1} and averaged over the cloud 5 s^{-1} (Fig. 7.20), which should be sufficient. After 11 s runaway evaporation is reached, characterized by an increasing collision rate. The ratio of good to bad collisions $\mathcal{R} = -NR/(\dot{N}_{\text{bgr}} + \dot{N}_{\text{2b}} + \dot{N}_{\text{3b}})$, i.e. the average elastic collision rate R divided by the collisional loss rate per atom

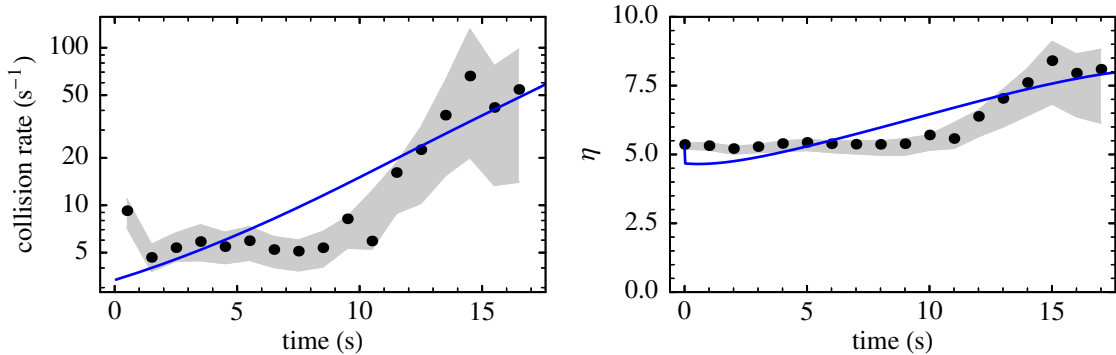


Figure 7.20. Average collision rate and truncation parameter as a function of sweep time. Curves and grey bands are used as in Fig. 7.19.

[37], increases during the sweep from 65 to at least 220. The truncation parameter η goes up from 5 to 8 (Fig. 7.20). For the determination of the possible error in the temperature calibration (§2.2.3), a range of η values is needed. We use $3 < \eta < 10$, encompassing deviations due to the slightly different circumstances in which the TOF signals concerned were measured.

To find the scattering length best describing the data, small sweeps are simulated for each interval between the data points. Starting from the experimental situation at one point with a constant σ in Eq. (7.34), the temperature at the end of the sweep is calculated. The values of σ for which the end temperature according to the model corresponds to the experimental temperature are given in the left plot of Fig. 7.21. The curve is the effective cross section according to Eq. (7.38) for $a = 10$ nm.

The scattering length determined with the experimental effective cross section and Eq. (7.38) is given in the right plot of Fig. 7.21. The two extra sets of points are according to the extreme offset velocities used in the calculation of the temperature error bar. The grey band is determined as before by combining this uncertainty with the 20% error in the calibration of the number of atoms and the uncertainty in the correction factors for the theoretical cloud size. The scattering length in this figure has been used with Eq. (7.52) to calculate the average collision rate in Fig. 7.20. The point in the first interval is omitted, because the effective cross section was unusually high. This in turn is caused by the unexpectedly large drop in temperature after turning on the rf power, which makes evaporation look very effective. It also affects the first point of the collision rate.

In the last part of the sweep the uncertainty in the scattering length becomes large due to the increasing uncertainty in the temperature determination. However, the possible error in a in the first half of the sweep may be larger than the grey bands in the figure, because the evaporation process seems not to behave entirely according to the model. Also, at the start we have to rely more on the model anyway, as the scattering length is only determined from evaporation, which then constitutes just a quarter of the atom loss rate (see Fig. 7.18). The average of all nominal and extreme values of a (dots and edges of grey band) is 10 nm, 26% larger than the value assuming σ_{eff} is constant. Although the energy dependence of the effective cross section leads to a significant correction of the determined scattering length, the data are too uncertain to confirm this

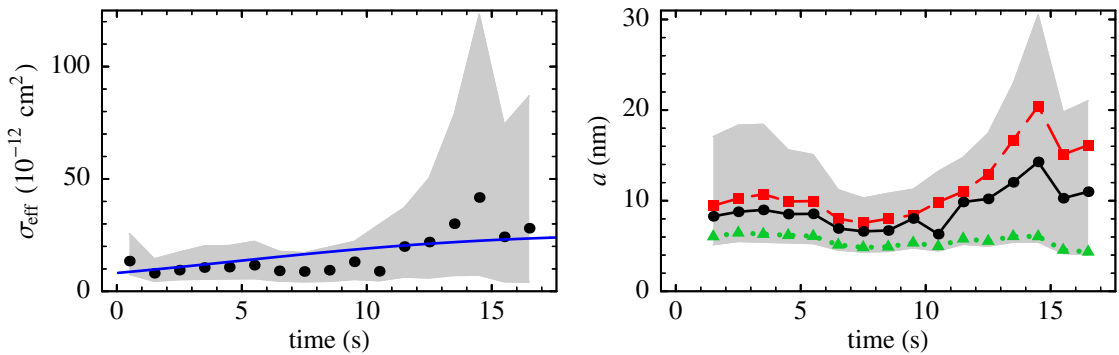


Figure 7.21. Effective cross section and scattering length as a function of sweep time. Points are given for a TOF simulation offset velocity of 0.18 m/s (squares), 0.21 m/s (dots), and 0.30 m/s (triangles), with corresponding values of f_α and f_β and the default MCP detector calibration. The curve in the left plot and the grey bands are used as in Fig. 7.19.

effect. Taking all uncertainties into account, a scattering length $|a| = 10(5)$ nm can be considered as consistent with the experimental data. This estimate compares well with the theoretical value $a = +12.2_{-4.1}^{+0}$ nm [16] (§7.2). The BEC experiment of the Orsay group originally yielded $a = +20(10)$ nm [69, 82]; later an improved value could be given of $a = +11.3_{-1.0}^{+2.5}$ nm [77]. The result of the ENS group is $a = +16(8)$ nm [65, 66], but later experiments are more consistent with a lower rather than a higher value within the uncertainty margin [42]. Although our value is determined at phase-space densities between 3 and 7 orders of magnitude away from the BEC transition, it is in good agreement with the other experimental results.

7.4.6 Optimization

To determine theoretically the best way of achieving BEC, an efficiency of evaporation α can be introduced, defined as

$$\alpha = -\frac{\dot{D}N}{D\dot{N}} = -\frac{d(\ln D)}{d(\ln N)}, \quad (7.68)$$

with phase-space density D [73]. This efficiency should be maximized at each moment during evaporative cooling to get a maximum increase in phase-space density while losing a minimum number of atoms. In a log-log plot of D versus N (Fig. 7.22), the slope is $-\alpha$ and should be as steep as possible. Care should be taken with loss due to spilling. While the negative effect of spilling is only seen at the time when the trap depth is lowered, the positive effect is also seen later by the fact that the evaporation rate has gone up. For a local optimization, one can best calculate the spilling loss as if η will be kept constant in the future. A program to this end was developed in Hannover [23]. It does not include gravitational sag and assumes a constant cross section. As input the average of the experimental effective cross section before $t = 11$ s is used (see Fig. 7.21), with the default offset velocity v_0 . The average scattering length in the low-temperature model is then $\sqrt{\sigma/8\pi} = 6.4$ nm. The starting point is the experimental temperature

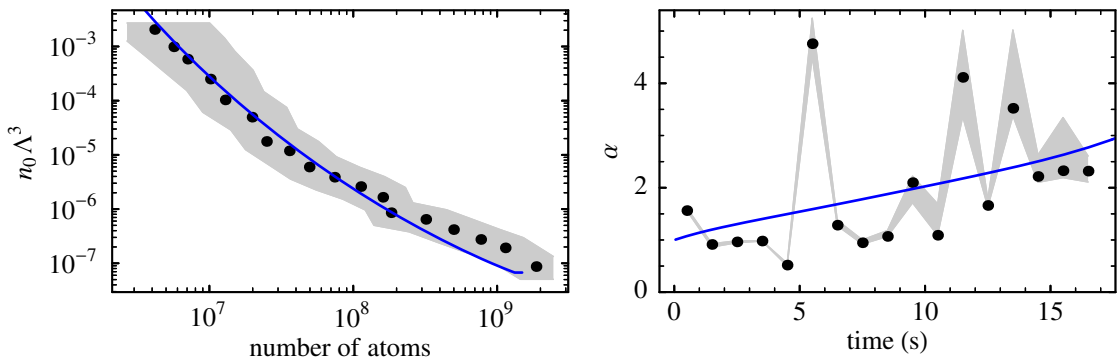


Figure 7.22. Phase-space density versus number of atoms, and the gradient of this function versus sweep time. Curves and grey bands are used as in Fig. 7.19.

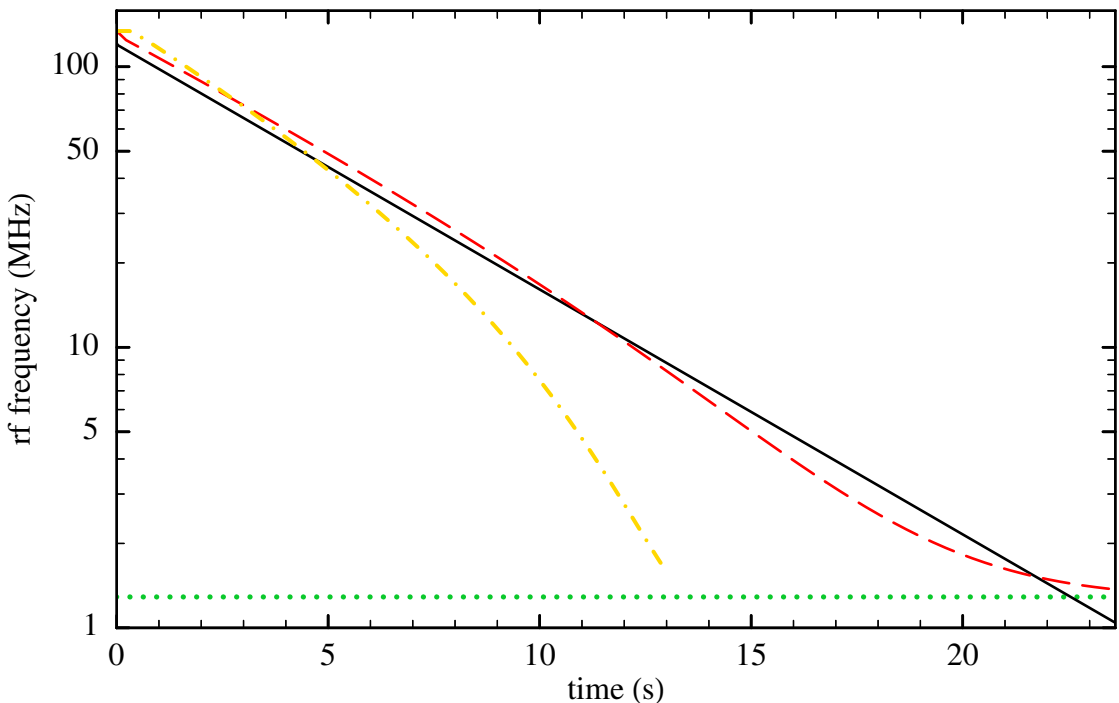


Figure 7.23. Rf frequency as a function of sweep time in the experiment (solid curve), according to a theoretical optimization with density correction (dashed curve) and without density correction (dot-dashed curve). The dotted line is the frequency corresponding to B_0 .

and number of atoms before rf is turned on. The optimized time dependence of the frequency is shown in Fig. 7.23 as the dashed curve, which only deviates significantly from the experimental sweep (solid curve) at the end. It confirms that the experimental optimization of the tempo yields the best possible sweep under the given circumstances. As expected, the sweep should become slower in the last seconds, but that stage is not reached yet. As a matter of interest, the optimized sweep ends in BEC with 3×10^5 atoms at $0.6 \mu\text{K}$, but the increasing cross section and gravitational sag are not taken into account.

This calculation is consistent with the experimentally found fact that the cloud is larger than it should be according to the model. If the correction factors for α and β are excluded, the cloud has a higher density and cooling can proceed twice as fast, shown as a dot-dashed curve in Fig. 7.23. This means theoretical optimization has limited use before an experimental sweep is examined, especially if the scattering length is unknown. However, it can help in finding improvements. For instance the same data without correction show that with a modest extra compression, BEC is achieved much easier, with a 4 times higher temperature and 25 times more atoms. Almost the same effect is reached if the trap lifetime is doubled to 25 s. We see this lifetime already when the slower valve is closed manually after trap loading, but that is not convenient. An automatic valve can be implemented, although care should be taken that vibrations do not disturb the trap. Other improvements are of course to make the rf generator more flexible to program and working at all frequencies. By rotating the trap so the stronger radial trap axis is vertical, gravitational sag is smaller and evaporation stays efficient at lower temperatures. At the moment detection of a condensate is difficult, because it would fall beside the MCP detector and the optical system is designed for large clouds before rf. All these points are addressed in the implementation of a newly designed trap, which is used in a fresh attempt to create a He^{*} condensate. This thesis may help with the interpretation of absorption and MCP data.

Bibliography

- [1] E. R. I. Abraham, W. I. McAlexander, J. M. Gerton, R. G. Hulet, R. Côté, and A. Dalgarno, ‘Triplet s-wave resonance in ${}^6\text{Li}$ collisions and scattering lengths of ${}^6\text{Li}$ and ${}^7\text{Li}^*$ ’, *Physical Review A* **55**, R3299–R3302 (May 1997).
- [2] M. Abramowitz and I. A. Stegun (eds.), *Handbook of Mathematical Functions with Formulas, Graphs, and Mathematical Tables*, National Bureau of Standards Applied Mathematics Series, No. 55 (U.S. GPO, Washington, DC, 1964).
- [3] M. H. Anderson, J. R. Ensher, M. R. Matthews, C. E. Wieman, and E. A. Cornell, ‘Observation of Bose-Einstein condensation in a dilute atomic vapor’, *Science* **269**, 198–201 (July 1995).
- [4] E. V. Baklanov and B. Ya. Dubetskii, ‘Fokker-Planck equation for gas atoms resonantly interacting with a light wave’, *Optics and Spectroscopy* **41**, 1–4 (July 1976) [*Optika i Spektroskopiya* **41**, 3–9 (July 1976)]. Constants t_0 and z_0 are given incorrectly.
- [5] F. Bardou, O. Emile, J.-M. Courty, C. I. Westbrook, and A. Aspect, ‘Magneto-optical trapping of metastable helium: Collisions in the presence of resonant light’, *Europhysics Letters* **20**, 681–686 (December 1992).
- [6] P. F. Bedaque, E. Braaten, and H.-W. Hammer, ‘Three-body recombination in Bose gases with large scattering length’, *Physical Review Letters* **85**, 908–911 (July 2000).
- [7] T. Bergeman, G. Erez, and H. J. Metcalf, ‘Magnetostatic trapping fields for neutral atoms’, *Physical Review A* **35**, 1535–1546 (February 1987).
- [8] C. C. Bradley, C. A. Sackett, J. J. Tollett, and R. G. Hulet, ‘Evidence of Bose-Einstein condensation in an atomic gas with attractive interactions’, *Physical Review Letters* **75**, 1687–1690 (August 1995).
- [9] C. C. Bradley, C. A. Sackett, and R. G. Hulet, ‘Bose-Einstein condensation of lithium: Observation of limited condensate number’, *Physical Review Letters* **78**, 985–989 (February 1997).

- [10] A. Browaeys, J. Poupard, A. Robert, S. Nowak, W. Rooijakkers, E. Arimondo, L. Marcassa, D. Boiron, C. I. Westbrook, and A. Aspect, ‘Two body loss rate in a magneto-optical trap of metastable He’, *The European Physical Journal D* **8**, 199–203 (February 2000).
- [11] A. Browaeys, A. Robert, O. Sirjean, J. Poupard, S. Nowak, D. Boiron, C. I. Westbrook, and A. Aspect, ‘Thermalization of magnetically trapped metastable helium’, *Physical Review A* **64**, 034703(4) (August 2001).
- [12] W. Chester, *Mechanics* (George Allen & Unwin, London, 1979).
- [13] E. Courtade, F. Marion, P.-J. Nacher, G. Tastevin, K. Kiersnowski, and T. Dohnalik, ‘Magnetic field effects on the 1083 nm atomic line of helium: Optical pumping of helium and optical polarisation measurement in high magnetic field’, *The European Physical Journal D* **21**, 25–55 (October 2002).
- [14] K. B. Davis, M.-O. Mewes, M. R. Andrews, N. J. van Druten, D. S. Durfee, D. M. Kurn, and W. Ketterle, ‘Bose-Einstein condensation in a gas of sodium atoms’, *Physical Review Letters* **75**, 3969–3973 (November 1995).
- [15] A. Derevianko and W. R. Johnson, ‘Two-photon decay of $2\ ^1S_0$ and $2\ ^3S_1$ states of heliumlike ions’, *Physical Review A* **56**, 1288–1294 (August 1997).
- [16] A. S. Dickinson, F. X. Gadéa, and T. Leininger, ‘Scattering lengths for spin-polarized metastable helium-3 and helium-4’, *Journal of Physics B: Atomic, Molecular and Optical Physics* **37**, 587–593 (February 2004).
- [17] G. W. F. Drake, ‘High precision calculations for helium’, in *Atomic, Molecular, & Optical Physics Handbook*, edited by G. W. F. Drake, chapter 11, pp. 154–171 (American Institute of Physics, Woodbury, NY, 1996).
- [18] G. W. F. Drake and W. C. Martin, ‘Ionization energies and quantum electrodynamic effects in the lower $1sns$ and $1snp$ levels of neutral helium (${}^4He\ I$)’, *Canadian Journal of Physics* **76**, 679–698 (September 1998).
- [19] P. O. Fedichev, M. W. Reynolds, U. M. Rahmanov, and G. V. Shlyapnikov, ‘Inelastic decay processes in a gas of spin-polarized triplet helium’, *Physical Review A* **53**, 1447–1453 (March 1996).
- [20] P. O. Fedichev, M. W. Reynolds, and G. V. Shlyapnikov, ‘Three-body recombination of ultracold atoms to a weakly bound s level’, *Physical Review Letters* **77**, 2921–2924 (September 1996).
- [21] V. V. Flambaum, G. F. Gribakin, and C. Harabati, ‘Analytical calculation of cold-atom scattering’, *Physical Review A* **59**, 1998–2005 (March 1999).
- [22] D. G. Fried, T. C. Killian, L. Willmann, D. Landhuis, S. C. Moss, D. Kleppner, and T. J. Greytak, ‘Bose-Einstein condensation of atomic hydrogen’, *Physical Review Letters* **81**, 3811–3814 (November 1998).

- [23] C. Fühner, *Numerische Simulation und Optimierung der Verdampfungskühlung*, Master's thesis, Institut für Quantenoptik der Universität Hannover, Ertmer group (December 1997).
- [24] F. X. Gadéa, T. Leininger, and A. S. Dickinson, 'Calculated scattering length for spin-polarized metastable helium', *Journal of Chemical Physics* **117**, 7122–7127 (October 2002).
- [25] B. Gao, 'Effects of Zeeman degeneracy on the steady-state properties of an atom interacting with a near-resonant laser field: Analytic results', *Physical Review A* **48**, 2443–2448 (September 1993). This article uses reduced Rabi frequency $\sqrt{2J_2 + 1} \Omega$, $f_m = \sqrt{C_{m,m}/(2J_2 + 1)}$ and $1/g_s = (2J_2 + 1)f$.
- [26] J. R. Gardner, R. A. Cline, J. D. Miller, D. J. Heinzen, H. M. J. M. Boesten, and B. J. Verhaar, 'Collisions of doubly spin-polarized, ultracold ^{85}Rb atoms', *Physical Review Letters* **74**, 3764–3767 (May 1995).
- [27] M. C. George, L. D. Lombardi, and E. A. Hessels, 'Precision microwave measurement of the $2\ ^3\text{P}_1 - 2\ ^3\text{P}_0$ interval in atomic helium: A determination of the fine-structure constant', *Physical Review Letters* **87**, 173002(4) (October 2001).
- [28] M. L. Goldberger and K. M. Watson, *Collision Theory* (John Wiley & Sons, New York, 1964).
- [29] N. Herschbach, P. J. J. Tol, W. Vassen, W. Hogervorst, G. Woestenenk, J. W. Thomsen, P. van der Straten, and A. Niehaus, 'Photoassociation spectroscopy of cold He($2\ ^3\text{S}$) atoms', *Physical Review Letters* **84**, 1874–1877 (February 2000).
- [30] N. Herschbach, P. J. J. Tol, W. Hogervorst, and W. Vassen, 'Suppression of Penning ionization by spin polarization of cold He($2\ ^3\text{S}$) atoms', *Physical Review A* **61**, 050702(R)(3) (April 2000).
- [31] N. Herschbach, P. J. J. Tol, A. S. Tychkov, W. Hogervorst, and W. Vassen, 'Magnetic trapping and evaporative cooling of metastable triplet helium', *Journal of Optics B: Quantum and Semiclassical Optics* **5**, S65–S74 (April 2003).
- [32] N. Herschbach, *Trapped Triplet Helium Atoms: Inelastic Collisions and Evaporative Cooling*, PhD thesis, Vrije Universiteit Amsterdam (April 2003).
- [33] R. C. Hilborn, 'Einstein coefficients, cross sections, f values, dipole moments, and all that', *American Journal of Physics* **50**, 982–986 (November 1982); **51**, 471(E) (May 1983); e-print physics/0202029 (February 2002).
- [34] J. C. Hill, L. L. Hatfield, N. D. Stockwell, and G. K. Walters, 'Direct demonstration of spin-angular-momentum conservation in the reaction $\text{He}(2\ ^3\text{S}_1) + \text{He}(2\ ^3\text{S}_1) \rightarrow \text{He}(1\ ^1\text{S}_0) + \text{He}^+ + \text{e}^-$ ', *Physical Review A* **5**, 189–195 (January 1972).

- [35] M. J. Jamieson, H. Sarbazi-Azad, H. Ouerdane, G.-H. Jeung, Y. S. Lee, and W. C. Lee, ‘Elastic scattering of cold caesium and rubidium atoms’, *Journal of Physics B: Atomic, Molecular and Optical Physics* **36**, 1085–1097 (February 2003).
- [36] P. S. Julienne, A. M. Smith, and K. Burnett, ‘Theory of collisions between laser cooled atoms’, *Advances in Atomic, Molecular, and Optical Physics* **30**, 141–198 (1993).
- [37] W. Ketterle and N. J. van Druten, ‘Evaporative cooling of trapped atoms’, *Advances in Atomic, Molecular, and Optical Physics* **37**, 181–236 (1996).
- [38] W. Ketterle, D. S. Durfee, and D. M. Stamper-Kurn, ‘Making, probing and understanding Bose-Einstein condensates’, in *Bose-Einstein Condensation in Atomic Gases*, edited by M. Inguscio, S. Stringari, and C. E. Wieman, Proceedings of the International School of Physics ‘Enrico Fermi’, Course CXL, pp. 67–176, Italian Physical Society (IOS Press, Amsterdam, 1999).
- [39] M. Kumakura and N. Morita, ‘Visible observation of metastable helium atoms confined in an infrared/visible double resonance trap’, *Japanese Journal of Applied Physics* **31**, L276–L279 (March 1992).
- [40] M. Kumakura and N. Morita, ‘Laser trapping of metastable ^3He atoms: Isotopic difference in cold Penning collisions’, *Physical Review Letters* **82**, 2848–2851 (April 1999).
- [41] G. Łach and K. Pachucki, ‘Forbidden transitions in the helium atom’, *Physical Review A* **64**, 042510(5) (October 2001).
- [42] M. Leduc, J. Léonard, F. Pereira dos Santos, E. Jahier, S. Schwartz, and C. Cohen-Tannoudji, ‘Hydrodynamic modes in a trapped gas of metastable helium above the Bose-Einstein transition’, *Acta Physica Polonica B* **33**, 2213–2224 (August 2002).
- [43] J. Léonard, M. Walhout, A. P. Mosk, T. Müller, M. Leduc, and C. Cohen-Tannoudji, ‘Giant helium dimers produced by photoassociation of ultracold metastable atoms’, *Physical Review Letters* **91**, 073203(4) (August 2003).
- [44] J. Léonard, A. P. Mosk, M. Walhout, P. van der Straten, M. Leduc, and C. Cohen-Tannoudji, ‘Analysis of photoassociation spectra for giant helium dimers’, *Physical Review A* **69**, 032702(12) (March 2004).
- [45] J. Léonard, *Photo-Association de l’Hélium Métastable au Voisinage de la Condensation de Bose-Einstein et Formation de Dimères Géants*, PhD thesis, Université Paris VI (November 2003).
- [46] R. J. Leroy and R. B. Bernstein, ‘Dissociation energies of diatomic molecules from vibrational spacings of higher levels: Application to the halogens’, *Chemical Physics Letters* **5**, 42–44 (February 1970).

- [47] V. S. Letokhov and V. G. Minogin, ‘Laser radiation pressure on free atoms’, *Physics Reports* **73**, 1–65 (July 1981).
- [48] P. D. Lett, W. D. Phillips, S. L. Rolston, C. E. Tanner, R. N. Watts, and C. I. Westbrook, ‘Optical molasses’, *Journal of the Optical Society of America B* **6**, 2084–2107 (November 1989).
- [49] P. D. Lett, K. Helmerson, W. D. Phillips, L. P. Ratliff, S. L. Rolston, and M. E. Wagshul, ‘Spectroscopy of Na₂ by photoassociation of laser-cooled Na’, *Physical Review Letters* **71**, 2200–2203 (October 1993).
- [50] P. D. Lett, P. S. Julienne, and W. D. Phillips, ‘Photoassociative spectroscopy of laser-cooled atoms’, *Annual Review of Physical Chemistry* **46**, 423–452 (October 1995).
- [51] O. J. Luiten, *Lyman- α Spectroscopy of Magnetically Trapped Atomic Hydrogen*, PhD thesis, Universiteit van Amsterdam (November 1993).
- [52] O. J. Luiten, M. W. Reynolds, and J. T. M. Walraven, ‘Kinetic theory of the evaporative cooling of a trapped gas’, *Physical Review A* **53**, 381–389 (January 1996).
- [53] H. C. Mastwijk, J. W. Thomsen, P. van der Straten, and A. Niehaus, ‘Optical collisions of cold, metastable helium atoms’, *Physical Review Letters* **80**, 5516–5519 (June 1998).
- [54] E. Merzbacher, *Quantum Mechanics* (John Wiley & Sons, New York, 1961).
- [55] A. J. Moerdijk, W. C. Stwalley, R. G. Hulet, and B. J. Verhaar, ‘Negative scattering length of ultracold ⁷Li gas’, *Physical Review Letters* **72**, 40–43 (January 1994).
- [56] H. W. Moos and J. R. Woodworth, ‘Observation of the forbidden 2 ³S₁ → 1 ¹S₀ spontaneous emission line from helium and measurement of the transition rate’, *Physical Review Letters* **30**, 775–778 (April 1973).
- [57] M. Movre and G. Pichler, ‘Resonance interaction and self-broadening of alkali resonance lines I: Adiabatic potential curves’, *Journal of Physics B: Atomic and Molecular Physics* **10**, 2631–2638 (September 1977).
- [58] M. W. Müller, A. Merz, M.-W. Ruf, H. Hotop, W. Meyer, and M. Movre, ‘Experimental and theoretical studies of the bi-excited collision systems He*(2 ³S) + He*(2 ³S, 2 ¹S) at thermal and subthermal kinetic energies’, *Zeitschrift für Physik D* **21**, 89–112 (August 1991).
- [59] R. J. Napolitano, S. C. Zilio, and V. S. Bagnato, ‘Adiabatic following conditions for the deceleration of atoms with the Zeeman tuning technique’, *Optics Communications* **80**, 110–114 (December 1990).

- [60] S. Nowak, A. Browaeys, J. Poupard, A. Robert, D. Boiron, C. I. Westbrook, and A. Aspect, ‘Magnetic trapping of metastable helium atoms’, *Applied Physics B: Lasers and Optics* **70**, 455–457 (March 2000).
- [61] N. Pacheco, ‘Helium’, in *Minerals Yearbook, Volume I: Metals and Minerals*, U.S. Geological Survey (U.S. GPO, Washington, DC, 2002).
- [62] N. Pacheco, ‘Helium’, in *Mineral Commodity Summaries 2004*, pp. 78–79, U.S. Geological Survey (U.S. GPO, Washington, DC, 2004).
- [63] F. Pereira dos Santos, F. Perales, J. Léonard, A. Sinatra, J. Wang, F. Saverio Pavone, E. Rasel, C. S. Unnikrishnan, and M. Leduc, ‘Efficient magneto-optical trapping of a metastable helium gas’, *The European Physical Journal – Applied Physics* **14**, 69–76 (April 2001).
- [64] F. Pereira dos Santos, F. Perales, J. Léonard, A. Sinatra, J. Wang, F. Saverio Pavone, E. Rasel, C. S. Unnikrishnan, and M. Leduc, ‘Penning collisions of laser-cooled metastable helium atoms’, *The European Physical Journal D* **14**, 15–22 (April 2001).
- [65] F. Pereira dos Santos, J. Léonard, J. Wang, C. J. Barrelet, F. Perales, E. Rasel, C. S. Unnikrishnan, M. Leduc, and C. Cohen-Tannoudji, ‘Bose-Einstein condensation of metastable helium’, *Physical Review Letters* **86**, 3459–3462 (April 2001).
- [66] F. Pereira dos Santos, J. Léonard, J. Wang, C. J. Barrelet, F. Perales, E. Rasel, C. S. Unnikrishnan, M. Leduc, and C. Cohen-Tannoudji, ‘Production of a Bose Einstein condensate of metastable helium atoms’, *The European Physical Journal D* **19**, 103–109 (April 2002).
- [67] P. W. H. Pinkse, A. P. Mosk, M. Weidemüller, M. W. Reynolds, T. W. Hijmans, and J. T. M. Walraven, ‘One-dimensional evaporative cooling of magnetically trapped atomic hydrogen’, *Physical Review A* **57**, 4747–4760 (June 1998).
- [68] J. Poupard, *Mesure de Deux Caractéristiques de l’Hélium Métastable Importantes pour le Refroidissement Radiatif: Taux de Pertes par Collisions en Présence de Lumière Quasi-Résonante et Taux de Transition des Raies Interdites $2^3P_1 \rightarrow 1^1S_0$ et $2^3P_2 \rightarrow 1^1S_0$* , PhD thesis, Université Paris XI Orsay (November 2000).
- [69] A. Robert, O. Sirjean, A. Browaeys, J. Poupard, S. Nowak, D. Boiron, C. I. Westbrook, and A. Aspect, ‘A Bose-Einstein condensate of metastable atoms’, *Science* **292**, 461–464 (April 2001).
- [70] W. Rooijackers, W. Hogervorst, and W. Vassen, ‘An intense collimated beam of metastable helium atoms by two-dimensional laser cooling’, *Optics Communications* **123**, 321–330 (January 1996).

- [71] W. Rooijakers, W. Hogervorst, and W. Vassen, ‘Laser deceleration and trapping of metastable helium atoms’, *Optics Communications* **135**, 149–156 (February 1997).
- [72] W. Rooijakers, *Laser Cooling and Trapping of Metastable Helium Atoms*, PhD thesis, Vrije Universiteit Amsterdam (January 1997).
- [73] C. A. Sackett, C. C. Bradley, and R. G. Hulet, ‘Optimization of evaporative cooling’, *Physical Review A* **55**, 3797–3801 (May 1997).
- [74] L. D. Schearer, M. Leduc, D. Vivien, A.-M. Lejus, and J. Thery, ‘LNA: A new cw Nd laser tunable around 1.05 and 1.08 μm ’, *IEEE Journal of Quantum Electronics* **22**, 713–717 (May 1986).
- [75] L. D. Schearer and L. A. Riseberg, ‘Spin conservation in ionizing collisions between He($2\ ^3\text{S}_1$) metastable atoms’, *Physics Letters A* **33**, 325–326 (November 1970).
- [76] S. Seidelin, O. Sirjean, J. Viana Gomes, D. Boiron, C. I. Westbrook, and A. Aspect, ‘Using ion production to monitor the birth and death of a metastable helium Bose-Einstein condensate’, *Journal of Optics B: Quantum and Semiclassical Optics* **5**, S112–S118 (April 2003).
- [77] S. Seidelin, J. Viana Gomes, R. Hoppeler, O. Sirjean, D. Boiron, A. Aspect, and C. I. Westbrook, ‘Getting the elastic scattering length by observing inelastic collisions in ultracold metastable helium atoms’, *Physical Review Letters* **93**, 090409(4) (August 2004).
- [78] K. Sengstock and W. Ertmer, ‘Laser manipulation of atoms’, *Advances in Atomic, Molecular, and Optical Physics* **35**, 1–44 (1995).
- [79] G. V. Shlyapnikov, J. T. M. Walraven, U. M. Rahmanov, and M. W. Reynolds, ‘Decay kinetics and Bose condensation in a gas of spin-polarized triplet helium’, *Physical Review Letters* **73**, 3247–3250 (December 1994).
- [80] W. A. Shurcliff and S. S. Ballard, *Polarized Light*, Van Nostrand Momentum Books 7 (D. Van Nostrand Company, Princeton, NJ, 1964).
- [81] A. E. Siegman, *Lasers* (University Science Books, Mill Valley, CA, 1986).
- [82] O. Sirjean, S. Seidelin, J. Viana Gomes, D. Boiron, C. I. Westbrook, A. Aspect, and G. V. Shlyapnikov, ‘Ionization rates in a Bose-Einstein condensate of metastable helium’, *Physical Review Letters* **89**, 220406(4) (November 2002).
- [83] J. Stärck and W. Meyer, ‘Long-range interaction potential of the $^5\Sigma_g^+$ state of He₂’, *Chemical Physics Letters* **225**, 229–232 (July 1994).
- [84] C. H. Storry, M. C. George, and E. A. Hessels, ‘Precision microwave measurement of the $2\ ^3\text{P}_1 - 2\ ^3\text{P}_2$ interval in atomic helium’, *Physical Review Letters* **84**, 3274–3277 (April 2000).

- [85] W. C. Stwalley, ‘The dissociation energy of the hydrogen molecule using long-range forces’, *Chemical Physics Letters* **6**, 241–244 (August 1970).
- [86] W. C. Stwalley and H. Wang, ‘Photoassociation of ultracold atoms: A new spectroscopic technique’, *Journal of Molecular Spectroscopy* **195**, 194–228 (June 1999).
- [87] K.-A. Suominen, ‘Theories for cold atomic collisions in light fields’, *Journal of Physics B: Atomic, Molecular and Optical Physics* **29**, 5981–6007 (December 1996).
- [88] D. Suter, *The Physics of Laser-Atom Interactions*, Cambridge Studies in Modern Optics (Cambridge University Press, Cambridge, 1997).
- [89] E. Tiesinga, C. J. Williams, P. S. Julienne, K. M. Jones, P. D. Lett, and W. D. Phillips, ‘A spectroscopic determination of scattering lengths for sodium atom collisions’, *Journal of Research of the National Institute of Standards and Technology* **101**, 505–520 (July/August 1996).
- [90] P. J. J. Tol, N. Herschbach, E. A. Hessels, W. Hogervorst, and W. Vassen, ‘Large numbers of cold metastable helium atoms in a magneto-optical trap’, *Physical Review A* **60**, R761–R764 (August 1999).
- [91] P. J. J. Tol, W. Hogervorst, and W. Vassen, ‘Theory of evaporative cooling with energy-dependent elastic scattering cross section and application to metastable helium’, *Physical Review A* **70**, 013404(10) (July 2004).
- [92] C. G. Townsend, N. H. Edwards, C. J. Cooper, K. P. Zetie, C. J. Foot, A. M. Steane, P. Sriftgiser, H. Perrin, and J. Dalibard, ‘Phase-space density in the magneto-optical trap’, *Physical Review A* **52**, 1423–1440 (August 1995).
- [93] R. S. Van Dyck, Jr., S. L. Zafonte, S. Van Liew, D. B. Pinegar, and P. B. Schwinberg, ‘Ultraprecise atomic mass measurement of the α particle and ${}^4\text{He}$ ’, *Physical Review Letters* **92**, 220802(4) (June 2004).
- [94] N. Vansteenkiste, C. Gerz, R. Kaiser, L. Hollberg, C. Salomon, and A. Aspect, ‘A frequency-stabilized LNA laser at $1.083\ \mu\text{m}$: Application to the manipulation of helium 4 atoms’, *Journal de Physique II* **1**, 1407–1428 (December 1991).
- [95] V. Venturi, I. B. Whittingham, P. J. Leo, and G. Peach, ‘Close-coupled calculation of collisions of magnetostatically trapped metastable helium atoms’, *Physical Review A* **60**, 4635–4646 (December 1999).
- [96] M. Walhout, U. Sterr, C. Orzel, M. D. Hoogerland, and S. L. Rolston, ‘Optical control of ultracold collisions in metastable xenon’, *Physical Review Letters* **74**, 506–509 (January 1995).
- [97] T. Walker, D. Sesko, and C. E. Wieman, ‘Collective behavior of optically trapped neutral atoms’, *Physical Review Letters* **64**, 408–411 (January 1990).

- [98] G. N. Watson, *A Treatise on the Theory of Bessel Functions* (Cambridge University Press, Cambridge, 1922).
- [99] J. Weiner, V. S. Bagnato, S. Zilio, and P. S. Julienne, ‘Experiments and theory in cold and ultracold collisions’, *Reviews of Modern Physics* **71**, 1–85 (January 1999).
- [100] J. Wells, *Nuclear Weapons: Challenges Remain for Successful Implementation of DOE’s Tritium Supply Decision*, Report GAO/RCED-00-24, U.S. General Accounting Office, Washington, DC (January 2000).
- [101] C. I. Westbrook, A. Robert, O. Sirjean, A. Browaeys, D. Boiron, and A. Aspect, ‘Bose-Einstein condensation of metastable helium: Some experimental aspects’, in *Proceedings of the XV International Conference on Laser Spectroscopy*, edited by S. Chu, V. Vuletić, A. J. Kerman, and C. Chin, pp. 12–20 (World Scientific, New Jersey, 2002).
- [102] J. L. Wiza, ‘Microchannel plate detectors’, *Nuclear Instruments and Methods* **162**, 587–601 (June 1979).
- [103] G. K. Woodgate, *Elementary Atomic Structure* (Clarendon Press, Oxford, 1980), second edition.
- [104] J. R. Woodworth and H. W. Moos, ‘Experimental determination of the single-photon transition rate between the $2\ ^3S_1$ and $1\ ^1S_0$ states of He I’, *Physical Review A* **12**, 2455–2463 (December 1975).
- [105] Z.-C. Yan and J. F. Babb, ‘Long-range interactions of metastable helium atoms’, *Physical Review A* **58**, 1247–1252 (August 1998).
- [106] P. Ziń, A. Dragan, S. Charzyński, N. Herschbach, P. J. J. Tol, W. Hogervorst, and W. Vassen, ‘The effect of atomic transfer on the decay of a Bose-Einstein condensate’, *Journal of Physics B: Atomic, Molecular and Optical Physics* **36**, L149–L154 (March 2003).

List of publications

LARGE NUMBERS OF COLD METASTABLE HELIUM ATOMS IN A MAGNETO-OPTICAL TRAP

P. J. J. Tol, N. Herschbach, E. A. Hessels, W. Hogervorst, and W. Vassen, *Physical Review A* **60**, R761–R764 (August 1999) [Chapter 3].

SUPPRESSION OF PENNING IONIZATION BY SPIN POLARIZATION OF COLD HE($2\ ^3S$) ATOMS

N. Herschbach, P. J. J. Tol, W. Hogervorst, and W. Vassen, *Physical Review A* **61**, 050702(R)(3) (April 2000) [Chapter 4].

PHOTOASSOCIATION SPECTROSCOPY OF COLD HE($2\ ^3S$) ATOMS

N. Herschbach, P. J. J. Tol, W. Vassen, W. Hogervorst, G. Woestenenk, J. W. Thomsen, P. van der Straten, and A. Niehaus, *Physical Review Letters* **84**, 1874–1877 (February 2000) [Chapter 5].

MAGNETIC TRAPPING AND EVAPORATIVE COOLING OF METASTABLE TRIPLET HELIUM

N. Herschbach, P. J. J. Tol, A. S. Tychkov, W. Hogervorst, and W. Vassen, *Journal of Optics B: Quantum and Semiclassical Optics* **5**, S65–S74 (April 2003).

THEORY OF EVAPORATIVE COOLING WITH ENERGY-DEPENDENT ELASTIC SCATTERING CROSS SECTION AND APPLICATION TO METASTABLE HELIUM

P. J. J. Tol, W. Hogervorst, and W. Vassen, *Physical Review A* **70**, 013404(10) (July 2004) [parts of Chapter 6 and 7].

THE EFFECT OF ATOMIC TRANSFER ON THE DECAY OF A BOSE-EINSTEIN CONDENSATE

P. Ziń, A. Dragan, S. Charzyński, N. Herschbach, P. J. J. Tol, W. Hogervorst, and W. Vassen, *Journal of Physics B: Atomic, Molecular and Optical Physics* **36**, L149–L154 (March 2003).

Summary

When a gas is cooled almost to absolute zero (-273.15°C , 0 K), the interaction between the slow gas atoms exhibits properties related to the wavelike behaviour of the atoms. For example, when a gas of bosons (e.g. ordinary hydrogen and helium atoms and many alkali-metal atoms) gets sufficiently cold and dense, Bose-Einstein condensation (BEC) takes place. This is an effect arising from the quantum behaviour of assemblies of identical particles: the quantum-mechanical waves that describe the atoms spread out and overlap, which forces the atoms into the same state with the lowest energy, even if there are no interactions present. For instance the phenomenon of superfluidity, the property of sufficiently cooled liquid helium to flow through channels without resistance, is explained by relying on the concept of BEC. However, the BEC process itself is obscured by the strong interactions in the liquid.

In the experiment described here, helium is not liquefied, but kept gaseous and cooled with photons from a laser beam. For helium in the ground state extreme ultra-violet light is needed, which renders the cooling practically impossible. The atoms are therefore excited in a discharge to a metastable state with a lifetime of more than two hours, while experiments last less than a minute. Then infrared light can be used to manipulate the atoms. Chapter 1 describes the experimental setup to do this.

Light is also used to determine the number of atoms in a gas cloud, by sending a pulse of laser light through the cloud on to a camera and by measuring the absorption. Textbooks give a simple expression relating the relative absorption to the number of atoms, cloud shape, and wavelength of the light. However, this expression is valid only for circularly polarized, low-intensity resonant laser light with a small bandwidth and for cold spin-polarized atoms (i.e. with their spins all lined up in the same direction). In Chapter 2 a derivation is given for the arbitrary case, from which the number of atoms can be determined accurately while the approximations for the simple case can be tested one by one. The temperature cannot be neglected in the case of helium. The camera is relatively insensitive to the infrared light used, but the intensity can be set just low enough to reach the low-intensity regime. The pulse duration is short to avoid pushing of the helium atoms, implying there is not enough time to spin-polarize the atoms. Using linearly polarized laser light diminishes the effect of the atomic state on the calculated number of atoms. The model also includes the influence of a magnetic field on absorption. Due to the large internal energy, metastable helium atoms almost

always release electrons when they hit a metal surface. This effect is used in a so-called microchannel plate detector to measure relative numbers of atoms. Because two detection techniques are available in the setup, results can be compared.

Clouds of several billion atoms at a temperature of 1 mK are confined in a magneto-optical trap, a combination of a magnetic field and six light beams. Never before were so many helium atoms loaded into this type of trap. The cloud density is limited by Penning ionization: collisions between two trapped atoms or between a trapped atom and a background atom transfer the large internal energy of a metastable helium atom to the other atom, which usually ionizes. To trap these numbers of atoms, the cloud is allowed to be large, with a diameter of about 1 cm. In Chapter 3 the method is explained and the trap is characterized, including the loss rate due to Penning ionization. In Chapter 5 this loss rate is measured as a function of laser frequency, showing previously unseen peaks, so-called photoassociation resonances. Penning ionization occurs at a smaller rate when the trap light is turned off for a moment and at a much smaller rate when additionally the atoms are spin-polarized, as demonstrated in Chapter 4. To be able to increase the cloud density, the atoms are therefore brought into a magnetic trap without light, where atoms in only one state are confined, ensuring spin polarization.

Chapter 6 describes the clouds in the magneto-optical trap and two types of purely magnetic traps, a quadrupole trap and a cloverleaf trap. Cloud sizes are compared with theoretical calculations. The implementation of the quadrupole trap is simple, but at its centre there is no magnetic field and the atoms can leak out. This problem is solved in the cloverleaf trap, although the coil geometry is more complicated. After the cloud has been loaded in this last trap, the confinement is made stronger to compress the cloud.

At the end of compression, the density has increased sufficiently to start using a technique known as evaporative cooling: the most energetic atoms leave the trap and by elastic collisions the energy of the remaining atoms is redistributed. The average energy of the remaining atoms becomes smaller, resulting in a colder and denser cloud. To keep the process going, the trap depth is gradually lowered using a radio frequency field. The efficiency of evaporative cooling is determined by the cross section of helium for elastic collisions, which increases when the temperature is lowered. Below 10 μK the cross section becomes almost a constant, and the evaporative cooling can be described with a set of relatively simple equations using a parameter called the scattering length. However, the cooling starts at 1 mK, when these equations are not valid. In Chapter 7 the relevant equations are derived again, but this time for arbitrary temperatures. This is followed by a comparison of the theory with experiment, which is consistent when the scattering length is assumed to be 10 nm. It can be 5 nm smaller or larger due to the remaining uncertainty in the number of atoms, temperature, and cloud size. This estimate compares well with the theoretical value of the scattering length, which is between 8 nm and 12 nm. It is also in good agreement with recent results of other experimental groups.

Due to technical difficulties, the cooling process stopped when the cloud contained about 4 million atoms at a temperature of 14 μK . According to theoretical extrapolations of the experimental results, if the cooling is continued maybe a condensate is formed, but only below 1 μK when the cloud no longer contains enough atoms to detect in the present setup.

Samenvatting

Metastabiel helium vangen en verdampingskoelen

Wanneer een gas bijna tot het absolute nulpunt ($-273,15^{\circ}\text{C}$, 0 K) gekoeld wordt, vertoont de wisselwerking tussen de langzame gasatomen eigenschappen die betrekking hebben op het golfkarakter van de atomen. Als bijvoorbeeld een gas van bosonen (zoals gewone waterstof- en heliumatomen en vele alkalimetaalatomen) voldoende koud en dicht wordt, treedt er Bose-Einsteincondensatie (BEC) op. Dit effect is een gevolg van het quantumgedrag van verzamelingen identieke deeltjes: de quantummechanische golven die de atomen beschrijven, spreiden zich uit en overlappen elkaar, wat de atomen in dezelfde toestand met de laagste energie dwingt, zelfs als er geen wisselwerkingen zijn. Zo steunt de verklaring van het verschijnsel superfluiditeit, de eigenschap van voldoende afgekoeld vloeibaar helium om zonder wrijving door kanalen te stromen, op het begrip BEC. Het verloop van BEC zelf is echter gecompliceerd door de sterke wisselwerkingen in de vloeistof.

In het hier beschreven experiment wordt helium niet vloeibaar gemaakt, maar gasvormig gehouden en gekoeld met fotonen uit een laserbundel. Voor helium in de grondtoestand is extreem-ultraviolet licht nodig, wat het koelen praktisch onmogelijk maakt. De atomen worden daarom met een ontlading in een metastabiele toestand gebracht die meer dan twee uurleeft, terwijl experimenten minder dan een minuut duren. Dan kan infrarood licht gebruikt worden om de atomen te manipuleren. Hoofdstuk 1 beschrijft de experimentele opstelling om dit te doen.

Licht wordt ook gebruikt om het aantal atomen in een gaswolk te bepalen, door een flits laserlicht door de wolk op een camera te laten vallen en de absorptie te meten. Leerboeken geven een simpele uitdrukking voor het verband tussen de relatieve absorptie, het aantal atomen, de vorm van de wolk en de golflengte van het licht. Deze uitdrukking is echter alleen geldig voor circulair gepolariseerd, resonant laserlicht met een lage intensiteit en een kleine bandbreedte, en voor koude spin gepolariseerde atomen (d.w.z. met al hun spins wijzend in dezelfde richting). In hoofdstuk 2 wordt een afleiding gegeven voor het algemene geval, waarmee het aantal atomen nauwkeurig bepaald kan worden terwijl de benaderingen voor het simpele geval één voor één getest kunnen worden. De temperatuur kan niet verwaarloosd worden in het geval van helium. De camera is betrekkelijk ongevoelig voor het gebruikte infrarood licht, maar de intensiteit kan juist

laag genoeg ingesteld worden om het lage-intensiteitsregime te bereiken. De flits duurt kort om te vermijden dat de heliumatomen geduwd worden, wat betekent dat er niet genoeg tijd is voor spinpolarisatie van de atomen. Het gebruik van lineair gepolariseerd laserlicht verkleint het effect van de atomaire toestand op het berekende aantal atomen. Het model bevat ook de invloed van een magneetveld op absorptie. Door hun grote interne energie maken metastabiele heliumatomen bijna altijd elektronen los als ze een metalen oppervlak raken. Dit effect wordt gebruikt in een zogenoemde *microchannel plate* detector om relatieve aantallen atomen te meten. Omdat er twee detectietechnieken beschikbaar zijn in de opstelling, kunnen resultaten vergeleken worden.

Wolken van enige miljarden atomen worden bij een temperatuur van 1 mK opgesloten in een magneto-optische val, een combinatie van een magneetveld en zes lichtbundels. Nooit eerder werden zoveel heliumatomen in dit type val geladen. De dichtheid van de wolk wordt beperkt door Penningionisatie: botsingen tussen twee gevangen atomen of tussen een gevangen atoom en een atoom uit de omgeving dragen de grote interne energie van een metastabiel heliumatoom over op het andere atoom, dat doorgaans ioniseert. Om deze aantallen atomen te vangen moet de wolk groot blijven, met een diameter van ongeveer 1 cm. In hoofdstuk 3 wordt de methode uitgelegd en de val gekarakteriseerd, inclusief de verliezen door Penningionisatie. In hoofdstuk 5 worden deze verliezen gemeten als functie van laserfrequentie, wat niet eerder gevonden pieken aantoont, die fotoassociatieresonanties genoemd worden. Penningionisatie gebeurt met een kleinere snelheid wanneer het licht in de val voor een moment uitgezet wordt en met een veel kleinere snelheid als de atomen bovendien spingepolariseerd zijn, zoals aangeïntroduceerd in hoofdstuk 4. Om de dichtheid van de wolk te kunnen vergroten, worden de atomen daarom in een magneetval zonder licht gebracht, waar slechts atomen in één toestand opgesloten zijn, wat spinpolarisatie zeker maakt.

Hoofdstuk 6 beschrijft de wolken in de magneto-optische val en twee soorten puur magnetische vallen, een quadrupoolval en een klaverbladval. Wolkgrootten worden vergeleken met theoretische berekeningen. De uitvoering van de quadrupoolval is simpel, maar in haar middelpunt is geen magneetveld en kunnen er atomen uit lekken. Dit probleem is opgelost in de klaverbladval, maar het spoelenstelsel is ingewikkelder. Nadat de wolk in deze laatste val geladen is, wordt de val sterker gemaakt om de wolk te verdichten.

Aan het einde van de samendrukking is de dichtheid voldoende toegenomen om te beginnen met een techniek die verdampingskoeling genoemd wordt: de atomen met de meeste energie verlaten de val en door elastische botsingen wordt de energie van de overgebleven atomen herverdeeld. De gemiddelde energie van de resterende atomen wordt kleiner, uitmondend in een koudere en dichtere wolk. Om het proces door te laten gaan wordt de valdiepte geleidelijk verlaagd met een rf-veld. De doelmatigheid van verdampingskoeling wordt bepaald door de doorsnede van helium voor elastische botsingen, die toeneemt als de temperatuur lager wordt. Beneden 10 μK wordt de doorsnede bijna een constante en kan de verdampingskoeling beschreven worden met een stel betrekkelijk simpele vergelijkingen waarbij de ‘verstrooiingslengte’ als parameter gebruikt wordt. De koeling begint echter bij 1 mK, waar deze vergelijkingen niet geldig zijn. In hoofdstuk 7 worden de desbetreffende vergelijkingen opnieuw afgeleid, maar deze keer voor willekeurige temperaturen. Dit wordt gevolgd door een vergelijking van

de theorie met het experiment, die consistent is als een verstrooiingslengte van 10 nm wordt aangenomen. Ze kan 5 nm kleiner of groter zijn vanwege de nog overgebleven onzekerheid in het aantal atomen, de temperatuur en de wolkgrootte. Deze schatting laat zich vergelijken met de theoretische waarde van de verstrooiingslengte, die tussen 8 nm en 12 nm ligt. Ze komt ook goed overeen met recente resultaten van andere experimentele groepen.

Door technische moeilijkheden stopte het koelingsproces als de wolk zo'n 4 miljoen atomen bevatte bij een temperatuur van 14 μK . Volgens theoretische extrapolaties van de experimentele resultaten wordt er misschien een condensaat gevormd als de koeling door zou gaan, maar alleen beneden 1 μK wanneer de wolk niet meer genoeg atomen bevat om in de huidige opstelling te detecteren.

